Syngas Conversion at the Rhodium–Metal Oxide Interface

vorgelegt von

M. Sc.

Phil Even Preikschas

ORCID: 0000-0003-1285-7813

an der Fakultät II – Mathematik und Naturwissenschaften

der Technischen Universität Berlin

zur Erlangung des akademischen Grades

Doktor der Naturwissenschaften

Dr. rer. nat.

genehmigte Dissertation

Promotionsausschuss:

Vorsitzender: Prof. Dr. Maria Andrea Mroginski (Technische Universität Berlin)

Gutachter: Prof. Dr. Matthias Driess (Technische Universität Berlin)

Gutachter: Prof. Dr. Martin Muhler (Ruhr-Universität Bochum)

Gutachter: Dr. Frank Rosowski (BASF SE)

Tag der wissenschaftlichen Aussprache: 30. September 2021

Berlin 2021

Abstract

The syngas-to-ethanol (StE) reaction is a promising alternative route to ethanol from fossil and nonfossil carbon resources. Rh-based catalysts offer the highest ethanol yields so far but suffer from low to moderate CO conversion and high methane selectivity. Despite serious research efforts, ethanol rates and selectivities still need to be improved for industrial application.

Current research focuses mainly on improving Rh-based catalysts by the addition of one or usually several promoters. Likewise, peak performance marks have been published readily without considering the catalyst's long-term stability, and as a consequence, a lack of spent sample characterization still exists. All these circumstances limit our fundamental understanding of promoter effects hampering a rational design of new catalysts.

However, an improvement of existing or the development of new catalytic systems is required before the conversion of StE can be economically feasible. Moreover, the drastically increased Rh price over the past five years necessitates the search for an alternative active metal. Still, the replacement of Rh seems to be challenging, although promising results have been achieved by modifying methanol and Fischer-Tropsch synthesis catalysts. Especially, the formation of higher alcohols and oxygenates are often not evitable over Rh-free catalysts. Thus, lowering the Rh content is required rather than replacing Rh in its entirety to develop cost-efficient ethanol synthesis catalysts. An in-depth understanding of Rh's intrinsic reactivity and the influence of promoters might lead to new strategies for decreasing the Rh content.

For this reason, this thesis aims to provide a holistic view of the crucial interplay of Rh–promoter interactions, reaction conditions, and reaction times. The thesis is based on three independent publications covering metal-organic synthesis approaches, detailed catalyst characterizations, formation phase studies, and long-term catalytic investigations.

Before more sophisticated catalyst design strategies became viable, specific promoter effects in traditionally prepared Rh-based catalysts needed to be clarified. On this account, a comprehensive study about the stability and formation of Mn- and Fe-promoted Rh/SiO_2 catalysts from metal nitrates has been conducted (**Paper 1**). Four different catalysts were systematically investigated in four different states: calcined, reduced, after long-term catalytic study (>22 days on stream), and after a high-temperature investigation (up to 320 °C). The thorough analysis of each catalyst in the different states led to the identification of specific promoter effects: Fe serves as an electronic modifier on Rh/SiO_2 through *in situ* RhFe nanoalloy formation, whereas MnO

is more likely a structural modifier and does not substantially change Rh's intrinsic product spectrum.

In both cases, RhFe nanoalloy formation or creation of Rh–MnO interfacial sites, a close proximity of Rh and the promoter is required. For this reason, a synthesis approach based on molecular single-source precursors (SSP) has been developed using hetero-bimetallic compounds with predefined Rh–Me (Me = Fe or Mn) bonds. **Paper 2** highlighted that the SSP approach is a compelling synthesis route toward well-defined bimetallic catalysts, as the Rh–MnO interface could be effectively tuned using a novel Rh_3Mn_3 carbonyl cluster as SSP. The increase in interfacial sites led to a significantly enhanced ethanol selectivity ranging among the best Rh-based catalysts reported in CO hydrogenation.

This SSP approach has been further applied to investigate the formation phase of a $RhFeO_x/SiO_2$ model catalyst (**Paper 3**), as the prevailing nanostructure and the role of RhFe nanoalloys have been controversially discussed in past literature. An extended catalyst characterization before and after the critical formation phase (>140 h on stream) allowed to ascribe a drastic decrease in ethanol formation to a structural change from an unalloyed $RhFeO_x$ to an alloyed $RhFe/FeO_x$ nanostructure. This investigation explains the great variation of reported catalytic results of RhFe catalysts. Likewise, the relevance of formation phase studies has been demonstrated.

Besides specific promoter effects, the stability of Rh-based catalysts over time-on-stream has been addressed by the three related publications. All Rh-based catalysts deactivated within an initial period of 80–120 h on stream depending on catalyst composition and synthesis approach. This deactivation behavior of Rh-based catalysts has not been reported yet. The thorough characterization of the unpromoted and promoted Rh/SiO_2 catalysts suggested particle growth through CO-induced sintering, similar to Ostwald ripening reported for Co-based Fischer-Tropsch catalysts.

In brief, this thesis demonstrated that Rh-based catalysts undergo significant changes under the influence of high-pressure synthesis gas conditions over time-on-stream. These changes in catalyst structure, morphology, and chemical state have a vital impact on the reactivity and stability of Rh-based catalysts. Whereas current research delivered a more static view on Rh's reactivity, this work addresses current needs in understanding the stability of Rh-based catalysts and the formation of Rh–promoter interactions under process-relevant reaction conditions. This profound knowledge might serve as a basis for the synthesis of new Rh-based catalysts and might provide the opportunity to lower the Rh content while retaining or even enhancing Rh's catalytic reactivity.

Kurzfassung

Die Umsetzung von Synthesegas (kurz Syngas; CO + H_2) ist eine vielversprechende Darstellungsmethode von Ethanol aus fossilen und erneuerbaren Kohlenstoffquellen. Die höchsten Ethanolausbeuten konnten mit Rh-basierten Katalysatoren realisiert werden, jedoch sind die erzielten CO-Umsätze zu gering und die Methanselektivität zu hoch. Trotz der intensiven Forschung zur Verbesserung von Rh-basierten Katalysatoren, ist weiterhin eine Steigerung der Ethanolbildungsraten und -selektivitäten für eine industrielle Anwendung erforderlich.

Aktuelle Studien konzentrierten sich bei der Verbesserung von Rh-basierten Katalysatoren vor allem auf das Hinzufügen von einem oder häufig mehreren Promotoren. Darüber hinaus ist das Langezeitverhalten und die Stabilität der verwendeten Katalysatoren nur selten betrachtet worden. All diese Umstände führen dazu, dass unser fundamentales Verständnis von Promotionseffekten begrenzt ist und somit die Darstellung von neuartigen Katalysatoren erschwert wird.

Eine Verbesserung von existierenden oder die Entwicklung von neuartigen Katalysatoren ist notwendig, um die Umsetzung von Synthesegas zu Ethanol (StE) ökonomisch zu betreiben. Außerdem führte der drastische Anstieg des Rh-Preises in den vergangen fünf Jahren zu einer verstärkten Suche nach einer Alternative für Rh als aktives Metall. Bei der Umsetzung von Synthesegas über Rh-freien Katalysatoren kommt es jedoch meist zur Bildung von höheren Alkoholen und Oxygenaten. Daher scheinen Strategien sinnvoll, die den Rh-Gehalt verringern, anstatt Rh vollständig zu ersetzen. Hierfür ist hingegen ein fundamentales Verständnis der intrinsischen Reaktivität von Rh und dem Einfluss von Promotoren von Nöten.

Aus diesem Grund ist das Ziel dieser Arbeit, die Wechselwirkung zwischen Rh und seinen Promotoren in Abhängigkeit der Reaktionsbedingungen und Katalysatorlaufzeit zu betrachten. Die vorliegende Arbeit basiert auf drei veröffentlichten Publikationen, welche metallorganische Synthesemethoden, Katalysatorcharakterisierung, Studien zur Formierungsphase und katalytische Langzeituntersuchungen beinhalten.

Zunächst wurden die Promotoreneffekte in klassischen Rh-Katalysatoren untersucht, um aus diesen Erkenntnissen neue Synthesemethoden entwickeln zu können. Hierzu wurde die Stabilität und Formierung von Mn- und Fe-promotierten Rh/SiO_2 Katalysatoren aus Metallnitraten untersucht (**Paper 1**). Diese Studie beinhaltete die Untersuchung von vier verschiedenen Katalysatoren in den verschiedenen Zuständen: kalziniert, reduziert, nach einer katalytischen Langzeitstudie (>22 Tage) und nach einer Stabilitätsuntersuchung unter erhöhten Temperaturen (bis zu 320 °C). Die umfängliche Charakterisierung der Katalysatoren in den verschiedenen Zuständen ermöglichte die Identifikation von spezifischen Promotoreffekten: die Zugabe von Fe führt zu einer

Veränderung der elektronischen Struktur von Rh/SiO_2 durch die *in situ*-Bildung von RhFe-Nanolegierungen; MnO hingegen ist vielmehr ein struktureller Promotor und bewirkt keine substanzielle Veränderung des Produktspektrums über Rh-Katalysatoren.

In beiden Fällen, nämlich der Bildung von RhFe-Nanolegierungen und der Erzeugung von Rh–MnO Grenzflächenzentren, ist die räumliche Nähe des Promotors zu Rh essenziell. Aus diesem Grund wurde eine Synthesemethode ausgehend von sogenannten Single-Source-Präkursoren (SSP) entwickelt. Als SSP dienten hetero-bimetallische Komplexverbindungen mit definierten Rh–Me (Me = Fe oder Mn) Bindungen. **Paper 2** verdeutlichte, dass der entwickelte SSP-Ansatz zu wohldefinierten bimetallischen, geträgerten Katalysatoren führen kann. In diesem speziellen Fall konnte durch die Verwendung eines neuartigen Rh_3Mn_3 Carbonylclusters als SSP die Anzahl an Rh–MnO Grenzflächenzentren erhöht werden, was zu einer signifikanten Steigerung der Ethanolselektivität führte und somit zu den höchsten veröffentlichten Ergebnissen zählt.

Dieser SSP-Ansatz wurde zudem für die Darstellung eines $RhFeO_x/SiO_2$ Modellkatalysators verwendet, um dessen Formierungsphase zu untersuchen, da die tatsächliche Nanostruktur und die Rolle von RhFe-Nanolegierung kontrovers diskutiert werden. Durch die Charakterisierung des Katalysators vor und nach der kritischen Formierungsphase (>140 h) konnte eine drastische Verringerung der Ethanolbildung der strukturellen Änderung von einer segregierten $RhFeO_x$ zu einer legierten $RhFe/FeO_x$ Nanostruktur zugesprochen werden. Diese Untersuchung lieferte schließlich eine Erklärung für die große Varianz von veröffentlichten katalytischen Resultaten. Des Weiteren wurde die Relevanz von Formierungsstudien exemplarisch aufgezeigt.

Neben der Untersuchung der Rolle von Promotoren wurde die Langzeitstabilität von Rh-basierten Katalysatoren in den drei Publikationen näher betrachtet. Alle Rh-Katalysatoren desaktivieren während den ersten 80–120 h der katalytischen Untersuchung, je nach Zusammensetzung und angewandter Darstellungsmethode. Ein solches Desaktivierungsverhalten von Rh-basierten Katalysatoren wurde vorher in Literatur noch nicht beschrieben. Die ausführliche Charakterisierung der unpromotierten und promotierten Rh/SiO_2 Katalysatoren legte den Schluss nahe, dass das Partikelwachstum einem CO-induzierten Sintermechanismus folgt, ähnlich wie die Ostwaldreifung bei Co-basierten Fischer-Tropsch-Katalysatoren.

Schließlich konnte mit der vorliegenden Arbeit gezeigt werden, dass sich Rh-basierte Katalysatoren unter dem Einfluss von Syngas bei hohem Druck über die Zeit verändern. Diese Veränderungen in der Katalysatorstruktur, der Morphologie und des chemischen Zustands haben einen großen Einfluss auf die Reaktivität und Stabilität von Rh-basierten Katalysatoren. Während die aktuellen Studien vielmehr ein statisches Bild vermitteln, konnte diese Arbeit die Relevanz für Studien über die Stabilität von Rh-basierten

Katalysatoren und die Formierung von Rh–Promotoren-Wechselwirkung unter Reaktionsbedingungen aufzeigen. Dieses fundamentale Verständnis könnte dazu dienen, neuartige Katalysatoren zu entwickeln und dabei potenziell den Rh-Gehalt bei gleichbleibender oder gesteigerter Reaktivität zu reduzieren.

Acknowledgements

Ich möchte an dieser Stelle die Gelegenheit nutzen, um mich bei all denjenigen zu bedanken, die mich unterstützt und maßgeblich an dem Gelingen dieser Arbeit beigetragen haben.

Zunächst gilt mein Dank Herrn Prof. Dr. Martin Muhler für die Erstellung des Zweitgutachtens, sowie Frau Prof. Dr. Maria Andrea Mroginski für die Übernahme Prüfungsvorsitzes der wissenschaftlichen Aussprache.

Mein besonderer Dank gilt Prof. Dr. Matthias Driess für das stetige Interesse an meiner Arbeit und den vielen wissenschaftlichen Diskussionen. Vielen Dank für das mir entgegengebrachte Vertrauen und den daraus resultierten Freiheiten, die es mir stets ermöglichten, eigene Ideen und Interessen in meinen Forschungsarbeiten einzubringen.

Im gleichen Maße danke ich Herrn Dr. Frank Rosowski für die Möglichkeit meine Promotion am BasCat anzufertigen. Teil eines interdisziplinären Teams am BasCat zu sein, ermöglichte mir die vielen Facetten der heterogenen Katalyse kennenzulernen. Vielen Dank zudem für die zahllosen Diskussionen, die stets offene Tür für Anliegen jeglicher Art und das Ermöglichen der Teilnahme an etlichen wissenschaftlichen Konferenzen.

Bei meinem Gruppenleiter Dr. Raoul Naumann d'Alnoncourt möchte ich mich besonders für die Betreuung während meiner Promotion bedanken. Die vielen wissenschaftlichen Diskussionen, deine Begeisterung für Forschung und unermüdliche Bereitschaft neue Ideen umzusetzen, machten es einfach, die Motivation nicht zu verlieren. Vielen Dank für die unzähligen Dinge, die ich von dir lernen durfte.

Für die gute Zusammenarbeit innerhalb unseres Synthesegasprojekts möchte ich mich bei allen Beteiligten der BASF, dem Fritz-Haber-Instituts, der hte und dem BasCat bedanken. Insbesondere gilt mein Dank Martin Konrad, Dr. Julia Bauer und Dr. Ralph Krähnert für die detaillierten Diskussionen der katalytischen Ergebnisse.

Ein wichtiger Bestandteil dieser Arbeit ist die umfangreiche Analytik der Vorstufen und Katalysatoren. Für die Durchführung und Hilfe bei der Auswertung sowie Interpretation möchte ich mich ebenfalls bedanken. Dr. Johannes Schmidt und Dr. Shuang Li danke ich für XPS-Messungen, Samantha Voges, Dr. Sebastian Kemper und Dr. Jan Dirk Epping für NMR-Messungen, Marc Griffel und Dr. Maria Schlagen für MS-Messungen, Paula Nixdorf für Einkristalldiffraktometrie sowie Dr. Somenath Garai und Dr. Elisabeth Irran für die Hilfe bei der Kristallstrukturverfeinerung. Vom Fritz-Haber-Institut danke ich Dr. Frank Girgsdies und Jasmin Allan für XRD-Messungen, Dr. Xing Huang und Dr. Milivoj Plodinec für TEM-Aufnahmen, Maike Hashagen für BET-Messungen, Jutta Kröhnert und Dr. Annette Trunschke für FTIR-Untersuchungen, Dr. Walid Hetaba, Dr. Christian Rohner

und Dr. Thomas Lunkenbein für die Möglichkeit am ChemiTEM-Projekt teilzunehmen. Dr. Matthias Keck und Prof. Dr. Christian Limberg danke ich für die Mößbauer-Spektroskopie. Zudem möchte ich mich bei der Arbeitsgruppe Metallorgansiche Chemie und Anorganische Materialien für die Unterstützung bei den metallorgansichen Synthesen bedanken. Mein besonderer Dank gilt hier Stefan Schutte, Dr. Shenglai Yao und Dr. Stephan Kohl.

Schließlich möchte ich mich bei dem gesamten BasCat-Team bedanken für die hervorragende Arbeitsatmosphäre während der letzten Jahre. Von der Vielzahl an großartigen Menschen, die ich am BasCat kennenlernen durfte, möchte ich ein paar Leute besonders hervorheben. Ema, was wäre das BasCat ohne dich. Vielen Dank für deine Hilfe im bürokratischen Dschungel und deine organisatorischen Kunststücke im Hintergrund. Micha, vielen Dank für den IT-Support des gesamten BasCats, deine unkomplizierte Problemlösung im Labor und die vielen Überstunden, damit wir unsere Experimente noch beenden konnten. Ein großer Dank gebührt auch Stephen für die stetige Hilfe im Labor und die unzähligen kleinen Dinge, die du so nebenbei erledigst. Katharina, vielen Dank für deine tatkräftige Unterstützung im Labor und deine unermüdliche Mitarbeit.

Ich möchte mich nicht ausschließlich für die Arbeitsatmosphäre, sondern auch für die Vielzahl an verbrachten Stunden neben der Arbeit, die gemeinsam erlebten Konferenzen und Summer Schools und Freundschaften bedanken; Christian und Verena für die grandiose Anfangszeit am BasCat, Rhea und Anton für die großartige Bürogemeinschaft in den ersten Jahren, Stephen und Felix für die lustigen Spieleabende, Piyush, Martin, Noah und Esteban für die unzähligen Beer Meetings, Gregor für die Kaffeepausen am FHI, Kristian für die endlosen gemeinsamen Stunden am Elektronenmikroskop, dem ein oder anderen Schnack und die entspannte Zeit im gemeinsamen Büro. Vielen Dank.

Zuletzt möchte ich mich bei meiner Familie und meinen Freunden bedanken, ohne dessen Unterstützung eine Promotion niemals möglich gewesen wären. Frank, vielen Dank für die einzigartigen Momente in den vergangenen Jahren. Julia, Worte könne kaum beschreiben, wie glücklich ich mich schätzen kann, dich an meiner Seite zu haben. Danke!

List of Publications

This thesis is based on the following three publications.

Paper 1: Formation, Dynamics, and Long-Term Stability of Mn- and Fe-Promoted Rh/SiO_2 Catalysts in CO Hydrogenation

Phil Preikschas, Julia Bauer, Kristian Knemeyer, Raoul Naumann d'Alnoncourt, Ralph Kraehnert, and Frank Rosowski

Catal. Sci. Technol. **2021**, *11* (17), 5802–5818. DOI: 10.1039/D1CY00421B.

Paper 2: From a Molecular Single-Source Precursor to a Selective High-Performance $RhMnO_x$ Catalyst for the Conversion of Syngas to Ethanol

Phil Preikschas, Julia Bauer, Xing Huang, Shenglai Yao, Raoul Naumann d'Alnoncourt, Ralph Kraehnert, Annette Trunschke, Frank Rosowski, and Matthias Driess

ChemCatChem **2019**, *11* (2), 885–892. DOI: 10.1002/cctc.201801978.

Paper 3: Tuning the $Rh–FeO_x$ Interface in Ethanol Synthesis through Formation Phase Studies at High Pressures of Synthesis Gas

Phil Preikschas, Milivoj Plodinec, Julia Bauer, Ralph Kraehnert, Raoul Naumann d'Alnoncourt, Robert Schlögl, Matthias Driess, and Frank Rosowski

ACS Catal. **2021**, *11* (7), 4047–4060. DOI: 10.1021/acscatal.0c05365.

Additional Publications

P. Ingale, K. Knemeyer, P. Preikschas, M. Ye, M. Geske, R. Naumann d'Alnoncourt, A. Thomas, and F. Rosowski. Design of PtZn Nanoalloy Catalysts for Propane Dehydrogenation through Interface Tailoring via Atomic Layer Deposition. *Catal. Sci. Technol.* **2021**, *11* (2), 484–493.

P. Preikschas, K. Trapp, M. Konrad, R. Naumann d'Alnoncourt, R. Kraehnert, M. Driess, and F. Rosowski. Enhancing the Reactivity of Rh-Based Alcohol Synthesis Catalysts through Solution Layer Deposition of Mn and Fe Oxides. **2021**, in Preparation.

M. Konrad, P. Preikschas, J. Bauer, M. Khatamirad, M. Geske, M. F. Gentzen, L. Karwacki, C. Boscagli, F. Rosowski, and R. Kraehnert. **2021**, to be submitted.

Contents

List of Abbreviations

AcOH	Acetic acid
ASF	Anderson-Schulz-Flory (distribution)
BEEF-vdW	Bayesian error estimation functional with van der Waals corrections
BET	Brunauer-Emmet-Teller
BF	Bright-field (detector)
C_2	Reaction products with a carbon number of 2
C_{2+}	Reaction products with a carbon number of at least 2
DCD	Dewar–Chatt–Duncanson (model)
DF	Dark-field (detector)
DFT	Density-functional theory
DME	Dimethyl ether
DMO	Dimethyl oxalate
DRIFTS	Diffuse reflectance infrared Fourier transform spectroscopy
EDX	Energy-dispersive X-ray spectroscopy
EELS	Electron energy loss spectroscopy
EPA	Environmental Protection Agency
FID	Flame ionization detector
FTIR	Fourier-transform infrared spectroscopy
FTS	Fischer-Tropsch synthesis
GC	Gas chromatography / Gas chromatograph
GHSV	Gas hourly space velocity
HAADF	High-angle annular dark field
HOMO	Highest occupied molecular orbital
ICP-OES	Inductively coupled plasma optical emission spectrometry
KIT-6	Korean Institute of Technology - 6
LUMO	Lowest unoccupied molecular orbital
MFC	Mass flow controller
MS	Methanol synthesis / Mass spectrometry
MTBE	Methyl *tert*-butyl ether
oxy	Oxygenates
rt. / RT	Room temperature
SBA-15	Santa Barbara amorphous – 15
StE	Syngas to ethanol
(S)TEM	(Scanning) transmission electron microscopy
TCD	Thermal conductivity detector
TM(s)	Transition metal(s)
TOS	Time-on-stream
TPD	Temperature-programmed desorption
TPDe	Temperature-programmed decomposition
TPSR	Temperature-programmed surface reaction
USD	United States dollar
WGSR	Water-gas shift reaction
XAS	X-ray absorption spectroscopy
XPS	X-ray photoelectron spectroscopy
XRD	X-ray diffractometry

1 Introduction

The growing world population and increasing depletion of fossil-fuel resources raise new challenges from a social and scientific perspective. Substitution of petroleum-derived fuels with alternatives from renewable resources will contribute to a more sustainable future. In this manner, ethanol is considered a prospective alternative fuel meeting the challenging energy and environmental requirements.[1]

Ethanol already serves as an additive for gasoline due to several technical and environmental benefits. Among the technical benefits, ethanol as fuel blending component raises the octane number and, thus, the combustion efficiency in automobiles.[2–4] Due to the phasing-out of methyl *tert*-butyl ether (MTBE) as an anti-knocking agent, a dramatic increase for its application is foreseen.[4,5] Moreover, regulations as the Renewable Fuel Standard by the U.S. Environmental Protection Agency (EPA) or the Directive 2009/28/EC of the European Union require an increase of the percentage share of energy from renewable sources in transportation. These regulations will further increase the demand for ethanol as fuel blending component.[6]

Besides using ethanol as a fuel or fuel additive, it becomes increasingly attractive as an alternative feedstock for base chemicals in view of growing climate and carbon management concerns.[7] Ethanol can undergo several industrially important chemical reactions due to its chemical properties, which the functional hydroxyl group greatly influences. On this account, ethanol serves as a building block for a wide range of products, e.g., ethylene, 1-butanol, acetaldehyde.[6,8] Furthermore, ethanol holds potential as an alternative hydrogen carrier to the more toxic and less energy-dense methanol in fuel cells.[9]

In summary, ethanol's wide range of applications and potential to lower net petroleum use led to an increased demand. Thus, the global bioethanol market was valued at 53 billion USD in 2016 and is estimated to reach 69 billion USD by 2022.[6]

1.1 Ethanol Production

To date, ethanol is mainly produced by the fermentation of sugars from starch or sugarcane with yeast. The world's ethanol production was about 39 Mt in 2007 and was more than doubled by 2019 with 87 Mt following the Renewable Fuel Association.[10] The USA (corn-ethanol) and Brazil (sugarcane-ethanol) are the leading producers with 85 % of the world production, followed by the European Union with 5 %. Although the fermentation route is mainly used to produce ethanol, this process is expensive and energy-inefficient due to the high energy demand from several energy-intensive

distillation steps.[7] This is also reflected in low energy balances[a] of corn- and sugarcane-ethanol of 1.2–1.6 and 4.3–9.4, respectively.[11,12] Utilization of other feedstocks like cellulose might warrant a higher energy balance. However, their production capacities are still far behind corn- and sugarcane-ethanol. For example, cellulosic ethanol remains at a kilotons scale.[6] More importantly, the production of ethanol by fermentation of sugars directly competes with food sources. This land-use change leads to ethical issues raised by the needs of a growing world population and increased greenhouse emissions through degradation of forest and grassland.[13]

Another industrially applied process for ethanol production is the hydration of petroleum-derived ethylene over a solid acid catalyst, such as phosphoric acid-coated silicon dioxide.[6,8,14] Although this route provides industrial-grade pure ethanol, a large-scale production is unattractive due to rising crude oil prices and very low single-pass conversions (5 %).[4,7]

Additionally, other processes starting from synthesis gas (syngas; CO + H_2) have been reported for ethanol formation, also not yet industrially or in large-scale applied (Figure 1.1).[15–21] Among them, the synthesis of ethanol *via* methanol as intermediate through homologation,[19,20] coupling with CO to form dimethyl oxalate (DMO),[17,18] and carbonylation to dimethyl ether (DME) or acetic acid (AcOH) have been proposed.[15,16] These processes in the form they are applied or proposed suffer from energy-consuming product separation or purification. Two promising strategies to avoid multi-step processes are tandem catalysis with two or more catalysts with different functionalities or the direct conversion of syngas to ethanol. This study focuses on the syngas-to-ethanol (StE) reaction.

[a] Energy balance as renewable energy produced per fossil energy used

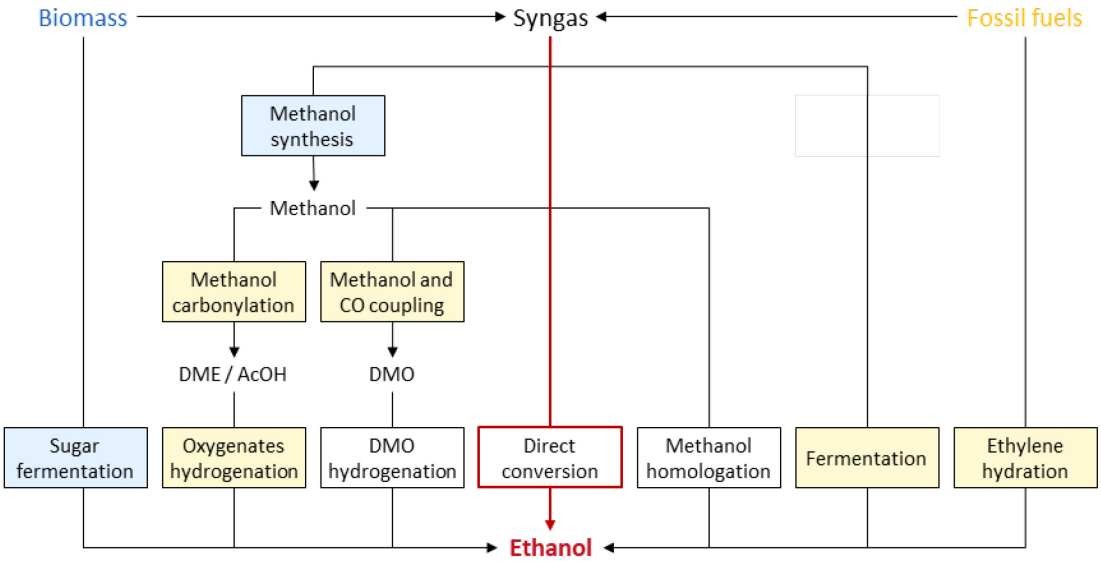

Figure 1.1. Ethanol production pathways from biomass and fossil fuels featuring processes commercialized in large-scale (blue), small scale (yellow), and uncommercialized (white). Adopted from Luk *et al.*[4] with permission from Royal Society of Chemistry.

1.2 CO Hydrogenation over Transition Metals

As the StE reaction is operated under similar reaction conditions like Fischer-Tropsch synthesis (FTS) and methanol synthesis (MS), their mechanistic differences should be discussed briefly.

FTS can be described as polymerization reaction of surface alky species (CH_x, x = 1–3) formed through the dissociative adsorption of CO. A carbide-based reaction mechanism is widely accepted, followed by hydrogenation of surface C species to form the mentioned alkyl monomers. These monomers can undergo a coupling resulting in long-chain hydrocarbons with an Anderson-Schulz-Flory (ASF) distribution (Figure 1.2a).[22,23] On the contrary, MS from syngas requires molecular adsorption of CO, forming surface formyl fragments (CHO). These CHO fragments are further hydrogenated to yield methanol (Figure 1.2b). As both reactions, FTS and MS, are essentially different in their reaction pathways, catalyst functionalities also differ significantly.

During the formation of C_2 oxygenates from syngas, both reactions co-occur.[4] The specific reaction pathways greatly depend on the catalyst nature and active sites present. Although the reaction mechanism and active sites are still elusive, ethanol is likely formed through hydrogen-assisted dissociation of adsorbed CO, formation of surface alkyl fragments, insertion of CHO/CO into metal–alkyl bonds, and subsequent hydrogenation (Figure 1.2c).

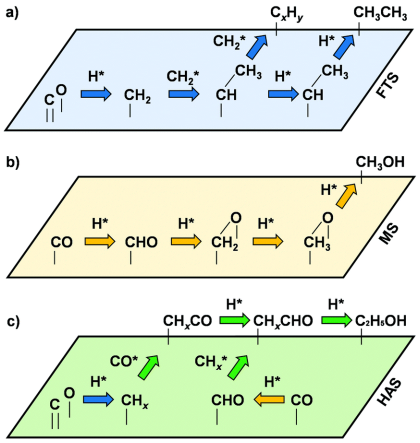

Figure 1.2. Simplified reaction pathways in CO hydrogenation: (a) Fischer-Tropsch synthesis following the carbide mechanism, (b) methanol synthesis, and (c) direct conversion of syngas to ethanol. Reproduced from Luk *et al.*[4] with permission from the Royal Society of Chemistry.

A clear trend of transition metals (TMs) active for FTS and MS can be observed in the periodic table of elements (Figure 1.3). Typical FTS catalysts (Fe, Co, Ru) can be found on the left side of 3d and 4d TMs, whereas Cu, as typical metal for MS, is located on the right side. Rh and Ni as monometallic catalysts for StE and methanation are situated between the TMs active for FTS and MS.

Early CO chemisorption experiments by Brodén *et al.* revealed a similar general trend in the 1970s.[24] Their *in situ* investigations of CO adsorption on single-crystal surfaces by ultraviolet photoemission spectroscopy provided a division line between metals that tend toward dissociative or molecular CO adsorption. These observations differ slightly from the reactivity trends reported for active metals under CO hydrogenation conditions. However, considering CO adsorption as endothermic chemical equilibration of gas-phase CO and adsorbed C* + O* species, the adsorption and dissociation of CO should depend on temperature and pressures applied. CO bond scissoring will become more favorable with high temperatures, which leads to a shift of the room temperature line to the right of the periodic table resulting in a "high" temperature line between FTS and MS catalysts.

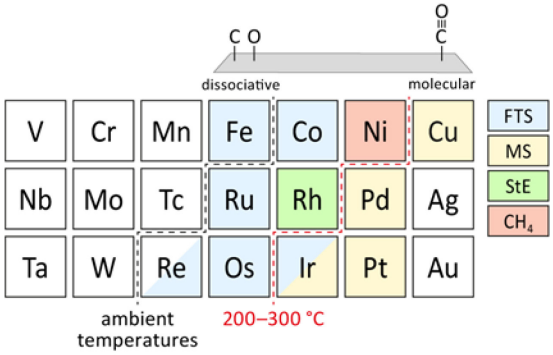

Figure 1.3. CO hydrogenation and CO adsorption trends of transition metals within the periodic table of elements. Metals to the left of the dotted black line adsorb CO dissociatively, whereas metals to the right adsorb CO molecularly at ambient temperatures.[24] For temperatures relevant in CO hydrogenation (200–300 °C), the dotted red line indicates the transition from dissociative to molecular CO adsorption. Metals active for FTS, MS, conversion of StE, and methanation are highlighted in blue, yellow, green, and red, respectively.

These simplified trends can be more accurately explained by the d band model proposed by Hammer and Nørskov.[25] This d band model describes the chemisorption of adatoms and molecules on transition metal surfaces from density functional theory (DFT). The electronic structure of a chemical bond is defined by the interaction of delocalized transition metal sp and d valence states with localized adsorbate atomic orbitals (Figure 1.4).[25,26] The energy contribution from the interaction between sp and adsorbate is similar among different TMs, and sp valence electron band occupation remains nearly constant.[26] Thus, surface reactivity trends are mainly determined by the interaction of adsorbate orbitals with the d band of a transition metal.

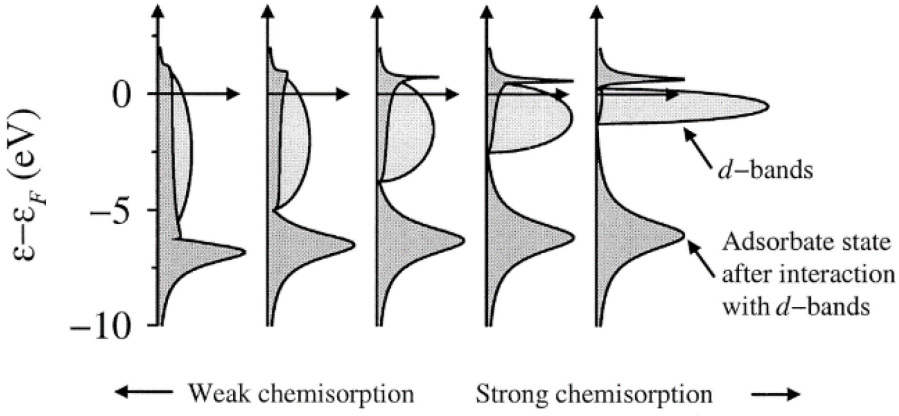

Figure 1.4. The d band model by Hammer and Nørskov. Adsorbate states and d band after forming a chemical bond between an adsorbate valence level and the s and d states of a transition metal surface. The chemisorption strength is characterized by the degree to which the antibonding state between the adsorbate and metal d states is occupied. The higher the d states are in energy relative to the Fermi level, the emptier the antibonding states and the stronger the adsorption bond.[27] Reproduced from Hammer *et al.*[25] with permission from Elsevier.

As the adsorbate–surface interaction is quite similar to a molecular complex of an adsorbate and surface metal atom, the chemical bonding of CO with a metal surface can be described through the Dewar–Chatt–Duncanson (DCD) model as a simple two-state problem.[28] The surface chemical bond of CO consists of electron donation from the 5σ highest occupied molecular orbital (HOMO) into the empty d valence electron orbital of the transition metal surface and backdonation of electrons from the transition metal into the 2π* lowest unoccupied molecular orbital (LUMO) of CO. According to the DCD model, CO dissociation or molecular adsorption depends on the filling of antibonding states. In the case of chemisorption on transition metals, the d band center's position relative to the Fermi level is most relevant for the filling level of antibonding states. Molecular adsorption occurs if the antibonding states are shifted upward through the Fermi level and become empty. On the contrary, CO dissociation occurs through a shift of the d band center downwards and thus, filling of antibonding states.

The d band and DCD models can then explain specific reactivity trends of TMs in CO hydrogenation. The d band center of TMs moves up in energy when going from left to right within the 3d, 4d, and 5d periods. Increasingly more antibonding adsorbate–metal

d states become empty and molecular adsorption of CO is favored. The d band model not only describes specific trends in the periodic table but also allows calculation and comparison of CO chemisorption energies under different conditions. A comparison of the molecular and dissociative CO chemisorption energies on 4d TMs revealed a crossover for Rh. Hence, Rh has the ability of molecular and dissociative CO adsorption at similar reaction conditions (Figure 1.5).

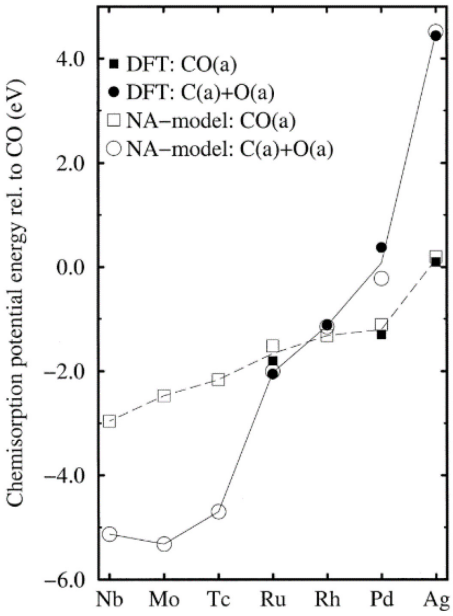

Figure 1.5. Chemisorption energies of molecular CO (squares) in comparison with atomically adsorbed C and O (circles) for the most close-packed surface of the 4d transition metals. Solid symbols are energies calculated by DFT, and hollow symbols are Newns–Anderson model calculations. Dissociative chemisorption appears to the left of rhodium. Reproduced from Hammer et al.[25] with permission from Elsevier.

1.3 The Syngas-to-Ethanol (StE) Reaction

More than 30 years after Ellgen and Bhasin firstly reported the direct conversion of syngas to ethanol in a patent filed by the Union Carbide Cooperation,[29] Spivey *et al.*[30] and Subramani *et al.*[7] comprehensively reviewed this topic in 2007–2008, including summaries on patent literature, thermodynamics, kinetics, reaction mechanism, and catalyst synthesis. More recently, Luk and co-workers published an extensive review about the status and prospects of higher alcohol synthesis in 2017, covering mechanistic insights from theoretical and experimental *in situ* studies mainly conducted within the 2010s.[4] Ao *et al.* contributed an overview about the currently discussed active sites in StE and their synergistic effects.[31]

1.3.1 Catalysts for Direct Conversion of StE

A wide variety of homogeneous and heterogeneous catalysts have been evaluated in the direct conversion of StE.[4,7] The former catalysts mainly contain Co, Ru, or Rh metal complexes in combination with halide salts, which directly produce ethanol and C_2

oxygenates from syngas through methanol homologation at extremely high pressures (up to 5000 bar).[7,32,33] Without the addition of halides, homogeneously catalyzed CO hydrogenation yields methanol as the main product.[34,35]

Heterogeneous catalysts for the StE reaction can be categorized into four groups: Rh-based, Mo-based, modified FTS, and modified MS catalysts.[4,30] As catalysts for ethanol formation require molecular and dissociative adsorption capabilities, common catalyst design strategies follow similar principles by combining both functionalities into one single material. Whereas monometallic Rh catalysts can transform syngas into ethanol through their intrinsic properties, FTS and MS catalysts need to be modified. For example, Cu is the most prominent promoter in modified FTS catalysts,[4] as its addition creates C–C coupling abilities through molecular adsorption, and alcohol synthesis becomes viable. Another way to generate both functionalities is tuning the electronic and geometric properties through tailored support interactions.[4]

Based on these principle concepts, serious research efforts have been made to synthesize suitable catalytic materials for converting syngas to higher alcohols and ethanol, in particular. Rh-based catalysts demonstrate the highest selectivities toward C_{2+} oxygenates with values of up to 65 % among the four different catalyst families (yellow, Figure 1.6). Although Mo-based and modified FTS catalysts exhibit higher C_{2+} oxygenate yields than Rh-based catalysts (green and blue, Figure 1.6), they mainly produce mixed higher alcohols and are less selective toward ethanol, acetaldehyde, and acetic acid. A direct comparison of ethanol productivity is often impossible due to a lack of ethanol selectivity data in reported studies of non-Rh-based catalysts. However, the fraction of ethanol in produced mixed alcohols is usually less than 20 %.[4,36–38] Likewise, most Rh-free catalyst systems produce significant amounts of CO_2 as a side product (up to 50 %) through the water-gas-shift reaction (WGSR).[4,36] As catalytic results are often reported on a CO_2-free basis, catalyst benchmarking among the different catalytic families can be challenging.[4]

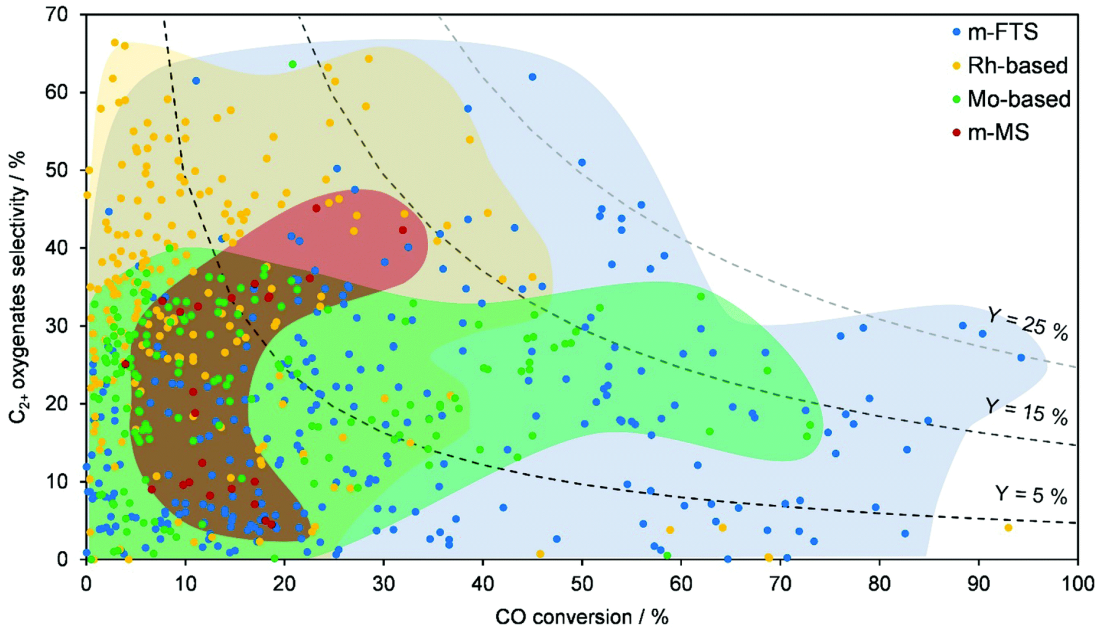

Figure 1.6. C_{2+} oxygenate selectivity as a function of CO conversion for catalysts within the four main groups: modified FTS (m-FTS, blue), Rh-based (yellow), Mo-based (green), and modified MS catalysts (m-MS, red). Reproduced from Luk *et al.*[4] with permission from the Royal Society of Chemistry.

In summary, Rh-based catalysts reached the highest ethanol yields but still suffer from low to moderate CO conversions and high selectivities toward methane. The expected economic and environmental benefits of ethanol over mixed alcohol synthesis make Rh-based catalysts the most promising systems for the selective conversion of syngas to alcohols. Furthermore, Rh-based materials are prospective first catalysts in tandem catalysis as they may warrant necessary ethanol yields through the hydrogenation of acetaldehyde or acetic acid over a second catalyst. For this reason, this study focuses on Rh-based catalysts, and their reactivity in syngas conversion will be discussed in the following.

1.3.2 Reaction Mechanism over Rh-Based Catalysts

Recent progress in DFT calculations and an exponential increase in computational speed led to several theoretical studies on the StE reaction mechanism within the last decade.[39–52] While most of these studies focused on (111) terrace, (211), and (533) stepped Rh surfaces, some calculations with supported Rh_4/Al_2O_3, Rh_{37}/TiO_2, and unsupported Rh_4 metal clusters have been published. Determination of activation barriers, stability of specific surface intermediates, and adsorption energies of surface adsorbates provided reaction pathways for syngas conversion over Rh. Over time, DFT calculations were combined with microkinetic analysis to predict the complex reaction network and to identify the dependence of the product distribution on operating conditions.

As mentioned earlier, the conversion of syngas to oxygenates follows the general pathway of CO adsorption, formation of CH_x surface fragments, CO insertion, and subsequent hydrogenation. Theoretical studies mainly focus on the formation of CH_x

fragments or CO insertion as one of them is expected to control ethanol productivity and selectivity. Yang and *et al.* combined a microkinetic model with DFT calculations based on BEEF-vdW[b].[53] Their model showed that the Rh(211) stepped surface is six orders of magnitude more active than the Rh(111) terrace site but also more selective toward methane. The high methane selectivity over Rh(211) could be explained by significantly lower C–O bond scission barriers, whereas the rates for acetaldehyde and ethanol are comparable on both surfaces. These aspects led to the assumption that the C_{2+} oxygenate selectivity is strongly structure-dependent, and acetaldehyde as an intermediate for ethanol synthesis is predominantly formed on Rh(111) terrace sites. Therefore, the mechanistic insights from theory discussed in the following will focus on reaction pathways over Rh(111) surfaces.

The most controversially discussed aspect is the formation of CH_x surface fragments. While Shetty and co-workers proposed a direct dissociation of CO and subsequent hydrogenation to form CH_x (x = 1–3),[46,54] hydrogenation of CO to CH_xO or CH_xOH followed by H-assisted or non-H-assisted C–O bond scission has been postulated in several other studies.[40,50,53,55] Still, non-consensus regarding the most favored CH_x (x = 1–3) fragment for ethanol formation was reached.[4] However, more recent studies tend to CH_3 as the most favorable monomer.[39–41] The formed CH_3 surface fragment can be hydrogenated to methane or undergo coupling with CO, CHO formyl, or CH_x alkyl species.

Although a direct coupling of CH_x surface fragments has been proposed for hydrocarbon formation earlier, it is now widely accepted that C–C coupling follows a CHO/CO insertion mechanism. Hence, oxygenates and long-chain hydrocarbons share CH_xCHO surface fragments as key intermediates, and the activation barrier for C–O bond scissoring decides whether hydrocarbons or oxygenates are formed. Still, it is controversially discussed which specific step controls ethanol productivity and selectivity. The selectivity-determining step varies from the hydrogenation of CH_2 and the formation of CH_3CHO surface species. Calculations by Yang *et al.* indicate a close competition between these two hydrogenation reactions based on free energies from DFT. They further stated that predictions about selectivity are difficult to make from DFT alone.[53]

For this reason, DFT is nowadays combined with microkinetic modeling in the form of scaling relationships to overcome the low accuracy of DFT-based reaction mechanism analysis.[41] Nevertheless, the reaction conditions used in these microkinetic models do not match the high-pressure conditions relevant for the StE reaction. Thus, a pressure gap between theoretical and catalytic studies still exists. Furthermore, the active sites

[b] Bayesian error estimation functional with van der Waals corrections

considered in theory differ significantly from those identified by experimental investigations. Whereas theoretical studies focus on metallic Rh surfaces constructed as slabs alone,[41,56] a crucial interplay of metallic Rh^0 and Rh^+ single sites have been proposed by experimental evidence.[31,57] Likewise, the influence of specific support interaction on the wide variety of active sites has not been addressed by DFT-based analyses so far.

Equally important, promoters have been included as metallic surface alloy structures in theoretical calculations, although metal oxides forming interfacial sites have been identified as vital for oxygenate synthesis experimentally.[53] Consequently, theoretical studies could lead to controversial conclusions. For example, recent DFT calculations combined with microkinetic analysis of fcc(111) transition metal surfaces yielded Co as the most active and selective metal for oxygenate formation.[41] In contrast, it is well established that supported Co is the preferred catalyst for FTS due to its high activity and chain-growth probability.[58,59] Nevertheless, modern DFT calculations have made severe progress within the last decades, and further improvement and involvement of other computational advances (e.g., exploitation of machine learning) will offer mechanistic insights into catalytic reaction on an atomic level that is currently inaccessible experimentally.[60,61]

1.3.3 Rhodium's Active Sites in CO Hydrogenation

A fundamental understanding of Rh's active sites is required to combat the complexity of multi-promoted systems and gain knowledge about specific promoter effects. The active sites of supported, monometallic Rh catalysts are still under debate and controversially discussed. As dissociative and molecular adsorption co-occur, the formation of dual active sites stable under reaction conditions is a prerequisite. Due to the absence of a second active metal, atomically adjacent Rh^+/Rh^0 sites have been considered.[31]

It has been proposed that dissociative CO adsorption occurs on metallic Rh sites to form CH_x surface fragments. This assumption agrees with theory suggesting H-assisted CO dissociation on both Rh(111) terrace and (211) stepped surfaces. These CH_x fragments can then be hydrogenated to form methane or coupled with CO/CHO from Rh^+ sites yielding CH_xCHO as the key intermediate for ethanol synthesis.

Experimental evidence of Rh^+ surface sites has been reported for freshly reduced supported Rh by several different methods. A frequently used method to probe Rh's surface is the *in situ* chemisorption of CO monitored by Fourier-transform infrared spectroscopy (FTIR). After CO adsorption, typical stretching vibration bands of linear (2065 cm^{-1}) and bridged CO (1700–1900 cm^{-1}) adsorbed on the reduced surface of Rh^0 crystallites can be observed. Additionally, two distinct bands at around 2090 and

2035 cm^{-1} could appear attributed to the symmetrical and asymmetrical C–O stretching on single Rh^+ sites from *gem*-dicarbonyl $Rh^+(CO)_2$ surface species (Figure 1.7).

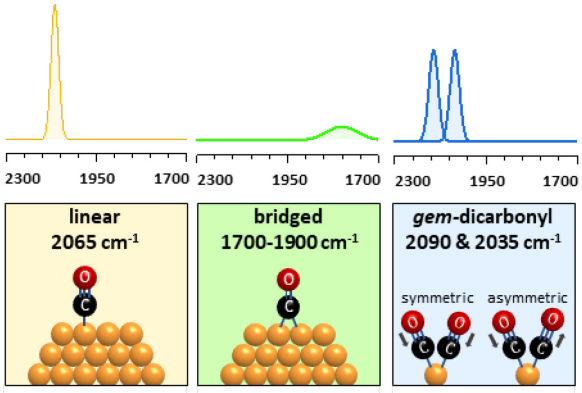

Figure 1.7. The three different vibrational modes after CO chemisorption: linear (yellow) and bridged (green) on metallic sites of Rh clusters and particles, and geminal on Rh^+ single sites (blue). Band positions are given as wavenumbers in cm^{-1}. Relative intensities correspond to a Rh/SiO_2 catalyst with a Rh^+/Rh^0 ratio of roughly 2.5.

These isolated Rh^+ sites are either formed already during synthesis or through Rh particle disintegration induced by molecular CO adsorption. Such a disintegration of Rh particles becomes reasonable as the Rh–CO bond energy is more than four times higher than a metallic Rh–Rh bond.[62] Suzuki *et al.* demonstrated in an *in situ* X-ray absorption spectroscopy (XAS) study that supported Rh nanoparticles can disintegrate into isolated $Rh^+(CO)_2/Al_2O_3$ species during CO adsorption at beam temperature within seconds (Figure 1.8).

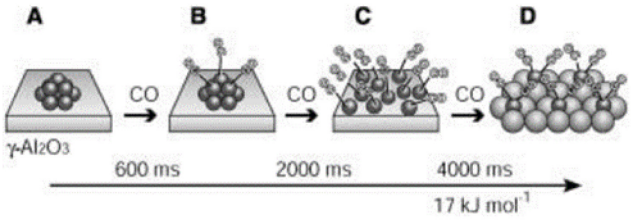

Figure 1.8. Illustrative disintegration mechanism of an Al_2O_3-supported Rh cluster during CO adsorption monitored by time-resolved XAS. Suzuki *et al.*'s experimental data suggest three elementary steps for the Rh cluster disintegration: (1) CO adsorbs rapidly on each atom of the outmost layer (0-600 ms), (2) the Rh–Rh bonds become weaker by further CO adsorptions yielding complete disintegration of the Rh cluster and formation of highly mobile Rh(CO) surfaces species (2000–4000 ms), and (3) formation of *gem*-dicarbonyl $Rh^+(CO)_2$ species, which interact with three surface O atoms (>4000 ms).[63] Reproduced from Suzuki *et al.*[63] with permission. Copyright © 2003 WILEY-VCH Verlag GmbH & Co. KGaA, Weinheim.

Although CO chemisorption is widely used for determining the different CO adsorption sites on Rh, some studies suggest that isolated Rh^+ sites are exclusively formed under CO atmospheres during FTIR investigation and do not exist after synthesis.[64–67] More importantly, direct evidence for the formation of isolated Rh^+ sites under realistic high-pressure synthesis gas conditions is still missing. Attempts to investigate supported Rh catalysts under process-relevant conditions were unsuccessful so far as *in situ* and *operando* investigations can be challenging when a process under high pressures is

studied. Specifically, infrared spectroscopic investigations are difficult to conduct at high CO partial pressures as gas-phase CO interferes with adsorbed carbonyl species. As a consequence, many reported *in situ* studies were performed under ambient pressure conditions. For this reason, the distinct role of isolated Rh^+ sites in CO hydrogenation remains unclear, and not even the stability of geminal dicarbonyl species under realistic conditions has been unraveled so far.

1.3.4 Reaction Network of Syngas Conversion over Rh/SiO_2

Some reaction networks have been proposed based on theoretical and experimental investigations.[4] The reaction network proposed by Bauer will be discussed in the following and will serve as a basis for the general discussion of this thesis. This reaction network is based on kinetic studies from long-term catalytic investigations, drop-out, and co-feed experiments (Figure 1.9).

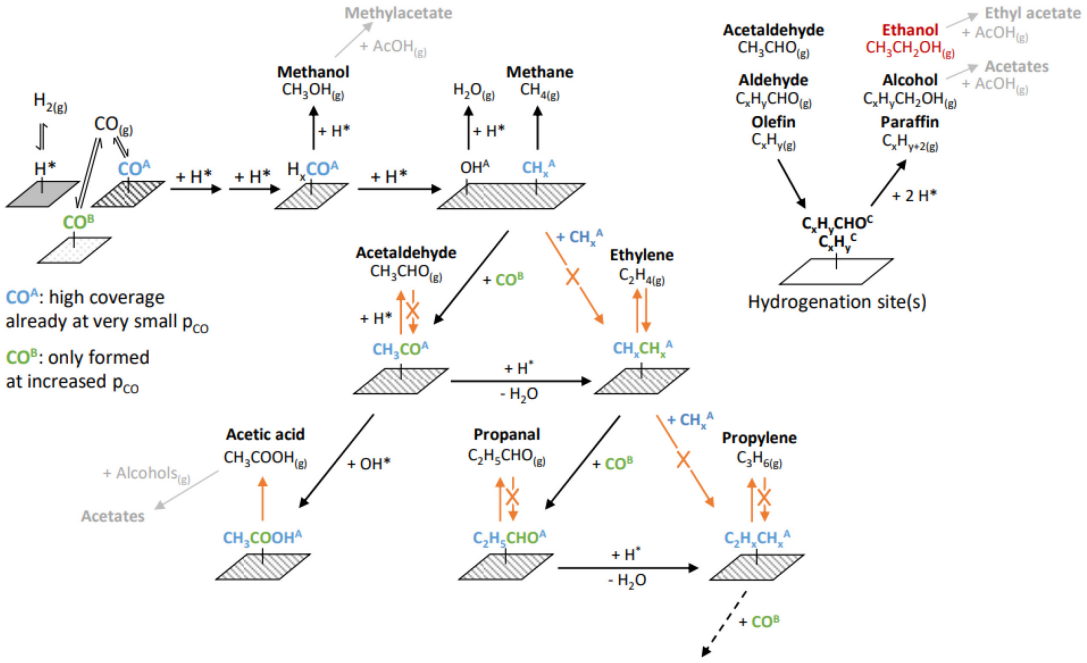

Figure 1.9. Reaction Network over Rh/SiO_2. Different patterns indicate different adsorption sites, including the hydrogen adsorption site (full grey), a "low CO pressure" adsorption site for CO* and other C-containing surface compounds potentially on metallic Rh nanoparticles (stripes), a "high CO pressure" adsorption site providing CO* for CO insertion (dotted), and a separate hydrogenation site (white). Reproduced from Bauer[68] with permission.

The proposed reaction network is based on the assumption that two different CO* surface species are involved in forming C_{2+} oxygenates and hydrocarbons. The two different CO* surface species exhibit different reactivities dependent on the CO partial pressure applied. Furthermore, extended equilibration phase and CO drop-out experiments have revealed CO as a structure-inducing component. Rising the CO partial pressure has major control on individual formation rates but does not affect the activity in terms of total CO consumption rate. The different CO* surface species are assigned as

CO^A and CO^B within the proposed reaction network (Figure 1.9). CO^A serves as a reservoir for complex surface intermediates, can be hydrogenated, and undergoes C–O bond cleavage. On the contrary, CO^B represents surface species formed only at high CO partial pressures and after long on-stream periods. This species is crucial for the CO insertion step to form oxygenated intermediates and, thus, controls ethanol productivity and selectivity.

Methanol formation occurs before C–O bond cleavage takes place. Over Rh/SiO_2, the rate of direct hydrogenation of molecular CO^A to form MeOH is slow. The availability of adsorbed H* is limited as H-assisted CO dissociation is favored resulting in CH_x^A surface fragment formation. As the direct coupling of CH_x fragments could be excluded experimentally and from theoretical studies, two reaction pathways originate from these CH_x^A surface fragments: direct hydrogenation to form methane and C–C coupling through CHO/CO insertion of a "high pressure" CO^B species.

After CO insertion, the key surface intermediate CH_3CO^A is formed, and three possible pathways yield expected C_2 products: (1) direct hydrogenation and desorption of acetaldehyde, (2) reaction with surface hydroxyls OH* to form acetic acid, or (3) formation of C_2 alkyl fragments through C–O bond cleavage. Besides hydrogenation for olefin and paraffin formation, these C_2 alkyl fragments can undergo another CHO/CO insertion of a CO^B species resulting in C_3 oxygenates and hydrocarbons. Repetitive CO/CHO insertion and subsequent C–O bond cleavage sequences could lead to long-chain products in the same way as discussed for $C_{2/3}$ products. Aldehyde and alkyl surface intermediates are most likely converted at an additional hydrogenation site into alcohols and paraffins, respectively.

1.3.5 Catalytic Results of Rh/SiO_2 Catalysts in CO Hydrogenation

The proposed reaction network firstly describes the complex product spectrum of monometallic Rh catalysts. Whereas a wide range of products can be formed over supported Rh catalysts, methane is still the main product with up to 70 % selectivity. The highest C_{2+} oxygenate selectivity reported so far is about 43 %. However, selectivities toward oxygenated products vary vastly for similar catalyst systems and reaction conditions, as indicated by exemplary catalytic results for CO hydrogenation over Rh/SiO_2 catalysts in Table 1.1.

Table 1.1. Exemplary results for CO hydrogenation over Rh/SiO_2 catalysts.[a]

Entry	Catalyst (wt% Rh)	T (°C)	p (bar)	GHSV (h^{-1})	H_2/CO	X_{CO} (%)	S_{CH_4} (%)	S_{EtOH} (%)	$S_{C_2\ oxy}$[b] (%)	$Y_{C_2\ oxy}$[c] (%)	Ref.
1	$2.5Rh/SiO_2$	300	69	-	1	3.1	52	17	43.1	1.3	69
2	$1.5Rh/SiO_2$	270	30	15000	2	0.80	64	8.5	14.8	0.16	70
3	$1.5Rh/SiO_2$	270	30	4000	2	5.0	70	8.2	14.3	0.72	71
4	$2.0Rh/SiO_2$	270	10	3300[d]	2	2.1	60	4.0	16.9	0.36	72
5	$2.0Rh/SiO_2$	270	20	8000[d]	1	0.75	51	0	0	0	73
6	$2.0Rh/SiO_2$	275	24	-	2	10	43	16	29	2.9	74
7	$3.0Rh/SiO_2$	285	20	-	2	4.3	30	0	0	0	75
8	$5.5Rh/SiO_2$	250	40	-	1	1.6	43	3.5	20.5	0.33	76

[a] Methane, ethanol, C_2 oxygenates are abbreviated with CH_4, EtOH, and C_2 oxy, respectively.
[b] Selectivity toward C_2 oxygenates includes ethanol, acetaldehyde, and acetic acid if provided.
[c] Yield toward C_2 oxygenates includes ethanol, acetaldehyde, and acetic acid if provided.
[d] Space velocity in $cm^3\ g_{cat}^{-1}\ h^{-1}$.

1.3.6 Role of Promoters and Modifiers in StE over Rh-Based Catalysts

As ethanol yields obtained over monometallic Rh catalysts are still far away from industrial application, modification and promotion of Rh-based catalysts are required. Based on the initial results of monometallic Rh catalysts and Rh's intrinsic ability to form C_{2+} oxygenates, broad promoter screenings including over 60 elements have been performed since the 1980s.[4] Fe and Mn appeared as the most effective and commonly applied promoters (Table 1.2). Therefore, the following discussion will focus on the specific promoter effects of these two elements.

Table 1.2. Top-10 Rh-based Catalysts. Reproduced from Luk *et al.*[4] with permission from The Royal Society of Chemistry.

Entry	Catalyst[a]	T (°C)	p (bar)	GHSV (h^{-1})	H_2/CO	X_{CO} (%)	$S_{C_2\ oxy}$ (%)	S_{HC} (%)	$Y_{C_2\ oxy}$ (%)	Ref.
1	$RhMn/SiO_2$	280	54	1700	2	39	54	42	21	77
2	$RhMnLi/Fe/SiO_2$	300	30	10000[b]	2	28	64	34	18	78
3	$RhMnLiFe/SiO_2$	300	30	10000[b]	2	28	58	40	16	79
4	$RhMn/SiO_2$	285	20	-	2	36	43	52	16	75
5	$Rh/C_{0.8}Zr_{0.2}O_2$	275	24	2400[b]	2	27	44	38	12	74
6	Rh/Mn-Fe-OMC	300	50	12000	2	26	46	38	12	80
7	$RhMnLi/SiO_2$	300	30	10000[b]	2	19	54	42	10	81
8	RhMn/MSN	270	30	6600[b]	2	20	47	47	10	82
9	RhMnLiFe/CMK-9	320	30	12000	2	14	65	22	9	83
10	$RhMn/SiO_2$	270	30	4000	2	17	46	52	8	71

[a] CMK: cubic-ordered mesoporous carbon, OMC: ordered mesoporous carbon, MSN: mesoporous silica nanoparticles.
[b] Space velocity in $cm^3\ g_{cat}^{-1}\ h^{-1}$.

Mn addition to Rh-based catalysts has shown a high potential to increase C_{2+} oxygenate yields (Table 1.2). Consequently, Mn's role in the StE reaction has been described as improving CO dissociation on Rh^0 sites and facilitating CO insertion on Rh^+ sites. This assumption is mainly based on theoretical studies.[4,24] Mao *et al.* have contributed experimental evidence for these specific promoter effects. From diffuse reflectance infrared Fourier transform spectroscopy (DRIFTS) investigations, they concluded that tilt-adsorbed CO species at $Rh–MnO_x$ interfacial sites facilitate CO dissociation on Rh^0 sites.[70] However, other studies contradict this hypothesis and doubt the relevance of

tilted adsorbed CO species in the conversion of StE.[84] Likewise, it has been proposed that MnO_x stabilizes Rh^+ sites in its vicinity based on TPD and TPSR experiments.[85,86] The increase in molecular CO adsorption sites might ultimately promote CO insertions and facilitate ethanol synthesis. In contrast, Yu *et al.* reported that Rh^+ sites are not stable under StE reaction conditions and thereby not relevant for ethanol formation.[87]

The influence of Mn on Rh's morphological and electronic properties has only rarely been discussed. Earlier theoretical and experimental studies suggested RhMn nanoalloy structures through the formation of zero-valent Mn on SiO_2.[45,88] Thus, Mn should have a direct influence on Rh's electronic properties and promotes ethanol formation. On the contrary, more recent studies have demonstrated that Mn is in an oxidized state. However, Mn's actual oxidation state could not be examined by these studies.[89,90] Current studies about Mn's role as promoter mainly cover investigations of freshly reduced samples. Hence, a lack of studies on spent catalysts and dynamics of Mn-promoted Rh catalysts under reaction conditions for extended periods on stream still exists.

The addition of Fe as a promoter has been mainly reported to increase ethanol selectivity and CO conversion. Fe emerged as one of the best promoters among the transition metals investigated.[4] Similar to the case of Mn, the exact nanostructure of supported $RhFeO_x$ catalysts is still under debate. Proposed structural models vary from unalloyed over core-shell to nanoalloyed RhFe structures.[72,73,76,82–83,93–97] To the same extent, the formation of oxygenates varies significantly on Fe-promoted Rh catalysts reported in the literature. The most apparent difference among the reported catalytic results is a great variation of reported methanol and ethanol selectivities. In this manner, Hartman *et al.* reported that the formation of RhFe nanoalloyed structures reduces tilted CO species and ultimately enhances CO insertion. Thus, RhFe nanoalloys facilitate ethanol formation.[91] Conversely, tilted CO adsorption sites have been reported as favorable for ethanol formation on $RhMnO_x$. In contrast to an increase in ethanol formation, Mo *et al.* observed higher selectivities toward methane and methanol after modifying supported Rh with Fe. Only a small improvement in ethanol selectivity has been observed.[92]

In both cases, modification of Rh-based catalysts with Mn or Fe, no systematic long-term investigations have been reported so far. As most studies focus on the characterization of fresh catalysts and only peak performance marks have been considered, specific promoter effects of Mn and Fe remain unclear.

1.3.7 Formation, Long-Term and Thermal Stability of Rh-Based Catalysts

Heterogeneous catalysts often undergo changes in their structure, morphology, chemical state, or even composition under the influence of medium to high temperatures and elevated pressures. This initial formation phase can cause significant changes in product distribution and activity, as reported for supported Au catalysts in CO_2

hydrogenation,[98,99] or $Cu/ZnO/Al_2O_3$ methanol synthesis catalysts.[100–103] In a recent XAS study, Divins *et al.* could correlate an increase in methanol and DME formation to a structural change of CuZn catalysts under reaction conditions.[100] In contrast, the stability of Rh-based catalysts has rarely been evaluated, and still, their formation under reaction conditions has not been addressed.[4] Only one exception has been reported with a catalytic run demonstrating stable catalytic performance for 60 h on stream without any changes to selectivity and activity.[104]

1.4 References

(1) Farrell, A. E. Ethanol Can Contribute to Energy and Environmental Goals. *Science (80).* **2006**, *311* (5760), 506–508.

(2) Thomas, V.; Kwong, A. Ethanol as a Lead Replacement: Phasing out Leaded Gasoline in Africa. *Energy Policy* **2001**, *29* (13), 1133–1143.

(3) Siwale, L.; Kristóf, L.; Adam, T.; Bereczky, A.; Penninger, A.; Mbarawa, M.; Andrei, K. Performance Characteristics of N-Butanol-Diesel Fuel Blend Fired in a Turbo-Charged Compression Ignition Engine. *J. Power Energy Eng.* **2013**, *01* (05), 77–83.

(4) Luk, H. T.; Mondelli, C.; Ferré, D. C.; Stewart, J. A.; Pérez-Ramírez, J. Status and Prospects in Higher Alcohols Synthesis from Syngas. *Chem. Soc. Rev.* **2017**, *46* (5), 1358–1426.

(5) Berg, C. World Fuel Ethanol – Analysis and Outlook. In *Sugar Trading Manual*; Elsevier, 2004.

(6) Mika, L. T.; Cséfalvay, E.; Németh, Á. Catalytic Conversion of Carbohydrates to Initial Platform Chemicals: Chemistry and Sustainability. *Chem. Rev.* **2018**, *118* (2), 505–613.

(7) Subramani, V.; Gangwal, S. K. A Review of Recent Literature to Search for an Efficient Catalytic Process for the Conversion of Syngas to Ethanol. *Energy & Fuels* **2008**, *22* (2), 814–839.

(8) Kosaric, N.; Duvnjak, Z.; Farkas, A.; Sahm, H.; Bringer-Meyer, S.; Goebel, O.; Mayer, D. Ethanol. In *Ullmann's Encyclopedia of Industrial Chemistry*; Wiley-VCH Verlag GmbH & Co. KGaA: Weinheim, Germany, 2011; Vol. 3, pp 1–72.

(9) Lamy, C.; Rousseau, S.; Belgsir, E. .; Coutanceau, C.; Léger, J.-M. Recent Progress in the Direct Ethanol Fuel Cell: Development of New Platinum–Tin Electrocatalysts. *Electrochim. Acta* **2004**, *49* (22–23), 3901–3908.

(10) Renewable Fuels Association. Statistics https://ethanolrfa.org/statistics/#1454098996479-8715d404-e546.

(11) Wang, M.; Han, J.; Dunn, J. B.; Cai, H.; Elgowainy, A. Well-to-Wheels Energy Use and Greenhouse Gas Emissions of Ethanol from Corn, Sugarcane and Cellulosic Biomass for US Use. *Efficiency and Sustainability in Biofuel Production: Environmental and Land-Use Research.* **2015**, 249–280.

(12) Manochio, C.; Andrade, B. R.; Rodriguez, R. P.; Moraes, B. S. Ethanol from Biomass: A Comparative Overview. *Renew. Sustain. Energy Rev.* **2017**, *80*, 743–755.

(13) Searchinger, T.; Heimlich, R.; Houghton, R. A.; Dong, F.; Elobeid, A.; Fabiosa, J.; Tokgoz, S.; Hayes, D.; Yu, T.-H. Use of U.S. Croplands for Biofuels Increases Greenhouse Gases Through Emissions from Land-Use Change. *Science (80).* **2008**, *319* (5867), 1238–1240.

(14) Fougret, C. M.; Hölderich, W. F. Ethylene Hydration over Metal Phosphates Impregnated with Phosphoric Acid. *Appl. Catal. A Gen.* **2001**, *207* (1–2), 295–301.

(15) Horton, T.; Jevtic, R.; Johnston, V. J.; Pan, T.; Warner, R. J.; Weiner, H.; Bower, N.; Chapman, J. T.; Grusendorf, G. US Patent US8552224B2, 2013.

(16) Johnston, V. J.; Orisco, A.; Sarager, L.; Scates, M. O.; Shaver, R. D.; Zink J. H. US Patent

8809598B2, 2014.

(17) Yue, H.; Ma, X.; Gong, J. An Alternative Synthetic Approach for Efficient Catalytic Conversion of Syngas to Ethanol. *Acc. Chem. Res.* **2014**, *47* (5), 1483–1492.

(18) Gong, J.; Yue, H.; Zhao, Y.; Zhao, S.; Zhao, L.; Lv, J.; Wang, S.; Ma, X. Synthesis of Ethanol via Syngas on Cu/SiO_2 Catalysts with Balanced Cu^0–Cu^+ Sites. *J. Am. Chem. Soc.* **2012**, *134* (34), 13922–13925.

(19) Lin, J.-J.; Knifton, J. F. US Patent 4424384A, 2003.

(20) Michio, K.; Setsunobu, A.; Yoshiaki, S. US Patent 3387043A, 1968.

(21) Younesi, H.; Najafpour, G.; Mohamed, A. R. Ethanol and Acetate Production from Synthesis Gas via Fermentation Processes Using Anaerobic Bacterium, Clostridium Ljungdahlii. *Biochem. Eng. J.* **2005**, *27* (2), 110–119.

(22) Mahmoudi, H.; Mahmoudi, M.; Doustdar, O.; Jahangiri, H.; Tsolakis, A.; Gu, S.; Lech Wyszynski, M. A Review of Fischer Tropsch Synthesis Process, Mechanism, Surface Chemistry and Catalyst Formulation. *Biofuels Eng.* **2018**, *2* (1), 11–31.

(23) Anderson, R. B.; Friedel, R. A.; Storch, H. H. Fischer-Tropsch Reaction Mechanism Involving Stepwise Growth of Carbon Chain. *J. Chem. Phys.* **1951**, *19* (3), 313–319.

(24) Brodén, G.; Rhodin, T. .; Brucker, C.; Benbow, R.; Hurych, Z. Synchrotron Radiation Study of Chemisorptive Bonding of CO on Transition Metals — Polarization Effect on Ir(100). *Surf. Sci.* **1976**, *59* (2), 593–611.

(25) Hammer, B.; Nørskov, J. K. Theoretical Surface Science and Catalysis—Calculations and Concepts. In *Advances in Catalysis*; 2000; Vol. 45, 71–129.

(26) Raman, A. S.; Vojvodic, A. Energy Trends in Adsorption at Surfaces. In *Handbook of Materials Modeling*; Springer International Publishing: Cham, 2018; 1–20.

(27) Hammer, B.; Norskov, J. K. Why Gold Is the Noblest of All the Metals. *Nature* **1995**, *376* (6537), 238–240.

(28) *Modern Heterogeneous Catalysis*; van Santen, R. A., Ed.; Wiley-VCH Verlag GmbH & Co. KGaA: Weinheim, Germany, 2017.

(29) Ellgen, P. C.; Bhasin, M. US Patent 4096164, 1976.

(30) Spivey, J. J.; Egbebi, A. Heterogeneous Catalytic Synthesis of Ethanol from Biomass-Derived Syngas. *Chem. Soc. Rev.* **2007**, *36* (9), 1514.

(31) Ao, M.; Pham, G. H.; Sunarso, J.; Tade, M. O.; Liu, S. Active Centers of Catalysts for Higher Alcohol Synthesis from Syngas: A Review. *ACS Catal.* **2018**, *8* (8), 7025–7050.

(32) Wender, I.; Friedel, R. A.; Orchin, M. Ethanol from Methanol. *Science (80).* **1951**, *113* (2930), 206–207.

(33) Gresham, W. F.; Schweitzer, C. E. US Patent 2534018A, 1950.

(34) Blank, J. H.; Hembre, R.; Ponasik, J.; Cole-Hamilton, D. J. Alternative Pathways in the Ruthenium Catalysed Hydrogenation of CO to Alcohols. *Catal. Sci. Technol.* **2014**, *4* (1), 218–223.

(35) Dombek, B. D. Hydrogenation of Carbon Monoxide to Methanol and Ethylene Glycol by Homogeneous Ruthenium Catalysts. *J. Am. Chem. Soc.* **1980**, *102* (22), 6855–6857.

(36) Prieto, G.; Beijer, S.; Smith, M. L.; He, M.; Au, Y.; Wang, Z.; Bruce, D. A.; de Jong, K. P.; Spivey, J. J.; de Jongh, P. E. Design and Synthesis of Copper-Cobalt Catalysts for the Selective Conversion of Synthesis Gas to Ethanol and Higher Alcohols. *Angew. Chem. Int. Ed.* **2014**, *53* (25), 6397–6401.

(37) Göbel, C.; Schmidt, S.; Froese, C.; Fu, Q.; Chen, Y.-T.; Pan, Q.; Muhler, M. Structural Evolution of Bimetallic Co-Cu Catalysts in CO Hydrogenation to Higher Alcohols at High Pressure. *J. Catal.* **2020**, *383*, 33–41.

(38) Göbel, C.; Schmidt, S.; Froese, C.; Bujara, T.; Viktor Scherer; Muhler, M. The Steady-State Kinetics of CO Hydrogenation to Higher Alcohols over a Bulk Co-Cu Catalyst. *J. Catal.* **2021**, *394*, 465–475.

(39) Zhang, R.; Peng, M.; Wang, B. Catalytic Selectivity of Rh/TiO_2 Catalyst in Syngas Conversion to Ethanol: Probing into the Mechanism and Functions of TiO_2 Support and Promoter. *Catal. Sci. Technol.* **2017**, *7* (5), 1073–1085.

(40) Wang, J.; Liu, Z.; Zhang, R.; Wang, B. Ethanol Synthesis from Syngas on the Stepped Rh(211) Surface: Effect of Surface Structure and Composition. *J. Phys. Chem. C* **2014**, *118* (39), 22691–22701.

(41) Schumann, J.; Medford, A. J.; Yoo, J. S.; Zhao, Z.-J.; Bothra, P.; Cao, A.; Studt, F.; Abild-Pedersen, F.; Nørskov, J. K. Selectivity of Synthesis Gas Conversion to C_{2+} Oxygenates on Fcc(111) Transition-Metal Surfaces. *ACS Catal.* **2018**, *8* (4), 3447–3453.

(42) Filot, I. A. W.; Shetty, S. G.; Hensen, E. J. M.; van Santen, R. A. Size and Topological Effects of Rhodium Surfaces, Clusters and Nanoparticles on the Dissociation of CO. *J. Phys. Chem. C* **2011**, *115* (29), 14204–14212.

(43) Lausche, A. C.; Medford, A. J.; Khan, T. S.; Xu, Y.; Bligaard, T.; Abild-Pedersen, F.; Norskov, J. K.; Studt, F. On the Effect of Coverage-Dependent Adsorbate-Adsorbate Interactions for CO Methanation on Transition Metal Surfaces. *J. Catal.* **2013**, *307*, 275–282.

(44) Yang, L.; Liu, P. Ethanol Synthesis from Syngas on Transition Metal-Doped Rh(111) Surfaces: A Density Functional Kinetic Monte Carlo Study. *Top. Catal.* **2014**, *57* (1–4), 125–134.

(45) Mei, D.; Rousseau, R.; Kathmann, S. M.; Glezakou, V.-A.; Engelhard, M. H.; Jiang, W.; Wang, C.; Gerber, M. A.; White, J. F.; Stevens, D. J. Ethanol Synthesis from Syngas over Rh-Based/SiO_2 Catalysts: A Combined Experimental and Theoretical Modeling Study. *J. Catal.* **2010**, *271* (2), 325–342.

(46) Shetty, S.; van Santen, R. A.; Stevens, P. A.; Raman, S. Molecular Steps for the Syngas Conversion on the Rh_6 Cluster. *J. Mol. Catal. A Chem.* **2010**, *330* (1–2), 73–87.

(47) Ma, X.; Su, H.; Deng, H.; Li, W.-X. Carbon Monoxide Adsorption and Dissociation on Mn-Decorated Rh(111) and Rh(553) Surfaces: A First-Principles Study. *Catal. Today* **2011**, *160* (1), 228–233.

(48) Schweicher, J.; Bundhoo, A.; Kruse, N. Hydrocarbon Chain Lengthening in Catalytic CO

Hydrogenation: Evidence for a CO-Insertion Mechanism. *J. Am. Chem. Soc.* **2012**, *134* (39), 16135–16138.

(49) Zhao, Y. H.; Sun, K.; Ma, X.; Liu, J.; Sun, D.; Su, H. Y.; Li, W. X. Carbon Chain Growth by Formyl Insertion on Rhodium and Cobalt Catalysts in Syngas Conversion. *Angew. Chem. Int. Ed.* **2011**, *50* (23), 5335–5338.

(50) Kapur, N.; Hyun, J.; Shan, B.; Nicholas, J. B.; Cho, K. Ab Initio Study of CO Hydrogenation to Oxygenates on Reduced Rh Terraces and Stepped Surfaces. *J. Phys. Chem. C* **2010**, *114* (22), 10171–10182.

(51) Filot, I. A. W.; Broos, R. J. P.; Van Rijn, J. P. M.; Van Heugten, G. J. H. A.; Van Santen, R. A.; Hensen, E. J. M. First-Principles-Based Microkinetics Simulations of Synthesis Gas Conversion on a Stepped Rhodium Surface. *ACS Catal.* **2015**, *5* (9), 5453–5467.

(52) Gu, T.; Wang, B.; Chen, S.; Yang, B. Automated Generation and Analysis of the Complex Catalytic Reaction Network of Ethanol Synthesis from Syngas on Rh(111). *ACS Catal.* **2020**, *10* (11), 6346–6355.

(53) Yang, N.; Medford, A. J.; Liu, X.; Studt, F.; Bligaard, T.; Bent, S. F.; Nørskov, J. K. Intrinsic Selectivity and Structure Sensitivity of Rhodium Catalysts for C_{2+} Oxygenate Production. *J. Am. Chem. Soc.* **2016**, *138* (11), 3705–3714.

(54) Shetty, S.; Jansen, A. P. J.; Van Santen, R. A. Direct versus Hydrogen-Assisted CO Dissociation. *J. Am. Chem. Soc.* **2009**, *131* (36), 12874–12875.

(55) Choi, Y.; Liu, P. Mechanism of Ethanol Synthesis from Syngas on Rh(111). *J. Am. Chem. Soc.* **2009**, *131* (36), 13054–13061.

(56) Yang, N.; Yoo, J. S.; Schumann, J.; Bothra, P.; Singh, J. A.; Valle, E.; Abild-Pedersen, F.; Nørskov, J. K.; Bent, S. F. Rh-MnO Interface Sites Formed by Atomic Layer Deposition Promote Syngas Conversion to Higher Oxygenates. *ACS Catal.* **2017**, *7* (9), 5746–5757.

(57) Abdelsayed, V.; Shekhawat, D.; Poston, J. A.; Spivey, J. J. Synthesis, Characterization, and Catalytic Activity of Rh-Based Lanthanum Zirconate Pyrochlores for Higher Alcohol Synthesis. *Catal. Today* **2013**, *207*, 65–73.

(58) Khodakov, A. Y.; Chu, W.; Fongarland, P. Advances in the Development of Novel Cobalt Fischer−Tropsch Catalysts for Synthesis of Long-Chain Hydrocarbons and Clean Fuels. *Chem. Rev.* **2007**, *107* (5), 1692–1744.

(59) Chen, W.; Pestman, R.; Zijlstra, B.; Filot, I. A. W.; Hensen, E. J. M. Mechanism of Cobalt-Catalyzed CO Hydrogenation: 1. Methanation. *ACS Catal.* **2017**, *7* (12), 8050–8060.

(60) Gaggioli, C. A.; Stoneburner, S. J.; Cramer, C. J.; Gagliardi, L. Beyond Density Functional Theory: The Multiconfigurational Approach To Model Heterogeneous Catalysis. *ACS Catal.* **2019**, *9* (9), 8481–8502.

(61) Toyao, T.; Maeno, Z.; Takakusagi, S.; Kamachi, T.; Takigawa, I.; Shimizu, K.-I. Machine Learning for Catalysis Informatics: Recent Applications and Prospects. *ACS Catal.* **2020**, 2260–2297.

(62) Solymosi, F.; Pasztor, M. Infrared Study of the Effect of Hydrogen on Carbon Monoxide-Induced Structural Changes in Supported Rhodium. *J. Phys. Chem.* **1986**, *90* (21), 5312–

5317.

(63) Suzuki, A.; Inada, Y.; Yamaguchi, A.; Chihara, T.; Yuasa, M.; Nomura, M.; Iwasawa, Y. Time Scale and Elementary Steps of CO-Induced Disintegration of Surface Rhodium Clusters. *Angew. Chem. Int. Ed.* **2003**, *42* (39), 4795–4799.

(64) Schwartz, V.; Campos, A.; Egbebi, A.; Spivey, J. J.; Overbury, S. H. EXAFS and FT-IR Characterization of Mn and Li Promoted Titania-Supported Rh Catalysts for CO Hydrogenation. *ACS Catal.* **2011**, *1* (10), 1298–1306.

(65) Van't Blik, H. F. J.; Van Zon, J. B. A. D.; Huizinga, T.; Vis, J. C.; Koningsberger, D. C.; Prins, R. Structure of Rhodium in an Ultradispersed Rhodium/Alumina Catalyst as Studied by EXAFS and Other Techniques. *J. Am. Chem. Soc.* **1985**, *107* (11), 3139–3147.

(66) Van't Blik, H. F. J.; Van Zon, J. B. A. D.; Huizinga, T.; Vis, J. C.; Koningsberger, D. C.; Prins, R. An Extended X-Ray Absorption Fine Structure Spectroscopy Study of a Highly Dispersed Rhodium/Aluminum Oxide Catalyst: The Influence of Carbon Monoxide Chemisorption on the Topology of Rhodium. *J. Phys. Chem.* **1983**, *87* (13), 2264–2267.

(67) Panayotov, P. B.; Yates, J. T. Rhodium-Carbon Monoxide Surface Chemistry: The Involvement of Surface Hydroxyl Groups on Al_2O_3 and SiO_2 Supports. *J. Am. Chem. Soc.* **1988**, *110* (7), 2074–2081.

(68) Bauer, J. U. Kinetic and Mechanistic Studies for the Direct Conversion of Syngas to Ethanol. Doctoral Thesis, Technische Universität Berlin, December 2020. DOI: 10.14279/depositonce-11359

(69) Bhasin, M. M.; Bartley, W. J.; Ellgen, P. C.; Wilson, T. P. Synthesis Gas Conversion over Supported Rhodium and Rhodium-Iron Catalysts. *J. Catal.* **1978**, *54* (2), 120–128.

(70) Mao, W.; Su, J.; Zhang, Z.; Xu, X. C.; Fu, D.; Dai, W.; Xu, J.; Zhou, X.; Han, Y. F. A Mechanistic Basis for the Effects of Mn Loading on C_{2+} Oxygenates Synthesis Directly from Syngas over Rh-MnO_x/SiO_2 Catalysts. *Chem. Eng. Sci.* **2015**, *135*, 301–311.

(71) Mao, W.; Su, J.; Zhang, Z.; Xu, X. C.; Dai, W.; Fu, D.; Xu, J.; Zhou, X.; Han, Y. F. Kinetics Study of C_{2+} Oxygenates Synthesis from Syngas over Rh-MnO_x/SiO_2 Catalysts. *Chem. Eng. Sci.* **2014**, *135*, 312–322.

(72) Burch, R.; Petch, M. I. Investigation of the Synthesis of Oxygenates from Carbon-Monoxide Hydrogen Mixtures on Supported Rhodium Catalysts. *Appl. Catal. A-General* **1992**, *88* (1), 39–60.

(73) Haider, M. A.; Gogate, M. R.; Davis, R. J. Fe-Promotion of Supported Rh Catalysts for Direct Conversion of Syngas to Ethanol. *J. Catal.* **2009**, *261* (1), 9–16.

(74) Liu, Y.; Murata, K.; Inaba, M.; Takahara, I.; Okabe, K. Synthesis of Ethanol from Syngas over $Rh/Ce_{1-x}Zr_xO_2$ Catalysts. *Catal. Today* **2011**, *164* (1), 308–314.

(75) Liu, J.; Tao, R.; Guo, Z.; Regalbuto, J. R.; Marshall, C. L.; Klie, R. F.; Miller, J. T.; Meyer, R. J. Selective Adsorption of Manganese onto Rhodium for Optimized $Mn/Rh/SiO_2$ Alcohol Synthesis Catalysts. *ChemCatChem* **2013**, *5* (12), 3665–3672.

(76) Liu, Y.; Göeltl, F.; Ro, I.; Ball, M. R.; Sener, C.; Aragão, I. B.; Zanchet, D.; Huber, G. W.; Mavrikakis, M.; Dumesic, J. A. Synthesis Gas Conversion over Rh-Based Catalysts

Promoted by Fe and Mn. *ACS Catal.* **2017**, *7* (7), 4550–4563.

(77) Hu, J.; Wang, Y.; Cao, C.; Elliott, D. C.; Stevens, D. J.; White, J. F. Conversion of Biomass-Derived Syngas to Alcohols and C_2 Oxygenates Using Supported Rh Catalysts in a Microchannel Reactor. *Catal. Today* **2007**, *120* (1), 90–95.

(78) Yu, J.; Mao, D.; Han, L.; Guo, Q.; Lu, G. Synthesis of C_2 Oxygenates from Syngas over Monodispersed SiO_2 Supported Rh-Based Catalysts: Effect of Calcination Temperature of SiO_2. *Fuel Process. Technol.* **2013**, *106*, 344–349.

(79) Yu, J.; Mao, D.; Han, L.; Guo, Q.; Lu, G. The Effect of Fe on the Catalytic Performance of Rh–Mn–Li/SiO_2 Catalyst: A DRIFTS Study. *Catal. Commun.* **2012**, *27*, 1–4.

(80) Song, X.; Ding, Y.; Chen, W.; Dong, W.; Pei, Y.; Zang, J.; Yan, L.; Lu, Y. Bimetal Modified Ordered Mesoporous Carbon as a Support of Rh Catalyst for Ethanol Synthesis from Syngas. *Catal. Commun.* **2012**, *19*, 100–104.

(81) Yu, J.; Mao, D.; Han, L.; Guo, Q.; Lu, G. Conversion of Syngas to C_{2+} Oxygenates over Rh-Based/SiO_2 Catalyst: The Promoting Effect of Fe. *J. Ind. Eng. Chem.* **2013**, *19* (3), 806–812.

(82) Huang, Y.; Deng, W.; Guo, E.; Chung, P. W.; Chen, S.; Trewyn, B. G.; Brown, R. C.; Lin, V. S. Y. Mesoporous Silica Nanoparticle-Stabilized and Manganese-Modified Rhodium Nanoparticles as Catalysts for Highly Selective Synthesis of Ethanol and Acetaldehyde from Syngas. *ChemCatChem* **2012**, *4* (5), 674–680.

(83) Kim, T.-W.; Kim, M.-J.; Chae, H.-J.; Ha, K.-S.; Kim, C.-U. Ordered Mesoporous Carbon Supported Uniform Rhodium Nanoparticles as Catalysts for Higher Alcohol Synthesis from Syngas. *Fuel* **2015**, *160*, 393–403.

(84) Lisitsyn, A. S.; Stevenson, S. A.; Knözinger, H. Carbon Monoxide Hydrogenation on Supported Rh-Mn Catalysts. *J. Mol. Catal.* **1990**, *63* (2), 201–211.

(85) Wang, S.; Guo, W.; Wang, H.; Zhu, L.; Qiu, K. Influence of Mn Promotion on CO Hydrogenation over Rh/CNTs Catalyst. *Catal. Letters* **2014**, *144* (7), 1305–1312.

(86) Chen, G.; Guo, C.-Y.; Zhang, X.; Huang, Z.; Yuan, G. Direct Conversion of Syngas to Ethanol over Rh/Mn-Supported on Modified SBA-15 Molecular Sieves: Effect of Supports. *Fuel Process. Technol.* **2011**, *92* (3), 456–461.

(87) Yu, J.; Yu, J.; Shi, Z.; Guo, Q.; Xiao, X.; Mao, H.; Mao, D. The Effects of the Nature of TiO_2 Supports on the Catalytic Performance of Rh–Mn/TiO_2 Catalysts in the Synthesis of C_2 Oxygenates from Syngas. *Catal. Sci. Technol.* **2019**, *9* (14), 3675–3685.

(88) Ma, X.; Deng, H.; Yang, M.-M.; Li, W.-X. Atomic and Molecular Adsorption on RhMn Alloy Surface: A First Principles Study. *J. Chem. Phys.* **2008**, *129* (24), 244711.

(89) Huang, X.; Teschner, D.; Dimitrakopoulou, M.; Fedorov, A.; Frank, B.; Kraehnert, R.; Rosowski, F.; Kaiser, H.; Schunk, S.; Kuretschka, C.; Schlögl, R.; Willinger, M.-G.; Trunschke, A. Atomic-Scale Observation of the Metal–Promoter Interaction in Rh-Based Syngas-Upgrading Catalysts. *Angew. Chem. Int. Ed.* **2019**, *58* (26), 8709–8713.

(90) Dimitrakopoulou, M.; Huang, X.; Kröhnert, J.; Teschner, D.; Praetz, S.; Schlesiger, C.; Malzer, W.; Janke, C.; Schwab, E.; Rosowski, F.; Kaiser, H.; Schunk, S.; Schlögl, R.;

Trunschke, A. Insights into Structure and Dynamics of (Mn,Fe)O_x-Promoted Rh Nanoparticles. *Faraday Discuss.* **2018**, *208*, 207–225.

(91) Hartman, T.; Geitenbeek, R. G.; Whiting, G. T.; Weckhuysen, B. M. Operando Monitoring of Temperature and Active Species at the Single Catalyst Particle Level. *Nat. Catal.* **2019**, *2* (11), 986–996.

(92) Mo, X.; Gao, J.; Umnajkaseam, N.; Goodwin Jr., J. G. La, V, and Fe Promotion of Rh/SiO_2 for CO Hydrogenation: Effect on Adsorption and Reaction. *J. Catal.* **2009**, *267* (2), 167–176.

(93) Wang, J.; Zhang, Q.; Wang, Y. Rh-Catalyzed Syngas Conversion to Ethanol: Studies on the Promoting Effect of FeO_x. *Catal. Today* **2011**, *171* (1), 257–265.

(94) Burch, R.; Hayes, M. J. The Preparation and Characterisation of Fe-Promoted Al2O3-Supported Rh Catalysts for the Selective Production of Ethanol from Syngas. *J. Catal.* **1997**, *165* (2), 249–261.

(95) Gogate, M. R.; Davis, R. J. X-Ray Absorption Spectroscopy of an Fe-Promoted Rh/TiO_2 Catalyst for Synthesis of Ethanol from Synthesis Gas. *ChemCatChem* **2009**, *1* (2), 295–303.

(96) Carrillo, P.; Shi, R.; Teeluck, K.; Senanayake, S. D.; White, M. G. In Situ Formation of FeRh Nanoalloys for Oxygenate Synthesis. *ACS Catal.* **2018**, *8* (8), 7279–7286.

(97) Palomino, R. M.; Magee, J. W.; Llorca, J.; Senanayake, S. D.; White, M. G. The Effect of Fe-Rh Alloying on CO Hydrogenation to C_{2+} Oxygenates. *J. Catal.* **2015**, *329*, 87–94.

(98) Rezvani, A.; Abdel-Mageed, A. M.; Ishida, T.; Murayama, T.; Parlinska-Wojtan, M.; Behm, R. J. CO2 Reduction to Methanol on Au/CeO2 Catalysts: Mechanistic Insights from Activation/Deactivation and SSITKA Measurements. *ACS Catal.* **2020**, *10* (6), 3580–3594.

(99) Abdel-Mageed, A. M.; Klyushin, A.; Knop-Gericke, A.; Schlögl, R.; Behm, R. J. Influence of CO on the Activation, O-Vacancy Formation, and Performance of Au/ZnO Catalysts in CO_2 Hydrogenation to Methanol. *J. Phys. Chem. Lett.* **2019**, *10* (13), 3645–3653.

(100) Divins, N. J.; Kordus, D.; Timoshenko, J.; Sinev, I.; Zegkinoglou, I.; Bergmann, A.; Chee, S. W.; Widrinna, S.; Karslıoğlu, O.; Mistry, H.; Lopez Luna, M.; Zhong, J. Q.; Hoffman, A. S.; Boubnov, A.; Boscoboinik, J. A.; Heggen, M.; Dunin-Borkowski, R. E.; Bare, S. R.; Cuenya, B. R. Operando High-Pressure Investigation of Size-Controlled CuZn Catalysts for the Methanol Synthesis Reaction. *Nat. Commun.* **2021**, *12* (1), 1–10.

(101) Behrens, M.; Studt, F.; Kasatkin, I.; Kuhl, S.; Havecker, M.; Abild-Pedersen, F.; Zander, S.; Girgsdies, F.; Kurr, P.; Kniep, B.-L.; Tovar, M.; Fischer, R. W.; Norskov, J. K.; Schlogl, R. The Active Site of Methanol Synthesis over Cu/ZnO/Al_2O_3 Industrial Catalysts. *Science* **2012**, *336* (6083), 893–897.

(102) Lunkenbein, T.; Schumann, J.; Behrens, M.; Schlögl, R.; Willinger, M. G. Formation of a ZnO Overlayer in Industrial Cu/ZnO/Al_2O_3 Catalysts Induced by Strong Metal-Support Interactions. *Angew. Chem. Int. Ed.* **2015**, *54* (15), 4544–4548.

(103) Laudenschleger, D.; Ruland, H.; Muhler, M. Identifying the Nature of the Active Sites in Methanol Synthesis over Cu/ZnO/Al_2O_3 Catalysts. *Nat. Commun.* **2020**, *11* (1).

(104) Pan, X.; Fan, Z.; Chen, W.; Ding, Y.; Luo, H.; Bao, X. Enhanced Ethanol Production inside Carbon-Nanotube Reactors Containing Catalytic Particles. *Nat. Mater.* **2007**, *6* (7), 507–511.

2 Motivation and Objectives

The syngas-to-ethanol (StE) reaction is a promising alternative route to ethanol from fossil and nonfossil carbon resources. Rh-based catalysts offer the highest ethanol yields so far but suffer from low to moderate CO conversions and high selectivities toward methane. Despite serious research efforts, ethanol rates and selectivities still need to be improved for industrial application.

One of the main strategies to improve Rh's performance in StE is the modification with one or usually several promoters. However, the complexity of these catalytic systems often hampers a fundamental understanding of promoter effects. Likewise, the identification of co-promotional effects might be complicated when investigating multi-promoted catalysts alone.

Current research focuses mainly on the improvement of Rh-based catalysts, and as a consequence thereof, peak performance marks have been published readily without considering the catalyst's time-on-stream (TOS) behavior. This lack of long-term catalytic data limits an industrial application of Rh-based catalysts in StE conversion as estimating catalyst lifetime is key to operating industrial-scale facilities in a resource- and cost-efficient manner. Likewise, our current knowledge is mostly limited to freshly reduced Rh-based catalysts as the characterization of spent samples is seldom reported. However, an in-depth investigation of used catalysts is of utmost importance, as heterogeneous catalysts often change their properties under the influence of high temperatures and elevated pressures during catalysis. All these circumstances might contribute to the significant variation in reported catalytic data of Rh-based catalysts in CO hydrogenation.

This thesis aims to provide a fundamental understanding of the formation of Rh–promoter interactions and their influence on the stability and reactivity of promoted Rh-based catalysts. Therefore, detailed investigations have been performed on Mn- and Fe-promoted Rh/SiO_2 catalysts targeting these main aspects:

i. Identification of promotional effects of Mn and Fe in traditionally prepared single- and multi-promoted Rh/SiO_2 catalysts: differences of Mn and Fe as promoter or modifier, their influence on Rh's morphological and electronic properties, and the presence of co-promotion

ii. Development of a metal-organic synthesis approach: optimal conditions for nanoalloy formation and increasing Rh–promoter interactions

iii. Understanding the formation of specific Rh–promoter interactions: role of nanoalloy formation in syngas conversion over Rh, the spatial distribution of

promoters and Rh over the support, and relevance of Rh–promoter interfacial sites

iv. Influence of reaction time and industrially relevant high-pressure conditions: long-term stability of Rh-based catalysts, reactant-induced changes to catalyst nanostructures and reactivity, and mechanism of deactivation

3 Paper 1: Formation, Dynamics, and Long-Term Stability of Mn- and Fe-Promoted Rh/SiO_2 Catalysts in CO Hydrogenation (accepted version)

Phil Preikschas, Julia Bauer, Kristian Knemeyer, Raoul Naumann d'Alnoncourt, Ralph Kraehnert, and Frank Rosowski

Paper 1: Formation, Dynamics, and Long-Term Stability of Mn- and Fe-Promoted Rh/SiO_2 Catalysts in CO Hydrogenation

Catal. Sci. Technol. **2021**, *11* (17), 5802–5818. DOI: 10.1039/D1CY00421B. (CC BY-NC)

Abstract: The conversion of syngas (CO/H_2) to ethanol (StE) is one promising example to generate a high-value fuel and key intermediate for various base chemicals, preferably from non-fossil carbon resources. Rh-based catalysts demonstrated the highest selectivities towards C_{2+} oxygenates and ethanol, in particular. However, the accomplished yields still must be increased, and the catalyst's stability must be improved for industrial application. One primary strategy to improve C_{2+} oxygenate yields over Rh is the addition of one or several promoters. Specifically, Mn and Fe are among the most frequently used metals to improve rhodium's catalytic performance in binary and ternary systems. To date, experimental studies primarily focused on increasing the C_{2+} oxygenate yields, but long-term catalytic investigations are only rarely reported. Consequently, Mn and Fe's specific role as promoter and their influence on the long-term and thermal stability of supported Rh catalysts are not clarified as yet. A holistic view of atomistic promoter effects and their impact on the stability and dynamics of Rh-based catalysts under reaction conditions is thereby highly desired. Herein, we report a comprehensive study about the stability and dynamics of Mn- and Fe-promoted Rh/SiO_2 catalysts at industrially relevant high-pressure conditions (54 bar). For this purpose, unpromoted Rh/SiO_2, single-promoted $RhMn/SiO_2$ and $RhFe/SiO_2$, and complex multi-promoted $RhMnFe/SiO_2$ catalysts were systematically investigated in four different states: calcined, reduced, after a long-term catalytic study (>22 days on stream), and after a high temperature stability investigation (T = 243–320 °C). The thorough analysis of each catalyst in the different states with integral and local characterization methods led to specific structural models before and after long-term catalytic investigations. These structural models provide a detailed view on compositions, electronic properties, and morphologies of promoted Rh/SiO_2 catalysts and serve as a basis for improved catalyst design strategies and more sophisticated computational modeling efforts.

3.1 Introduction

Depletion of fossil resources and the increasing demand of a growing world population lead to new challenges to provide industry and society with chemicals. In this manner, syngas (CO/H_2) as an alternative feedstock for the production of base chemicals becomes increasingly interesting in view of growing climate and carbon management concerns.[1] The production of synthetic ethanol is one promising example of this transition. To date, ethanol is mainly produced by fermentation of sugars from corn or sugarcane. This process is inefficient, energy-intensive, and directly competes with food sources raising ethical issues.[2] For this reason, the direct conversion of syngas to ethanol (StE) is a promising alternative route from non-fossil carbon resources.

Over the last decades, various catalyst systems have been tested for the direct conversion of StE, and Rh-based catalysts offer the most promising results.[1–4] However, the accomplished yields still must be increased, and the catalyst's stability must be improved before industrial applications become viable. Despite these heavy research efforts, the entire complexity of this reaction at process-relevant conditions has not been unraveled so far.[2,5] Until now, experimental studies primarily focused on increasing the C_{2+} oxygenate yields, but long-term investigations (>100 h on stream) are still limited.[2,6] Subsequently, the stability of Rh-based catalysts and the influence of promoters on Rh's deactivation behavior are only rarely studied. Furthermore, specific promoter effects and related structure-function relationships cover mainly the initial reactivity of Rh-based catalysts.[5] However, studies on supported metal catalysts have shown that a catalyst can undergo a change in activity and selectivity over time on stream during an initial formation phase.[7–9]

One primary strategy to improve C_{2+} oxygenate yields over Rh is the addition of one or several promoters. In this manner, a wide range of metallic and oxidic promoters, including transition metals and rare-earth elements, have been tested. Mn and Fe are among the most frequently used metals to improve Rh's catalytic performance in binary and ternary systems.[2]

Even so the reaction network and active Rh sites are still elusive, ethanol is likely formed on Rh through hydrogen-assisted dissociation of adsorbed CO, formation of CH_x (x = 1–3) surface fragments, insertion of CHO/CO into Rh–CH_x bond, and subsequent hydrogenation.[1–3,10,11] As Mn addition has shown high potential to increase C_{2+} oxygenate yields and ethanol, in particular, its role in the StE reaction has been described as promoting CO dissociation and CO insertion.[2] However, the influence of Mn on Rh's morphological and electronic properties is rarely discussed. Experimental evidence of specific promoter effects has been contributed by Mao *et al.* that tilted adsorbed CO species at Rh–MnO_x interfacial sites cause increased CO dissociation rates that lead to enhanced activity and selectivity.[12] Other studies contradict this hypothesis and doubt

the relevance of tilted adsorbed CO species for reactivity.[13] Whereas others proposed that MnO_x stabilizes Rh^+ sites at their interface and ultimately promotes CO insertion.[14–18] On the contrary, Yu and co-workers proposed that Rh^+ sites are not stable under reaction conditions and thereby not relevant for the StE reaction.[19]

Similarly, the role of Fe as promoter for Rh-based catalysts is still under debate and controversially discussed. On the one hand, increased ethanol selectivities and suppressed methane formation were observed and ascribed to the formation of RhFe nanoalloy structures under reaction conditions.[20–23] In contrast, the stabilization of Rh^+ sites has been proposed through FeO_x species in their vicinity.[24–26] Similar to $RhMnO_x$, these sites enhance molecular CO adsorption and finally CO insertion. Besides the promotional effect of Fe in enhancing ethanol formation, Mo and co-workers ascribed higher selectivities towards methane and methanol to the addition of Fe. Subsequently, only a small improvement in EtOH selectivity was observed.[27]

Despite these conversely discussed promoter effects, it is widely accepted that a close proximity of the promoter and Rh is needed, the so-called strong metal–promoter interactions.[28–30] However, a lack of long-term catalytic investigations and thorough characterization of spent samples after catalytic reaction have limited atomistic insights into the Rh–promoter interface. Likewise, the specific role of each promoter and their influence on Rh's catalytic properties over longer periods of time are not clarified yet. For these reasons, a holistic view of promoter effects on an atomic level and their impact on Rh-based catalysts under reaction conditions is highly desired.

Herein, we report a comprehensive study about the stability and dynamics of Mn- and Fe-promoted Rh-based catalysts under industrially relevant high-pressure conditions (54 bar, 243–320 °C). Long-term catalytic investigations (>22 days on stream time) combined with an extended catalyst characterization provided simplified structural models of each catalyst before and after catalysis. We foresee that these structural models will serve as a basis for improved catalyst design strategies and more sophisticated computational modeling efforts.

3.2 Experimental Section

Catalyst synthesis. The four different catalysts were synthesized according to a previously reported procedure.[6,29] Aqueous solutions of the respective metal nitrates were impregnated on the silica support (Davisil Grade 636, Sigma-Aldrich) by incipient wetness impregnation method. Drying and calcination were performed in four steps under a constant flow of synthetic air (500 mL/min) with a ramp of 5 K/min at 80, 100, 120, and 350 °C for 30, 30, 180, and 180 min, respectively. After calcination, the pre-catalysts were sieved to receive the target particle size for catalytic testing of 250–315 µm. Metal loadings from ICP-OES (wt%): 2.2 Rh (Rh/SiO_2); 2.4 Rh, 1.6 Mn ($RhMn/SiO_2$); 2.3 Rh, 0.5 Fe ($RhFe/SiO_2$); 2.3 Rh, 1.5 Mn, 0.5 Fe ($RhMnFe/SiO_2$). Atomic percent of metals (at%): 1.0 Rh (Rh/SiO_2); 1.0 Rh, 1.3 Mn ($RhMn/SiO_2$); 1.0 Rh, 0.4 Fe ($RhFe/SiO_2$); 1.0 Rh, 1.2 Mn, 0.4 Fe ($RhMnFe/SiO_2$).

Catalyst characterization. All samples have been transferred under ambient conditions after calcination, reduction, long-term catalytic investigation, and high temperature study for sample characterization.

Powder X-ray diffraction (XRD) measurements were performed in Bragg-Brentano geometry on a D8 Advance II theta/theta diffractometer (Bruker AXS), using Ni-filtered Cu $K\alpha_{1,2}$ radiation and a position sensitive energy dispersive LynxEye silicon strip detector. The sample powder was filled into the recess of a cup-shaped sample holder, the surface of the powder bed being flush with the sample holder edge (front loading).

Scanning transmission electron microscopy (STEM), energy-dispersive X-ray spectroscopy (EDX) were conducted on a FEI Talos F200X microscope. The microscope was operated at an acceleration voltage of 200 kV. STEM-EDX elemental maps were recorded by a Super-X system including four silicon drift detectors. Background-corrected and fitted intensities were used for image visualization. All samples were prepared on holey carbon-coated copper grids (Plano GmbH, 400 mesh). Particle size distributions were determined by measuring at least 250 particles by using ImageJ software[31].

X-ray photoelectron spectroscopy (XPS) was measured on K-Alpha™ + X-ray Photoelectron Spectrometer System (Thermo Scientific), with Hemispheric 180° dual-focus analyzer with 128-channel detector. This system uses a micro-focused, monochromatic Al Kα X-ray source powered at 6 mA and 12 kV. Charge compensation was performed using a dual-beam flood source of low-energy Ar^+ ions and low energy electrons (less than 1 eV). For the measurement, the as-prepared samples were directly loaded on the sample holder. The data was collected with X-ray spot size of 200 µm, 20 scans for survey, and 50 scans for regions. The pass energy was set at 200 eV for survey and 50 eV for high-resolution spectra. All survey spectra (1400–0 eV, 1.0 eV step size)

and high-resolution spectra (0.1 eV step size) of Si 2p (116–92 eV), C 1s (300–276 eV), Rh 3d (328–296 eV), O 1s (544–524 eV), and Fe 2p (740–700 eV) regions are provided in the Supporting Information. Data analysis was carried out using Thermo Scientific Avantage software. For composition analysis, a method for carbon contamination correction proposed by Smith has been applied.[32]

Elemental analysis (Rh, Mn, Fe, Mg) was performed *via* inductively coupled plasma optical emission spectrometry *(*ICP-OES*)* by the contract laboratory Mikroanalytisches Labor Kolbe, Oberhausen (Germany).

Catalytic testing for synthesis gas conversion. The catalytic testing of the syngas-to-ethanol reaction was performed in a 4-fold parallel testing unit. Catalyst amounts of 0.1–0.5 g (approx. 0.2–1.0 mL) with a particle size of 100–200 µm were loaded into each stainless-steel reactor with an effective inner diameter of 6.25 mm. The reaction temperature was monitored by temperature sensors with three thermocouples along the catalyst bed.

Four mass flow controllers were used to adjust the flow rates of the inlet gases N_2 (99.999 %), CO (99.997 %), H_2 (99.999 %) and Ar (99.999 %, all Air Liquide). The CO feed line was equipped with a carbonyl trap to remove all metal carbonyls that might be formed by high-pressure of CO in contact with stainless steel. The carbonyl trap consisted of a U-shaped ½" stainless steel tube filled with Al_2O_3 and heated to 170 °C by a heating sleeve.

Compounds in the effluent gas that condense at 180 °C were removed by a coalescence filter in the downstream oven. All remaining compounds in the effluent gas were analyzed with an online gas chromatograph (Agilent 7890B) equipped with one thermal conductivity detector (TCD) and one flame ionization detector (FID) using He as the carrier gas. TCD detects the inlet gases H_2, Ar, N_2, and CO. The FID is used to detect a large variety of paraffins, olefins and oxygenates (alcohols, acetaldehyde, acetic acid) using a Poraplot Q column. Installation of a Polyarc® reactor allowed detection of CO and CO_2 with the FID and precise quantification of all compounds. The carbon balance was between 96–102 % for all measurements.

The catalysts were reduced *in situ* at 54 bar, 265 °C with 5 % H_2 in N_2 for 1 h with a volume flow of 41.6 NmL min^{-1}. Subsequently, synthesis gas feedstock mixture containing CO:H_2:N_2:Ar (20:60:10:10%, v:v) was admitted at a total pressure of 54 bar. The volume flow was kept constant to achieve a GHSV of 2500–12500 h^{-1}. The amount of catalyst was chosen to yield approx. 5 % CO conversion at standard conditions. The temperature was varied in a range of 243–320 °C. Each step was held constant for at least 15 h to allow the catalysts to equilibrate.

The obtained concentrations of all compounds were corrected for volume changes due to the reaction and the subsequent N_2 dilution. Therefore, the mole fraction of Ar was used as inert internal standard according to equation 1.

$$x_{i,corrected} = x_{i,GC} \cdot \frac{x_{Ar,bypass}}{x_{Ar,reactor}} \quad (1)$$

$x_{i,corrected}$ is the corrected mole fraction of compound i. $x_{Ar,reactor}$ and $x_{Ar,bypass}$ are the mole fractions of Ar originally obtained by the gas chromatograph sampling the respective reactor or the bypass line.

Carbon monoxide conversion X_{CO} was calculated based on the sum of carbon numbers in all products (equation 2).

$$X_{CO} = \frac{\sum n_j C_j}{n_{CO,0}} \quad (2)$$

$n_{CO,0}$ is the mole fraction of CO in the inlet gas and C_i is the carbon number of the product *i*. The selectivity *S* for each product *i* was determined based on the number of C atoms by equation 3.

$$S_i = \frac{n_i C_i}{\sum n_{i,j} C_{i,j}} \quad (3)$$

3.3 Results and Discussion

Four different Rh-based samples were synthesized by co-impregnation of metal nitrates, drying, and calcination at 350 °C in flowing air. Besides a pure Rh/SiO_2 catalyst with a nominal loading of 2.4 wt%, three modified catalysts with Mn and/or Fe as promoters were investigated with nominal loadings of 1.5 and 0.5 wt%, respectively (for exact values from ICP-OES analysis see catalyst synthesis in Experimental Section). These Mn and Fe loadings were selected based on preliminary catalytic tests to identify the highest ethanol space-time yields. Especially the Fe loading has a crucial impact on methanol and ethanol formation rates.[22,33] In the case of Mn, the chosen Mn:Rh ratio is in agreement with the optimal molar ratio of 1 reported by Ojeda and co-workers.[34]

Throughout this work, the catalysts will be referred to with the simplified expressions Rh/SiO_2, $RhMn/SiO_2$, $RhFe/SiO_2$, and $RhMnFe/SiO_2$ due to readability. This denotation does not contain information about oxidation states or different morphologies.

The four catalysts were tested in two independent catalytic tests: (1) a comprehensive long-term catalytic study with over 22 days on stream at 243–260 °C and (2) a high temperature study, which focused on the stability of the materials investigated, with a maximum temperature of 320 °C applied. For both studies, the as-prepared, calcined pre-catalysts were reduced *in situ* prior to catalytic testing at 265 °C in 5 % H_2/N_2 and measured under industrially high-pressure conditions (54 bar). To investigate the stability and surface dynamics of the $Rh/Mn/Fe/SiO_2$ catalysts under high-pressure conditions, every catalyst system was thoroughly characterized in the four different states: calcined (black), reduced (blue; after *in situ* H_2 treatment), after long-term catalytic study (dark green), and after high temperature stability investigation (light green; Scheme 3.1).

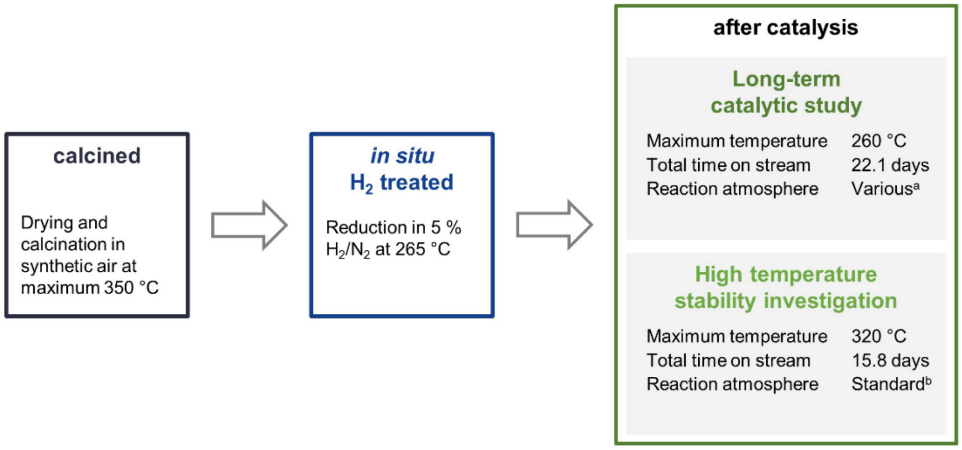

Scheme 3.1. Overview of the four different states in which each sample was investigated. [a]Reaction atmosphere was varied: $CO:H_2:Ar:N_2$ = 2.5-20:30-60:10:balance in 18 steps at 54 bar total pressure. [b]Standard reaction atmosphere: $CO:H_2:Ar:N_2$ = 20:60:10:10 at 54 bar total pressure.

The characterization results of different states provide meaningful insights into catalyst composition, electronic properties, and morphology. Their different nanostructures before and after catalysis are represented as simplified structural models, which provide the opportunity to clarify the role of Mn and Fe in binary and ternary Rh catalysts on an atomic level and industrially relevant reaction times.

3.3.1 Bulk and Surface Compositions of Rh/Mn/Fe/SiO_2 Catalysts

The bulk compositions of all four catalysts remained the same before and after catalytic testing, as proved by ICP-OES. Therefore, any influence of changing bulk compositions on the reactivity during catalysis can be excluded.

Moreover, stable bulk compositions are necessary to investigate surface compositions of each catalyst *via* XPS. These surface compositions were determined by comparing the respective elemental peak areas from high-resolution scans after carbon contamination correction (see Experimental Section for more details). The Si 2p signal (103.5 eV) was used as charge reference. For all samples, the Si:O ratio is about 1:2, as expected for SiO_2 as support. Si and O together make up 98–99 at% of the entire surface (Table 3.1).

Table 3.1. Surface compositions of all catalysts investigated by XPS and metal bulk ratios from ICP-OES analysis.[a]

Entry	Sample	Treatment	Surface composition (at%)					Mn/Fe/Rh surface ratio	Mn/Fe/Rh bulk ratio from ICP
			Si	O	Rh	Mn	Fe		
1	SiO_2	calcination	33	66	-	-	-	-	-
2	Rh/SiO_2	calcination	33	66	0.38	-	-	-	-
3		reduction	33	66	0.32	-	-	-	-
4		high temperatures	33	66	0.34	-	-	-	-
5		long-term study	33	66	1.02	-	-	-	-
6	RhMn/SiO_2	calcination	33	66	0.42	0.46	-	1.1/-/1	1.2/-/1
7		reduction	33	66	0.31	0.48	-	1.5/-/1	
8		high temperatures	33	66	0.37	0.84	-	2.3/-/1	
9		long-term study	33	65	0.65	1.43	-	2.2/-/1	
10	RhFe/SiO_2	calcination	33	66	0.46	-	0.52	-/1.1/1	-/0.4/1
11		reduction	33	66	0.54	-	0.78	-/1.4/1	
12		high temperatures	33	66	0.27	-	0.60	-/2.2/1	
13		long-term study	33	66	0.52	-	0.85	-/1.6/1	
14	RhMnFe/SiO_2	calcination	33	66	0.40	0.45	0.41	1.1/1.1/1	1.2/0.4/1
15		reduction	33	66	0.33	0.60	0.48	1.8/1.4/1	
16		high temperatures	33	66	0.29	0.55	0.49	1.8/1.7/1	
17		long-term study	33	65	0.58	1.01	0.79	1.7/1.4/1	

[a] Surface compositions have been determined from high-resolution scans. Si 2p, O 1s, Rh 3d, and Fe 2p high-resolution spectra are provided in the Supporting Information, and Mn 2p spectra as Figure 3.2.

An overall Rh surface content of around 0.38 at% was found for the unpromoted Rh/SiO_2 sample, which was slightly decreased after H_2 reduction. Interestingly, the Rh surface content increased by a factor of 3.2 to 1.02 at% after the long-term catalytic study (Table 3.1, entries 3 and 5). This finding suggests that a significantly higher Rh dispersion on the silica surface is present after catalysis.

For the calcined $RhMn/SiO_2$ sample, the Mn:Rh ratio was about 1.1 as expected from bulk composition analysis (Table 3.1, entry 6). Rh and Mn show thereby a comparable distribution over the sample, and their ratio is slightly increased after H_2 treatment. After catalysis, the Mn:Rh ratio was significantly increased with values of 2.3 and 2.2, respectively (Table 3.1, entries 8 and 9). This suggests an increased mobility of MnO_x under reaction conditions.

Moreover, this increased ratio and a lower increase in Rh dispersion (factor of 2.1; Table 3.1, entries 7 and 9) might be an indication for migration of MnO_x species to Rh nanoparticles and partial coverage of Rh surface sites. A complementary observation was also reported for similar Mn-promoted Rh/SiO_2 catalysts, suggesting the formation of MnO_x overlayers at the Rh–MnO_x interface through strong metal–promoter interactions.[28]

In the case of $RhFe/SiO_2$, a Fe:Rh ratio of 1.1 was determined after calcination (Table 3.1, entry 10). This ratio does not fit the bulk composition (0.33), which leads to the assumption that Fe is finely distributed over the support surface, and thereby an agglomeration of Fe can be excluded. After catalysis, the Fe surface content was further increased, but to a smaller extent compared to Mn (Table 3.1, entries 11 and 13). Therefore, Fe might also be mobile on the surface of silica under reaction conditions, similar to the case of Mn. In contrast to the unpromoted and Mn-promoted Rh catalyst, the Rh dispersion remained the same after long-term catalytic study and was significantly decreased after the high temperature investigation.

The complex multi-promoted $RhMnFe/SiO_2$ catalyst shows similar trends as described for the single-promoted systems resulting in Mn/Fe/Rh ratio of 1.1/1.1/1 after calcination (Table 3.1, entry 14). Reduction in H_2 leads to an increase in Mn surface content. In contrast, the reduction of the pre-catalyst has no significant influence on the surface content of Fe. After catalysis, further enrichment of Mn and Fe contents by factors of 1.7 and 1.6 were observed, respectively (Table 3.1, entries 15 and 17).

To conclude, the Rh dispersion increased in the monometallic and Mn-containing samples after the catalytic conversion of syngas to ethanol. Mn and Fe seem to be mobile under reaction conditions, and partial coverage of Rh by a MnO_x phase is rather likely. Overall, the XPS analysis reveals a significant influence of the applied reaction conditions on the specific surface composition.

3.3.2 Oxidation States and Electronic Properties of $Rh/Mn/Fe/SiO_2$ Catalysts

To investigate the oxidation states, electronic properties, and phase compositions in the four states mentioned in Scheme 3.1, XPS and XRD were applied. In the calcined state of all pre-catalysts investigated, Rh is present as Rh_2O_3 as indicated by the most intense reflection of Rh_2O_3 at $2\theta = 35°$ in the respective X-ray diffractograms (Figure 3.1a). This

reflection is clearly visible in direct comparison with the diffractogram of the pure SiO_2 support (grey; Figure 3.1). In the case of $RhFe/SiO_2$, this feature is broader, which might be caused by formation of a complex mixture of Rh and Fe oxides as reported for $Rh(Mn,Fe)O_x/SiO_2$ catalysts.[28,29] The XRD data is further consistent with XPS analysis showing typical binding energy peaks of Rh^{3+} at 308.6–308.9 eV in corresponding Rh 3d spectra (Figures S3.1a–d).

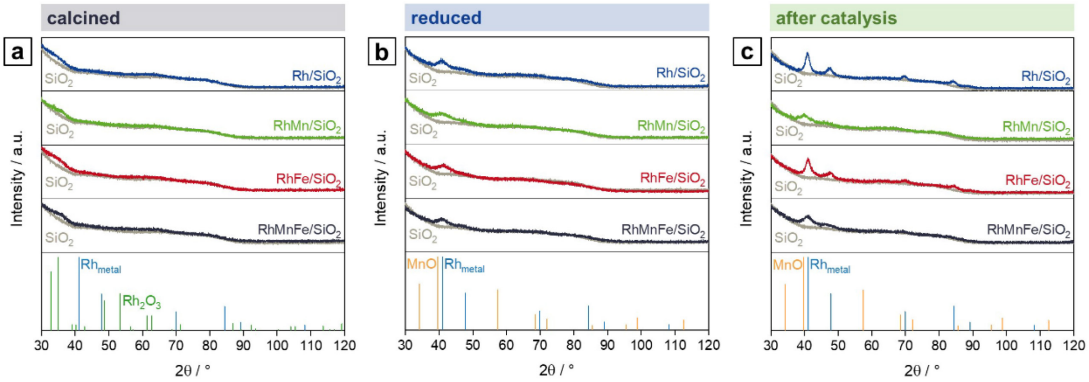

Figure 3.1. X-ray diffractograms of Rh/SiO_2 (blue), $RhMn/SiO_2$ (green), $RhFe/SiO_2$ (red), and $RhMnFe/SiO_2$ (black) in direct comparison with pure SiO_2 (grey) after (a) calcination (350 °C, synthetic air), (b) reduction (265 °C, 5 % H_2/N_2), and (c) after catalysis (long-term catalytic study; 54 bar, max. 260 °C; 530 h on stream). Rh (blue; C5-685), Rh_2O_3 (green; C41-541), and MnO(orange; 065-0638) references were taken from ICDD database.

The H_2 treatment leads to a full reduction of Rh reflected in binding energy shifts to the typical region for metallic Rh from 307.4–306.9 eV (Figures S3.1a–d and Table S3.1). Subsequent exposure to ambient air after reduction does not cause oxidation of supported Rh. The full reduction of Rh_2O_3 to Rh also becomes visible in XRD spectra of Rh/SiO_2 and $RhFe/SiO_2$, showing a broad peak at the position of the typical main reflection of metallic Rh ($2\theta = 41°$; Figure 3.1b). An exact assignment is not possible regarding the Mn-promoted catalysts due to a broadening of the signal and the common detection limit of XRD below crystallite sizes of 3 nm.[35] Moreover, this broadening might be a result of an overlap with a MnO reflection, which usually appears in the same range ($2\theta = 39.7°$; Figure 3.1b). Hence, it can be assumed that the addition of Mn to Rh/SiO_2 catalysts leads to a higher Rh dispersion after synthesis and *in situ* reduction.

Respective Mn 2p spectra of $RhMn/SiO_2$ and $RhMnFe/SiO_2$ show binding energy peaks in the distinct region of oxidized Mn at 641.6 and 641.5 eV, respectively (Figures 3.2a,b). Not even the reduction in H_2, or the long-term catalytic study under high-pressure syngas condition, led to a further reduction of Mn. This is in accordance with one of our previously reported studies about $RhMnO_x/SiO_2$ catalysts. In this study, we demonstrated that the oxidation of Mn to MnO_x is inevitable on silica supports. Impregnation of $Na[Mn(CO)]_5$, bearing Mn in the low oxidation state of -1, did not lead to the formation of a zero-valent Mn species.[30] The presence of typical satellite peaks in all Mn 2p spectra after reduction or catalysis indicates that Mn is presumably in a formal

oxidation state of +2 (Figures 3.2a,b). It is consequently assumed that most likely MnO is the prevailing phase.

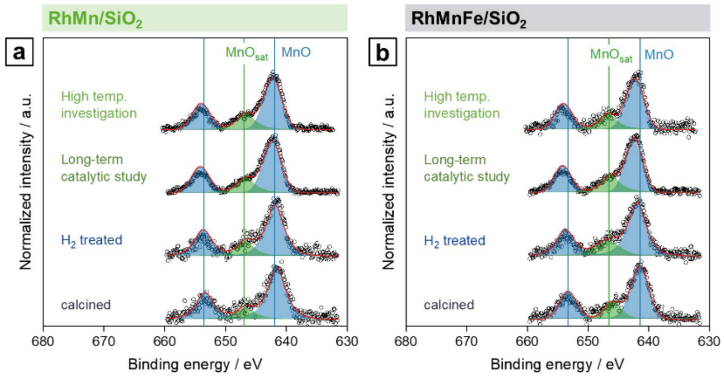

Figure 3.2. Mn 2p high-resolution XP spectra (660–630 eV, 0.1 eV step size) of (a) $RhMn/SiO_2$ and (b) $RhMnFe/SiO_2$ in four different states: calcined (350 °C, synthetic air), reduced (265 °C, 5 % H_2/N_2), after long-term catalytic study (54 bar, max. 260 °C; 530 h on stream), and after high temperature stability investigation (54 bar, max. 320 °C; 350 h on stream). For corresponding Rh 3d and Fe 2p spectra see Figures S3.1 and S3.2.

After long-term catalysis, significant binding energy shifts of 0.7 eV to higher binding energies (642.3 and 642.2 eV, respectively) were observed in respective spectra of $RhMn/SiO_2$ and $RhMnFe/SiO_2$ (Figures 3.2a,b and Table S3.1). These shifts are probably caused by forming Mn acetates and/or carbonates under the reductive syngas conditions. In a recent study, we reported the formation of surface carbonates on MnO_x-supported Rh catalysts during the conversion of syngas based on XRD analysis of respective spent catalysts.[36] Due to the low Mn loading, the formation of acetate or carbonate species on $RhMn/SiO_2$ and $RhMnFe/SiO_2$ could not be verified by XRD. Therefore, further investigations are required for a clear statement.

On the contrary, no significant changes in the high-resolution Fe 2p spectra have been observed for the Fe-containing samples, $RhFe/SiO_2$ and $RhMnFe/SiO_2$, after catalytic reactions. Subsequently, the Fe 2p XPS data indicate that Fe is mainly in an oxidized state, probably in the form of Fe_2O_3 (Figures S3.2a,b). However, a shift to lower binding energies indicating that Fe got more reduced under reaction conditions or a contribution of metallic Fe states have been expected as observed for similar $RhFe/SiO_2$ catalysts due to RhFe nanoalloy formation.[36] Concerning the low Fe content and thereby low intensities of corresponding Fe 2p signals, no reliable information regarding a metallic Fe phase was available from XPS. Furthermore, the formation of a surface passivation layer upon sample handling under ambient conditions might explain the apparently high amounts of Fe oxides present after catalytic reaction. However, additional investigations might be required to clarify the Rh and Fe speciation, e.g., in the form of in situ experimentation.

3.3.3 Influence of Reaction Conditions on Particle Sizes of Rh/Mn/Fe/SiO_2 Catalysts

For all catalysts in each specific state, particle size distributions were determined by systematically measuring at least 250 different particles per sample (Figure S3.3). For this purpose, bright-field scanning transmission electron microscopy (BF-STEM) images of three different areas were examined. The calcined samples have not been investigated due to their high beam-sensitivity and consequent insignificance.[28] All particle diameters of metallic Rh particles and crystallite sizes of Rh_2O_3 are summarized in Table 3.2.

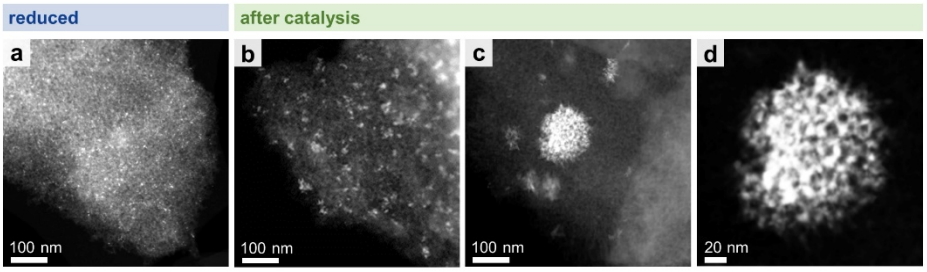

Figure 3.3. HAADF-STEM images of Rh/SiO_2 after (a) *in situ* reduction (265 °C, 5 % H_2/N_2) and (b–d) catalysis (long-term catalytic study; 54 bar, max. 260 °C; 530 h on stream). (b) Representative domain with smaller agglomerates (<10 particles) and (c) minority domain with larger agglomerates. (d) High-resolution STEM of one single agglomerate from image (c).

The four catalysts show relatively small mean Rh_2O_3 crystallite sizes after calcination ranging from 1.3–1.6 nm from XRD (Table 3.2). *In situ* reduction in H_2 led to metallic Rh particles with the smallest mean particle sizes of 2.4 and 2.2 nm for RhMn/SiO_2 and RhMnFe/SiO_2, respectively. The mean particle sizes of Rh/SiO_2 and RhFe/SiO_2 are significantly larger with a value of 2.9 nm. It is assumed that Mn addition leads to a higher Rh dispersion already after *in situ* reduction. All catalysts show a similar, narrow particle size distribution reflected in small standard deviations of 0.5–0.8 nm (Table 3.2 and Figure S3.3).

Table 3.2. Particle diameters from STEM and crystallite sizes from XRD[a] in nm.

Treatment	Rh	RhMn	RhFe	RhMnFe
calcination	1.3 (XRD)	1.4 (XRD)	1.5 (XRD)	1.6 (XRD)
reduction	2.9±0.9	2.4±0.7	2.9±0.8	2.2±0.5
high temperature	3.9±0.9	2.5±0.7	2.8±0.7	2.2±0.5
long-term study	4.4±1.4	2.9±1.0	3.3±1.2	3.1±0.9

[a] Crystallite sizes were estimated with Langford and Wilson's representation of the Scherrer equation.[37]

After long-term catalytic study, a slight particle growth was observed for all catalysts, which is further consistent with XRD results. The unpromoted Rh/SiO_2 catalyst shows the largest increase in particle size with a factor of 1.5 and a value of 4.4 nm. The particles on the promoted catalysts are about 25–35 % smaller in size than on Rh/SiO_2. Interestingly, the addition of Mn leads to the smallest particles with mean sizes of 2.9 nm for RhMn/SiO_2 and 3.1 nm for RhMnFe/SiO_2 (Table 3.2).

However, these findings are in contrast to the aforementioned surface compositions obtained from XPS data, showing a higher Rh dispersion after catalysis for all catalysts investigated. Suzuki *et al.* reported that metallic Rh clusters on Al_2O_3 could disintegrate into isolated Rh^+ sites through CO chemisorption.[38] A similar Rh particle disintegration on silica under the influence of high CO partial pressures could explain the increased Rh dispersion besides a slight particle growth. It should be noted that those Rh^+ sites are not detectable by STEM or XRD due to common detection limits. However, further investigations about the disintegration of Rh particles on SiO_2 are part of further studies and will be required for a clear proof.

Although the $RhMnFe/SiO_2$ catalyst shows the smallest mean particle size after reduction, its particles are slightly larger after catalysis in comparison to $RhMn/SiO_2$, which is further consistent with respective surface compositions from XPS analysis (Table 3.1). Considering the indication of RhFe nanoalloys formation from XPS in this context, the alloy formation probably follows incorporation of Fe into Rh nanoparticles. This incorporation would then lead to larger particles and would explain the more pronounced particle growth. This assumption is in accordance with our previous study about the *in situ* formation of RhFe nanoalloy structures through reduction of FeO_x at $Rh–FeO_x$ interfacial sites *via* hydrogen spillover.[36]

To summarize, Mn addition to silica-supported Rh catalysts leads to a stabilization of the Rh particles and prevents agglomeration by reducing the mobility of Rh on the support. Consequently, Rh particles on MnO/SiO_2 almost retained their size after high temperature investigation and are slightly increased after long-term catalytic study. Therefore, an expected particle growth has been reduced. The addition of Fe does not suppress particle growth to the same extent and leads to larger particles on $RhMnFe/SiO_2$ compared to $RhMn/SiO_2$. This increase in particle size suggests RhFe nanoalloy formation through the incorporation of Fe into Rh nanoparticles.

3.3.4 Influence of Reaction Conditions on the Morphology of $Rh/Mn/Fe/SiO_2$ Catalysts

STEM in combination with EDX spectroscopy was performed on the freshly reduced and spent samples after long-term catalytic study and high temperature investigation. The morphology and general structural features of the four different Rh-based catalysts were evaluated from images taken with dark-field (DF), bright-field (BF), and high-angle annular dark-field (HAADF) detectors. STEM-EDX mappings were used to investigate the elemental distribution over the silica support, and line profile scans were performed to analyze the elemental composition of the nanoparticles.

Representative overview STEM images of the unpromoted Rh/SiO_2 catalyst show well-dispersed particles over the support after *in situ* reduction (Figure 3.3a). The

corresponding EDX mapping clearly demonstrates that only pure Rh nanoparticles are present, indicated by the overlap of the HAADF and Rh EDX signals (Figure S3.4a). The respective EDX spectrum further proved that no contaminations such as Fe are present (Figure S3.4b). Those contaminations are often correlated with the reactivity of Rh/SiO_2 catalysts in syngas conversion.[39] After long-term catalysis, the Rh nanoparticles are unevenly distributed over the support and structured mostly in agglomerates of a few particles (<10 particles; Figure 3.3b).

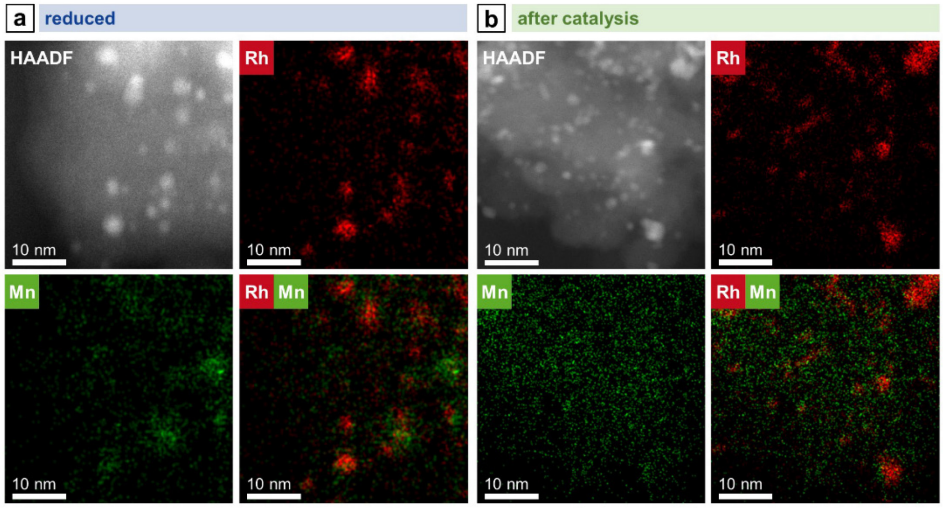

Figure 3.4. STEM-EDX mappings of $RhMn/SiO_2$ after (a) reduction and (b) catalysis (long-term catalytic study; 54 bar, max. 260 °C; 530 h on stream). Rh L and Mn K EDX signals were used. For additional single-element maps and corresponding EDX spectra see Figures S3.5 and S3.6.

While this is the case for most of the domains investigated, some areas are also found containing large agglomerates with sizes of 20–200 nm (Figure 3.3c). High-resolution STEM could resolve their individual nanoparticles (Figure 3.3d).

In the case of $RhMn/SiO_2$, the STEM-EDX mapping of the freshly reduced sample visualizes that Rh nanoparticles are surrounded by a MnO phase (Figure 3.4a). Likewise, the formation of RhMn nanoalloy structures can be excluded, as no overlap between the Rh and Mn EDX signals were found (Figure 3.4a). In addition, Mn is probably in an amorphous, oxidized phase as no crystalline particles were observed.

In contrast to the unpromoted Rh/SiO_2 catalyst, the Rh nanoparticles on $RhMn/SiO_2$ stay well-dispersed also after catalysis, and agglomeration of individual particles to the same extent was not observed (Figure 3.5a). In addition, corresponding STEM-EDX mapping of $RhMn/SiO_2$ after catalysis reveals a higher dispersion of Mn (Figure 3.4b), which is in accordance with previously mentioned XPS results and an X-ray absorption spectroscopy (XAS) study demonstrating a higher Rh dispersion on a Mn-promoted Rh catalyst after exposure to a CO/He atmosphere at elevated temperatures.[40] It is consequently assumed that the Rh nanoparticles are anchored through the well-

dispersed MnO phase, reducing their mobility over the support. Thus, the amorphous MnO phase prevents mainly sintering and agglomeration of Rh particles.

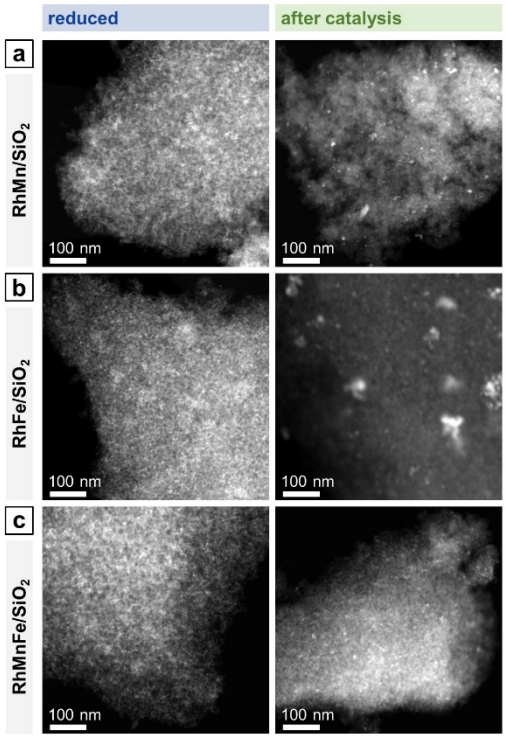

Figure 3.5. Representative overview STEM images of (a) $RhMn/SiO_2$, (b) $RhFe/SiO_2$, and (c) $RhMnFe/SiO_2$ after reduction (265 °C, 5 % H_2/N_2) and after catalysis (long-term catalytic study; 54 bar, max. 260 °C; 530 h on stream). $RhFe/SiO_2$: Like Rh/SiO_2 (Figure 3.3), agglomerates of individual Rh particles can be seen beside relatively small nanoparticles after catalysis.

Complementary STEM overview imaging (Figure 3.5b) and STEM-EDX investigations on the reduced $RhFe/SiO_2$ catalyst suggest the presence of well-dispersed Rh nanoparticles and a finely distributed Fe phase before catalytic studies (Figure S3.7). Furthermore, no domains with local enrichments of Rh and Fe in the same areas are found. RhFe nanoalloy formation does thereby not occur during *in situ* reduction. However, after long-term catalytic study, overlapping Rh and Fe signals in the superimposed STEM-EDX mapping indicate the formation of RhFe nanoalloy structures (Figure 3.6a). Corresponding difference maps of Rh L and Fe K of two independent domains visualize the distribution of Fe which is not in the vicinity to Rh (Figure S3.9; for all maps and EDX spectra see Figures S3.8 and S3.10). As no agglomeration of Fe has been observed, it is consequently assumed that the "free" Fe is still finely distributed over the silica support and most likely in an oxidized state.

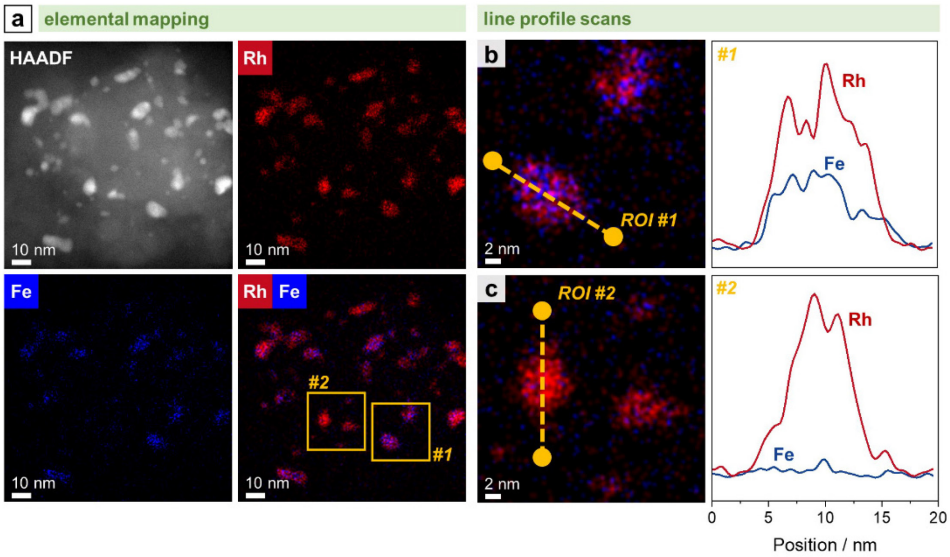

Figure 3.6. STEM-EDX analyses of $RhFe/SiO_2$ after catalysis (long-term catalytic study; 54 bar, max. 260 °C; 530 h on stream): (a) HAADF micrograph and STEM maps of Fe K and Rh L with domains investigated with line profile scans highlighted in yellow. Elemental line profile scans and corresponding line profiles of Fe K and Rh L for a representative (b) RhFe alloy particle within area #1 and (c) metallic Rh particle within area #2. For additional single-element maps and corresponding EDX spectrum, see Figure 3.S8.

The *in situ* transformation of pure Rh nanoparticles to RhFe nanoalloys during StE reaction is in accordance with our recent study about similar $RhFeO_x/SiO_2$ catalysts[36] and other reported RhFe nanoalloy structures.[20,23,39]

Representative elemental line profile scans further proved the alloying of Rh with Fe (Figures 3.6b and S3.11). Owing to the shape of the corresponding line profile intensities, RhFe bulk alloy formation is rather likely than surface alloy structures. Compositional analyses based on EDX area-selective investigations of several RhFe alloy particles indicate the formation of nanoalloys with an average molar Fe:Rh ratio of 0.34 (Figure S3.12 and Table S3.2). However, no exact composition could be determined due to different degrees of alloying. In this manner, Rh-rich alloy nanoparticles and even pure Rh nanoparticles were found (Figure 3.6c). The elemental line profile scan on a representative Rh particle clearly shows the absence of Fe (Figure 3.6c). In comparison to the bulk composition obtained from ICP-OES (Fe:Rh = 0.40), about 15 % of the Fe is not found in RhFe alloy structures and probably present as oxidic species. However, these findings are in contrast with the previously mentioned Fe 2p XPS results indicating Fe mainly in an oxidized state and no indications from metallic Fe states (Figure S3.2). The formation of a passivation layer during sample handling might explain the apparently high amounts of Fe oxides detected by XPS due to its surface sensitivity. Furthermore, the main reflection in the corresponding X-ray diffractogram is slightly shifted to $2\theta = 41.1°$ compared to the (111) reflection of metallic Rh at 40.9° of the unpromoted Rh/SiO_2 (Figure S3.13). This shift and the asymmetric tailing toward higher 2θ values might indicate an underlying contribution of Rh-rich bimetallic RhFe phases which should appear between metallic Rh and RhFe (42.7; C25-1408). However, no

reliable information about the exact composition of the bimetallic RhFe phases could be obtained from XRD data due to the relatively broad reflections from the small crystallites.

Combining both elements as modifiers in RhMnFe/SiO_2 catalyst also results in a combination of both features observed in the bimetallic catalysts. After the H_2 treatment, the Rh nanoparticles are well-dispersed over the support (Figure 3.5c), and no correlation of Rh, Mn, and Fe EDX signals was observed in the corresponding STEM-EDX mappings (Figure 3.7a). Therefore, it is assumed that Rh is in an unalloyed state surrounded by well-dispersed oxidic Mn and Fe species.

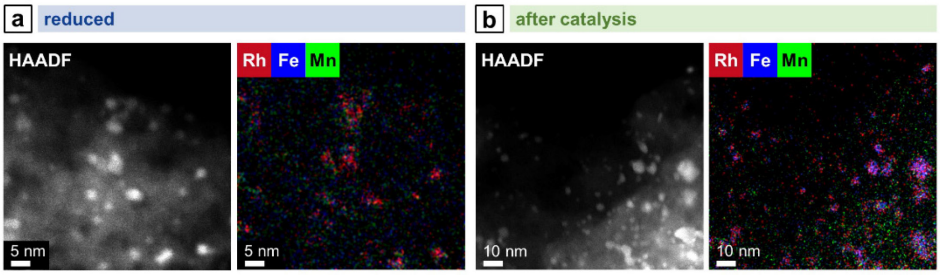

Figure 3.7. STEM-EDX mappings of RhMnFe/SiO_2 after (a) reduction (265 °C, 5 % H_2/N_2) and (b) catalysis (long-term catalytic study; 54 bar, max. 260 °C; 530 h on stream). Rh L, Mn K, and Fe K EDX signals were used. For additional single-element maps and corresponding EDX spectra see Figures S3.14 and S3.15.

After catalysis, the nanoparticles remain relatively small, as indicated by the overview STEM image (Figure 3.5c). The superimposed mapping of Rh and Mn visualizes that MnO is in vicinity to nanoparticles that mainly appear as alloyed RhFe nanostructures probably formed under high-pressure syngas conditions (Figure 3.7b). Furthermore, MnO leads to the anchoring of the RhFe alloy nanoparticles and reduces their mobility on the support, similar to the single-promoted RhMn/SiO_2 catalyst.

3.3.5 Selectivity at Iso-Conversion and Reactivity of Rh/Mn/Fe/SiO_2 Catalysts

To investigate the influence of the described structural models of Mn and/or Fe-promoted Rh/SiO_2 catalysts on their reactivity in the conversion of syngas, all four catalysts are compared at process-relevant reaction conditions (Figure 3.8). As the addition of Fe and Mn to Rh/SiO_2 leads to a significant increase in CO conversion, a preliminary catalytic study was conducted to identify the catalyst amounts necessary for iso-conversions after equilibration (>120 h on stream). Based on this study, the amounts of catalysts were varied to yield approx. 5 % CO conversion. Only 33 % (RhMnFe), 30 % (RhMn), and 20 % (RhFe) of promoted catalysts were required to match the conversion level of pure Rh/SiO_2 catalyst. This procedure was necessary as the product selectivities of Rh-based catalysts are highly dependent on conversion during StE reaction.

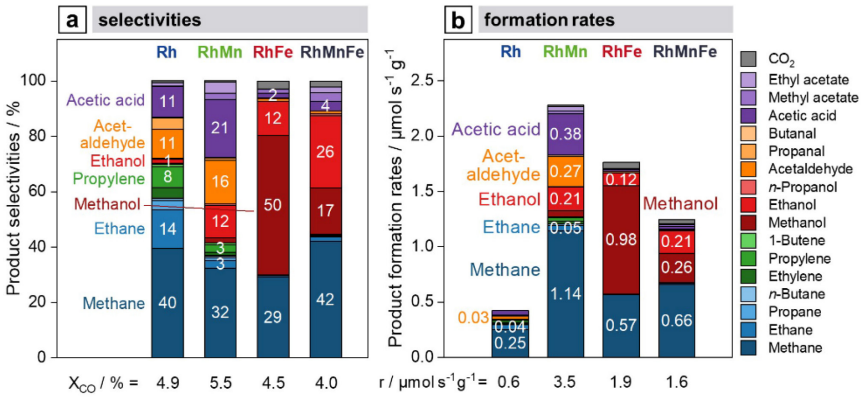

Figure 3.8. Comparison of (a) product selectivities at iso-conversion and (b) product formation rates among the four catalysts investigated. Below each column, CO conversion (a) and total CO consumption rate (b) are given. Reaction conditions: 54 bar, 260 °C, H_2:CO:N_2:Ar = 60:20:10:10, 41.7 mL/min total flow per reactor, GHSVs = 2500–12500 h^{-1}, 170–190 h on stream. Catalyst amounts were varied to yield approx. 5 % CO conversion: V(Rh) = 1.0 mL, V(RhMn) = 0.2 mL, V(RhFe) = 0.3 mL, V(RhMnFe) = 0.33 mL.

Rh/SiO_2 and $RhMn/SiO_2$ catalysts show a similar overall product spectrum at iso-conversions (Figure 3.8a). The main differences are significantly increased C_{2+} oxygenate and suppressed methane selectivities. An improvement in the C_{2+} oxygenate selectivity by the addition of Mn is well-known for Rh/SiO_2 catalysts, as reported in previous studies.[28,30,40] However, a clear explanation is still missing, and the role of Mn as a modifier or promoter for Rh-based catalysts is still elusive, to the best of our knowledge. By considering the aforementioned structural model of $RhMn/SiO_2$, we propose that the MnO phase stabilizes the relatively small Rh nanoparticles and mainly prevents agglomeration. As the product spectrum does not change essentially, we assume that MnO has mainly an effect on the structural properties. This assumption is in accordance with an FTIR study indicating that Mn does not change Rh's electronic properties.[41] Owing to the stability of Rh nanoparticles and the almost retained Rh dispersion, the $RhMn/SiO_2$ catalyst demonstrated the highest observed CO consumption rate among the catalysts tested (Figure 3.8b).

In contrast, the conversion of syngas on $RhFe/SiO_2$ yields methanol as main product with a selectivity of 50 % (Figure 3.8a). Therefore, it is apparent that the addition of Fe leads to a tremendous loss of C–C coupling ability and thus to an overall C_{2+} oxygenate selectivity below 20 %. We reasoned that this strongly altered product spectrum is most likely caused by the close interaction of Rh and Fe. Therefore, the proposed alloying with Fe might have a vital impact on the electronic properties of Rh/SiO_2 catalysts. Therefore, the changed electronic structure leads to fast hydrogenation of initially formed CH_xO^* (x = 1–3) surface fragments, which, in turn, are the main reaction intermediates for the formation of C_{2+} oxygenates.

Once again, the combination of Mn and Fe as modifiers on $RhMnFe/SiO_2$ catalysts also leads to combined effects on their structural and electronic properties. This finding is also reflected in the catalyst reactivity (Figure 3.8a). Compared to the monometallic

Rh/SiO_2 catalyst, $RhMnFe/SiO_2$ shows an increased C_{2+} oxygenate selectivity in general and the highest ethanol selectivity among the catalysts investigated. Furthermore, the selectivity towards methanol is increased, accompanied by a reduced selectivity towards C_{2+} alkanes and alkenes.

3.3.6 Long-Term and Thermal Stability of $Rh/Mn/Fe/SiO_2$ Catalysts

Two independent long-term catalytic studies were performed to investigate the influence of Mn and Fe on the stability of Rh/SiO_2 catalysts during the conversion of syngas. With over 22 days (530 h) for the long-term catalytic study and over 14 days (350 h) on stream for the high temperature investigation, these catalytic experiments are the longest tests of Rh-based catalysts in the conversion of syngas to oxygenates reported in literature, to the best of our knowledge. These long periods of time on stream (TOS) are necessary to investigate Rh catalysts regarding their stability and performance in CO hydrogenation, as 120 h on stream are required to obtain stable catalytic behavior (see formation phase in Figure 3.9).

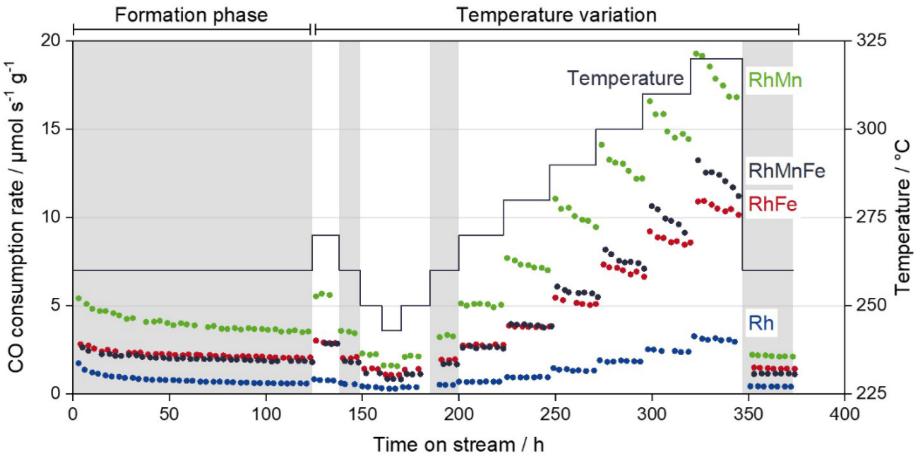

Figure 3.9. Overall CO consumption rate of Rh/SiO_2, $RhMn/SiO_2$, $RhFe/SiO_2$, and $RhMnFe/SiO_2$ over TOS during high temperature stability investigation. Reaction conditions: 54 bar, 243–320 °C, H_2:CO:N_2:Ar = 60:20:10:10, 41.7 mL/min total flow per reactor, GHSVs = 2500–12500 h^{-1}. Catalyst amounts were varied to yield approx. 5 % CO conversion: V(Rh) = 1.0 mL, V(RhMn) = 0.2 mL, V(RhFe) = 0.3 mL, V(RhMnFe) = 0.33 mL. Reference conditions are highlighted in grey.

During this initial formation phase, all catalysts lose activity in terms of the overall CO consumption rate. This deactivation follows a similar trend as observed for particle growth after long-term catalytic investigation (Table 3.2). It is consequently assumed that sintering contributes to the deactivation of Rh-based catalysts under CO hydrogenation conditions, which has also been proposed for similar Rh-based catalysts.[28] Besides migration of particles followed by coalescence, the migration of atoms (Ostwald ripening) has been described as the most important sinter mechanism.[42] In this manner, a CO-assisted mechanism of sintering through Ostwald ripening has been proposed for supported cobalt catalysts under similar reaction conditions. The *in situ* formation of cobalt subcarbonyl species, $Co(CO)_x$ (x = 1–3), may increase the mobility of

cobalt atoms over the hydroxylated support surface.[43] Moreover, a theoretical study has been reported suggesting a similar sinter mechanism for Rh-based catalysts.[44] As the formation of $Rh(CO)_2$ dicarbonyl species under CO-containing atmosphere has been postulated,[38] it is consequently proposed that sintering through migration of $Rh(CO)_x$ (x = 1,2) carbonyl species is also relevant for supported Rh catalysts under high-pressure syngas conditions. However, further experimental and theoretical investigations are required for a clear statement.

Besides the described loss in activity, selectivities also gradually change during the initial formation phase. These changes are mainly caused by the increased mobility of Mn and Fe on the supports, yielding probably the formation of Rh–MnO interfacial sites and/or RhFe nanoalloy structures. In our high temperature investigation, we observed critical temperatures above 280–290 °C, which cause an accelerated loss in activity within each iso-thermal step (Figure 3.9; TOS > 250 h). Interestingly, this deactivation is more pronounced for the Mn-containing catalysts and has a minor impact on Rh/SiO_2 and $RhFe/SiO_2$ catalysts.

To illustrate these differences in deactivation, linear regression analyses were performed for each individual temperature step, and the resulting activity loss rates were compared among the four catalysts investigated (Table S3.3; Figure S3.16). The Mn-containing catalysts show significant activity loss already above temperatures of 280 °C, whereas Rh/SiO_2 and $RhFe/SiO_2$ are still stable in terms of their CO consumption rates at these temperatures. The fastest deactivation represented in the lowest activity loss rate value of -0.13 µmol/(s g_{cat} h_{TOS}) was determined for the $RhMn/SiO_2$ catalyst. With this value, the Mn-promoted catalyst deactivates three times faster than the single-promoted $RhFe/SiO_2$ catalyst. Similar trends can be seen for the multi-promoted $RhMnFe/SiO_2$ with the second-lowest activity loss rate of -0.08 µmol/(s g_{cat} h_{TOS}) (Table S3.3).

Although the deactivation of the Mn-containing catalysts is more pronounced within each temperature step, the percentage changes in CO consumption rate between reference conditions (TOS: 190–199 h and >352 h) are comparable among the promoted catalysts with values ranging from -25.5 to -34.1 % (Table 3.3).

Table 3.3. Deactivation as the percentage change of CO consumption rate during high temperature investigation.

Catalyst	Step	TOS (h)	CO consumption rate (µmol/s/g_{Cat})	Percentage change (%)	Deactivation factor
Rh/SiO_2	Formation phase	3	1.74	-66.6	2.99
		121	0.58		
	Temperature Variation	190–197	0.52	-18.8	1.23
		351–372	0.42		
$RhMn/SiO_2$	Formation phase	3	5.42	-34.7	1.53
		122	3.54		
	Temperature Variation	190–197	3.27	-34.1	1.52
		352–373	2.16		
$RhFe/SiO_2$	Formation phase	4	2.82	-26.7	1.36
		123	2.07		
	Temperature Variation	191–198	1.94	-25.5	1.34
		353–374	1.44		
$RhMnFe/SiO_2$	Formation phase	5	2.63	-31.5	1.46
		124	1.80		
	Temperature Variation	192–199	1.71	-33.1	1.50
		353–374	1.14		

We consequently assume that the deactivation during temperature variation does not only result from a growth in particle size. This is also in agreement with our particle size investigations mentioned above, showing that the mean particle sizes of Rh nanoparticles on Mn-containing catalysts are only slightly increased after the catalytic testing (Table 3.2). For this reason, the deactivation might be caused by a temperature-induced surface restructuring, and it seems to be that this restructuring is reversible when returning to lower temperatures at the reference conditions. At these conditions, all four catalysts show stable CO consumption rates again. A further deactivation of the catalysts has not been observed during additional 20 h on stream at 260 °C. Therefore, it is assumed that temperatures above 280 °C facilitate MnO overlayer formation like catalysts in a strong or reactive metal–support interaction state.[45–47] With longer reaction times, more active Rh sites might be blocked by MnO, which, in turn, leads to the strong deactivation behavior during the individual temperature steps above 290 °C (Figure 3.9). This partial coverage of Rh active sites by MnO is in agreement with an FTIR study reported by Ojeda *et al.*[34] and with a combined XAS and FTIR investigation by Schwartz and co-workers.[41]

3.4 Conclusions

To gather a fundamental understanding of promoter effects in the complex multi-promoted RhMnFe/SiO_2 catalyst, the monometallic Rh/SiO_2, and single-promoted catalysts, RhMn/SiO_2 and RhFe/SiO_2, were systematically investigated in four different states: calcined, reduced, after a long-term catalytic study, and after a high temperature investigation at industrially relevant high-pressure conditions (243–320 °C, 54 bar). The thorough analysis of each catalyst in the different states with integral and local characterization methods led to specific structural models before and after catalytic investigations (Scheme 3.2). These structural models provide a detailed view on compositions, electronic properties, and morphologies of silica-supported Rh-based catalysts.

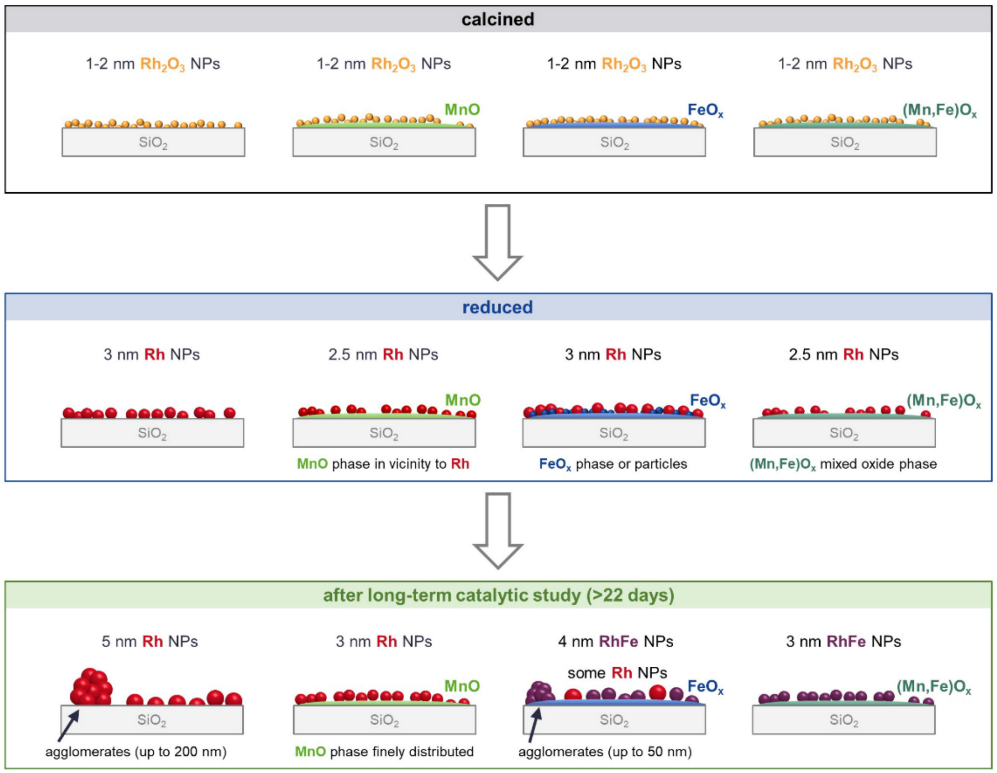

Scheme 3.2. Structural models of Rh/SiO_2, RhMn/SiO_2, RhFe/SiO_2, and RhMnFe/SiO_2 after calcination, *in situ* H_2 treatment and long-term catalytic study. Representation of the different morphologies based on combined analysis of XRD, STEM with EDX mapping, selective-area EDX analyses, elemental line profile scans, and XPS.

Comparing the specific nanostructures before and after long-term catalytic studies (>22 days on stream) allowed us to ascribe individual reactivities to intrinsic promoter effects of Mn and Fe on silica-supported Rh catalysts. The distinct interactions of Rh with Mn and/or Fe develops during a relatively long time on stream of about 120 h under reaction conditions. Fe serves as an electronic modifier on Rh/SiO_2 probably through the *in situ* formation of RhFe nanoalloy structures under the influence of high-pressure syngas conditions at elevated temperatures. Although the detailed STEM-EDX analysis suggested RhFe nanoalloy formation, no indications could be determined from XPS. For

this reason, additional investigations might be required to clarify the Rh and Fe speciation. Nevertheless, the presumable change in Rh's electronic properties might reason the alteration of the overall product spectrum resulted in less C–C coupling abilities and fast hydrogenation of CHO* surface fragment to methanol. On the contrary, MnO does not substantially change the intrinsic product spectrum of Rh/SiO_2 and serves more likely as a structural modifier. In both Mn-containing catalysts, $RhMn/SiO_2$ and $RhMnFe/SiO_2$, respective Rh and/or RhFe nanoparticles are anchored to the silica-support by a MnO phase in their vicinity. With this structural feature, overall CO consumption rates and C_2 oxygenate selectivity are significantly enhanced. MnO might be present as an overlayer, which probably blocks active Rh adsorption sites and gets more pronounced at temperatures above 260 °C. As this effect is of reversible nature, it might result from strong metal–promoter interaction similar to catalysts in reactive metal-support interaction states.

To conclude, the individual nanostructures represented as simplified structural models provide atomistic insights into the role of Mn and Fe in single- and multi-promoted Rh/SiO_2 catalysts. The influence of both promoters on the deactivation and thermal stability could be clarified through long-term catalytic studies at process-relevant reaction conditions with more than 22 days on stream time. We foresee that these structural models will serve as a basis for improved catalyst design strategies and more sophisticated computational modeling efforts.

3.5 References

(1) Subramani, V.; Gangwal, S. K. A Review of Recent Literature to Search for an Efficient Catalytic Process for the Conversion of Syngas to Ethanol. *Energy & Fuels* **2008**, *22* (2), 814–839.

(2) Luk, H. T.; Mondelli, C.; Ferré, D. C.; Stewart, J. A.; Pérez-Ramírez, J. Status and Prospects in Higher Alcohols Synthesis from Syngas. *Chem. Soc. Rev.* **2017**, *46* (5), 1358–1426.

(3) Spivey, J. J.; Egbebi, A. Heterogeneous Catalytic Synthesis of Ethanol from Biomass-Derived Syngas. *Chem. Soc. Rev.* **2007**, *36* (9), 1514.

(4) Ellgen, P. C.; Bhasin, M. US Patent 4096164, 1976.

(5) Ao, M.; Pham, G. H.; Sunarso, J.; Tade, M. O.; Liu, S. Active Centers of Catalysts for Higher Alcohol Synthesis from Syngas: A Review. *ACS Catal.* **2018**, *8* (8), 7025–7050.

(6) Hu, J.; Wang, Y.; Cao, C.; Elliott, D. C.; Stevens, D. J.; White, J. F. Conversion of Biomass-Derived Syngas to Alcohols and C_2 Oxygenates Using Supported Rh Catalysts in a Microchannel Reactor. *Catal. Today* **2007**, *120* (1), 90–95.

(7) Chen, S.; Abdel-Mageed, A. M.; Li, D.; Bansmann, J.; Cisneros, S.; Biskupek, J.; Huang, W.; Behm, R. J. Morphology-Engineered Highly Active and Stable Ru/TiO_2 Catalysts for Selective CO Methanation. *Angew. Chem. Int. Ed.* **2019**, *58* (31), 10732–10736.

(8) Rezvani, A.; Abdel-Mageed, A. M.; Ishida, T.; Murayama, T.; Parlinska-Wojtan, M.; Behm, R. J. CO_2 Reduction to Methanol on Au/CeO_2 Catalysts: Mechanistic Insights from Activation/Deactivation and SSITKA Measurements. *ACS Catal.* **2020**, *10* (6), 3580–3594.

(9) Abdel-Mageed, A. M.; Klyushin, A.; Knop-Gericke, A.; Schlögl, R.; Behm, R. J. Influence of CO on the Activation, O-Vacancy Formation, and Performance of Au/ZnO Catalysts in CO_2 Hydrogenation to Methanol. *J. Phys. Chem. Lett.* **2019**, *10* (13), 3645–3653.

(10) Zhao, Y. H.; Sun, K.; Ma, X.; Liu, J.; Sun, D.; Su, H. Y.; Li, W. X. Carbon Chain Growth by Formyl Insertion on Rhodium and Cobalt Catalysts in Syngas Conversion. *Angew. Chem. Int. Ed.* **2011**, *50* (23), 5335–5338.

(11) Zhang, R.; Peng, M.; Wang, B. Catalytic Selectivity of Rh/TiO_2 Catalyst in Syngas Conversion to Ethanol: Probing into the Mechanism and Functions of TiO_2 Support and Promoter. *Catal. Sci. Technol.* **2017**, *7* (5), 1073–1085.

(12) Mao, W.; Su, J.; Zhang, Z.; Xu, X. C.; Fu, D.; Dai, W.; Xu, J.; Zhou, X.; Han, Y. F. A Mechanistic Basis for the Effects of Mn Loading on C_{2+} Oxygenates Synthesis Directly from Syngas over Rh-MnO_x/SiO_2 Catalysts. *Chem. Eng. Sci.* **2015**, *135*, 301–311.

(13) Lisitsyn, A. S.; Stevenson, S. A.; Knözinger, H. Carbon Monoxide Hydrogenation on Supported Rh-Mn Catalysts. *J. Mol. Catal.* **1990**, *63* (2), 201–211.

(14) Wang, S.; Guo, W.; Wang, H.; Zhu, L.; Qiu, K. Influence of Mn Promotion on CO Hydrogenation over Rh/CNTs Catalyst. *Catal. Letters* **2014**, *144* (7), 1305–1312.

(15) Chen, G.; Zhang, X.; Guo, C.-Y.; Yuan, G. Manganese-Promoted Rh Supported on a Modified SBA-15 Molecular Sieve for Ethanol Synthesis from Syngas. Effect of Manganese Loading. *Comptes Rendus Chim.* **2010**, *13* (11), 1384–1390.

(16) Yang, N.; Yoo, J. S.; Schumann, J.; Bothra, P.; Singh, J. A.; Valle, E.; Abild-Pedersen, F.; Nørskov, J. K.; Bent, S. F. Rh-MnO Interface Sites Formed by Atomic Layer Deposition Promote Syngas Conversion to Higher Oxygenates. *ACS Catal.* **2017**, *7* (9), 5746–5757.

(17) Wang, Y.; Song, Z.; Ma, D.; Luo, H.; Liang, D.; Bao, X. Characterization of Rh-Based Catalysts with EPR, TPR, IR and XPS. *J. Mol. Catal. A Chem.* **1999**, *149* (1–2), 51–61.

(18) Wang, Y.; Luo, H.; Liang, D.; Bao, X. Different Mechanisms for the Formation of Acetaldehyde and Ethanol on the Rh–Based Catalysts. *J. Catal.* **2000**, *196* (1), 46–55.

(19) Yu, J.; Yu, J.; Shi, Z.; Guo, Q.; Xiao, X.; Mao, H.; Mao, D. The Effects of the Nature of TiO_2 Supports on the Catalytic Performance of Rh–Mn/TiO_2 Catalysts in the Synthesis of C_2 Oxygenates from Syngas. *Catal. Sci. Technol.* **2019**, *9* (14), 3675–3685.

(20) Hartman, T.; Geitenbeek, R. G.; Whiting, G. T.; Weckhuysen, B. M. Operando Monitoring of Temperature and Active Species at the Single Catalyst Particle Level. *Nat. Catal.* **2019**, *2* (11), 986–996.

(21) Haider, M.; Gogate, M.; Davis, R. Fe-Promotion of Supported Rh Catalysts for Direct Conversion of Syngas to Ethanol. *J. Catal.* **2009**, *261* (1), 9–16.

(22) Palomino, R. M.; Magee, J. W.; Llorca, J.; Senanayake, S. D.; White, M. G. The Effect of Fe-Rh Alloying on CO Hydrogenation to C_{2+} Oxygenates. *J. Catal.* **2015**, *329*, 87–94.

(23) Carrillo, P.; Shi, R.; Teeluck, K.; Senanayake, S. D.; White, M. G. In Situ Formation of FeRh Nanoalloys for Oxygenate Synthesis. *ACS Catal.* **2018**, *8* (8), 7279–7286.

(24) Wang, J.; Zhang, Q.; Wang, Y. Rh-Catalyzed Syngas Conversion to Ethanol: Studies on the Promoting Effect of FeO_x. *Catal. Today* **2011**, *171* (1), 257–265.

(25) Liu, W.; Wang, S.; Sun, T.; Wang, S. The Promoting Effect of Fe Doping on Rh/CeO_2 for the Ethanol Synthesis. *Catal. Letters* **2015**, *145* (9), 1741–1749.

(26) Carrillo, P.; Shi, R.; Senanayake, S. D.; White, M. G. In Situ Structural Study of Manganese and Iron Oxide Promoted Rhodium Catalysts for Oxygenate Synthesis. *Appl. Catal. A Gen.* **2020**, *608*, 117845.

(27) Gao, J.; Mo, X.; Goodwin Jr., J. G. La, V, and Fe Promotion of Rh/SiO_2 for CO Hydrogenation: Detailed Analysis of Kinetics and Mechanism. *J. Catal.* **2009**, *268* (1), 142–149.

(28) Huang, X.; Teschner, D.; Dimitrakopoulou, M.; Fedorov, A.; Frank, B.; Kraehnert, R.; Rosowski, F.; Kaiser, H.; Schunk, S.; Kuretschka, C.; Schlögl, R.; Willinger, M.-G.; Trunschke, A. Atomic-Scale Observation of the Metal–Promoter Interaction in Rh-Based Syngas-Upgrading Catalysts. *Angew. Chem. Int. Ed.* **2019**, *58* (26), 8709–8713.

(29) Dimitrakopoulou, M.; Huang, X.; Kröhnert, J.; Teschner, D.; Praetz, S.; Schlesiger, C.; Malzer, W.; Janke, C.; Schwab, E.; Rosowski, F.; Kaiser, H.; Schunk, S.; Schlögl, R.; Trunschke, A. Insights into Structure and Dynamics of (Mn,Fe)O_x-Promoted Rh Nanoparticles. *Faraday Discuss.* **2018**, *208*, 207–225.

(30) Preikschas, P.; Bauer, J.; Huang, X.; Yao, S.; Naumann d'Alnoncourt, R.; Kraehnert, R.; Trunschke, A.; Rosowski, F.; Driess, M. From a Molecular Single-Source Precursor to a Selective High-Performance $RhMnO_x$ Catalyst for the Conversion of Syngas to Ethanol.

ChemCatChem **2019**, *11* (2), 885–892.

(31) Schneider, C. A.; Rasband, W. S.; Eliceiri, K. W. NIH Image to ImageJ: 25 Years of Image Analysis. *Nat. Methods* **2012**, *9* (7), 671–675.

(32) Smith, G. C. Evaluation of a Simple Correction for the Hydrocarbon Contamination Layer in Quantitative Surface Analysis by XPS. *J. Electron Spectros. Relat. Phenomena* **2005**, *148* (1), 21–28.

(33) Liu, Y.; Göeltl, F.; Ro, I.; Ball, M. R.; Sener, C.; Aragão, I. B.; Zanchet, D.; Huber, G. W.; Mavrikakis, M.; Dumesic, J. A. Synthesis Gas Conversion over Rh-Based Catalysts Promoted by Fe and Mn. *ACS Catal.* **2017**, *7* (7), 4550–4563.

(34) Ojeda, M.; Granados, M. L.; Rojas, S.; Terreros, P.; Garcia-Garcia, F. J.; Fierro, J. L. G. Manganese-Promoted Rh/Al_2O_3 for C_2-Oxygenates Synthesis from Syngas. *Appl. Catal. A Gen.* **2004**, *261* (1), 47–55.

(35) O'Connell, K.; Regalbuto, J. R. High Sensitivity Silicon Slit Detectors for 1 Nm Powder XRD Size Detection Limit. *Catal. Letters* **2015**, *145* (3), 777–783.

(36) Preikschas, P.; Plodinec, M.; Bauer, J.; Kraehnert, R.; Naumann d'Alnoncourt, R.; Schlögl, R.; Driess, M.; Rosowski, F. Tuning the $Rh–FeO_x$ Interface in Ethanol Synthesis through Formation Phase Studies at High Pressures of Synthesis Gas. *ACS Catal.* **2021**, *11* (7), 4047–4060.

(37) Langford, J. I.; Wilson, A. J. C. Scherrer after Sixty Years: A Survey and Some New Results in the Determination of Crystallite Size. *J. Appl. Crystallogr.* **1978**, *11* (2), 102–113.

(38) Suzuki, A.; Inada, Y.; Yamaguchi, A.; Chihara, T.; Yuasa, M.; Nomura, M.; Iwasawa, Y. Time Scale and Elementary Steps of CO-Induced Disintegration of Surface Rhodium Clusters. *Angew. Chem. Int. Ed.* **2003**, *42* (39), 4795–4799.

(39) Yang, N.; Medford, A. J.; Liu, X.; Studt, F.; Bligaard, T.; Bent, S. F.; Nørskov, J. K. Intrinsic Selectivity and Structure Sensitivity of Rhodium Catalysts for C_{2+} Oxygenate Production. *J. Am. Chem. Soc.* **2016**, *138* (11), 3705–3714.

(40) Bao, H.; Sun, X.; Jiang, Z.; Huang, Y.; Wang, J. Structural Changes of Rh-Mn Nanoparticles inside Carbon Nanotubes Studied by X-Ray Absorption Spectroscopy. *Chinese J. Catal.* **2014**, *35* (8), 1418–1427.

(41) Schwartz, V.; Campos, A.; Egbebi, A.; Spivey, J. J.; Overbury, S. H. EXAFS and FT-IR Characterization of Mn and Li Promoted Titania-Supported Rh Catalysts for CO Hydrogenation. *ACS Catal.* **2011**, *1* (10), 1298–1306.

(42) Goodman, E. D.; Johnston-Peck, A. C.; Dietze, E. M.; Wrasman, C. J.; Hoffman, A. S.; Abild-Pedersen, F.; Bare, S. R.; Plessow, P. N.; Cargnello, M. Catalyst Deactivation via Decomposition into Single Atoms and the Role of Metal Loading. *Nat. Catal.* **2019**, *2* (9), 748–755.

(43) Claeys, M.; Dry, M. E.; van Steen, E.; van Berge, P. J.; Booyens, S.; Crous, R.; van Helden, P.; Labuschagne, J.; Moodley, D. J.; Saib, A. M. Impact of Process Conditions on the Sintering Behavior of an Alumina-Supported Cobalt Fischer–Tropsch Catalyst Studied with an in Situ Magnetometer. *ACS Catal.* **2015**, *5* (2), 841–852.

(44) Ouyang, R.; Liu, J.-X.; Li, W.-X. Atomistic Theory of Ostwald Ripening and Disintegration of Supported Metal Particles under Reaction Conditions. *J. Am. Chem. Soc.* **2013**, *135* (5), 1760–1771.

(45) Penner, S.; Armbrüster, M. Formation of Intermetallic Compounds by Reactive Metal-Support Interaction: A Frequently Encountered Phenomenon in Catalysis. *ChemCatChem* **2015**, *7* (3), 374–392.

(46) Braunschweig, E. Reversibility of Strong Metal-Support Interactions on Rh/TiO_2. *J. Catal.* **1989**, *118* (1), 227–237.

(47) van Deelen, T. W.; Hernández Mejía, C.; de Jong, K. P. Control of Metal-Support Interactions in Heterogeneous Catalysts to Enhance Activity and Selectivity. *Nat. Catal.* **2019**, *2* (11), 955–970.

3.6 Supporting Information

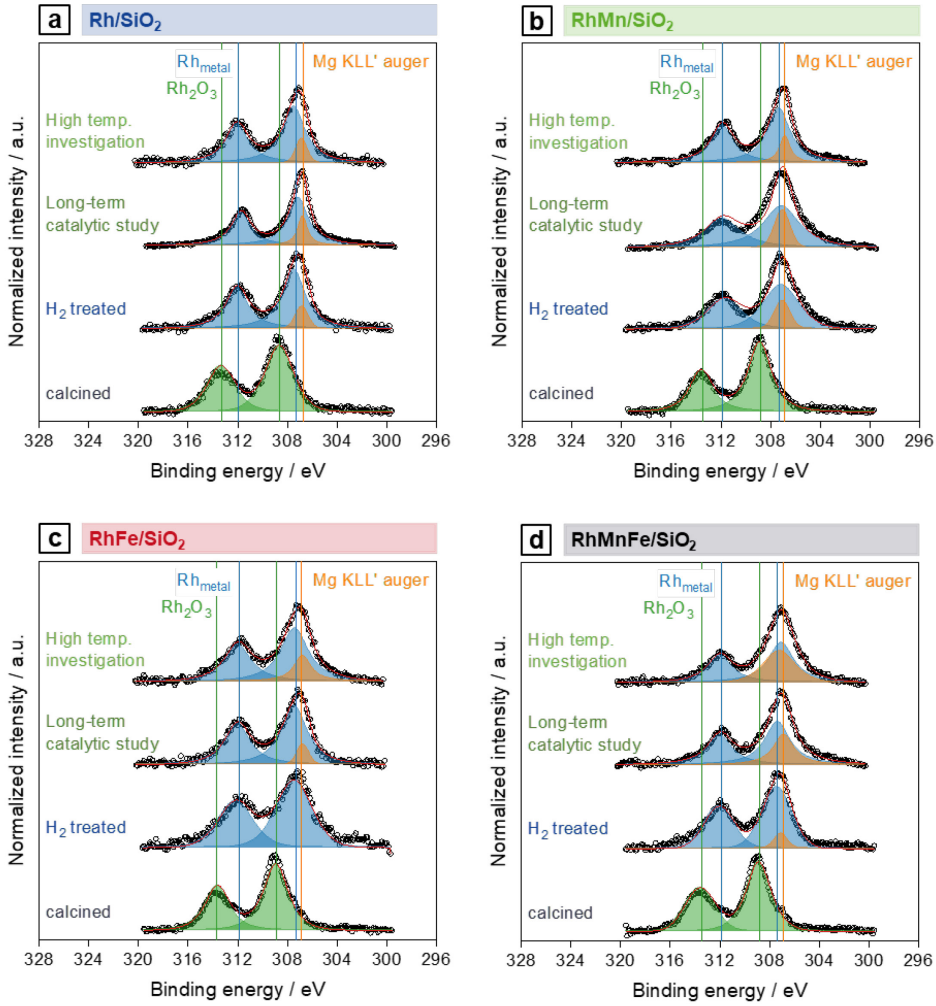

Figure S3.1. Rh 3d XP spectra of (a) Rh/SiO_2, (b) $RhMn/SiO_2$, (c) $RhFe/SiO_2$, and (d) $RhMnFe/SiO_2$ in four different states: calcined, reduced, after long-term catalytic study, and after high temperature stability investigation.

Table S3.1. Binding energy shifts of promoted and pure Rh/SiO_2 after different treatments.

Sample	Treatment	Binding energy (eV)		
		Rh 3d 5/2	Mn 2p 3/2	Fe 2p 3/2
Rh/SiO_2	calcination	308.6	-	-
	reduction	307.4	-	-
	high temperature	307.4	-	-
	long-term study	307.1	-	-
$RhMn/SiO_2$	calcination	308.8	641.6	-
	reduction	306.9	641.9	-
	high temperature	307.3	642.3	-
	long-term study	307.3	642.3	-
$RhFe/SiO_2$	calcination	308.9	-	710.7
	reduction	307.4	-	710.3
	high temperature	307.4	-	710.5
	long-term study	307.3	-	710.3
$RhMnFe/SiO_2$	calcination	308.9	641.5	710.6
	reduction	307.4	641.9	710.4
	high temperature	307.3	642.0	710.7
	long-term study	307.0	642.2	710.5

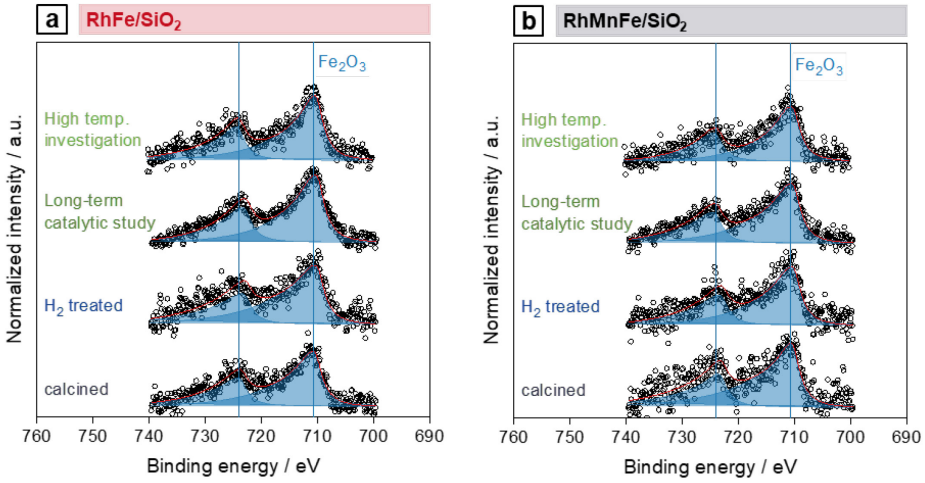

Figure S3.2. Fe 2p XP spectra of (a) $RhFe/SiO_2$ and (b) $RhMnFe/SiO_2$ in four different states: calcined, reduced, after long-term catalytic study, and high temperature stability investigation.

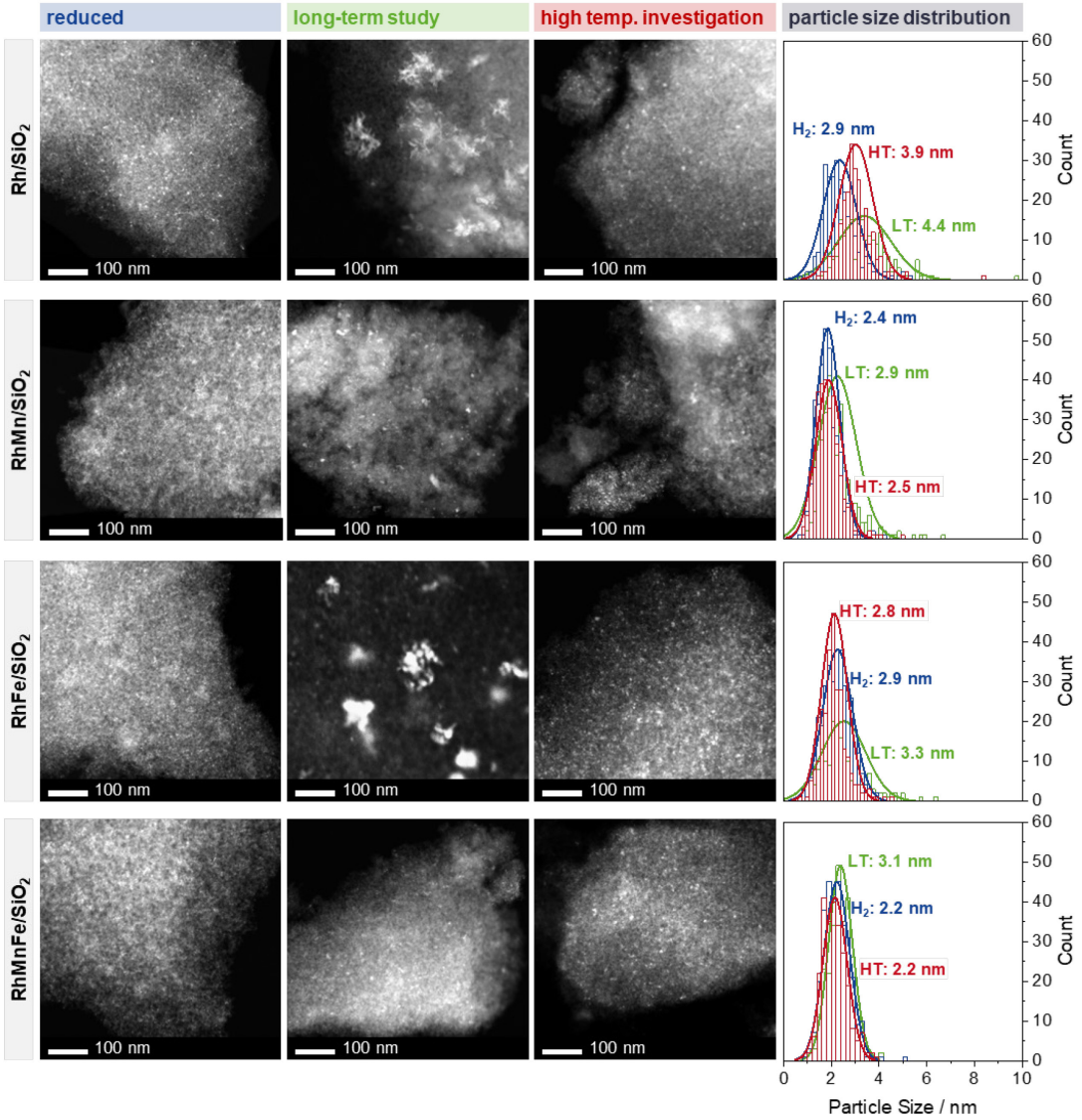

Figure S3.3. Overview HAADF-STEM images of Rh/SiO_2, $RhMn/SiO_2$, $RhFe/SiO_2$, and $RhMnFe/SiO_2$ and corresponding particle size distributions.

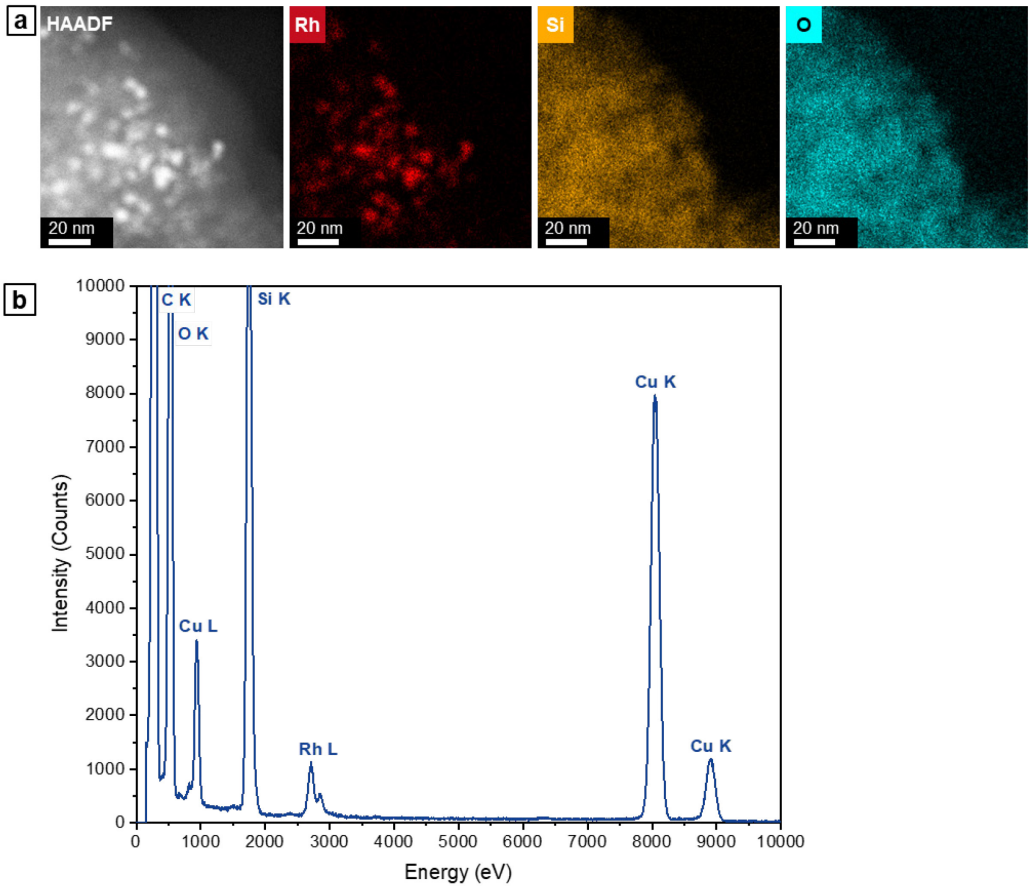

Figure S3.4. STEM-EDX analysis of reduced Rh/SiO_2 catalyst: (a) HAADF micrograph, single-element maps (Rh L, Si K, O K), and (b) corresponding EDX spectrum.

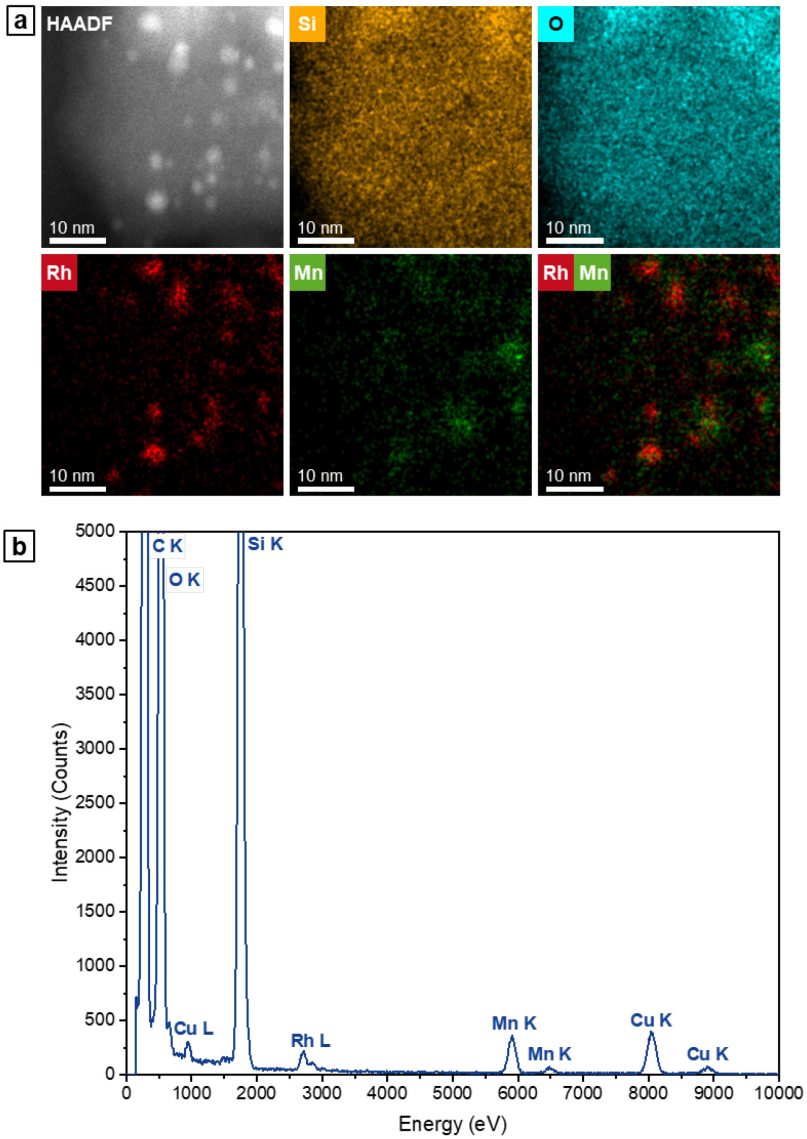

Figure S3.5. STEM-EDX analysis of reduced $RhMn/SiO_2$ catalyst: (a) HAADF micrograph, single-element maps (Rh L, Si K, O K, Mn K), superimposed map of Rh L and Mn K, and (b) corresponding EDX spectrum.

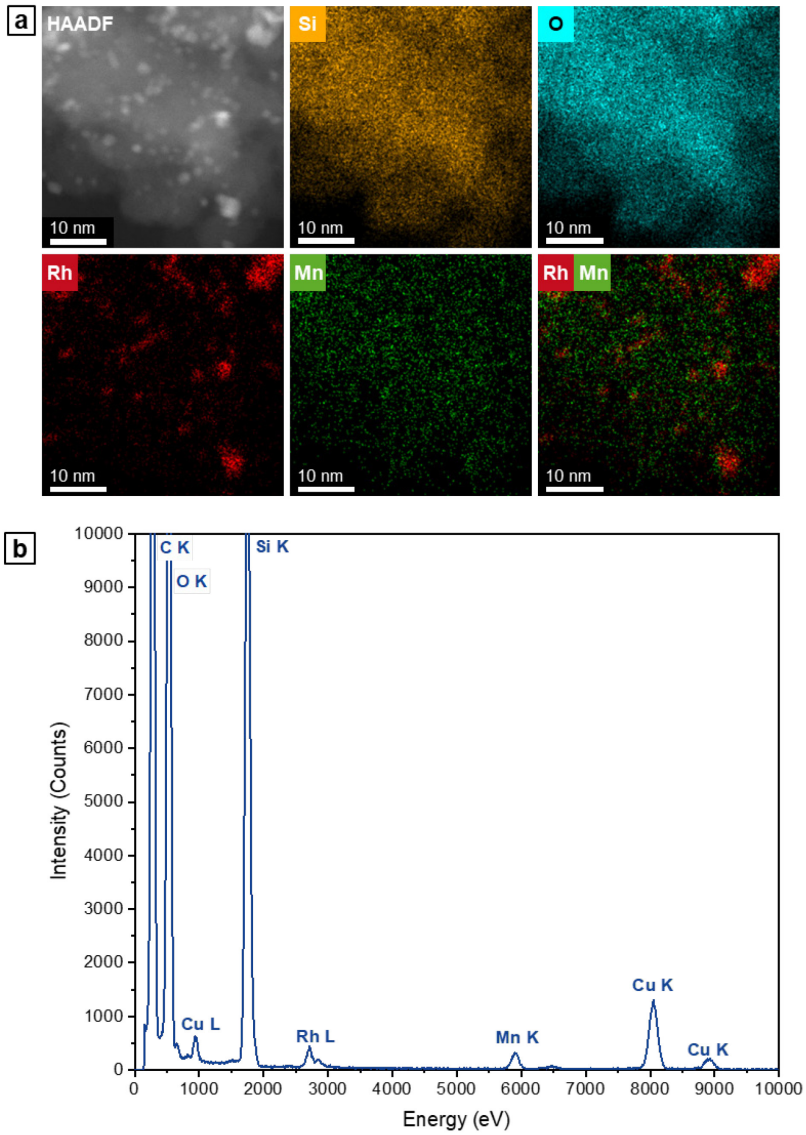

Figure S3.6. STEM-EDX analysis of $RhMn/SiO_2$ catalyst after long-term catalytic study: (a) HAADF micrograph, single-element maps (Rh L, Si K, O K, Mn K), superimposed map of Rh L and Mn K, and (b) corresponding EDX spectrum.

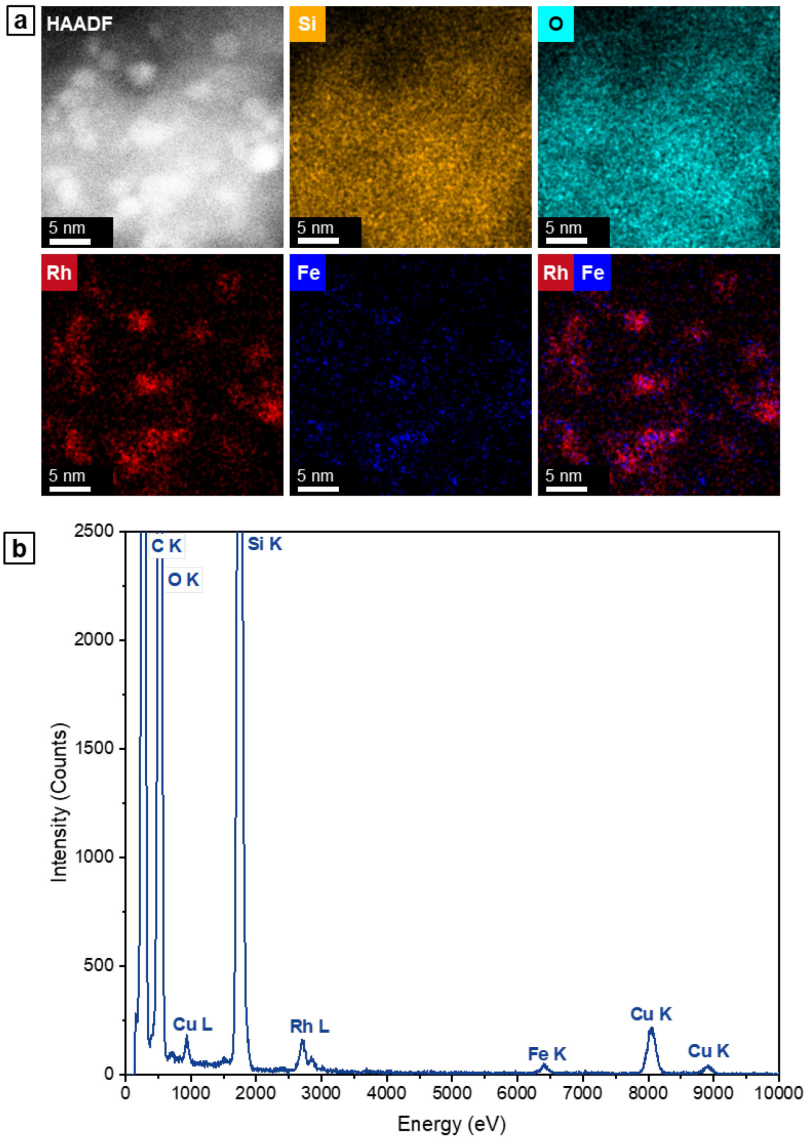

Figure S3.7. STEM-EDX analysis of reduced $RhFe/SiO_2$ catalyst: (a) HAADF micrograph, single-element maps (Rh L, Si K, O K, Fe K), superimposed map of Rh L and Fe K, and (b) corresponding EDX spectrum.

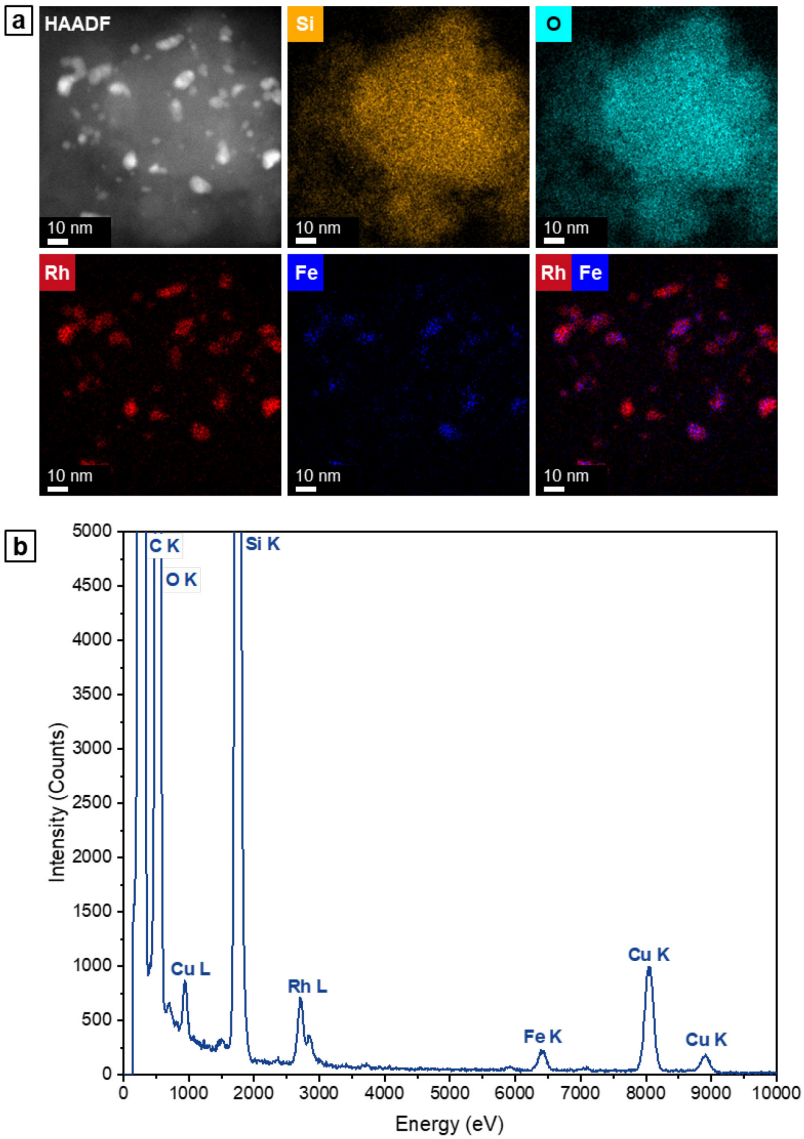

Figure S3.8. STEM-EDX analysis of $RhFe/SiO_2$ catalyst after long-term catalytic study: (a) HAADF micrograph, single-element maps (Rh L, Si K, O K, Fe K), superimposed map of Rh L and Fe K, and (b) corresponding EDX spectrum.

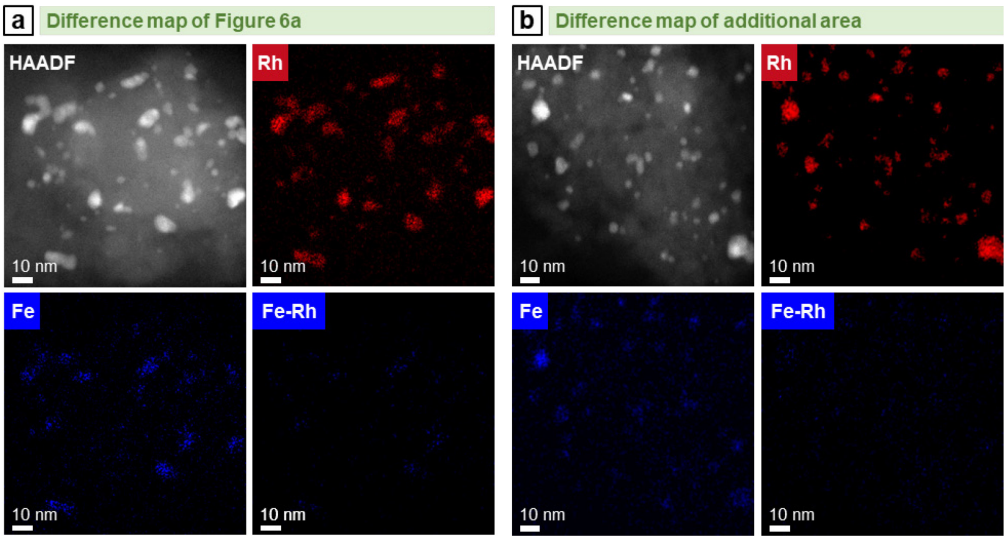

Figure S3.9. STEM-EDX mapping of RhFe/SiO_2 after long-term catalytic study (54 bar, max. 260 °C; 530 h on stream) within two different domains. Rh L and Fe K EDX signals were used. For additional single-element maps and corresponding EDX spectrum of (a) see Figure S3.8 and (b) see Figure S3.10.

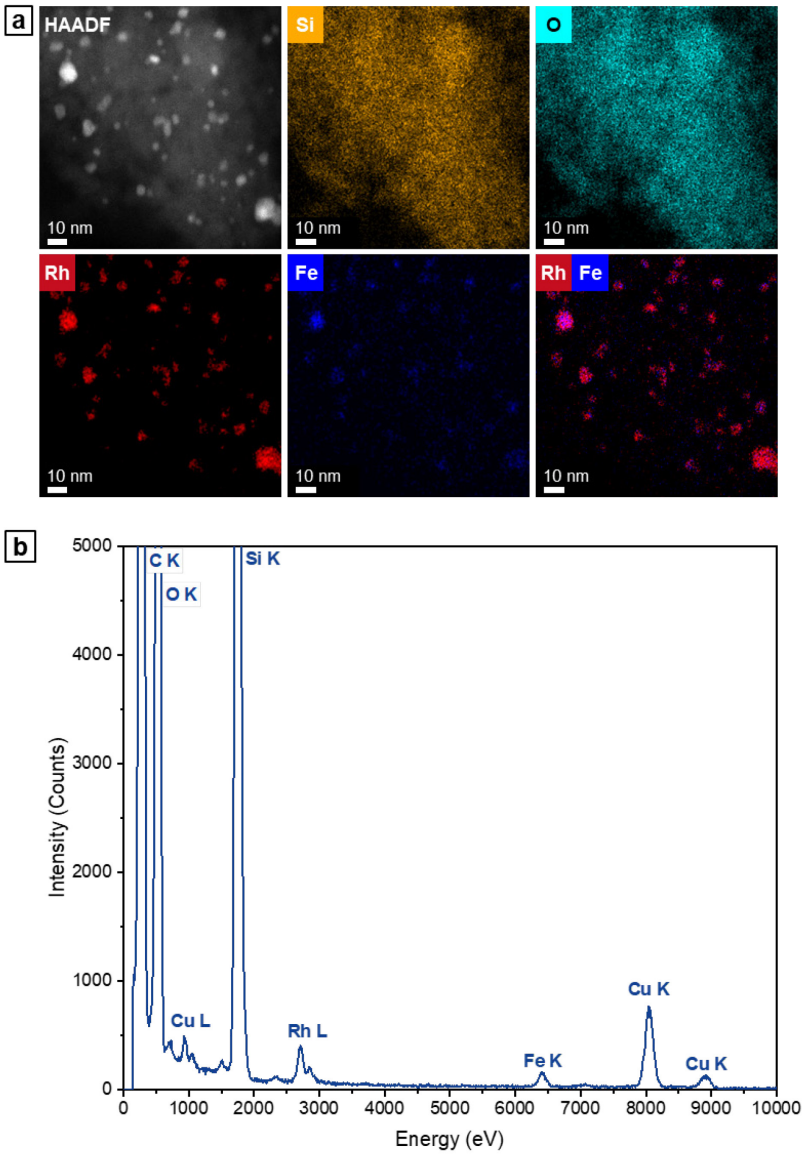

Figure S3.10. Additional STEM-EDX analysis of $RhFe/SiO_2$ catalyst after long-term catalytic study: (a) HAADF micrograph, single-element maps (Rh L, Si K, O K, Fe K), superimposed map of Rh L and Fe K, and (b) corresponding EDX spectrum.

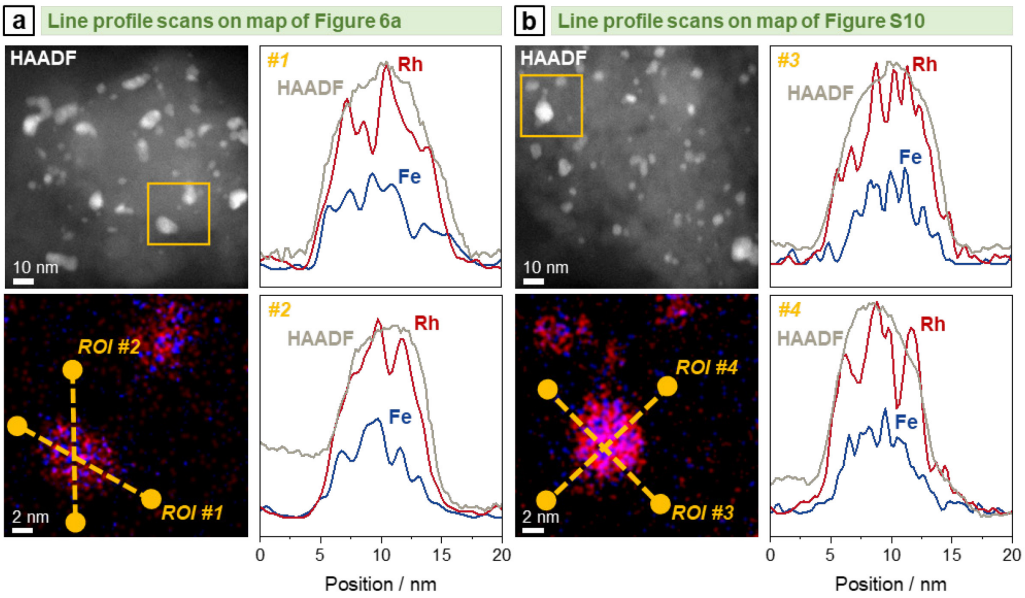

Figure S3.11. Additional STEM-EDX line profile analysis of $RhFe/SiO_2$ catalyst after long-term catalytic study from two different domains. For additional single-element maps and corresponding EDX spectrum of (a) see Figure S3.8 and (b) see Figure S3.10.

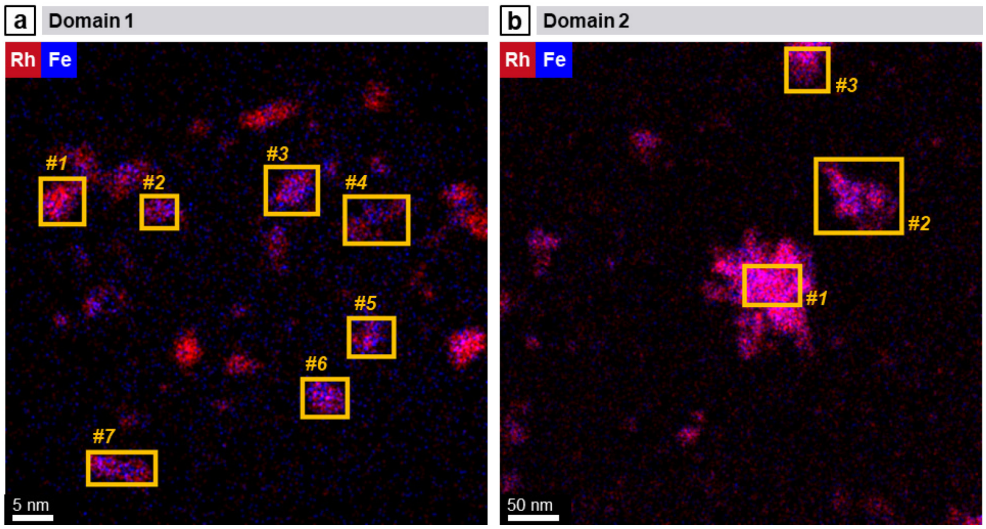

Figure S3.12. STEM-EDX area-selective analysis of $RhFe/SiO_2$ after long-term catalytic study. Investigated areas are highlighted in yellow. Corresponding elemental compositions area provided in Table S3.2.

Table S3.2. Elemental composition of Rh and Fe containing particles and aggregates from STEM area-selective analysis.

Area	Composition / atom-%				Rh:Fe ratio
	Si	O	Rh	Fe	
Domain 1	31 ± 7	67 ± 9	1.5 ± 0.3	0.5 ± 0.1	3.00
Area #1	19 ± 4	48 ± 7	28 ± 5	4.9 ± 0.9	5.71
Area #2	30 ± 7	63 ± 8	4.4 ± 0.9	2.0 ± 0.4	2.20
Area #3	29 ± 7	66 ± 8	3.0 ± 0.6	1.6 ± 0.3	1.88
Area #4	30 ± 7	67 ± 8	2.6 ± 0.5	0.8 ± 0.2	3.25
Area #5	30 ± 7	65 ± 8	3.5 ± 0.7	1.4 ± 0.3	2.50
Area #6	28 ± 6	60 ± 7	8.6 ± 1.5	3.6 ± 0.6	2.39
Area #7	23 ± 5	52 ± 7	19 ± 3	6.0 ± 1.0	3.17
Domain 2	35 ± 8	64 ± 9	0.8 ± 0.2	0.4 ± 0.1	2.00
Area #1	28 ± 6	53 ± 6	11 ± 2	7.7 ± 1.3	1.42
Area #2	33 ± 8	62 ± 8	2.9 ± 0.5	2.1 ± 0.4	1.38
Area #3	29 ± 7	60 ± 7	6.1 ± 1.1	4.2 ± 0.7	1.45

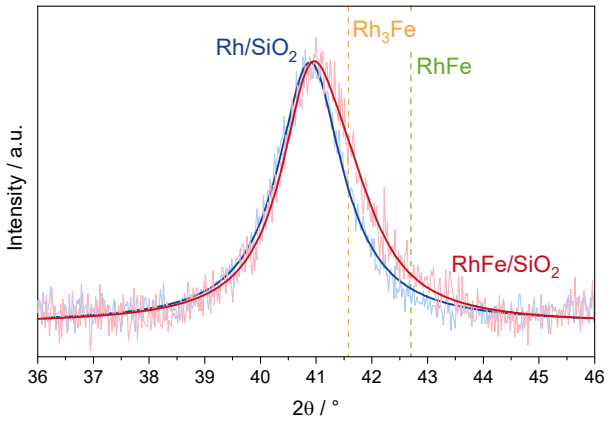

Figure S3.13. X-ray diffractograms after long-term catalytic study of Rh/SiO_2 (blue) and $RhFe/SiO_2$ (red) in the region of the (111) reflections. For the full X-ray diffractograms see Figure 1. RhFe reference (green; C25-1408) has been taken from ICDD database. Rh_3Fe reference (orange; 347421) has been calculated from Open Quantum Materials Database (OQMD).

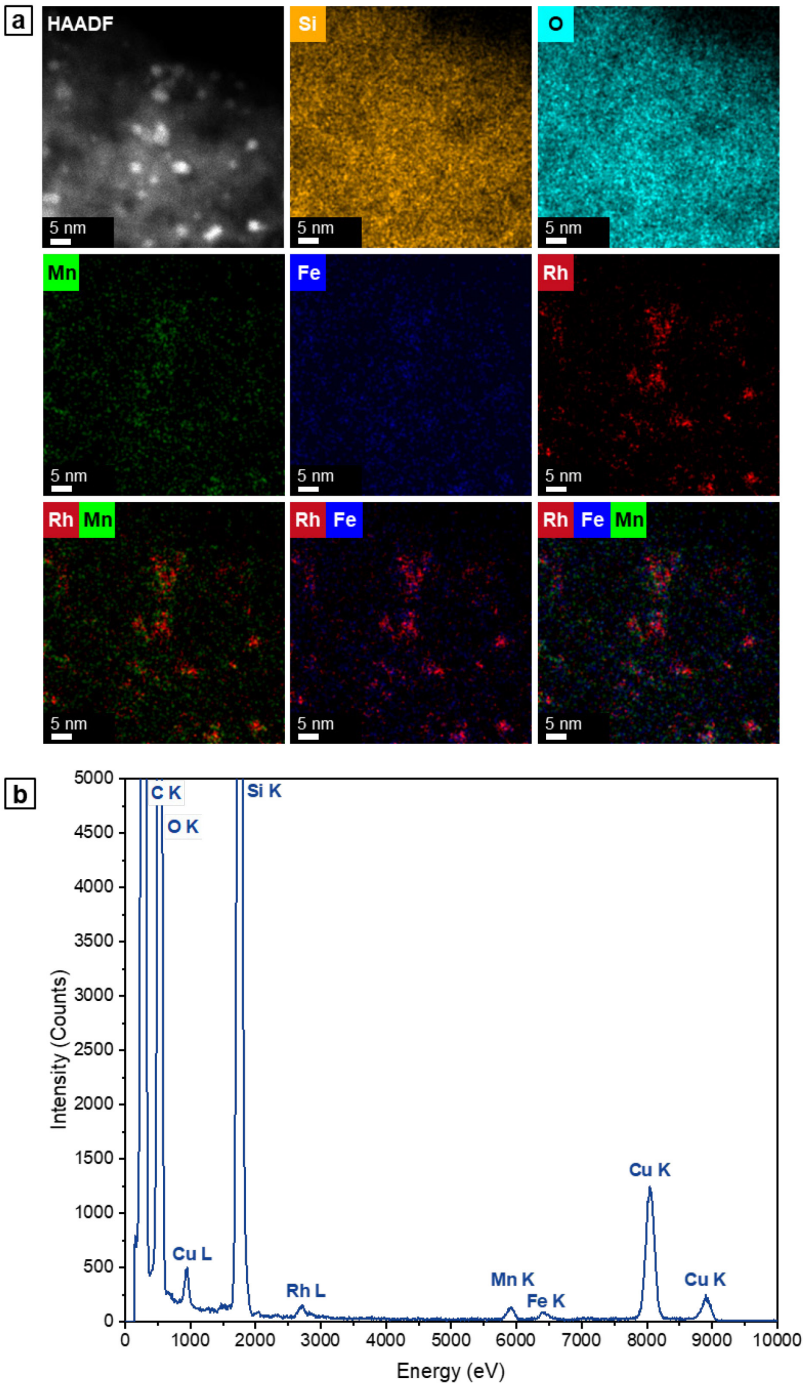

Figure S3.14. STEM-EDX analysis of reduced RhMnFe/SiO_2 catalyst: (a) HAADF micrograph, single-element maps (Rh L, Si K, O K, Fe K, Mn K), superimposed maps of Rh L, Mn K, and Fe K, and (b) corresponding EDX spectrum.

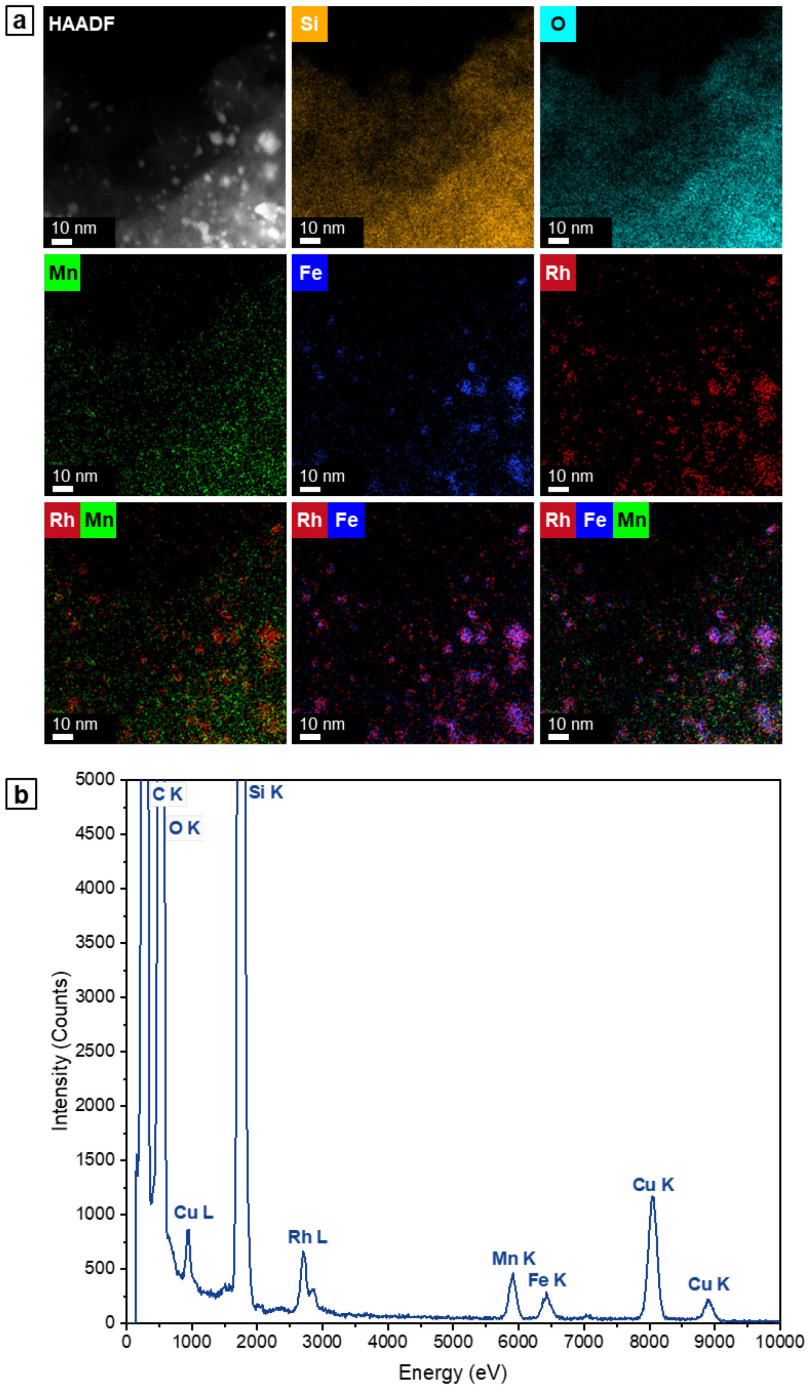

Figure S3.15. STEM-EDX analysis of RhMnFe/SiO_2 catalyst after long-term catalytic study: (a) HAADF micrograph, single-element maps (Rh L, Si K, O K, Fe K, Mn K), superimposed maps of Rh L, Mn K, and Fe K, and (b) corresponding EDX spectrum.

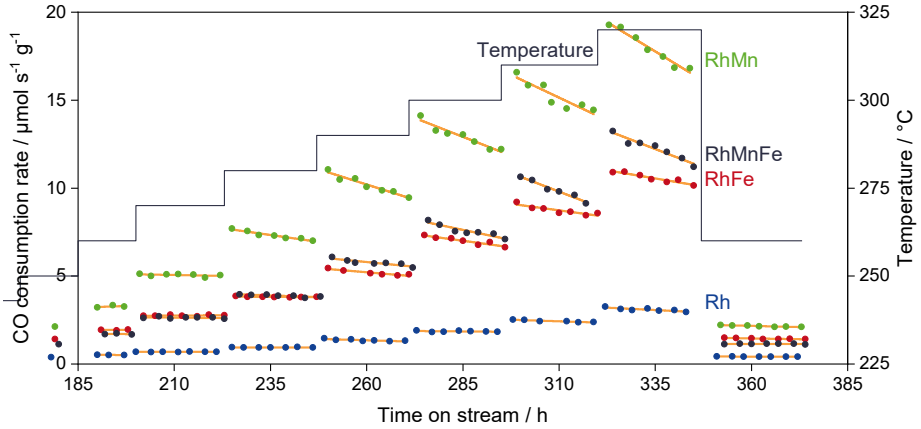

Figure S3.16. Linear regression for all four catalyst and each temperature step. Fit curves are highlighted in orange. Corresponding activity loss rates are given in Table S3.3.

Table S3.3. Activity loss rates from linear regression analysis at different temperatures.

Step	Temperature (°C)	Activity loss rate (µmol/s/g_{cal}/h_{TOS})			
		Rh	RhMn	RhFe	RhMn
1	260	0.00	0.01	0.00	0.00
2	270	0.00	0.00	0.00	0.00
3	280	0.00	-0.03	0.00	-0.01
4	290	-0.01	-0.07	-0.02	-0.02
5	300	0.00	-0.09	-0.03	-0.05
6	310	-0.01	-0.10	-0.03	-0.08
7	320	-0.01	-0.13	-0.04	-0.08
8	260	0.00	-0.01	0.00	0.00

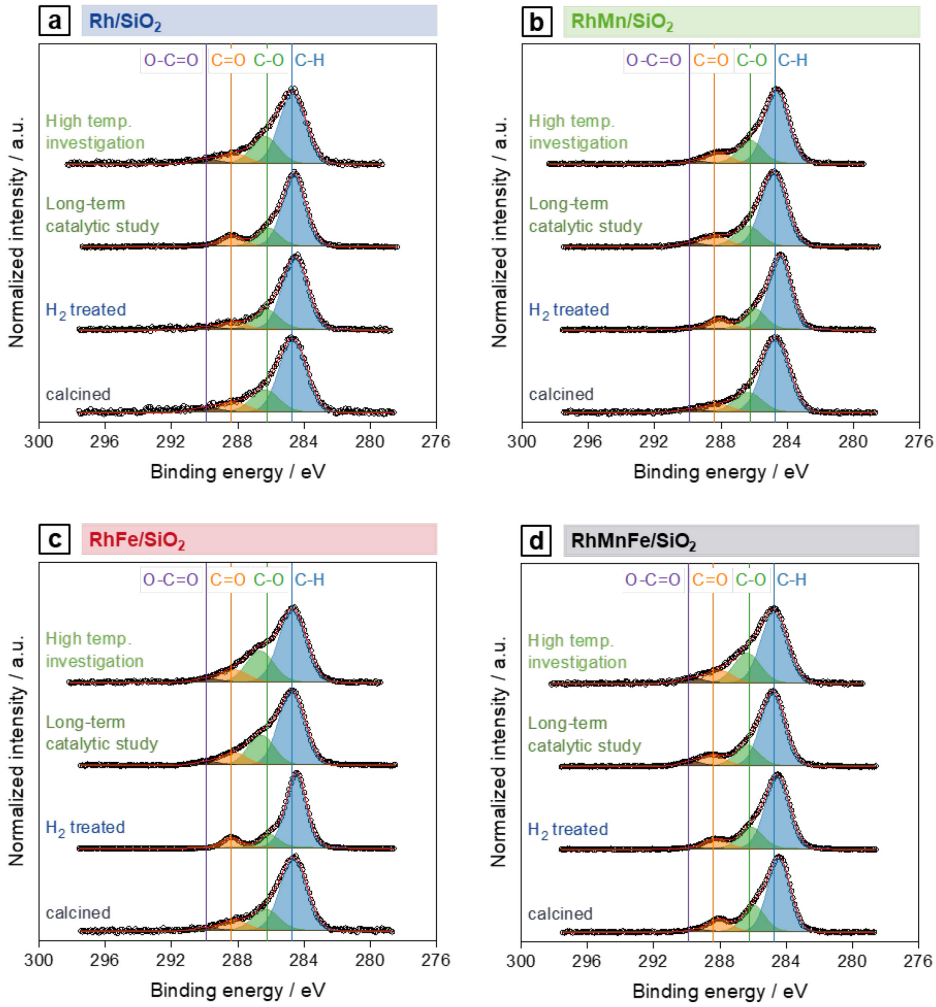

Figure S3.17. C 1s XP spectra of (a) Rh/SiO_2, (b) $RhMn/SiO_2$, (c) $RhFe/SiO_2$, and (d) $RhMnFe/SiO_2$ in four different states: calcined, reduced, after long-term catalytic study, and after high temperature stability investigation.

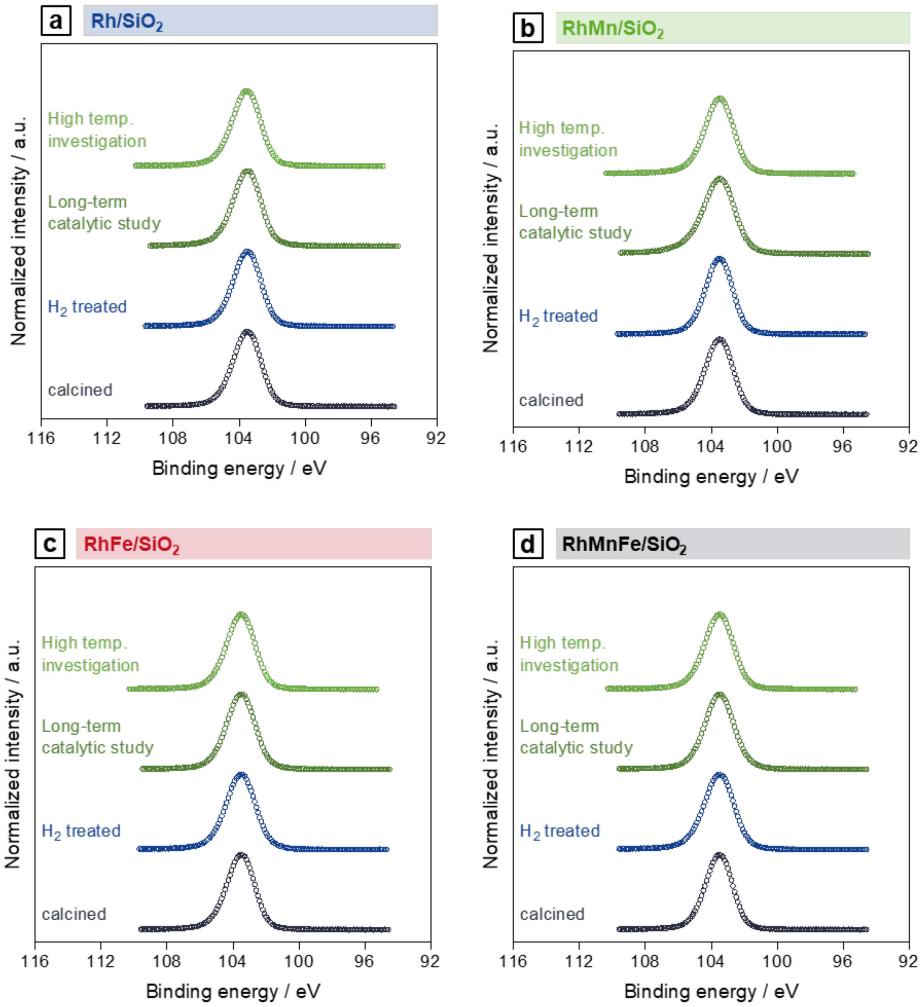

Figure S3.18. Si 2p XP spectra of (a) Rh/SiO_2, (b) $RhMn/SiO_2$, (c) $RhFe/SiO_2$, and (d) $RhMnFe/SiO_2$ in four different states: calcined, reduced, after long-term catalytic study, and after high temperature stability investigation.

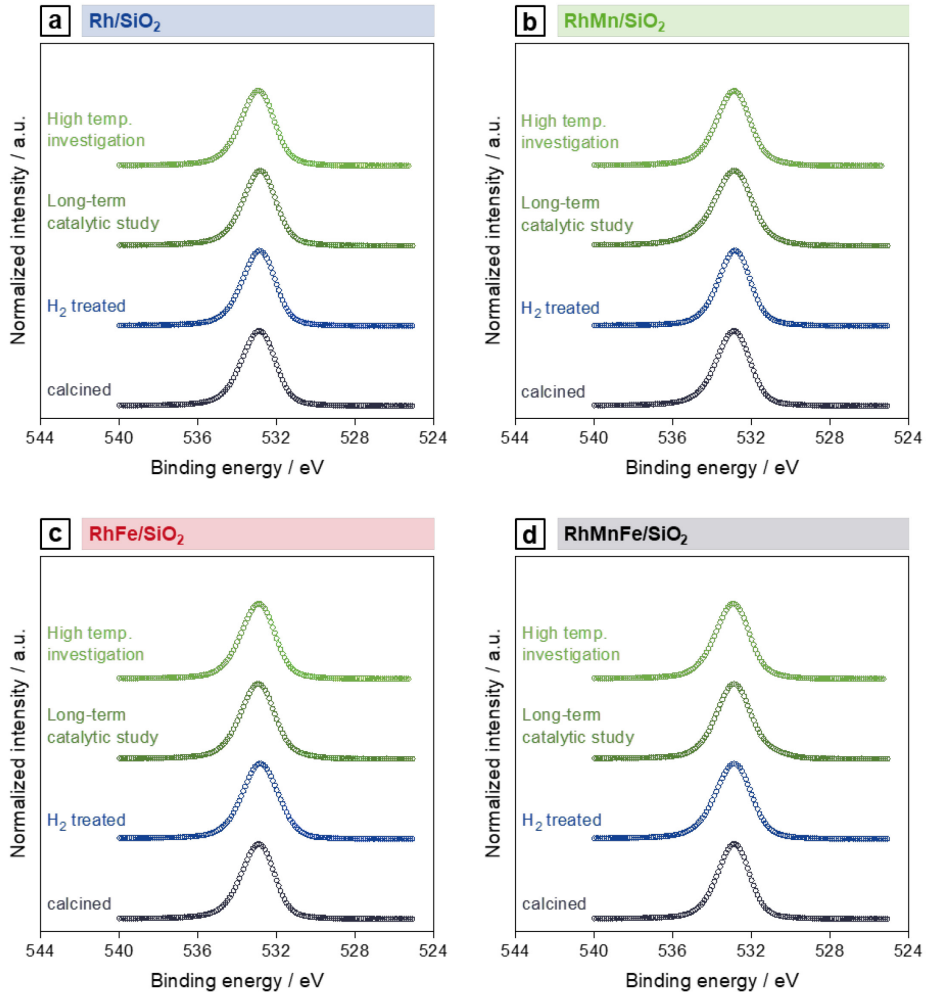

Figure S3.19. O 1s XP spectra of (a) Rh/SiO_2, (b) $RhMn/SiO_2$, (c) $RhFe/SiO_2$, and (d) $RhMnFe/SiO_2$ in four different states: calcined, reduced, after long-term catalytic study, and after high temperature stability investigation.

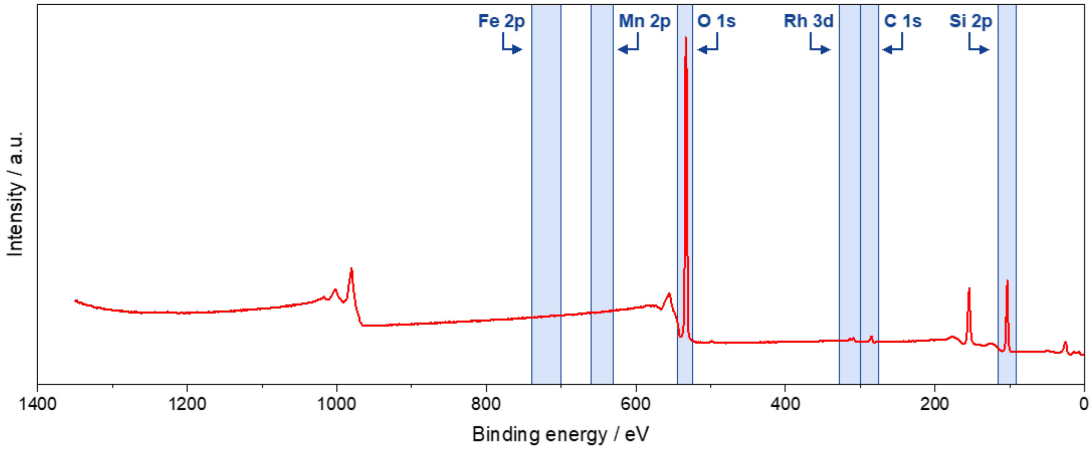

Figure S3.20. XP survey spectrum of calcined Rh/SiO_2 catalyst. Regions selected for high-resolution spectra are highlighted in blue.

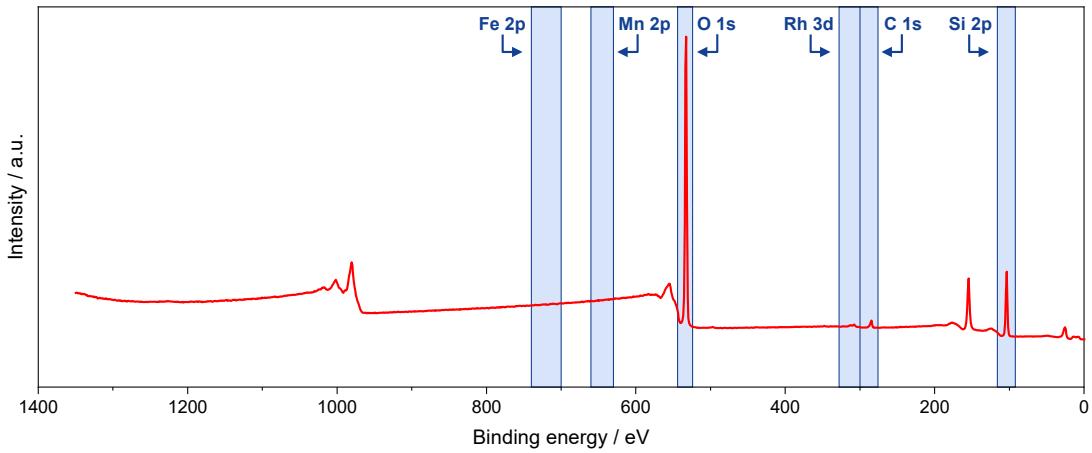

Figure S3.21. XP survey spectrum of reduced Rh/SiO_2 catalyst. Regions selected for high-resolution spectra are highlighted in blue.

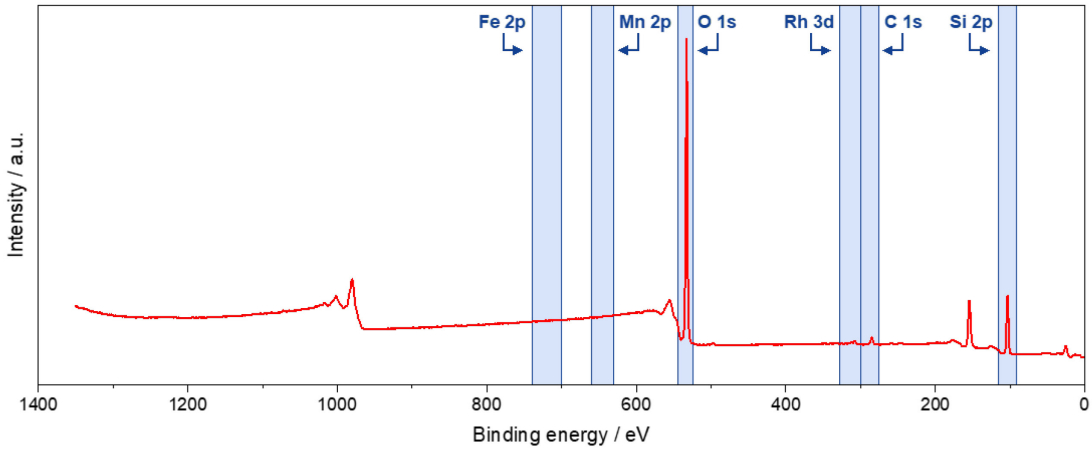

Figure S3.22. XP survey spectrum of Rh/SiO_2 catalyst after high temperature investigation. Regions selected for high-resolution spectra are highlighted in blue.

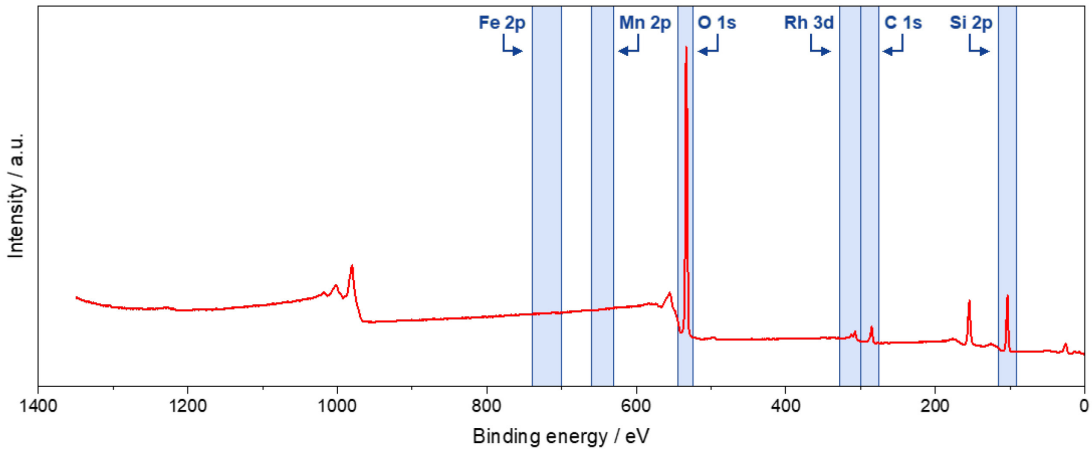

Figure S3.23. XP survey spectrum of Rh/SiO_2 catalyst after long-term study. Regions selected for high-resolution spectra are highlighted in blue.

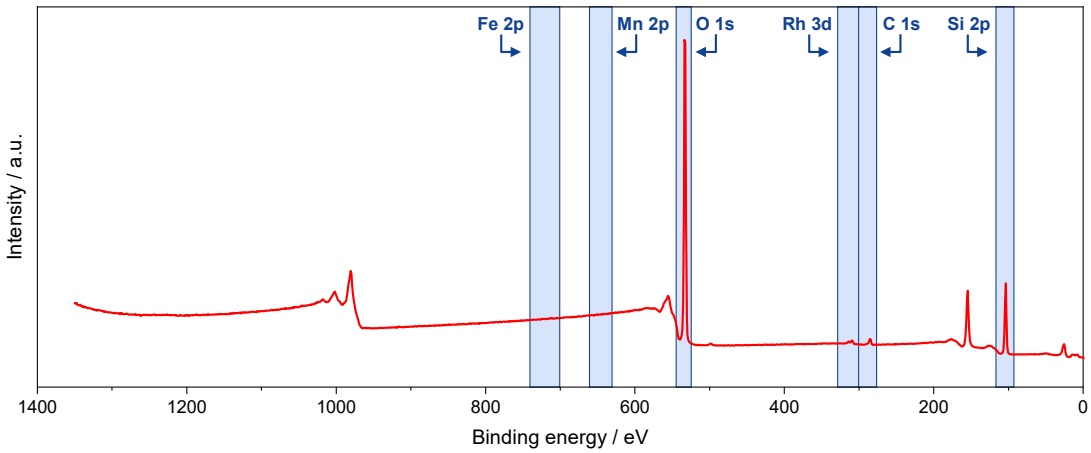

Figure S3.24. XP survey spectrum of calcined $RhMn/SiO_2$ catalyst. Regions selected for high-resolution spectra are highlighted in blue.

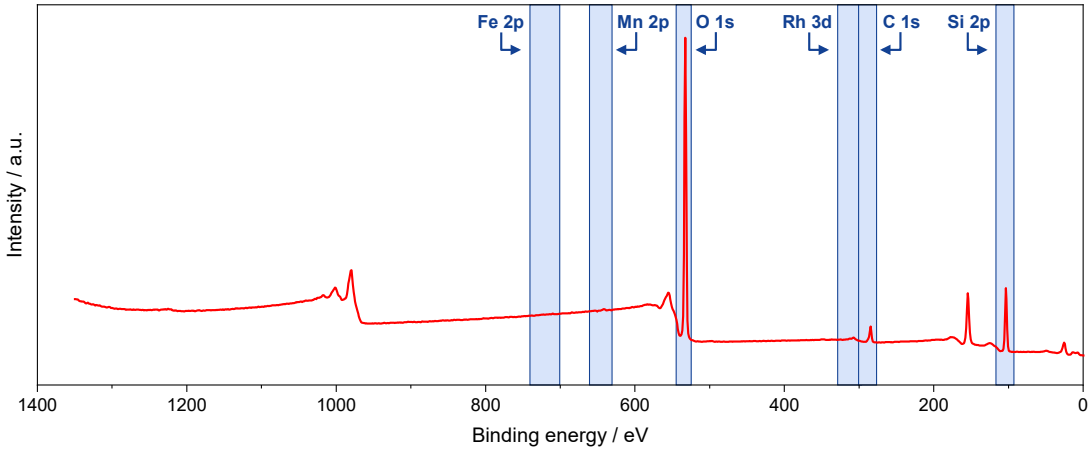

Figure S3.25. XP survey spectrum of reduced $RhMn/SiO_2$ catalyst. Regions selected for high-resolution spectra are highlighted in blue.

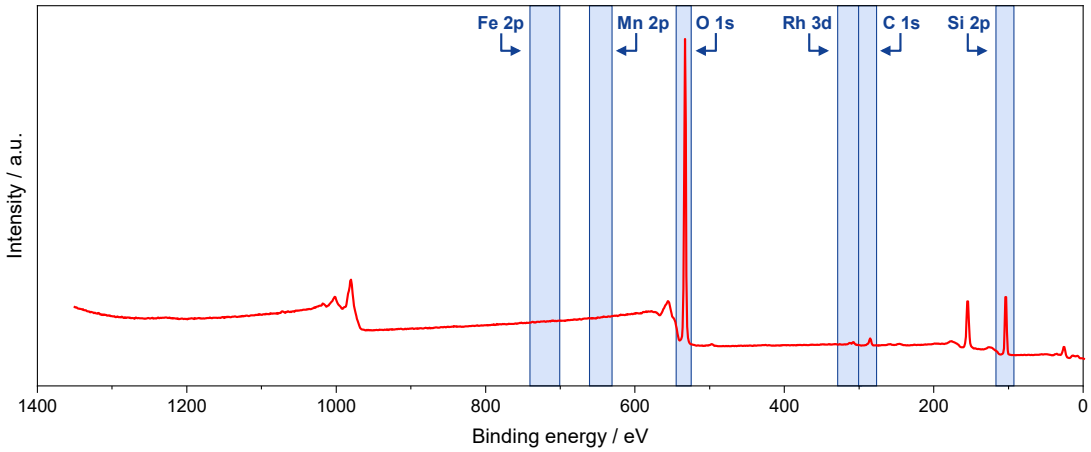

Figure S3.26. XP survey spectrum of $RhMn/SiO_2$ catalyst after high temperature investigation. Regions selected for high-resolution spectra are highlighted in blue.

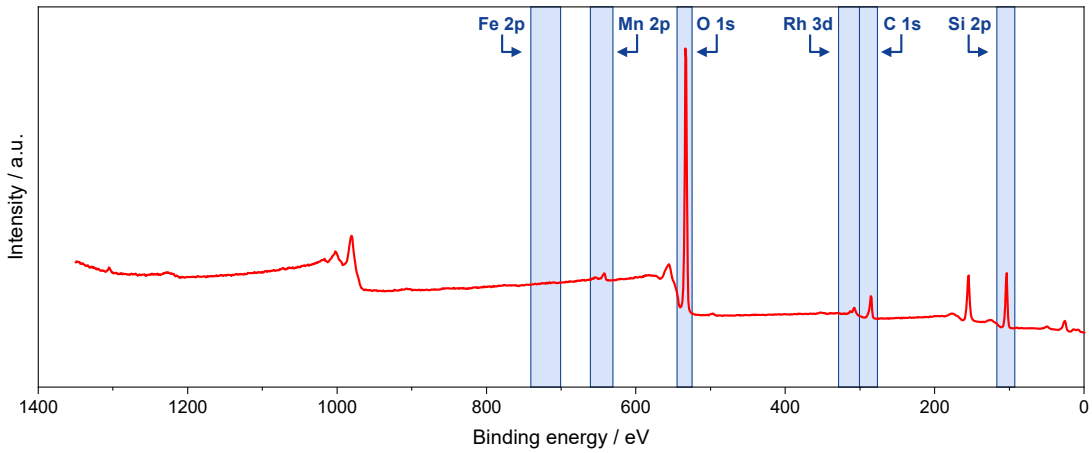

Figure S3.27. XP survey spectrum of $RhMn/SiO_2$ catalyst after long-term study. Regions selected for high-resolution spectra are highlighted in blue.

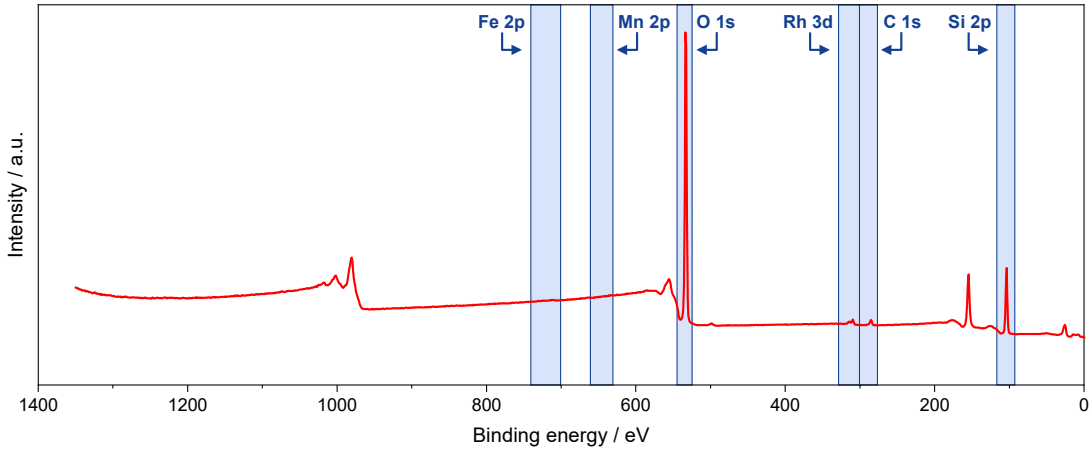

Figure S3.28. XP survey spectrum of calcined $RhFe/SiO_2$ catalyst. Regions selected for high-resolution spectra are highlighted in blue.

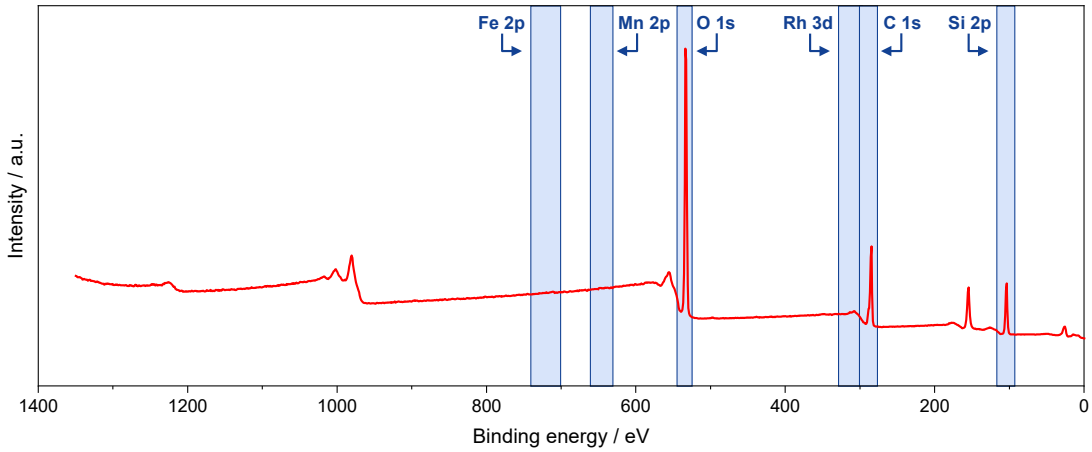

Figure S3.29. XP survey spectrum of reduced $RhFe/SiO_2$ catalyst. Regions selected for high-resolution spectra are highlighted in blue.

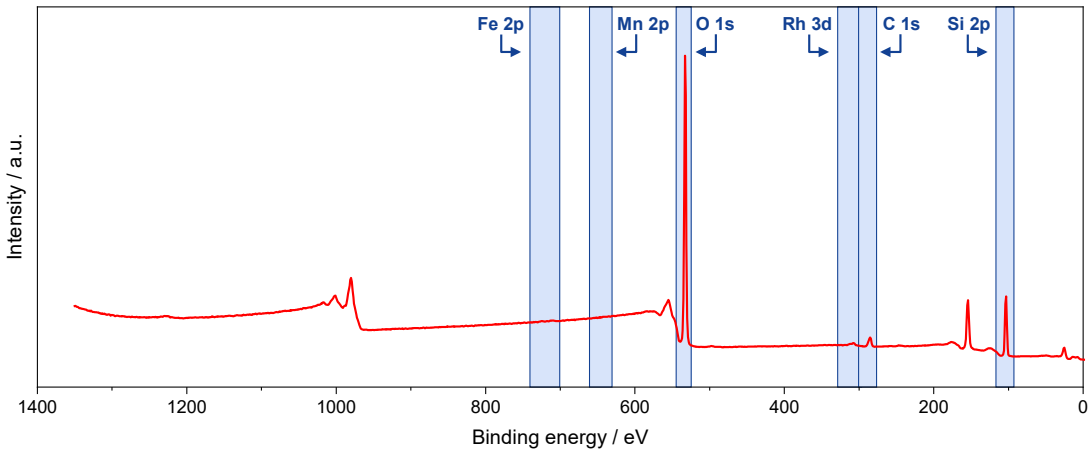

Figure S3.30. XP survey spectrum of $RhFe/SiO_2$ catalyst after high temperature investigation. Regions selected for high-resolution spectra are highlighted in blue.

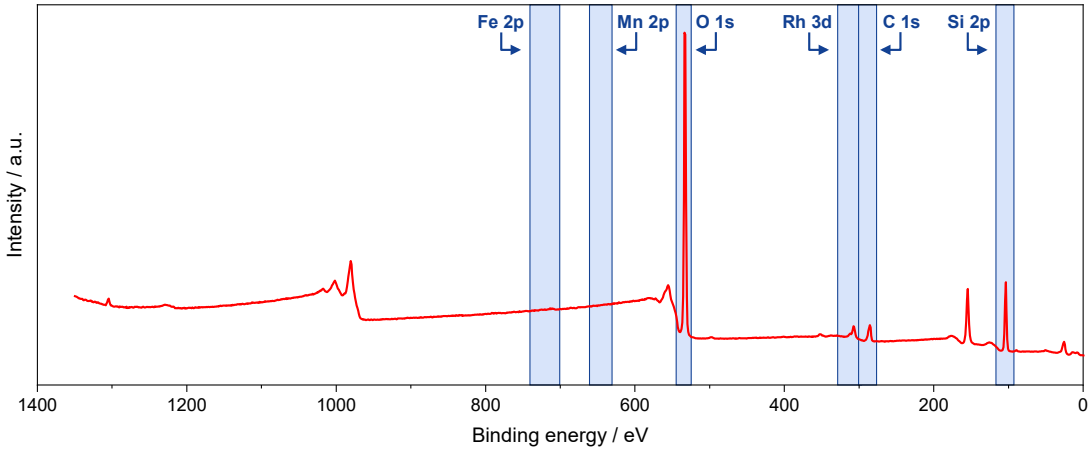

Figure S3.31. XP survey spectrum of $RhFe/SiO_2$ catalyst after long-term study. Regions selected for high-resolution spectra are highlighted in blue.

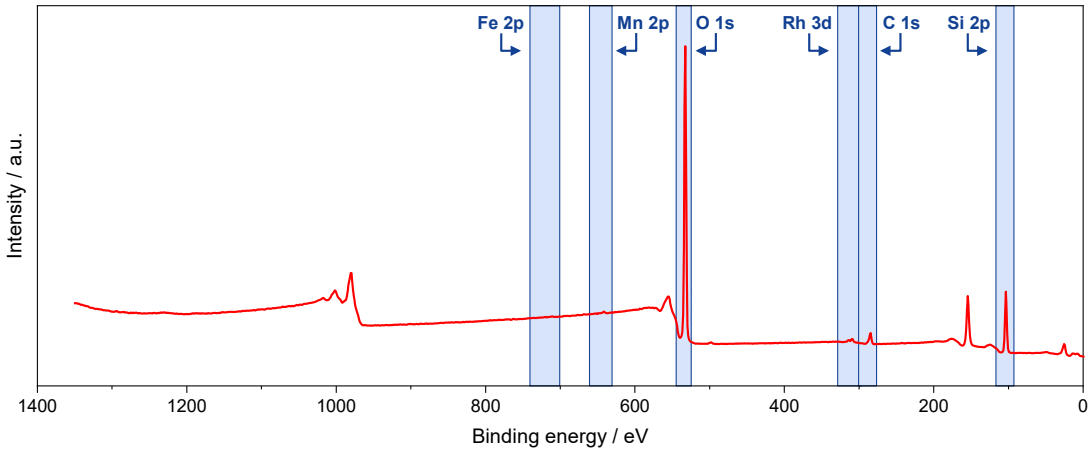

Figure S3.32. XP survey spectrum of calcined $RhMnFe/SiO_2$ catalyst. Regions selected for high-resolution spectra are highlighted in blue.

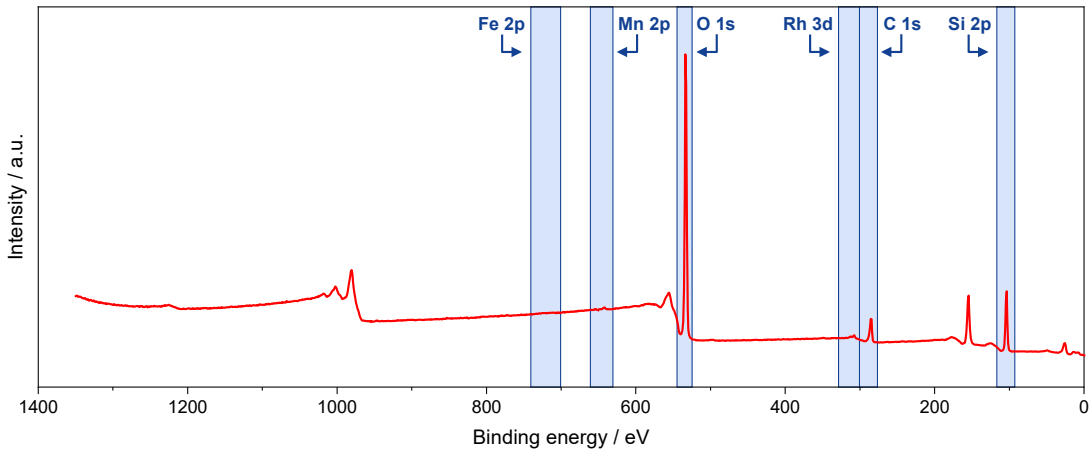

Figure S3.33. XP survey spectrum of reduced RhMnFe/SiO_2 catalyst. Regions selected for high-resolution spectra are highlighted in blue.

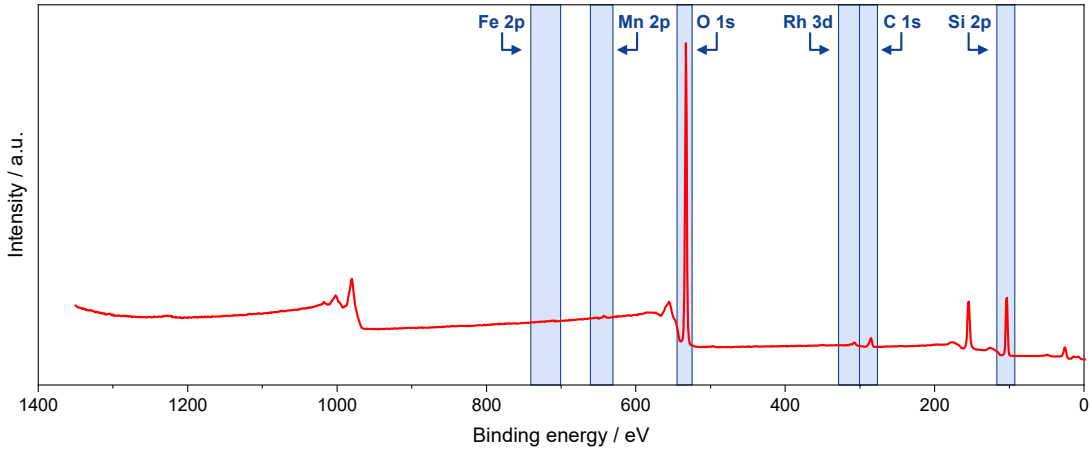

Figure S3.34. XP survey spectrum of RhMnFe/SiO_2 catalyst after high temperature investigation. Regions selected for high-resolution spectra are highlighted in blue.

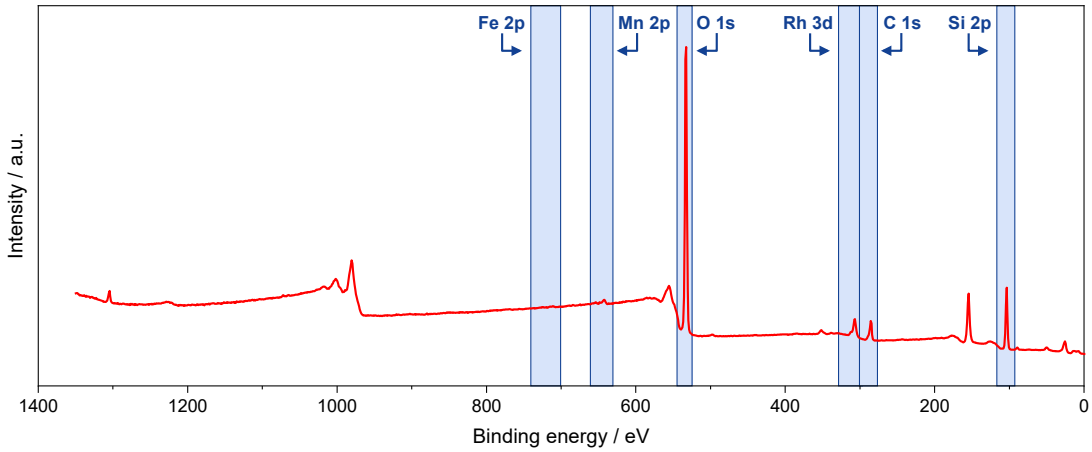

Figure S3.35. XP survey spectrum of RhMnFe/SiO_2 catalyst after long-term study. Regions selected for high-resolution spectra are highlighted in blue.

4 Paper 2: From a Molecular Single-Source Precursor to a Selective High-Performance $RhMnO_x$ Catalyst for the Conversion of Syngas to Ethanol (published version)

Phil Preikschas, Julia Bauer, Xing Huang, Shenglai Yao, Raoul Naumann d'Alnoncourt, Ralph Kraehnert, Annette Trunschke, Frank Rosowski, and Matthias Driess

ChemCatChem **2019**, *11* (2), 885–892. DOI: 10.1002/cctc.201801978.

Abstract: The first molecular carbonyl RhMn cluster $Na_2[Rh_3Mn_3(CO)_{18}]$ **2** with highly labile CO ligands and predefined Rh-Mn bonds could be realized and successfully used for the preparation of the silica (davisil)-supported $RhMnO_x$ catalysts for the conversion of syngas (CO, H_2) to ethanol (StE); it has been synthesized through the salt metathesis reaction of $RhCl_3$ with $Na[Mn(CO)_5]$ 1 and isolated in 49 % yields. The dianionic Rh_3Mn_3 cluster core of **2** acts as a molecular single-source precursor (SSP) for the low-temperature preparation of selective high-performance $RhMnO_x$ catalysts. Impregnation of **2** on silica (davisil) led to three different silica-supported $RhMnO_x$ catalysts with dispersed Rh nanoparticles tightly surrounded by a MnO_x matrix. By using this molecular SSP approach, Rh and MnO_x are located in close proximity on the oxide support. Therefore, the number of tilted CO adsorption sites at the $RhMnO_x$ interface increased leading to a significant enhancement in selectivity and performance. Investigations on the spent catalysts after several hours time-on-stream revealed the influence of rhodium carbide RhC_x formation on the long-term stability.

ChemPubSoc Europe

DOI: 10.1002/cctc.201801978

CHEMCATCHEM Full Papers

From a Molecular Single-Source Precursor to a Selective High-Performance $RhMnO_x$ Catalyst for the Conversion of Syngas to Ethanol

Phil Preikschas,[a] Julia Bauer,[a] Xing Huang,[b] Shenglai Yao,[c] Raoul Naumann d'Alnoncourt,[a] Ralph Kraehnert,[a] Annette Trunschke,[d] Frank Rosowski,[a, e] and Matthias Driess*[a, c]

The first molecular carbonyl RhMn cluster $Na_2[Rh_3Mn_3(CO)_{18}]$ **2** with highly labile CO ligands and predefined Rh-Mn bonds could be realized and successfully used for the preparation of the silica (davisil)-supported $RhMnO_x$ catalysts for the conversion of syngas (CO, H_2) to ethanol (StE); it has been synthesized through the salt metathesis reaction of $RhCl_3$ with $Na[Mn(CO)_5]$ **1** and isolated in 49% yields. The dianionic Rh_3Mn_3 cluster core of **2** acts as a molecular single-source precursor (SSP) for the low-temperature preparation of selective high-performance $RhMnO_x$ catalysts. Impregnation of **2** on silica (davisil) led to three different silica-supported $RhMnO_x$ catalysts with dispersed Rh nanoparticles tightly surrounded by a MnO_x matrix. By using this molecular SSP approach, Rh and MnO_x are located in close proximity on the oxide support. Therefore, the number of tilted CO adsorption sites at the $RhMnO_x$ interface increased leading to a significant enhancement in selectivity and performance. Investigations on the spent catalysts after several hours time-on-stream revealed the influence of rhodium carbide RhC_x formation on the long-term stability.

Introduction

Depletion of fossil fuel resources and rising crude oil prices lead to one of the most important scientific challenges of the 21st century – finding a promising alternative to petroleum-derived fuels. In this manner, ethanol is being considered as a potential alternative fuel or as fuel additive in automobiles.[1,2] The use of bioethanol produced by fermentation of biomass-derived sugars could lead to rising food prices and ethical problems.[3]

A promising alternative would be a process to synthetic ethanol, which could also be used as a feedstock for synthesis of a wide range of industrial chemicals, polymers, or as fuel in direct alcohol fuel cells.[4,5] The direct conversion of syngas to ethanol (StE) is a promising process utilizing coal, natural gas, or preferably biomass as carbon source for syngas generation. To make this process technically and commercially feasible, a selective high-performance catalyst for StE is highly desired.

As supported rhodium is the only monometallic catalyst that has demonstrated selectivity towards ethanol,[6,7] a wide range of promoters were tested, e.g. containing Fe,[8,9] Mn,[10] Li,[11] and even rare earth oxides, such as CeO_2 or Pr_6O_{11}.[12] From these studies, it turned out that Mn-promoted Rh catalysts are among the best systems known as yet for the conversion of syngas to ethanol and other C_{2+} oxygenates (e.g., acetaldehyde, acetic acid).[10] By using Mn as a promoter, a higher selectivity towards ethanol as well as an increase of CO conversion can be achieved. According to a recent review by Luk *et al.*,[2] the most performant Mn-promoted Rh catalysts in the conversion of StE showed an ethanol selectivity of 17.7% and an overall C_{2+} oxygenate selectivity of 42.0% at a CO conversion of 17.0%. These catalysts were prepared by incipient wetness impregnation of the respective metal nitrates and subsequent calcination.[13]

Despite these promising results, the production of undesirable methane is still present with selectivities up to 43.7%.[13] A theoretical study has shown that methane formation is inevitable on supported RhMn catalysts due to a low activation barrier for methanation.[14] However, the number of active sites for the methane formation decreases, if Mn is in close proximity to Rh.[15,16] These close interactions not only decrease the selectivity towards methane but also promote the formation of ethanol by modifying the surface structure for the conversion of StE. One promising strategy to bring about Rh and Mn in

[a] P. Preikschas, J. Bauer, Dr. R. Naumann d'Alnoncourt, Dr. R. Kraehnert, Dr. F. Rosowski, Prof. M. Driess
BasCat – UniCat BASF JointLab
Technische Universität Berlin
Berlin 10623 (Germany)
E-mail: matthias.driess@tu-berlin.de
[b] Dr. X. Huang
Scientific Center for Optical and Electron Microscopy
ETH Zürich
Zürich 8093 (Switzerland)
[c] Dr. S. Yao, Prof. M. Driess
Metalorganic Chemistry and Inorganic Materials
Department of Chemistry
Technische Universität Berlin
Berlin 10623 (Germany)
[d] Dr. A. Trunschke
Department of Inorganic Chemistry
Fritz-Haber-Institut der Max-Planck-Gesellschaft
Berlin 14195 (Germany)
[e] Dr. F. Rosowski
BASF SE
Process Research and Chemical Engineering
Heterogeneous Catalysis
Ludwigshafen 67056 (Germany)

Supporting information for this article is available on the WWW under https://doi.org/10.1002/cctc.201801978

close proximity could be achieved by the molecular single-source precursor (SSP) approach with a well-defined Rh:Mn ratio and Rh–Mn bonds. Encouraged by the recent progress in using molecular SSPs for solid catalyst design and preparation,[17] we synthesized the first molecular RhMn SSP and investigated its suitability to produce more selective RhMn-based StE catalysts. Here we present the synthesis and characterization of the carbonyl heterobimetallic $Na_2[Rh_3Mn_3(CO)_{18}]$ cluster **2** that acts as a suitable SSP for the low-temperature preparation of a silica-supported $RhMnO_x$ catalyst, which shows the highest selectivity for the conversion of syngas to ethanol reported to date.

Results and Discussion

Synthesis and Characterization of a Suitable Molecular Single-Source Precursor to Give $RhMnO_x$ Catalysts

The novel Rh_3Mn_3 cluster **2** was synthesized from the salt metathesis reaction of $RhCl_3$ with $Na[Mn(CO)_5]$ **1** in THF as a fine black powder in 49% yields (Scheme 1). The composition of **2**

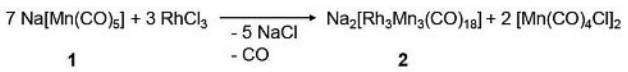

Scheme 1. Synthesis of $Na_2[Rh_3Mn_3(CO)_{18}]$ **2**.

was confirmed by elemental analysis; **2** is sensitive towards air and readily soluble in protic and nonprotic polar solvents (ethanol, acetonitrile, acetone, THF, and DMF).

Single crystals suitable for an X-ray diffraction (XRD) analysis were obtained by diffusion of pentane vapors into a concentrated solution of **2** in THF at −37 °C. Compound **2** crystallized as a separate ion-pair; the dianionic Rh_3Mn_3 cluster core consists of an array of the six metal atoms, which are distributed as a central triangle of three rhodium atoms with a bridging manganese atom on each site (Figure 1).

This hexanuclear metal core has a nearly planar geometry with three roughly straight angles of Mn–Rh–Mn (av. 174.0(9)°), leading to a mean deviation of 0.14 Å to the best plane. The latter cluster core is stabilized by 12 terminal and 6 bridging CO ligands that additionally link the Mn atoms with the Rh_3 subunit. These bridging CO ligands protrude out of the plane and are coordinated to a Na ion on each site resulting in a small bending to the middle of the hexanuclear Rh_3Mn_3 metal core (Figure S1 in *Supporting Information*). The terminal CO ligands are distributed over the Mn as well as Rh atoms. Each Mn atom carries three terminal CO ligands, one of them within and the others out of the plane. The remaining three terminally bound COs are in-plane and each attached to a Rh atom. They are slightly bended with an av. Rh–C–O bond angle of 174.1°. The central Rh_3 triangle has an almost equilateral structure with an average bond angle of 60.00(7)°. The mean Rh–Rh distance of

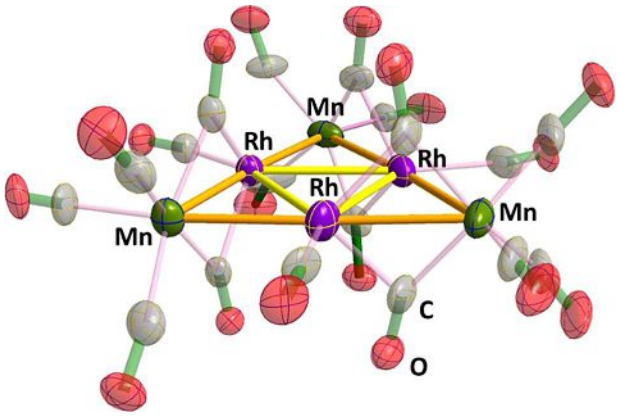

Figure 1. Molecular structure of the cluster dianion of **2**. Thermal ellipsoids are drawn at 50% probability level. Sodium cations and stabilizing THF molecules are omitted for clarity. An overall image is provided as Figure S1 in the *Supporting Information.* Selected distances (Å) and angles (°): Rh1-Rh2 2.877(3), Rh1-Mn1 2.640(6), Rh1-Rh2-Rh3 60.26(7), Mn1-Rh1-Mn3 173.08(16).

2.870(3) Å is significantly longer than those observed in other rhodium species, such as $Rh_3(\mu\text{-}CO)_2(Cp)_3$ (av. 2.59 Å) or $Rh_3(\mu\text{-}CO)_3(Cp)_3$ (av. 2.65 Å).[18,19] The six Rh–Mn bonds have an average bond length of 2.638(4) Å and are slightly shorter than the other reported Rh–Mn bond (2.70 Å).[20] The dianionic Rh_3Mn_3 cluster core of **2** is highly symmetric with an overall C_3 symmetry, which is in accordance with a singlet resonance observed in the ^{55}Mn-NMR spectrum at $\delta = -2702.5$ ppm.

The structural features of the Rh_3Mn_3 core of **2** are reminiscent of the reported hexanuclear $Na_3[Cu_3Fe_3(CO)_{12}]$ and $Os_6(CO)_{21}$ compounds.[21–25]

Transformation of Supported Precursors into StE Catalysts

Compound **2** was used as a molecular SSP for three different silica-supported $RhMnO_x$ catalysts. In the first case, a solution of **2** in acetonitrile was impregnated *via* incipient wetness method on davisil, a commercially available silica with a BET surface area of 480 m^2/g.

FT-IR measurements confirmed the integrity of **2** on the silica-support (Figure S2). The present Rh–Mn bonds in **2** could be advantageous for the preparation of a metallic Rh catalyst with a close proximity to MnO_x sites generated through low-temperature decomposition. To identify the proper conditions for such a mild transformation of supported **2**, a temperature-programmed decomposition (TPDe) investigation was performed after impregnation (Figure S3). A two-step decarbonylation could be observed which begins at approx. 70 °C and reaches its maximum at 96 °C. This might be attributed to the weaker bonded bridging CO ligands, whereas the decarbonylation of the terminal CO ligands occurs at the second maximum at 113 °C. Based on these observations, silica-supported **2** has been transformed into the $NaRhMnO_x/SiO_2$ catalyst **3** with a nominal loading of 1.25 wt% Na, 1.50 wt% Mn, 2.80 wt% Rh by a low-temperature decomposition in 10% dihydrogen with two heating steps at 75 and 115 °C, respec-

tively. These temperatures are far below of a classical preparation route using single metal (Rh, Mn) nitrates (350 °C) which might avoid the sintering of Rh particles at temperatures above StE reaction conditions (260 °C).

To investigate the role of sodium on the RhMn system, two different routes to sodium-free $RhMnO_x/SiO_2$ catalysts were pursued: a) the Na ions were removed from as-synthesized **3** by a Soxhlet extraction with methanol leading to a sodium-free $RhMnO_x/SiO_2$ catalyst **4**, and b) the Na cations in **2** were replaced by the trimethylbenzylammonium cation to give another sample of sodium-free $RhMnO_x/SiO_2$ catalysts **5**. The absence of sodium in both catalysts was confirmed by elemental analysis *via* inductively coupled plasma optical emission spectrometry (ICP-OES).

Powder XRD measurements were accomplished for phase identification of the as-synthesized materials **3–5** (Figures S4 and S5). No specific reflections could be identified due to the limit of XRD for the detection of supported, crystalline nanoparticles (around 3.0 nm).[26] On this account, high-resolution transmission electron microscopy (HR-TEM) and annular dark-field scanning transmission microscopy (ADF-STEM) combined with energy-dispersive X-ray (EDX) mapping were conducted to determine the structure, morphology and atomic composition of **5**.

The overview TEM image showed relatively small nanoparticles with a mean particle size of 1.30 nm, which are homogeneously distributed on the silica-support (Figure 2a). Lattice fringes analyses were then performed on the HR-TEM images to determine the atomic structure of the nanoparticles, which are size-representative according to the particles size distribution in Figure 2b. The crystalline particles show lattice fringes with *d*-spacings of 2.2 (Figure 2c) and 1.9 Å (Figure 2d). They are consistent with fcc{111} and fcc{200} planes of metallic Rh in the space group Fm-3 m (Figure 2c,d). Metallic Mn or crystalline MnO_x particles could not be observed. This leads to the assumption that Mn is in an amorphous phase. In addition, it is not possible to distinguish between MnO_x and SiO_2 due to the low loading and the weak phase contrast compared to that of the silica-support.

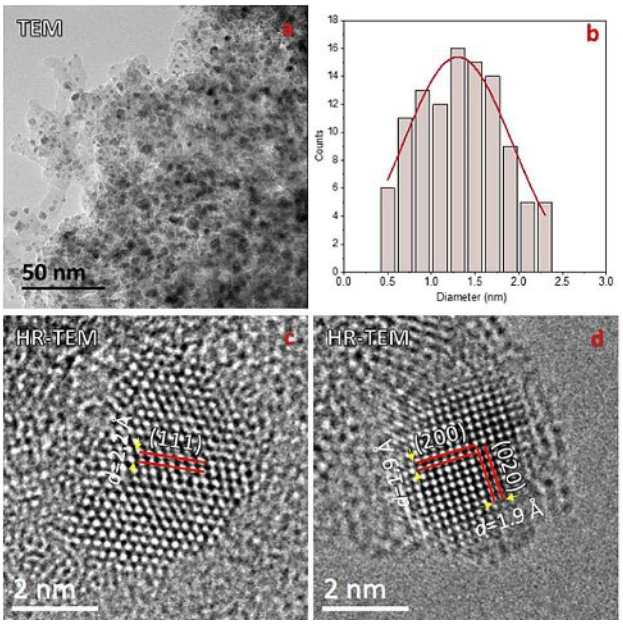

Figure 2. (HR-)TEM images of the as-prepared silica-supported $RhMnO_x/SiO_2$ catalyst **5** after reduction in H_2 at 260 °C: a,b) Rh nanoparticles are homogenously dispersed on silica and surrounded by a MnO_x matrix; c,d) the indicated lattice fringes of the crystalline particles correspond to the fcc {111} and fcc{200} planes of metallic Rh.

The structural information based on lattice fringes are not sufficient to differentiate between metallic Rh and RhMn alloy particles. Therefore, ADF-STEM in combination with EDX was conducted to investigate the composition of catalytic particles. The ADF-STEM images recorded from three different domains show homogeneously dispersed nanoparticles with mean particles sizes of 1.30, 2.80 and 1.55 nm in the domains 1, 2 and 3 (Figure S10), respectively. It also confirms a narrow size distribution of the synthesized nanoparticles (Figure S10). The composition analyses were focused on domain 2, since particles smaller than 2 nm are difficult to study due to the insufficient EDX signal. The EDX mapping (Figure 3; for more EDX mappings

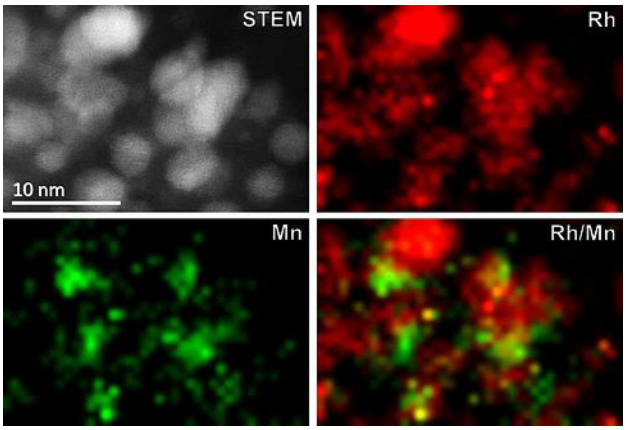

Figure 3. Composition analysis of the as-synthesized $RhMnO_x/SiO_2$ catalysts **5** after reduction in H_2 at 260 °C. ADF-STEM with EDX mapping: Small particles of metallic rhodium (red) are closely contacted to a MnO_x species (green). No separated MnO_x or Rh nanoparticles could be observed.

Figure S11) and an EDX line-scan profile (Figure S12) indicate homogeneously dispersed Rh nanoparticles, which are surrounded by a finely distributed Mn species. Thus, Rh is in close proximity to manganese and no separated Rh or MnO_x particles are found in all three domains (Figures 3 and S10).

Since no crystalline Mn particles are observed in ADF-STEM images, it is assumed that Mn is in an oxidized state. This assumption was confirmed by XPS measurements without contact to an oxidative atmosphere (Figure S8) and is also known for related $RhMnO_x$ catalysts.[16] However, the chemical state of Mn under reaction conditions is controversially discussed assuming that zero-valent Mn atoms might be alloyed with Rh.[14] Furthermore, a theoretical study described RhMn alloys as active species in the conversion of StE.[27] In this

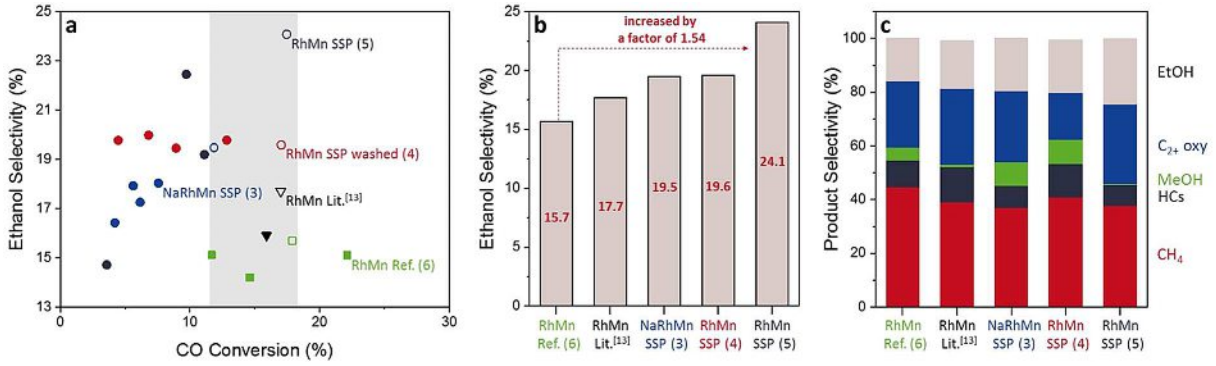

Figure 4. a) Ethanol selectivities (mol%) as function of CO conversions. Different CO conversion levels were realized by application of three different reaction temperatures. The range of iso-conversion which was chosen to compare the product selectivities are highlighted in grey. b,c) Product selectivities (mol%) of measurements points marked with a hollow symbol at iso-conversion (11–16%). The CO_2 selectivity is not shown here, as it is below 1% for all tested catalysts. Measuring conditions: 243–260 °C, 54.0 bar, p(H_2) = 32.4 bar, p(CO) = 10.8 bar, GHSV 3500 h^{-1}. CH_4, HCs, MeOH, C_{2+} oxy, and EtOH abbreviate methane, hydrocarbons, methanol, C_{2+} oxygenates, and ethanol, respectively. S(C_{2+} oxy) mainly includes acetaldehyde and acetic acid. For more details about the products, see Table S2 in Supporting Information.

study, it can be shown that the formation of a supported RhMn nanoalloy is unfavourable on silica supports.

Not even the use of $Na_2[Rh_3Mn_3(CO)_{18}]$ **2** as molecular SSP with both metals in low oxidation states and predefined metal-metal bonds led to the formation of an alloy. The considerations that a reduction of Mn is induced by a close proximity to Rh might be attributed to classical preparation methods with precursors bearing Mn in high oxidation states. In this case, it cannot be distinguished whether the oxidation state of Mn in as-synthesized catalysts is caused by the used metal precursor or through the oxidation by an oxide support. On this account, the decomposition of silica-supported $Na[Mn(CO)_5]$ **1** metallate bearing Mn in the low oxidation state of −1 could not lead to the preparation of a zero-valent Mn species. The weakly Brønsted acidic silanol groups are likely to cause the immediate oxidation of the metallate **1** (Figure S9). It is therefore suggested that the oxidation of Mn to give MnO_x species is inevitable on silica, even under reaction conditions.

Catalytic Performance of the As-Synthesized $RhMnO_x$ Catalysts

The as-prepared materials **3–5** were tested as catalysts for the direct conversion of StE in a fixed-bed parallel test setup at common reaction conditions for syngas chemistry (GHSV = 3500 h^{-1}, p = 54.0 bar, and T = 243–260 °C; see *Experimental Section*). The catalysts were directly compared with a Mn-promoted Rh catalysts **6** prepared by incipient wetness impregnation of the respective metal nitrates and subsequent calcination at 350 °C, and Rh/SiO_2 **8** prepared in a similar fashion (Table S2). For this comparison, different CO conversion levels were realized by variation of the reaction temperature from 243–260 °C.

Compared to the monometallic Rh/SiO_2 catalyst **8** (X_{CO} = 4.8%, S_{EtOH} = 6.5%; Table S2), all Mn-promoted catalysts show a substantially higher activity and ethanol selectivity. The enhancement of the catalytic performance due to the close proximity between Rh and MnO_x was also observed for other reported $RhMnO_x$ catalysts.[13,28] The catalytic results show a lower CO conversion of the SSP-originated catalysts **3–5** compared to the 'traditionally' prepared catalyst **6**. This finding might be attributed to a reduced metal loading of 0.6 wt% Rh which was confirmed by ICP-OES. However, the catalysts **3–5** show an increase in ethanol selectivity compared to the reference catalyst **6** as well as the mentioned literature-reported catalysts at iso-conversion denoted with hollow symbols in Figure 4a. In the case of **5**, the selectivity towards ethanol could be substantially enhanced by a factor of 1.54 and is – to our knowledge – the highest reported ethanol selectivity compared to literature examples (Figure 4b).[2,13,29–31] We reason that the enhancement in selectivity is due to a higher dispersion of Rh nanoparticles in a tightly surrounded MnO_x matrix in the SSP-originated catalysts **3–5**, because this situation can increase the number of tilted CO adsorption sites which, in turn, facilitate the formation of ethanol (Scheme S1). In fact, previous IR studies suggested that CO adsorbs in a tilted manner at Rh-MnO_x interfaces.[32,33] Moreover, results from diffuse reflectance infrared Fourier transform spectroscopy (DRIFTS) and kinetic investigations confirmed the enhancement of ethanol selectivity due to the tilted adsorption mode on $RhMnO_x$ which promotes CO dissociation on Rh^0 sites.[13,28] Furthermore, density functional theory (DFT) calculations proposed the lowering of the activation barrier for CO insertion into adsorbed CH_x fragments due to a tilted adsorption.[14] The Na content in RhM SSP catalysts has an influence on activity and selectivity but only at very low conversions. At higher conversions both SSP-originated catalysts **3** and **4** exhibit similar ethanol selectivities.

Methane is the main product for all tested catalysts and its selectivity is reduced by factors of 0.83, 0.92, and 0.84 for catalysts **3–5**, respectively. The lower methanation might also be attributed to the close proximity of Rh and MnO_x. With a methane selectivity of 37.1%, the Na containing catalyst **3** lowers the methane formation in a significant amount com-

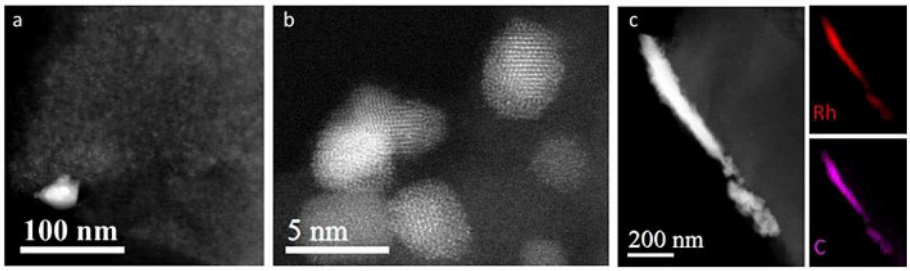

Figure 5. a,b) ADF-STEM images of the spent catalyst **5**: after 220 h TOS, some big particles are formed due to sintering but most of the particles remain relatively small. c) EDX mapping and EELS measurements (Figure S13) suggest the presence of a carbide phase in the bigger particles.

pared to the reference catalyst **6** with 44.8%. Further products are other light hydrocarbons, methanol and oxygenates, mainly acetaldehyde and acetic acid.

Stability of the Synthesized $RhMnO_x$ Catalysts

After several hours time-on-stream (TOS), the catalysts **3** (105 h; Figure S14) and **5** (220 h; Figure S15) show a slight decrease in CO conversion due to deactivation. In the case of **5**, a notable deactivation in the first 20 h TOS can be observed (X_{CO} = 27.7 to 17.5%). After this initial deactivation phase, the catalyst remains quite stable after additional 200 h TOS. However, the selectivity patterns remain similar and a difference in ethanol selectivity was not observed (Table S2, entry 3 and 7). The aforementioned deactivation might be induced by the formation of some larger particles due to sintering (Figure 5a). For those larger particles a local enrichment of C was observed by ADF-STEM with EDX mapping (Figure 5c), while respective EELS measurements suggest the presence of a rhodium carbide RhC_x phase (Figure S13). However, most of the particles remain relatively small (Figure 5b), which is the reason for the long-term stability of the system.

Conclusions

In summary, the first carbonyl RhMn cluster **2** with highly labile CO ligands and predefined Rh–Mn bonds could be realized and successfully used for the preparation of the silica (davisil)-supported $RhMnO_x$ catalysts **3–5**. The utilization of **2** as molecular SSP facilitates the formation of small Rh nanoparticles embedded in a finely distributed MnO_x matrix. This close proximity between Rh and MnO_x leads to a superior selectivity towards ethanol and also to a lower methane formation compared to reference as well as reported $RhMnO_x$ catalysts. The RhMn SSP catalysts **3–5** show the best performance of a Mn-promoted Rh catalyst in the conversion of StE reported as yet. In addition, the usage of the RhMn cluster **2** as molecular SSP shows that the formation of a RhMn alloy is unfavorable on silica supports due to the inevitable oxidation of Mn.

Long-term stability tests showed only a moderate deactivation after an initial phase and several hours TOS. Based on ADF-STEM images with EDX mapping and EELS measurements, the formation of a rhodium carbide RhC_x phase is suggested which might lead to the deactivation of $RhMnO_x$ catalysts besides sintering of Rh nanoparticles.

The molecular SSP approach is therefore a powerful tool for solid catalysts design resulting in highly dispersed metals embedded in oxide matrices and might lead to a better understanding of catalyst structure-function relationships. In this manner, it might be applicable to other catalysts systems, such as silica-supported $RhFeO_x$ and $Rh(Mn,Fe)O_x$ catalysts by choosing suitable molecular SSPs, e.g. $Na[RhFe_2(CO)_{11}]$ or a [RhMnFe] carbonyl cluster.[34]

Experimental Section

General considerations. All manipulations involving air- and moisture sensitive organometallic compounds were carried out under an atmosphere of dry, oxygen-free argon by using standard Schlenk techniques or glove boxes (MBraun LABmaster Pro) under a purified nitrogen or argon atmosphere. Solvents were taken from a solvent purification system (MBraun SPS-800) or purified using conventional procedures, freshly distilled under argon atmosphere and degassed prior to use.

NMR spectroscopy. NMR samples of air- and moisture-sensitive compounds were prepared in a J. Young NMR tube (sealed with a polytetrafluoroethylene valve) under nitrogen atmosphere inside a glove box. The deuterated solvents were dried over a 4 Å molecular sieves and degassed prior to use. The ^{13}C- and ^{55}Mn-NMR spectra were recorded on a Bruker Avance III (^{13}C: 125 MHz, ^{55}Mn: 124 MHz) spectrometer. The $^{13}C\{^1H\}$-NMR spectra were referenced to residual solvent signal as internal standards (acetonitrile-d_3: δ_C = 1.32 ppm) and the ^{55}Mn-NMR spectra were referenced to a solution of $KMnO_4$ in D_2O. The abbreviations used to denote the multiplicity of the signals are singlet (s) and multiplet (m).

FT-IR spectroscopy. IR spectra (4000–400 cm^{-1}) of air- or moisture sensitive samples were recorded on a Nicolet iS5 spectrometer inside a glove box. Solid samples were measured with an attenuated total reflectance sampling technique and are directly placed on an ATR crystal (diamond). All other samples were placed as solid or as drop of a solution on an ATR crystal (diamond) of a Bruker ALPHA FT-IR spectrometer. The spectra were collected as data point tables by using OMNIC (Thermo Fisher Scientific Inc.) or OPUS (Bruker Corporation) software and were analyzed with Origin (OriginLab Corporation). Intensities of absorption bands were assigned on basis of visual inspection and were abbreviated as very strong (vs), strong (s), medium (m) and weak (w).

Mass spectroscopy. Mass spectra were recorded using HR-ESI-MS-method on an LTQ Orbitrap XL spectrometer.

Elemental analyses. The determination of the mass fractions of carbon, hydrogen, nitrogen and sulfur were carried out on a Thermo Finnigan FlashEA 1112 Organic Elemental Analyzer. Air- or moisture sensitive samples were prepared in silver capsules in a glove box. Mass fractions of transition or alkali metals were achieved by ICP-OES with a Varian 715 Emission Spectrometer.

Single crystal X-ray diffraction. An analytically pure crystal was directly placed on a glass capillary with perfluorinated oil and measured in a cold nitrogen steam. The data of all measurements were collected on an Agilent Technologies SuperNova diffractometer at 150 K (Cu-K_α-radiation, $\lambda = 1.5418$ Å). The structure was solved by direct methods using SHELXT,[35] space group determinations were performed with XPREP and crystal structure refinements with SHELXL.[36] All aforementioned programs were handled with Olex^2 Crystallography Software.[37] The CCDC number 1868848 (**2**) contain the supplementary crystallographic data for this paper. The data can be obtained free of charge by contacting The Cambridge Crystallographic Data Centre, 12, Union Road, Cambridge CB2 1EZ, UK; fax: +44 1223 336033.

Powder X-ray diffraction. Powder X-ray diffraction (XRD) measurements were performed in Bragg-Brentano geometry on a D8 Advance II theta/theta diffractometer (Bruker AXS), using Ni-filtered Cu $K\alpha_{1,2}$ radiation and a position sensitive energy dispersive LynxEye silicon strip detector. The sample powder was filled into the recess of a cup-shaped sample holder, the surface of the powder bed being flush with the sample holder edge (front loading).

Electron microscopy. The samples were investigated by an aberration-corrected JEOL JEM-ARM200CF transmission electron microscope. The microscope is equipped with a high angle silicon drift EDX detector with the solid angle of up to 0.98 steradians from a detection area of 100 mm^2 that allows for EDX measurement.

Temperature-programmed decomposition (TPDe). TPDe-MS experiments were performed with a MicrotracBEL BelCat II setup, which was coupled to a mobile Pfeifer Vacuum QMG 220 mass spectrometer. In a typical experiment, a certain amount of the sample (around 50 mg) was placed in the sample cell inside a glove box and placed in the BelCat II setup. Helium was used as carrier gas with a flow rate of 54 mL/min and hydrogen was used for the decomposition with a flow rate of 6 mL/min. The temperature was linearly and continuously increased from RT to 873 K with a temperature ramp of 5 K/min. The reaction products were analyzed by the computer controlled quadrupole mass spectrometer.

X-ray photoelectron spectroscopy. XPS was measured on K-Alpha™ + X-ray Photoelectron Spectrometer (XPS) System (Thermo Scientific), with Hemispheric 180° dual-focus analyzer with 128-channel detector. X-ray monochromator is Micro focused Al–Kα radiation. For the measurement, the as-prepared samples were directly loaded on the sample holder for measurement. The data was collected with X-ray spot size of 200 µm, 20 scans for survey, and 50 scans for regions.

Catalytic testing for synthesis gas conversion. The catalytic testing of the syngas to ethanol reaction was performed in a 4-fold parallel testing unit. 0.5 g (~1 mL) catalyst with a particle size of 100–200 µm were loaded into each stainless steel reactor with an effective inner diameter of 6.25 mm. The reaction temperature was monitored by temperature sensors with three thermocouples along the catalyst bed.

Four mass flow controllers were used to adjust the flow rates of the inlet gases N_2 (99.999 %), CO (99.997 %), H_2 (99.999 %) and Ar (99.999 %, all Air Liquide). The CO feed line was equipped with a carbonyl trap in order to remove all metal carbonyls that might be formed by high pressure of CO in contact with stainless steel. The carbonyl trap consisted of a U-shaped $^1/_2$" stainless steel tube filled with Al_2O_3 and heated to 170 °C by a heating sleeve.

Compounds in the effluent gas that condense below 180 °C were removed by a coalescence filter in the downstream oven. All remaining compounds in the effluent gas were analyzed with an online gas chromatograph (Agilent 7890B) equipped with two thermal conductivity detectors (TCD) and one flame ionization detector (FID) using He as the carrier gas. TCDs detect the inlet gases H_2, Ar, N_2, CO and in addition methane, CO_2 and H_2O. The FID is used to detect a large variety of paraffins, olefins and oxygenates (alcohols, acetaldehyde, acetic acid) with a combination of a Porabond Q and an RTX-Wax column. The carbon balance was between 96–102 % for all measurements.

The catalysts are reduced *in-situ* at 54 bar, 265 °C with 5 % H_2 in N_2 for 1 h with a volume flow of 58.3 mL min^{-1}. Subsequently, the temperature was decreased to 243 °C and synthesis gas feedstock mixture containing CO:H_2:N_2:Ar (20:60:10:10 %, v:v) was admitted. The volume flow was kept constant to achieve a GHSV of 3500 h^{-1}. The temperature was increased to 260 °C in three steps and subsequently decreased in the same manner. Each step was held constant for at least 15 h to allow the catalysts to equilibrate.

The obtained concentrations of all compounds were corrected for volume changes due to the reaction and the following N_2 dilution. Therefore, the mole fraction of Ar was used as inert internal standard according to Equation (1).

$$n_{i,corrected} = n_{i,GC} \cdot \frac{n_{Ar,bypass}}{n_{Ar,reactor}} \quad (1)$$

$n_{i,corrected}$ is the corrected mole fraction of compound *i*.$n_{i,reactor}$ and $n_{i,bypass}$ are the mole fractions of compound *i* originally obtained by the gas chromatograph sampling the respective reactor or the bypass line.

Additionally, the results for all compounds detected by the FID were corrected using the mole fraction of methane obtained by FID and TCD according to Equation (2).

$$n_i = n_{i,corrected} \cdot \frac{n_{methane,TCD}}{n_{methane,FID}} \quad (2)$$

n_i is the mole fraction of compound *i* that is finally used for further calculations. $n_{methane,TCD}$ and $n_{methane,FID}$ are the methane concentrations detected by TCD and FID after correction with the Ar standard [Equation (1)].

Carbon monoxide conversion X_{CO} was calculated indirectly from the summation of carbon numbers in all products rather than directly from the CO concentration as at small conversions the quantification of CO *via* TCD was not precise enough [Equation (3)].

$$X_{CO} = \frac{\sum n_j C_j}{n_{CO,0}} \quad (3)$$

$n_{CO,0}$ is the mole fraction of CO in the inlet gas and C_i is the carbon

number of the product *i*. The selectivity *S* for each product *i* was determined based on the number of C atoms by Equation (4).

$$S_i = \frac{n_i C_i}{\sum n_{i,j} C_{i,j}} \quad (4)$$

Synthesis of Na[Mn(CO)$_5$]·0.5THF (1). Metallate **1** was synthesized by a modified literature-known preparation.[38] Metallic sodium (3.04 g, 0.133 mol) was cut in small pieces and suspended in 50 mL THF. This suspension was stirred at r.t. overnight. A yellow solution of manganese carbonyl $Mn_2(CO)_{10}$ (5.18 g, 13.3 mmol) in dry THF (45 mL) was added to the suspension. The mixture was stirred at r.t. for 72 h, during which time a color change from yellow over red to brown was observed. The suspension was then filtered and washed with additional 25 mL THF. The combined filtrates were evaporated to dryness in vacuum for 12 h, providing a light green solid. Yield: 4.60 g, 21.1 mmol, 81.2% (Based on $Mn_2(CO)_{10}$). Note: THF molecules are still coordinated to Na, which was quantified by dynamic flash combustion analysis. This material was used for subsequent procedures without further purification. Elemental analysis (%): calcd for $C_7H_4O_{5.5}NaMn$: C, 33.10; H, 1.59 Found: C, 32.36; H, 1.86. $^{13}C\{1H\}$ NMR (125 MHz, CD_3CN, 298 K, ppm): $\delta = 238.68$ (s, Mn–CO). ^{55}Mn NMR (124 MHz, CD_3CN, 298 K, ppm): $\delta = -2702.57$. ESI-MS: m/z: calcd for $[M–Na]^-$: 194.9, found: 194.9. IR (ATR, cm^{-1}): $\nu = 1936$ (w), 1884 (m), 1826 (s).

Synthesis of Na$_2$[Rh$_3$Mn$_3$(CO)$_{18}$]·2THF (2). Rhodium(III) chloride $RhCl_3$ (602 mg, 2.88 mmol) was suspended in 100 mL ethanol (EtOH) and cooled down to −78 °C in an acetone/dry ice bath. A solution of Na[Mn(CO)$_5$] (**1**, 1.79 g, 4.12 mmol) in 25 mL EtOH was added dropwise. The suspension was warmed up slowly to r.t. within 6 h, during which time a color change from green to dark brown and precipitation of a crystalline solid was observed. After stirring for 24 h, the mixture was filtered through a glass frit and the residue was washed two times with additional 10 mL of EtOH. The combined filtrates were evaporated under vacuum at 38 °C and dried in vacuum. This crude product was washed four times with 25 mL *n*-hexane and dried under vacuum overnight. The title compound was obtained as dark brown solid. Analytically pure black block-shaped crystals were obtained by diffusion of pentane vapors into a concentrated and filtered solution in THF at −37 °C. Yield: 520 mg, 4.66 mmol, 48.6% (based on $RhCl_3$). Elemental analysis (%): calcd for $C_{26}H_{16}O_{20}Na_2Mn_3Rh_3$: C, 26.70; H, 1.38 Found: C, 26.70; H, 1.37. $^{13}C\{1H\}$ NMR (125 MHz, CD_3CN, 298 K, ppm): $\delta =$ 210.69 (s, Mn–*C*O), 214.50 (s, Mn–*C*O), 216.67 (m, μ-*C*O). ^{55}Mn NMR (124 MHz, CD_3CN, 298 K, ppm): $\delta = -2606.78$. ESI-MS: m/z: calcd for $[M–Na]^-$: 1000.3, found: 1000.4. IR (ATR, cm^{-1}): $\nu = 2077$ (w), 2025 (m), 2001 (m), 1917 (m), 1798 (br, m). ATR-FTIR of a drop the *n*-hexane washing solution confirmed $[Mn(CO)_4Cl]_2$ as by-product. IR of $[Mn(CO)_4Cl]_2$ (ATR, cm^{-1}): 2115 (w), 2045 (m), 2006 (vs), 1934 (vs). Bands are in accordance to literature, IR (chloroform solution, cm^{-1}): 2104, 2047, 2006, 1977.[39] After serval days, $Mn_2(CO)_{10}$ crystallized from the solution in form of yellow needles due to the disproportion of $[Mn(CO)_4Cl]_2$ to $Mn_2(CO)_{10}$ and $MnCl_2$. The formation of $Mn_2(CO)_{10}$ was confirmed by single-crystal XRD. The lability of $[Mn(CO)_4Cl]_2$ in *n*-hexane solution and the subsequent disproportion was also observed elsewhere.[40]

Synthesis of NaRhMnO$_x$/SiO$_2$ SSP (3). A solution of **2** (141 mg, 20 mmol) in acetonitrile (3.70 mL) was added to 3.26 g SiO_2 (sieve fraction 100–200 μm) under mixing with a spatula. The addition of the solution was conducted in three steps á 1.23 mL which corresponded to the specific pore volume of the support (0.90 mL/g) according to the incipient wetness impregnation method. After impregnation, the silica-supported precursor was dried under high vacuum for 12 h at room temperature. The pre-catalyst was activated by thermal treatment in flowing 10% H_2/Ar (total flow 500 mL/min). A temperature program in accordance to the TPDe studies (Figure S2) was chosen (Table 1). The final NaRhMnO$_x$/SiO$_2$ catalyst (3) was kept under inert gas atmosphere prior use. Metal loadings by ICP-OES (wt%): 2.21 Rh, 1.34 Mn.

Synthesis of RhMnO$_x$/SiO$_2$ SSP washed (4). The NaRhMnO$_x$/SiO$_2$ SSP catalyst (3) was washed with methanol by a soxhlet extraction. The washed pre-catalyst was dried in high vacuum yielding the final RhMnO$_x$/SiO$_2$ SSP (4). Metal loadings by ICP-OES (wt%): 1.82 Rh, 0.87 Mn.

Synthesis of RhMnO$_x$/SiO$_2$ SSP (5). The final RhMnO$_x$/SiO$_2$ SSP catalyst (5) was synthesized in a similar manner as catalyst **3**. Incipient wetness impregnation of a solution of **7** (252 mg, 0.197 mmol) in 3.6 mL THF on silica (1.36 g) in 3 steps, drying in high vacuum for 12 h at r.t. and activation in flowing 10% H_2/Ar (total flow 500 mL/min) at 260 °C (ramp 5 K/min, holding time 2 h). Metal loadings by ICP-OES (wt%): 2.2 Rh, 0.70 Mn.

Synthesis of RhMnO$_x$/SiO$_2$ reference catalyst (6). The RhMnO$_2$/SiO$_2$ reference catalyst (6) was prepared according a previously reported procedure.[16] A aqueous solution of rhodium(III) nitrate Rh$(NO_3)_3\cdot xH_2O$ and Manganese(II) nitrate $Mn(NO_3)_2\cdot xH_2O$ in water (HPLC grade) was impregnated on silica (pre-treated at 550 °C in air for 6 h). A subsequent calcination in synthetic air at 350 °C was conducted providing the $Rh_2O_3MnO_x/SiO_2$ pre-catalyst. The precatalyst was reduced by H_2 at 265 °C *in-situ* prior the catalyst testing. Metal loadings by ICP-OES (wt%): 2.6 Rh, 1.3 Mn.

Synthesis of [NBnzMe$_3$]$_2$[Rh$_3$Mn$_3$(CO)$_{18}$] (7). Benzyltrimethylammonium chloride [NBnzMe$_3$]Cl (155 mg, 0.835 mmol) was suspended in 15 mL acetone and a solution of Na$_2$[Rh$_3$Mn$_3$(CO)$_{18}$] (2, 133 mg, 0.120 mmol) in 10 mL acetone was added dropwise to the suspension. The suspension was stirred at room temperature for 24 h and filtered through a glass frit. The residue was washed with additional 10 mL of acetone. The combined filtrates were evaporated under vacuum at 45 °C and then dried in vacuum for 12 h. The crude product was washed three times with 5 mL toluene and dissolved in 10 mL THF. Evaporation of the solvent and drying in vacuum overnight led to a tacky compound which was not isolatable. Yield: 71.4 mg, 0.04 mmol, 31.8% (Based on cluster **2**). This material was used for subsequent procedures without further purification. IR (ATR, cm^{-1}): $\nu = 2068$ (w), 2020 (w), 1992 (m), 1958 (m), 1917 (m), 1793 (m). ESI-MS: m/z: calcd for $[M\text{-}NBnzMe_3]^-$: 1071.6, found: 1070.8.

Synthesis of Rh/SiO$_2$ reference catalyst (8). The Rh/SiO$_2$ reference catalyst (8) was prepared in a similar manner as reference catalyst **6**.[16] A aqueous solution of rhodium(III) nitrate $Rh(NO_3)_3\cdot xH_2O$ in water (HPLC grade) was impregnated on silica (pre-treated at 550 °C in air for 6 h). A subsequent calcination in synthetic air was conducted providing the Rh_2O_3/SiO_2 pre-catalyst. The precatalyst was activated *in-situ* prior the catalyst testing. Metal loading by ICP-OES (wt%): 2.8 Rh.

Table 1. Temperature Program of Catalyst Activation.

Step	Temperature [°C]	Holding Time [h]
1	75	4
2	115	4
3	260	1

Acknowledgements

This work was conducted in the framework of the BasCat collaboration between BASF SE, TU Berlin, Fritz Haber Institute of the Max Planck Society, and the Cluster of Excellence UniCat (EXC 314–2; financed by the Deutsche Forschungsgemeinschaft). We thank Dr. Somenath Garai for crystal structure refinement, Dr. Frank Girgsdies for XRD, Shuang Li for XPS measurements, and Stephen Lohr for technical assistance.

Conflict of Interest

The authors declare no conflict of interest.

Keywords: Heterobimetallic Catalysis · Hydrogenation · Rhodium · Manganese · Oxygenates

[1] A. K. Agarwal, *Prog. Energy Combust. Sci.* **2007**, *33*, 233–271.
[2] H. T. Luk, C. Mondelli, D. C. Ferré, J. A. Stewart, J. Pérez-Ramírez, *Chem. Soc. Rev.* **2017**, *46*, 1358–1426.
[3] J. Hill, E. Nelson, D. Tilman, S. Polasky, D. Tiffany, *Proc. Natl. Acad. Sci. USA* **2006**, *103*, 11206–10.
[4] V. Subramani, S. K. Gangwal, *Energy Fuels* **2008**, *22*, 814–839.
[5] M. Z. F. Kamarudin, S. K. Kamarudin, M. S. Masdar, W. R. W. Daud, *Int. J. Hydrogen Energy* **2013**, *38*, 9438–9453.
[6] P. C. Ellgen, M. Bhasin (Union Carbide Corp.), U. S. Patent 4096164A, **1976**.
[7] W. J. Bartley, T. P. Wilson (Union Carbide Corp.), U. S. Patent 4446251A, **1982**.
[8] F. Xue, W. Chen, X. Song, X. Cheng, Y. Ding, *RSC Adv.* **2016**, *6*, 35348–35353.
[9] M. Haider, M. Gogate, R. Davis, *J. Catal.* **2009**, *261*, 9–16.
[10] M. Ojeda, M. L. Granados, S. Rojas, P. Terreros, F. J. Garcia-Garcia, J. L. G. Fierro, *Appl. Catal. A* **2004**, *261*, 47–55.
[11] X. Mo, J. Gao, J. G. Goodwin, *Catal. Today* **2009**, *147*, 139–149.
[12] D. Yu-hua, C. De-An, T. Khi-Rui, *Appl. Catal.* **1987**, *35*, 77–92.
[13] W. Mao, J. Su, Z. Zhang, X.-C. Xu, W. Dai, D. Fu, J. Xu, X. Zhou, Y.-F. Han, *Chem. Eng. Sci.* **2015**, *135*, 312–322.
[14] D. Mei, R. Rousseau, S. M. Kathmann, V.-A. Glezakou, M. H. Engelhard, W. Jiang, C. Wang, M. A. Gerber, J. F. White, D. J. Stevens, *J. Catal.* **2010**, *271*, 325–342.
[15] Y. Choi, P. Liu, *J. Am. Chem. Soc.* **2009**, *131*, 13054–13061.
[16] M. Dimitrakopoulou, X. Huang, J. Kröhnert, D. Teschner, S. Praetz, C. Schlesiger, W. Malzer, C. Janke, E. Schwab, F. Rosowski, H. Kaiser, S. Schunk, R. Schlogl, A. Trunschke, *Faraday Discuss.* **2018**, *208*, 207–225.
[17] C. Panda, P. W. Menezes, M. Driess, *Angew. Chem. Int. Ed.* **2018**, *57*, 11130–11139; *Angew. Chem.* **2018**, *130*, 11298–11308.
[18] A. C. Bray, M. Green, D. R. Hankey, J. A. K. Howard, O. Johnson, F. Gordon, A. Stone, *J. Organomet. Chem.* **1985**, *281*, c12–c16.
[19] D. Braga, F. Grepioni, H. Wadepohl, S. Gebert, M. J. Calhorda, L. F. Veiros, *Organometallics* **1995**, *14*, 5350–5361.
[20] M. L. Aldridge, M. Green, J. A. K. Howard, G. N. Pain, S. J. Porter, F. G. A. Stone, P. Woodward, *J. Chem. Soc. Dalton Trans.* **1982**, 1333.
[21] G. Longoni, M. Manassero, M. Sansoni, *J. Am. Chem. Soc.* **1980**, *102*, 7973–7974.
[22] M. J. Freeman, A. D. Miles, M. Murray, A. Guy Orpen, F. G. a. Stone, *Polyhedron* **1984**, *3*, 1093–1097.
[23] G. Doyle, K. A. Eriksen, D. Van Engen, *J. Am. Chem. Soc.* **1986**, *108*, 445–451.
[24] A. Bott, J. G. Jeffrey, B. F. G. Johnson, J. Lewis, *J. Organomet. Chem.* **1990**, *394*, 533–554.
[25] A. Antiaolo, F. A. Jalon, A. Otero, M. Fajardo, B. Chaudret, F. Lahozd, J. A. Lopezd, **1991**, 1861–1866.
[26] K. O'Connell, J. R. Regalbuto, *Catal. Lett.* **2015**, *145*, 777–783.
[27] X. Ma, H. Deng, M.-M. Yang, W.-X. Li, *J. Chem. Phys.* **2008**, *129*, 244711.
[28] W. Mao, J. Su, Z. Zhang, X. C. Xu, D. Fu, W. Dai, J. Xu, X. Zhou, Y. F. Han, *Chem. Eng. Sci.* **2015**, *135*, 301–311.
[29] J. Liu, R. Tao, Z. Guo, J. R. Regalbuto, C. L. Marshall, R. F. Klie, J. T. Miller, R. J. Meyer, *ChemCatChem* **2013**, *5*, 3665–3672.
[30] G. Chen, C.-Y. Guo, X. Zhang, Z. Huang, G. Yuan, *Fuel Process. Technol.* **2011**, *92*, 456–461.
[31] D. Mei, R. Rousseau, S. M. Kathmann, V.-A. Glezakou, M. H. Engelhard, W. Jiang, C. Wang, M. A. Gerber, J. F. White, D. J. Stevens, *J. Catal.* **2010**, *271*, 325–342.
[32] X. Pan, Z. Fan, W. Chen, Y. Ding, H. Luo, X. Bao, *Nat. Mater.* **2007**, *6*, 507–511.
[33] W. M. H. Sachtler, M. Ichikawa, *J. Phys. Chem.* **1986**, *90*, 4752–4758.
[34] A. Ceriotti, G. Longoni, M. Manassero, M. Sansoni, R. Della Pergola, B. T. Heaton, D. O. Smith, *J. Chem. Soc. Chem. Commun.* **1982**, *3*, 886–887.
[35] G. M. Sheldrick, *Acta Crystallogr. Sect. A Found. Crystallogr.* **2015**, *71*, 3–8.
[36] G. M. Sheldrick, *Acta Crystallogr. Sect. C Struct. Chem.* **2015**, *71*, 3–8.
[37] O. V. Dolomanov, L. J. Bourhis, R. J. Gildea, J. A. K. Howard, H. Puschmann, *J. Appl. Crystallogr.* **2009**, *42*, 339–341.
[38] S. Banerjee, M. K. Karunananda, S. Bagherzadeh, U. Jayarathne, S. R. Parmelee, G. W. Waldhart, N. P. Mankad, *Inorg. Chem.* **2014**, *53*, 11307–15.
[39] E. W. Abel, I. S. Butler, *Trans. Faraday Soc.* **1967**, *63*, 45.
[40] C. H. Bamford, J. W. Burley, M. Coldbeck, *J. Chem. Soc. Dalton Trans.* **1972**, 1846.

Manuscript received: December 4, 2018
Accepted manuscript online: December 6, 2018
Version of record online: January 9, 2019

4.6 Supporting Information

Details of the Crystal Structure Refinement

Table S4.1. Crystal data and structure refinement for $Na_2[Rh_3Mn_3(CO)_{18}]$ (**2**).

Identification code	shelx	
Empirical formula	C42 H48 Mn3 Na2 O24 Rh3	
Formula weight	1456.33	
Temperature	150.00(10) K	
Wavelength	1.54178 Å	
Crystal system	Orthorhombic	
Space group	P n m a	
Unit cell dimensions	a = 15.9667(8) Å	α = 90°
	b = 18.5536(13) Å	β = 90°
	c = 18.6281(17) Å	γ = 90°
Volume	5518.4(7) $Å^3$	
Z	4	
Density (calculated)	1.753 Mg/m^3	
Absorption coefficient	13.343 mm^{-1}	
F(000)	2896	
Crystal size	0.240 x 0.174 x 0.088 mm^3	
Theta range for data collection	3.362 to 66.595°	
Index ranges	-18<=h<=19, -22<=k<=18, -22<=l<=22	
Reflections collected	20153	
Independent reflections	5003 [R(int) = 0.0657]	
Completeness to theta = 66.596°	99.4 %	
Refinement method	Full-matrix least-squares on F^2	
Data / restraints / parameters	5003 / 33 / 337	
Goodness-of-fit on F^2	1.048	
Final R indices [I>2sigma(I)]	R1 = 0.0780, wR2 = 0.2227	
R indices (all data)	R1 = 0.1072, wR2 = 0.2495	
Extinction coefficient	n/a	
Largest diff. peak and hole	0.893 and -1.337 $e.Å^{-3}$	

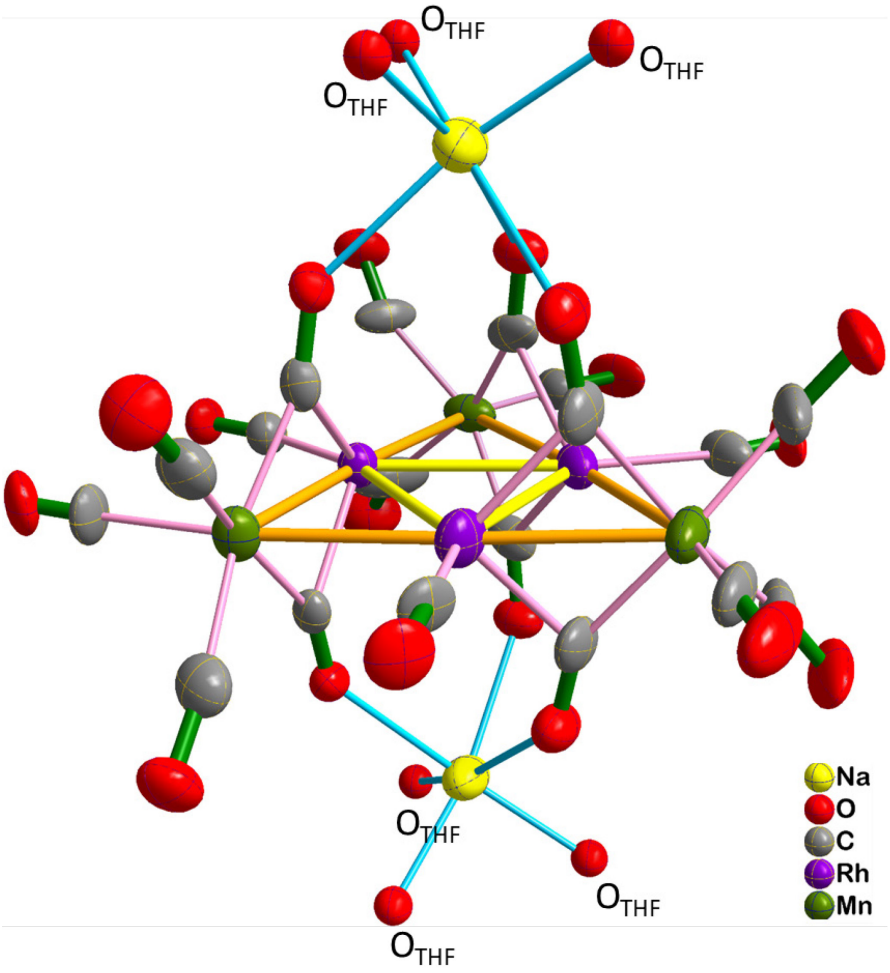

Figure S4.1. Molecular structure of the cluster of **2**. Thermal ellipsoids are drawn at 50 % probability level.

Details of the FTIR Measurements

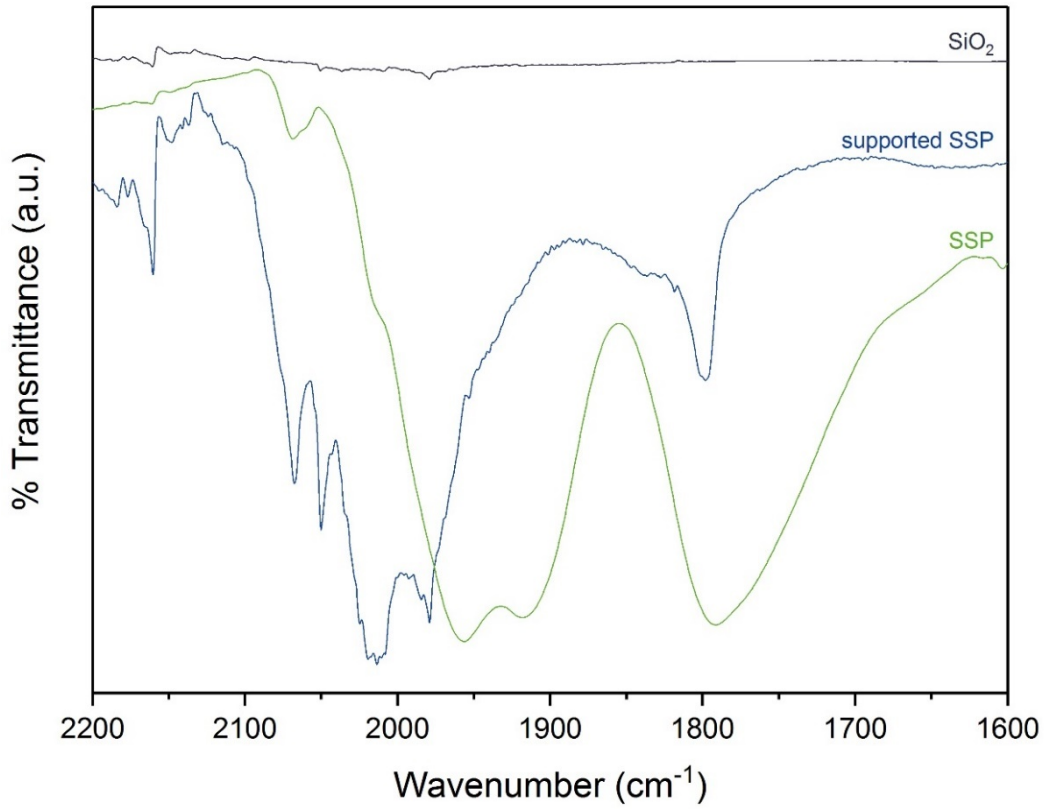

Figure S4.2. FTIR of silica-supported cluster $Na_2[Rh_3Mn_3(CO)_{18}]$ (**2**): The number of CO stretching vibration bands remains the same after impregnation and therefore also the overall symmetry of the cluster **2**. However, the bands of the terminal CO ligands are shifted to higher wavenumber which indicates less electron density at the hexanuclear metal core and a lower π backbonding. This can be explained by the chemisorption of the cluster **2** on the oxide support.

Details of the TPDe Studies

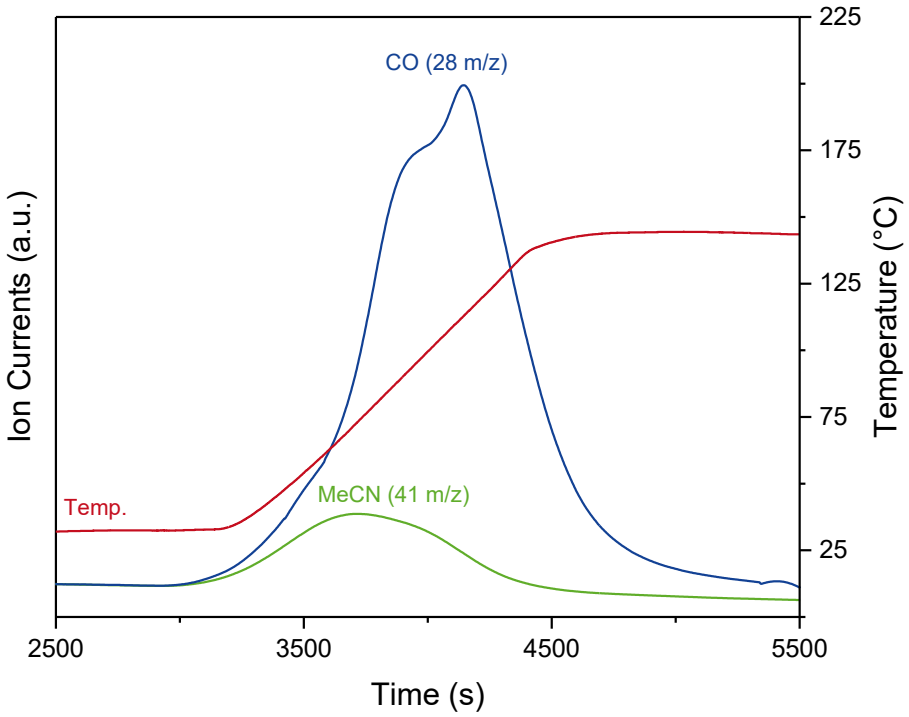

Figure S4.3. TPDe of silica-supported cluster $Na_2[Rh_3Mn_3(CO)_{18}]$ in 10 % H_2/He (2): The decomposition begins at approx. 70 °C (onset decarbonylation temperature) and reaches its first maximum at 96.4 °C which might be attributed to the weaker bonded bridging carbonyl ligands. Whereas the decarbonylation of the terminal CO ligands might lead to a second maximum at 113 °C. No other species were detected by MS with the exception of acetonitrile (41 m/z) which was used for the incipient wetness impregnation.

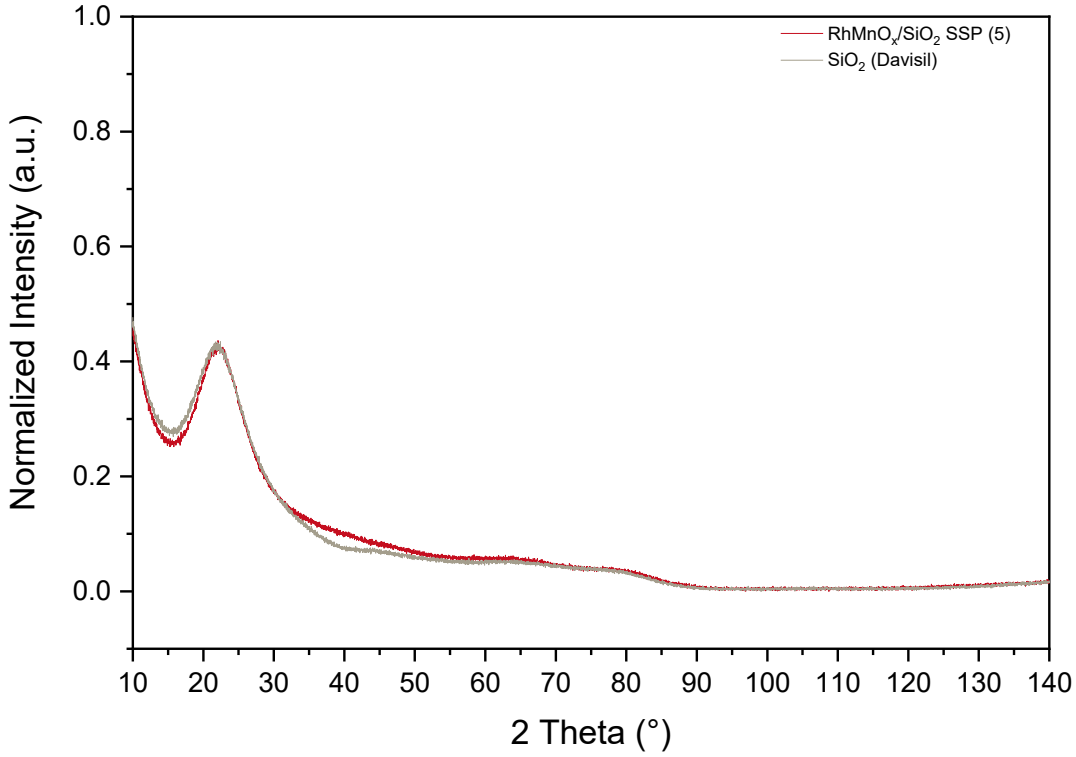

Figure S4.4. XRD raw data of the fresh $RhMnO_x/SiO_2$ SSP catalyst (5, red) in comparison with SiO_2 (Davisil, grey): A small deviation could be observed in the range of $2\theta = 41°$ which might be attributed to Rh(111) phase (40.77°). However, a phase identification cannot be conducted due to the XRD detection limit which is usually taken below a crystallite size of 3 nm. In addition to the (S)TEM images, the majority of the nanoparticles are relatively small and the investigated (S)TEM domains can be considered as representative for the characterized sample.

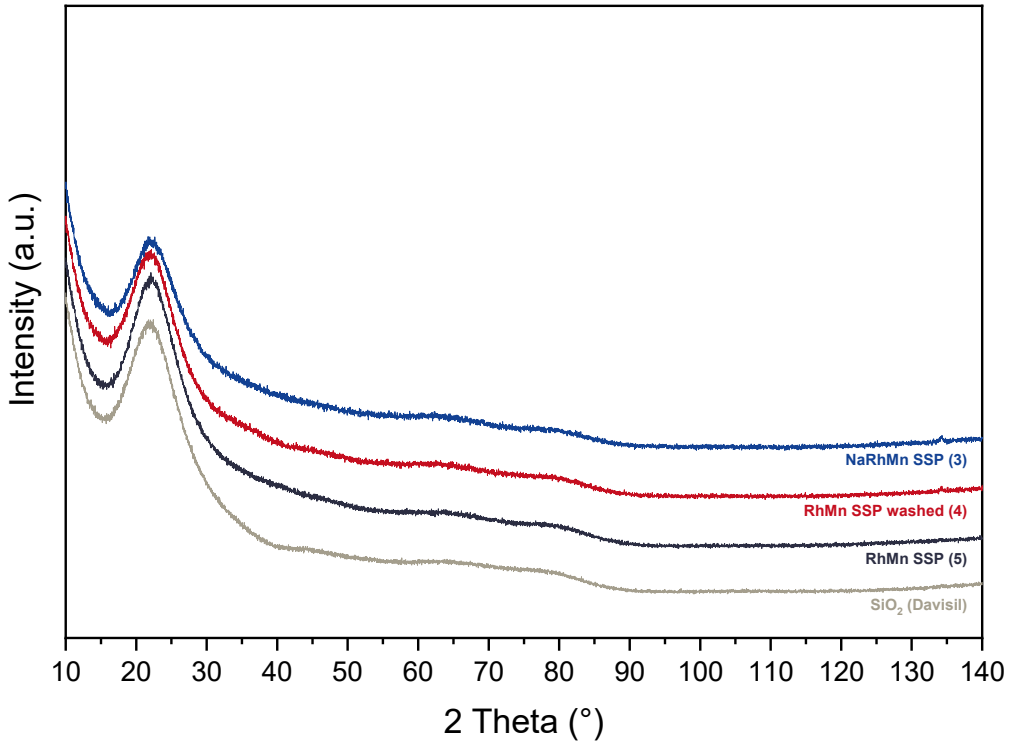

Figure S4.5. XRD raw data of fresh $NaRhMnO_x/SiO_2$ SSP (3, blue), $RhMnO_x/SiO_2$ SSP washed (4, red) and $RhMnO_x/SiO_2$ SSP (5, black) catalysts in comparison with SiO_2 (Davisil, grey).

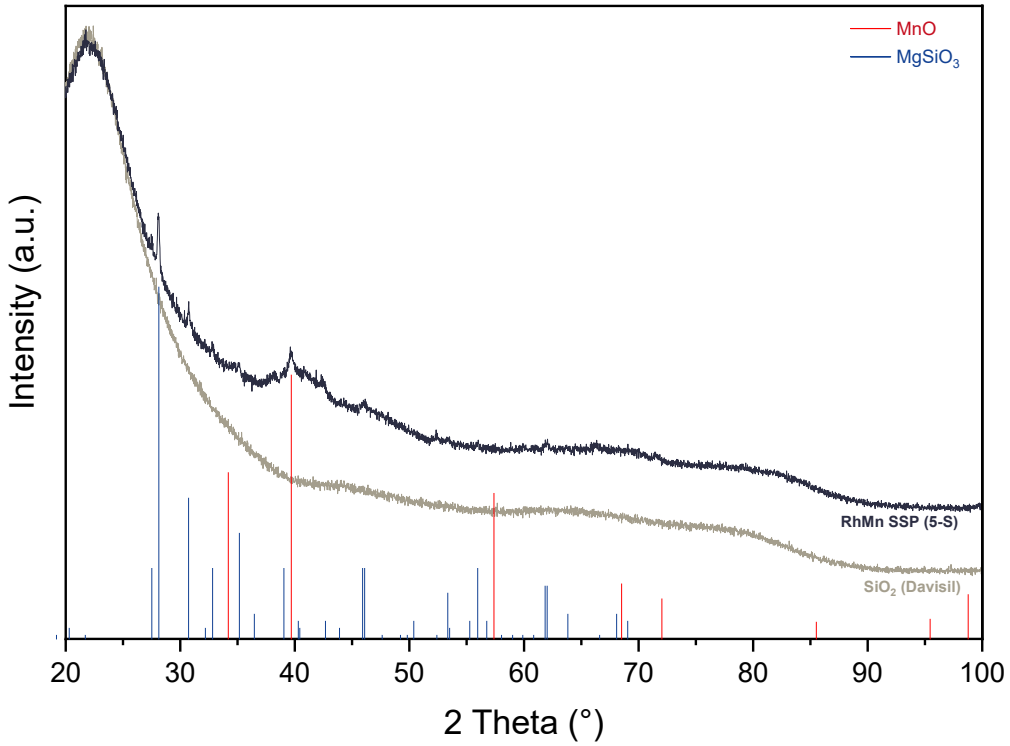

Figure S4.6. XRD raw data of the spent $RhMnO_x/SiO_2$ SSP catalysts (5-S, black) in comparison with SiO_2 (Davisil, grey): The detected diffractogram is in agreement with steatite (ICDD 011-0273) which was used as inert material in the catalytic test (see also the Experimental Section). The remaining reflection at $2\theta = 39.7°$ corresponds to the fcc{200} phase of MnO (ICDD 065-0638).

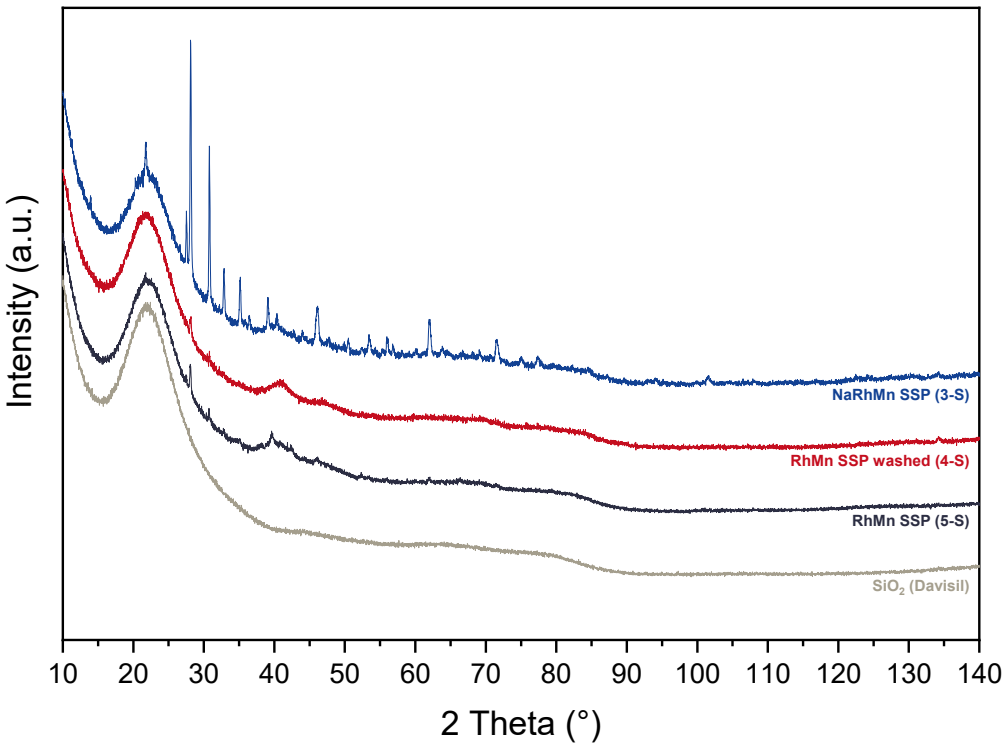

Figure S4.7. XRD raw data of spent $NaRhMnO_x/SiO_2$ SSP (3-S, blue), $RhMnO_x/SiO_2$ SSP washed (4-S, red) and $RhMnO_x/SiO_2$ SSP (5-S, black) catalysts in comparison with SiO_2 (Davisil, grey): Similar to the previously discussed diffractogram (Figure S4.6), the reflections are in agreement with steatite (ICDD 011-0273) which was used as inert material in the catalytic test. The difference in intensity is derived from the amount of steatite that could not be separated from the samples.

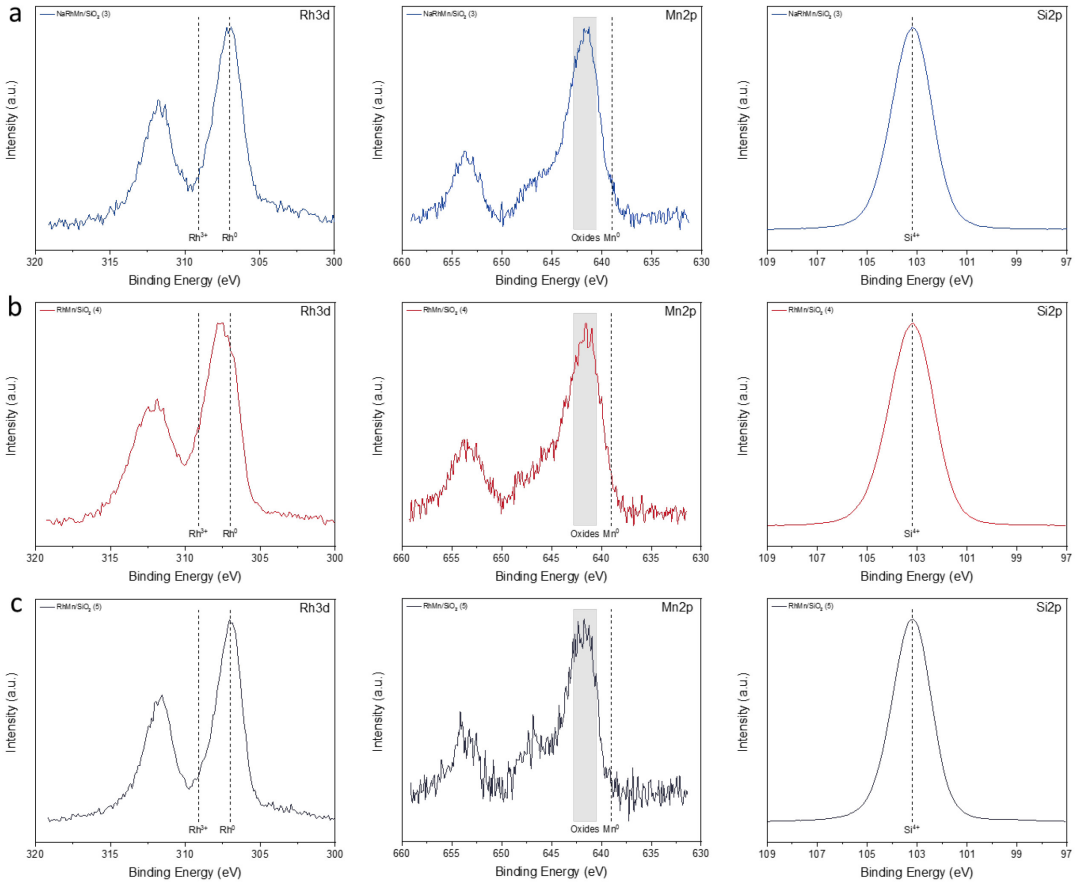

Figure S4.8. XPS data of the fresh (a) $NaRhMnO_x/SiO_2$ SSP (3), (b) $RhMnO_x/SiO_2$ SSP washed (4) and (c) $RhMnO_x/SiO_2$ SSP (5) catalysts: comparison of the Rh3d (left), Mn2p (middle) and Si2p (right) background-corrected spectra. Si2p (103.2 eV) was used as a binding energy reference.[1] All three samples show similar XPS results and the following explanation is consistent for the catalysts **3**-**5**. The electronic structure of rhodium is in agreement with the typical binding energy of metallic rhodium (307.0 eV).[2] An impact of Mn on the electronic structure of Rh is barely visible. Signals for metallic Mn (629.0 eV) in the Mn2p spectra (middle) cannot be found.[3] However, it is clearly visible that Mn is in an oxide state due to the common binding energy range of 641.1–643.4 eV.[4] These findings are in accordance to previously reported XPS data of $RhMnO_x$ catalysts.[5] Si2p was used as a binding energy reference. The catalyst 4 was not handled under an inert gas atmosphere which leads to small shift in Rh^0 binding energy due to a partial oxidation.

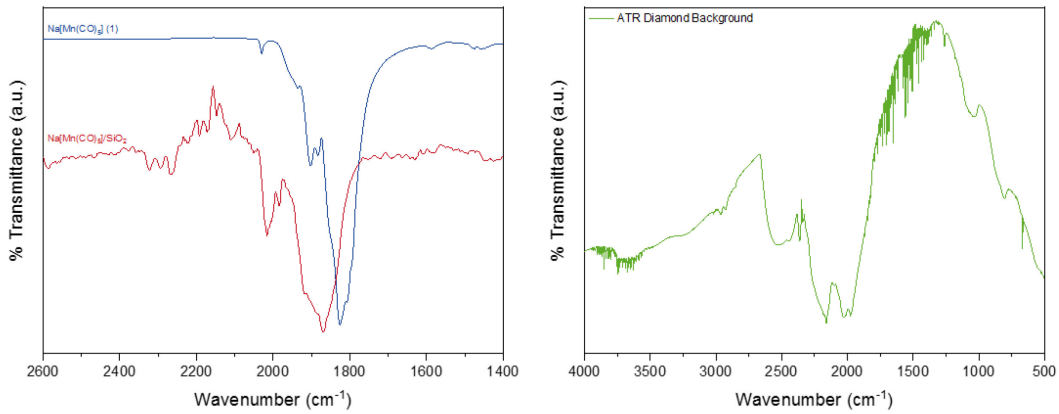

Figure S4.9. ATR-FTIR spectra of $Na[Mn(CO)_5]$ **1** before (red) and after incipient wetness impregnation in acetonitrile on silica (blue). The CO carbonyl stretching vibrations ν_{CO} are clearly shifted to higher wavenumbers implicating a stronger C-O bond accompanied by less electron density at the metal center and less π-back donation. This finding might be a indication for the oxidation of Mn(-I) to Mn(I) by formation of a $Mn^{I}(CO)_x(O_s)_{6-x}$ (x = 2–4) surface species which was also found for MgO-supported $Mn_2(CO)_{10}$.[6,7] The low signal to noise ratio in the supported metalate (red) is affect by the low nominal loading of approx. 6 wt%. The measurement artifact in the range of ν = 2050–2250 cm^{-1} is attributed to the self-absorption of the used diamond ATR crystal and its low intensity in this range (see background spectrum on the left).

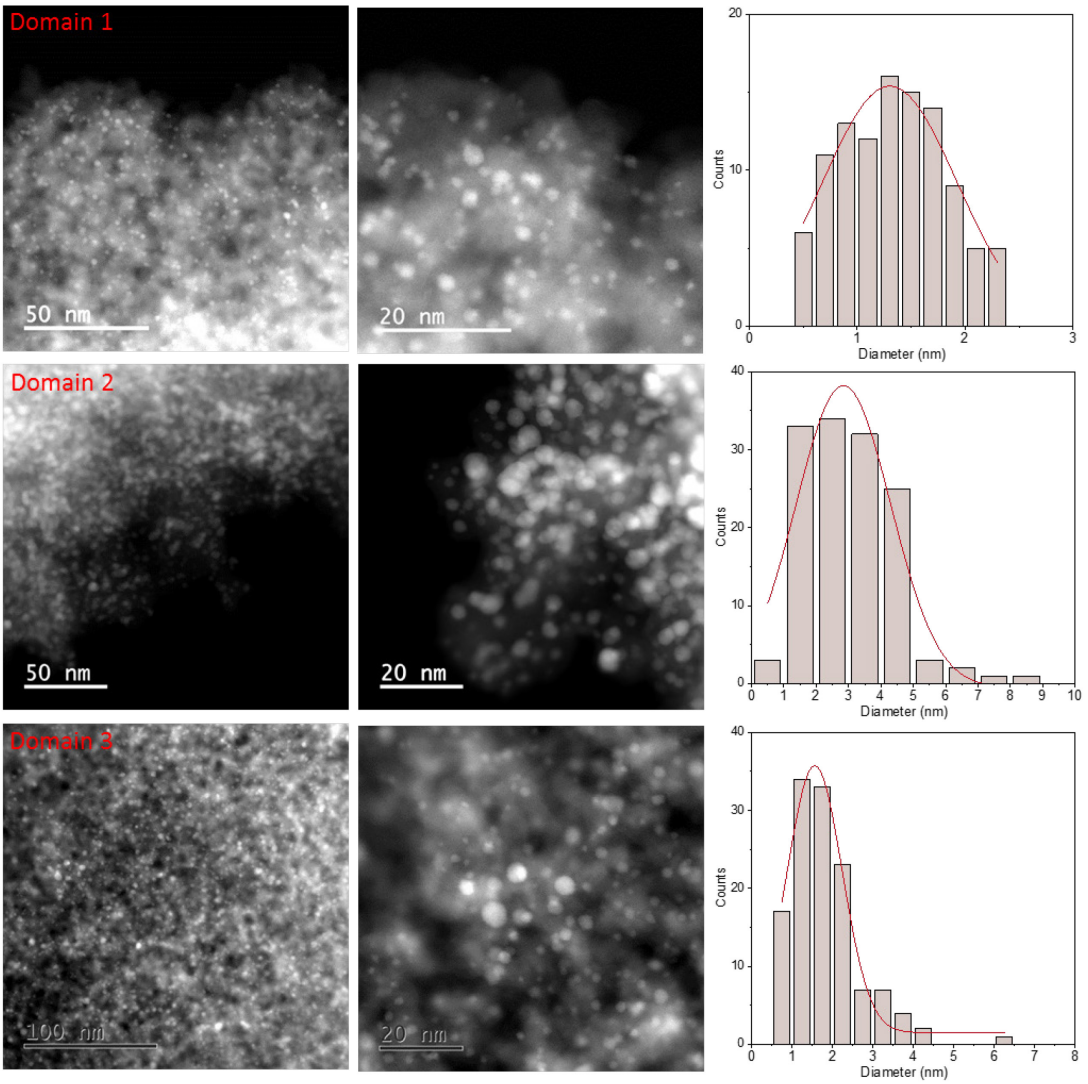

Figure S4.10. Additional ADF-STEM images of the fresh $RhMnO_x/SiO_2$ SSP catalysts (5): homogeneously dispersed nanoparticles with a mean particle size of 1.30, 2.80, and 1.55 nm and a narrow particle size distribution in domain 1, 2, and 3, respectively.

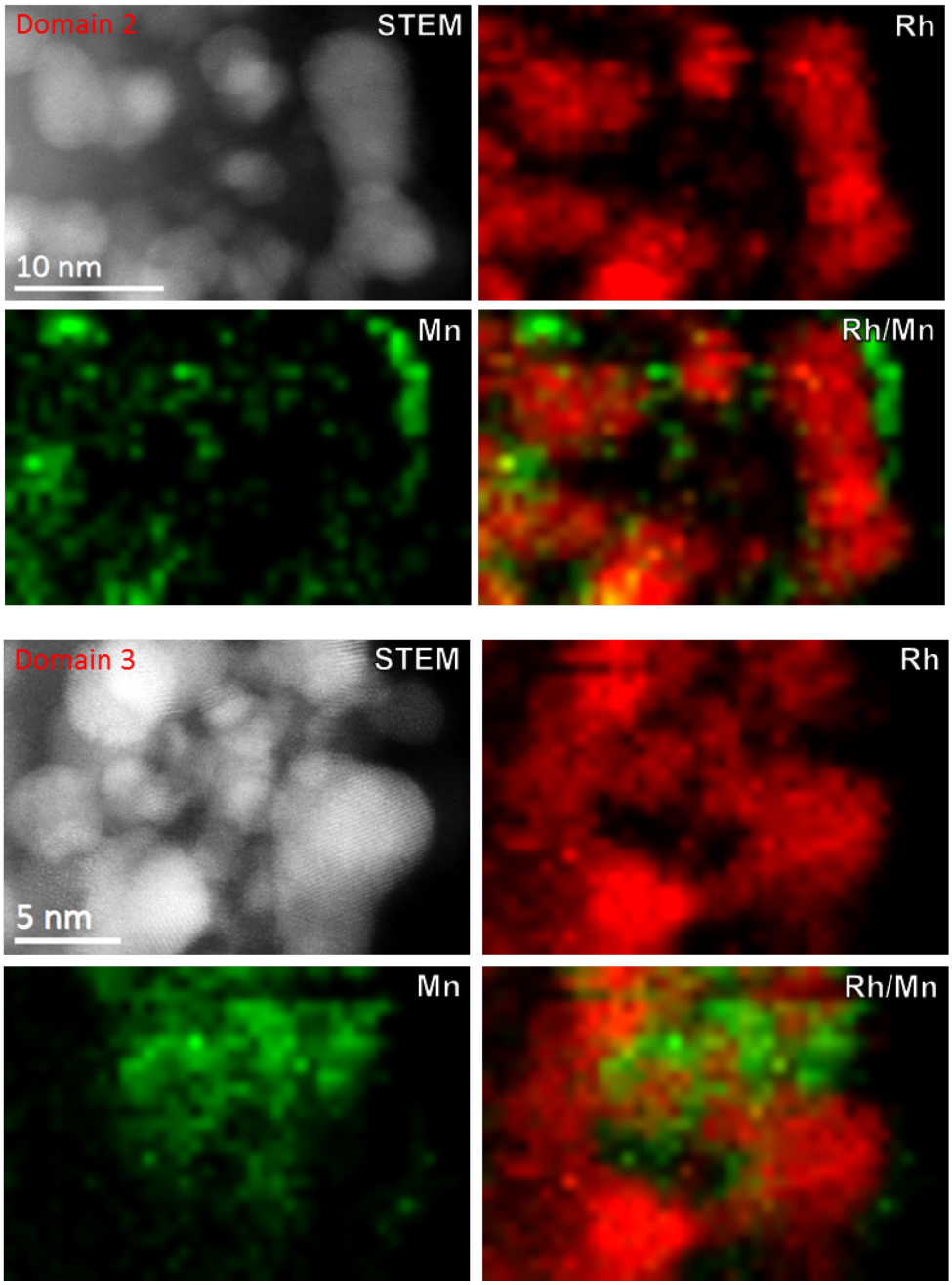

Figure S4.11. Additional composition analyses of the fresh $RhMnO_x/SiO_2$ SSP catalyst (5) by ADF-STEM with EDX mapping: Small particles of metallic rhodium (red) are closely contacted to a MnO_x species (green). No separated MnO_x or Rh nanoparticles could be found.

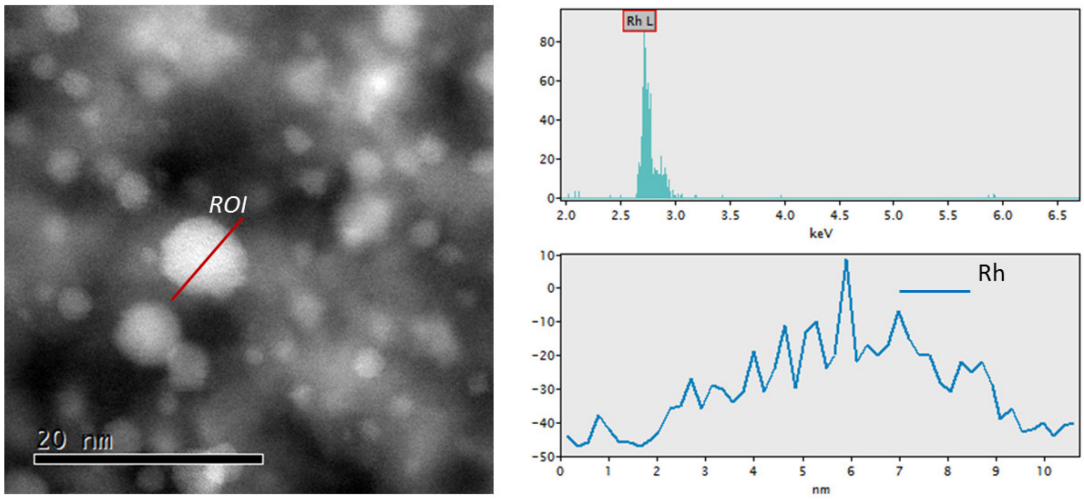

Figure S4.12. EDX line-scan profile of the fresh $RhMnO_x/SiO_2$ SSP catalyst (5).

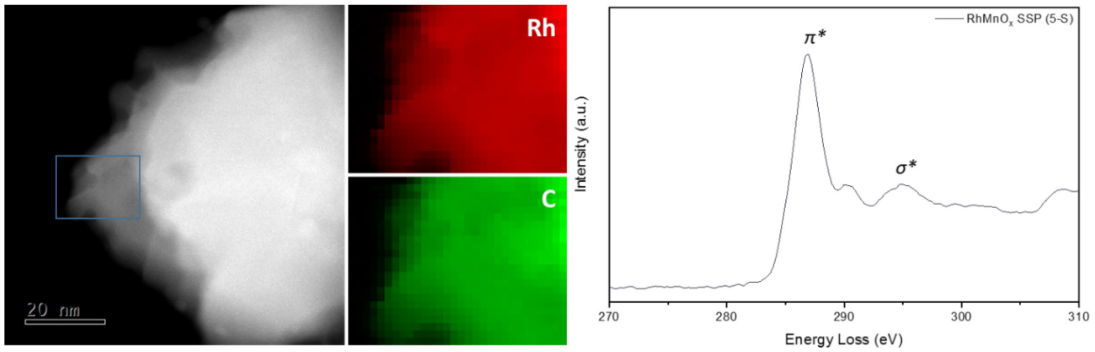

Figure S4.13. HAADF-STEM images of a sintered particle in the spent $RhMnO_x/SiO_2$ SSP catalyst (5-S) and the corresponding EELS spectrum with the carbon K edge fine structure of rhodium carbide: A sharp peak at 286.85 eV is observed corresponding to the excitations of 1s electrons to unoccupied π^* states. In addition, a broad band near 295 eV is attributed to the excitations to σ^* states.[8] The EELS spectrum resembles the spectra of metallic carbides and it is therefore assumed that a rhodium carbide RhC_x has been formed.[9] This assumption is in accordance to the clearly visible overlap of the Rh and C signals in the EELS maps.

Scheme of the Proposed Tilted Adsorption

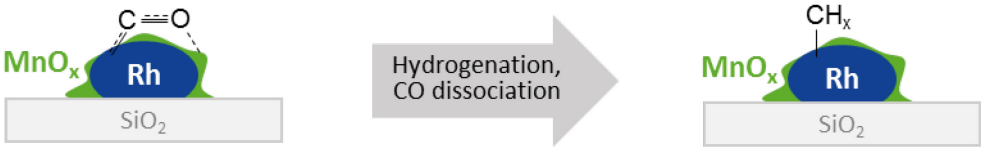

Scheme S1. Proposed adsorption of CO at the $RhMnO_x$ interface in a tilted manner with a C atom bonded to Rh and the O atom bonded to MnO_x.[10]

Details of the Long-Term Stability Tests

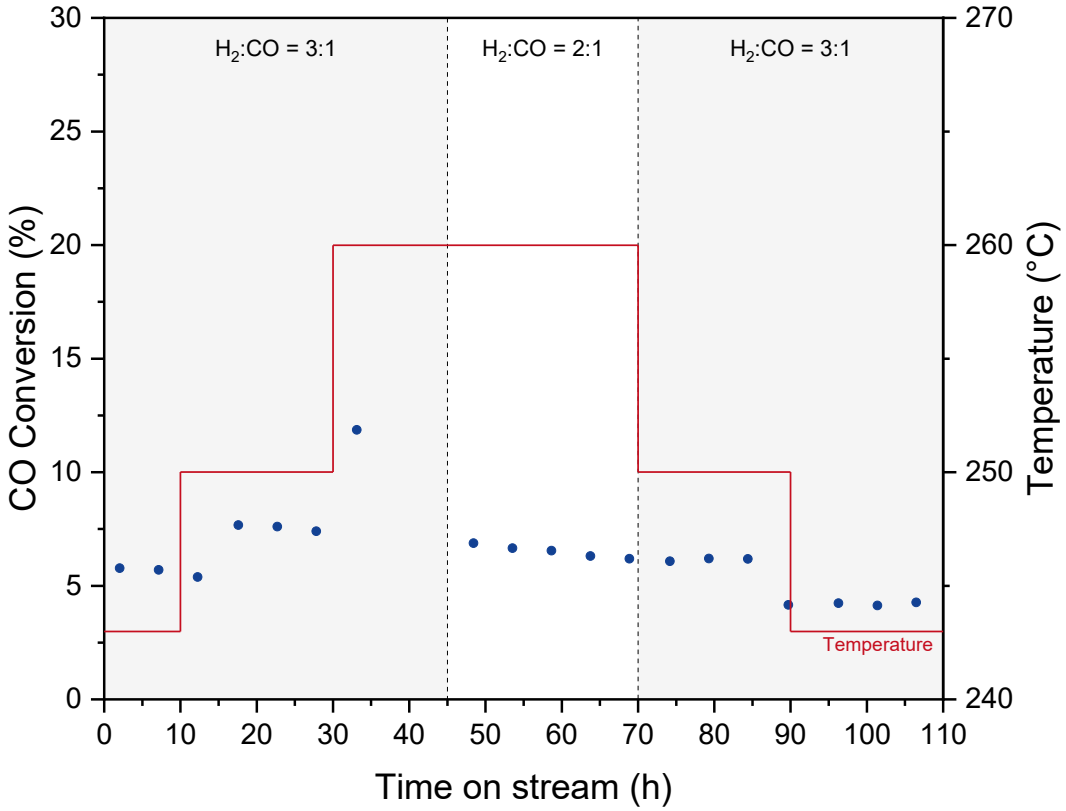

Figure S4.14. Long-term stability of the $NaRhMnO_x/SiO_2$ (3) SSP catalyst: Only a slightly deactivation can be observed after 105 h time-on-stream. Measuring conditions: 243–260 °C, 54 bar, GHSV 3500 h^{-1}.

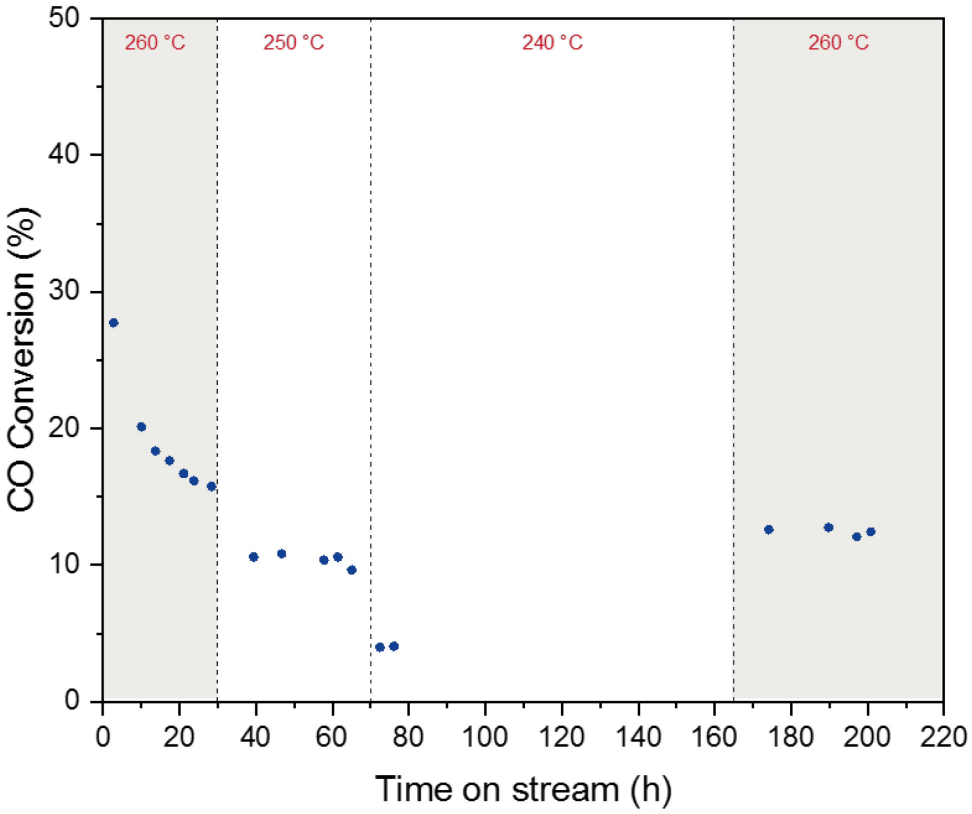

Figure S4.15. Long-term stability of the $RhMnO_x/SiO_2$ (5) SSP catalyst: In the first 20 h TOS, an initial decrease in CO conversion can be observed. After this initial phase, the catalyst is quite stable and shows only a slightly deactivation after additional 200 h TOS. Measuring conditions: 243–260 °C, 54.0 bar, $p(H_2)$ = 32.4 bar, p(CO) = 10.8 bar, GHSV 3500 h^{-1}.

Table of the Product Selectivities, Yields and Space Time Yields

Table S4.2. Catalytic activity and product selectivities of catalysts **3**–**6**, **8**, and a literature example.

Entry	Sample[a]	T (°C)	X_{CO} (%)	S_{CH_4} (%)	S_{MeOH} (%)	S_{EtOH} (%)	$S_{C_{2+}\,Oxy}$[b] (%)	$S_{C_{2+}\,HC}$ (%)	$S_{Olefins}$ (%)	Y_{EtOH} (%)	STY_{EtOH}[c] (µg/mg$_{Rh}$/s)
1	NaRhMnO$_x$/SiO$_2$ SSP (3)	260	11.9	37.1	8.70	19.5	45.9	5.32	2.93	2.32	0.60
2	RhMnO$_x$/SiO$_2$ SSP washed (4)	260	17.0	41.1	9.20	19.6	36.9	8.77	3.53	3.33	1.24
3	RhMnO$_x$/SiO$_2$ SSP (5)	260	17.5	37.7	0.20	24.1	52.0	7.96	3.56	4.22	1.06
4	RhMnO$_x$/SiO$_2$ Ref. (6)	250	17.9	44.8	4.78	15.7	40.5	9.96	3.61	2.81	0.58
5	RhMnO$_x$/SiO$_2$ Lit.[59]	270	17.0	39.2	0.8	17.7	46.0	13.2	-	3.01	-[d]
6	Rh/SiO$_2$ Ref. (8)	260	4.78	59.8	0.70	6.54	31.8	6.49	1.12	0.31	0.08
7	RhMnO$_x$/SiO$_2$ SSP (5)	260	27.7	39.5	0.66	23.6	52.0	6.43	1.01	6.54	1.64

[a]The catalysts were compared at iso-conversion (entry 1-5) after an initial deactivation phase. For catalysts **5**, the selectivity pattern is also provided at the highest measured conversion before deactivation (entry 7). Measuring conditions for tested catalysts **3**–**6**, and **8**: 250–260 °C, 54.0 bar, p(H_2) = 32.4 bar, p(CO) = 10.8 bar, GHSV = 3500 h^{-1}; for literature-known catalyst:[11] 270 °C, 30.0 bar, p(H_2) = 18 bar, p(CO) = 9 bar, GHSV = 4000 h^{-1}. [b]Mainly including ethanol, acetaldehyde and acetic acid. [c]Space time yield of ethanol calculated with the ethanol formation rate divided by active mass Rh (ICP-OES). [d]STYs per active mass Rh were not provided in the mentioned reference. They could not be calculated due to a lack of information (catalyst volume, flow rates, etc.) and may not comparable as a higher reaction temperature was used.

4.7 References of Supporting Information

(1) Alexander, M. R.; Short, R. D.; Jones, F. R.; Stollenwerk, M.; Zabold, J.; Michaeli, W. An X-Ray Photoelectron Spectroscopic Investigation into the Chemical Structure of Deposits Formed from Hexamethyldisiloxane/ Oxygen Plasmas. J. Mater. Sci. 1996, 31 (7), 1879–1885.

(2) Okamoto, Y.; Ishida, N.; Imanaka, T.; Teranishi, S. ChemInform Abstract: Active States of Rhodium in Rhodium Exchanged Y Zeolite Catalysts for Hydrogenation of Ethylene and Acetylene and Dimerization of Ethylene Studied with X-ray Photoelectron Spectroscopy. *Chem. Inform.* **1979**, *10* (35).

(3) Chourasia, A. R.; Chopra, D. R. Elemental Manganese Studied by X-ray Photoemission Spectroscopy Using Mg and Zr Radiations. Surf. Sci. Spectra 1994, 3 (1), 74–81.

(4) V. Naumkin, A.; Kraut-Vass, A.; Gaarenstroom, S. W.; Powell, C. J. NIST X-ray Photoelectron Spectroscopy Database, NIST Standard Reference Database Number 20.

(5) Dimitrakopoulou, M.; Huang, X.; Kröhnert, J.; Teschner, D.; Praetz, S.; Schlesiger, C.; Malzer, W.; Janke, C.; Schwab, E.; Rosowski, F.; Kaiser, H.; Schunk, S.; Schlögl, R.; Trunschke, A. Insights into Structure and Dynamics of (Mn,Fe)O_x-Promoted Rh Nanoparticles. Faraday Discuss. 2018, 208, 207–225.

(6) Keyes, M. P.; Gron, L. U.; Watters, K. L. Interactions of Nickel and Manganese Carbonyls with Oxide Surfaces: Formation of Reduced, Oxidized, and Zerovalent Metal Species. Inorg. Chem. 1989, 28 (7), 1236–1242.

(7) Khabuanchalad, S.; Wittayakun, J.; Lobo-Lapidus, R. J.; Stoll, S.; Britt, R. D.; Gates, B. C. Formation of MgO-Supported Manganese Carbonyl Complexes by Chemisorption of $Mn(CO)_5CH_3$. Langmuir 2013, 29 (21), 6279–6286.

(8) Alvarado Rupflin, L.; Mormul, J.; Lejkowski, M.; Titlbach, S.; Papp, R.; Gläser, R.; Dimitrakopoulou, M.; Huang, X.; Trunschke, A.; Willinger, M. G.; Schlögl, R.; Rosowski, F.; Schunk, S. A. Platinum Group Metal Phosphides as Heterogeneous Catalysts for the Gas-Phase Hydroformylation of Small Olefins. ACS Catal. 2017, 7 (5), 3584–3590.

(9) Jin, Y.; Xu, H.; Datye, A. K. Electron Energy Loss Spectroscopy (EELS) of Iron Fischer-Tropsch Catalysts. Microsc. Microanal. 2006, 12 (2), 124–134.

(10) Mao, W.; Su, J.; Zhang, Z.; Xu, X. C.; Fu, D.; Dai, W.; Xu, J.; Zhou, X.; Han, Y. F. A Mechanistic Basis for the Effects of Mn Loading on C_{2+} Oxygenates Synthesis Directly from Syngas over Rh-MnO_x/SiO_2 Catalysts. Chem. Eng. Sci. 2015, 135, 301–311.

(11) Mao, W.; Su, J.; Zhang, Z.; Xu, X.-C.; Dai, W.; Fu, D.; Xu, J.; Zhou, X.; Han, Y.-F. Kinetics Study of C_{2+} Oxygenates Synthesis from Syngas over Rh–MnO_x/SiO_2 Catalysts. Chem. Eng. Sci. 2015, 135, 312–322.

5 Paper 3: Tuning the Rh-FeO_x Interface in Ethanol Synthesis through Formation Phase Studies at High Pressures of Synthesis Gas (accepted version)

Phil Preikschas, Milivoj Plodinec, Julia Bauer, Ralph Kraehnert,
Raoul Naumann d'Alnoncourt, Robert Schlögl, Matthias Driess, and Frank Rosowski

ACS Catal. **2021**, *11* (7), 4047–4060. DOI: 10.1021/acscatal.0c05365.

Abstract: As-prepared materials tested for a catalytic reaction are usually only pre-catalysts that become active and/or selective under specific conditions. During this initial formation phase, catalysts can undergo a change in their structure, morphology, chemical state, or even composition. This dynamic behavior has a vital impact on reactivity, and we identified that this initial formation phase is also critical for Rh in the catalytic conversion of synthesis gas to oxygenates and ethanol in particular. The syngas-to-ethanol reaction (StE) is a promising alternative route to ethanol from fossil and non-fossil carbon resources. Despite heavy research efforts, rates and selectivities still need to be improved for industrial operations. For this reason, structure-function relationships at industrially relevant reaction conditions must be clarified. Although some *in situ* and *operando* studies have been reported, a pressure gap still exists between experimental and process-relevant high-pressure conditions. To overcome this pressure gap and investigate the dynamic behavior of Rh-based catalysts under reaction conditions, we applied a generic method for formation phase studies at high partial pressures of synthesis gas where standard *operando* methods are inapplicable. Combining integral and local characterization methods before and after a long-term catalytic test of a $RhFeO_x/SiO_2$ catalyst (>140 h on stream) allowed us to ascribe a drastic decrease in ethanol formation to a structural change from an unalloyed $RhFeO_x$ to an alloyed $RhFe/FeO_x$ nanostructure. Our investigation provides an explanation for the great variation of reported catalytic results of RhFe catalysts and their nanostructures in synthesis gas conversion. The structure-function relationship we identified finally provides the opportunity for improved catalyst design strategies: stabilizing the Rh-FeO_x interface by preventing RhFe nanoalloy formation. As one example, we report a $RhFeO_x$ catalyst on a high surface area Mn_2O_3 support which decreases the Fe mobility and reducibility through the formation of a $(Fe,Mn)O_x$ mixed surface oxide. Stabilizing the Rh-FeO_x interface finally led to stable ethanol selectivity, and the formation of RhFe nanoalloy structures was not observed.

5.1 Introduction

Heterogeneous catalysts often change their properties during chemical transformations under common reaction conditions such as medium to high temperatures and elevated pressures. This change in catalyst structure, morphology, composition, and chemical state affects their reactivity and stability over time.[1–3] Knowledge of catalytic behavior under process-relevant conditions is not only crucial for a fundamental understanding of promoter effects and reaction mechanisms, it is also important for estimating catalyst lifetime, which in turn is key to operating industrial-scale facilities in a resource- and cost-efficient manner.[4] In this context, predicting and designing an efficient catalyst is not possible when considering peak performance marks only. Long-term catalytic tests need to identify changes encountered in the stability and reactivity of catalysts. Neglecting this crucial aspect might lead to converse or incomparable catalytic results for similar catalyst systems, e.g., significant variation in selectivity patterns of pure Rh/SiO_2 catalysts in CO hydrogenation.[5]

One way to overcome these issues are *in situ* and/or *operando* experiments, which often provide desired insights into the properties of working catalysts under relevant conditions, such as identification of titled carbonyl species on Rh/SiO_2 samples that are probable precursors for hydrogen-assisted CO dissociation in the conversion of synthesis gas to oxygenates.[6] However, those *in situ* or *operando* investigations can be challenging when a process under high pressures is studied, and a pressure gap still exists between experimental and industrially relevant conditions.[7] Specifically, spectroscopic investigations are difficult at high CO partial pressures as gas-phase CO interferes with adsorbed carbonyl species. Common workarounds to minimize the void volume require cell designs that prohibit homogeneous heat and mass distribution within the cell.[7–10] As a consequence, many reported *in situ* studies were performed under ambient pressure conditions. Conclusions drawn from those studies should be regarded with caution when correlated with catalyst reactivity under high pressure reaction conditions.

When *in situ* or *operando* investigations are inaccessible or inapplicable, the detailed characterization of a catalytic material prior to and after catalytic reaction can yield meaningful information as reported for the deactivation of Pd catalysts through the disintegration of particles into single atoms.[11] In this case, it is apparent that the materials investigated need to be activated under the same conditions as in the catalytic process since the as-prepared materials are usually only pre-catalysts that become active under these specific conditions.[4] Moreover, all catalysts have to be handled under a protective atmosphere or, in the case of as-prepared materials, should be activated *in situ* prior to characterization.

For example, syngas (CO/H_2) conversion reactions are often difficult to investigate with *in situ* and *operando* techniques because the applied reaction conditions usually involve high pressures and atmospheres with high CO content.[7] However, syngas as alternative feedstock for the production of base chemicals is becoming increasingly interesting in light of growing climate and carbon management concerns. The production of ethanol is a good example of this transition. To date, ethanol is produced primarily by fermentation from corn or sugarcane. However, growing demand for synthetic ethanol as a fuel or fuel additive requires alternative, more scalable production routes.

The direct synthesis of ethanol from synthesis gas has been studied extensively but ethanol yields still need to be improved for industrial application.[12–14] As Rh-based catalysts have shown the most promising results, several promoter screenings were conducted in which Fe, Mn, and Li were shown to be the most-effective.[12] Accordingly, supported $Rh(Mn,Fe)O_x$ materials rank among the best catalysts in terms of ethanol yield in CO hydrogenation. Although a wide range of catalysts has been tested, the intrinsic reaction mechanism is still elusive and the role of promoters is unclear due to the complexity of the multi-promoted catalyst systems and the above-mentioned inapplicability of standard *operando* methods.[15–17] To combat this complexity and further improve these multi-promoted Rh-based catalysts, an in-depth understanding of the respective single-promoted $RhMnO_x$ and $RhFeO_x$ systems is needed.

In case of single-promoted $RhMnO_x$ systems, it is widely accepted that the superior reactivity is based on close proximity between Rh and MnO_x through strong metal-promoter interactions.[12,18–20] Although the formation of a RhMn nanoalloy structure was initially proposed, the actual nanostructure of $RhMnO_x$ catalysts has been found to consist of metallic Rh particles decorated with an amorphous MnO_x phase.[20] Furthermore, we demonstrated in a previous publication that not even the use of $Na_2[Rh_3Mn_3(CO)_{18}]$ as a molecular precursor with both metals in low oxidation states and predefined metal-metal bonds led to the formation of a RhMn nanoalloy.[21]

In contrast, the nanostructure of $RhFeO_x$ catalysts is still under debate and the proposed structural models vary from unalloyed $RhFeO_x$ over core-shell to nanoalloyed RhFe structures.[6,22–30] Likewise, the formation of oxygenate products varies significantly on similar catalyst systems, resulting in reported methanol selectivities ranging from 0–13.5 % and ethanol selectivities from 8–35 %. According to Haider and co-workers, the addition of Fe leads to an increased selectivity towards ethanol by stabilizing $Rh^+(CO)_2$ sites on unalloyed $RhFeO_x$ catalysts, which promotes CO insertion.[22] In contrast, Hartman *et al.* stated that RhFe nanoalloyed structures reduce tilted carbonyl species at the surface, thus enhancing CO insertion and selectivity towards ethanol.[6] However, Mo and co-workers ascribe higher selectivities towards methane and methanol to the modification of Rh-based catalysts with Fe and only a small improvement in EtOH

selectivity was observed.[28] Although several structural models have been proposed, a systematic investigation of the impact of time on stream under relevant reaction conditions has not been performed to the best of our knowledge.

Herein, we report a generic method for formation phase studies at high partial pressure of synthesis gas. We identified this formation phase to be critical for the conversion of synthesis gas to ethanol and observed a significant change in oxygenate selectivity. Combining integral and local characterization methods before and after this long-term catalytic study (>140 h on stream) allowed us to ascribe this dynamic behavior to a structural change from an unalloyed Rh–FeO_x to an alloyed RhFe/FeO_x nanostructure (Scheme 5.1, top). In this study, we propose an explanation for the great variation of reported catalytic results of Fe-promoted Rh catalysts in CO hydrogenation. The structure-function relationship we identified finally provides the opportunity for improved catalyst design strategies. As one example, we report a $RhFeO_x$ catalyst on a novel high surface area Mn_2O_3 support[31] which prevents RhFe alloying through formation of a $(Fe,Mn)O_x$ mixed surface oxide (Scheme 5.1, bottom).

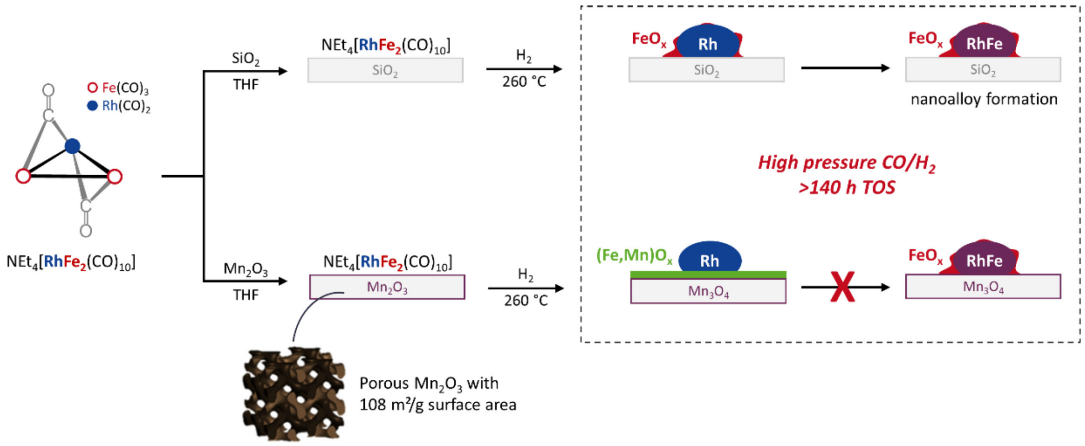

Scheme 5.1. Synthesis of $RhFeO_x$ model catalysts over a single-source precursor approach: using $NEt_4[RhFe_2(CO)_{10}]$ as single-source precursor (SSP) leads to a well-defined, unalloyed $RhFeO_x/SiO_2$ model catalyst (top). During the critical formation phase in CO hydrogenation, the catalyst undergoes a structural transformation from an unalloyed $RhFeO_x$ to an alloyed RhFe/FeO_x nanostructure accompanied by a significant change in oxygenate selectivity. The same SSP approach on a high surface area Mn_2O_3 support leads to a Rh/$(Fe,Mn)O_x$ catalyst (bottom). The formation of $(Fe,Mn)O_x$ mixed surface oxides prevents RhFe nanoalloy formation.

5.2 Experimental Section

General considerations. All manipulations involving air and moisture sensitive organometallic compounds were carried out under an atmosphere of dry, oxygen-free argon by using standard Schlenk techniques or glove boxes (MBraun LABmaster Pro) under a purified nitrogen or argon atmosphere. The solvents were taken from a solvent purification system (MBraun SPS-800) or purified using conventional procedures, freshly distilled under argon atmosphere, and degassed prior to use. NMR spectra were recorded on a Bruker AvanceIII (1H: 700 MHz, 13C: 125 MHz) spectrometer and referenced to residual solvent signal as internal standards (tetrahydrofuran-d_8: δH = 1.72 ppm, δC = 25.3 ppm). IR spectrum was recorded on a Nicolet iS5 spectrometer inside a glove box. Mass spectrum was recorded using HR-ESI-MS-method on a LTQ Orbitrap XL spectrometer. The mass fractions of C, H, N, and S were determined on a Thermo Finnigan FlashEA 1112 Organic Elemental Analyzer. The starting material $NEt_4[FeH(CO)_4]$ was synthesized according to a known literature procedure.[32] SiO_2 (Davisil grade 635) was preheated at 100 °C under vacuum overnight before use. All other reagents were used as received.

Synthesis of $NEt_4[RhFe_2(CO)_{10}]$. $NEt_4[FeH(CO)_4]$ (3.27 g, 10.9 mmol) was dissolved in 30 mL tetrahydrofuran (THF) and a solution of $[Rh(CO)_2Cl]_2$ (1.23 g, 3.18 mmol) in THF (40 mL) was added dropwise. Stirring at r.t. overnight resulted in the precipitation of a colorless solid. The residue was washed with addition of 20 mL THF, and the combined filtrates were evaporated under vacuum overnight leading to a black powder. Yield: 2.98 g, 4.77 mmol, 43.7 % (based on $NEt_4[FeH(CO)_4]$). Elemental analysis (%): calcd. for $C_{18}H_{20}NO_{10}Fe_2Rh$: C, 34.6; H, 3.23; N, 2.24; found: C, 34.9; H, 3.55; N, 2.16. HR-ESI-MS (m/z): calcd. for $[M\text{-}NEt_4]^-$: 494.72, found: 494.73. ^{1}H NMR (700 MHz, THF-d_8, 298 K, ppm): δ = 1.35 (t, CH_3), 3.35 (q, CH_2). ^{13}C{^{1}H} NMR (125 MHz, THF-d_8, 298 K, ppm): δ = 6.58 (s, *C*H$_3$), 52.1 (s, *C*H$_2$), 216 (m, *C*O). IR (ATR, cm^{-1}): ν = 2055 (m), 1994 (w), 1974 (m), 1908 (s), 1870 (s).

Synthesis of carbonyl-derived $RhFeO_x/SiO_2$. A solution of $NEt_4[RhFe_2(CO)_{10}]$ (0.236 g, 0.377 mmol) in THF (3.63 mL) was added to 1.35 g SiO_2 under mixing with a spatula inside a glove box. The addition of the solution was conducted in three steps á 1.21 mL, which corresponds to the specific pore volume of the support (0.90 mL/g) according to the incipient wetness impregnation method. After each impregnation step, the silica-supported precursor was dried under high vacuum for 12 h at room temperature. The pre-catalyst was reduced by thermal treatment in flowing 10 % H_2/Ar (total flow 500 mL/min) at 260 °C (T ramp 10 K/min) for 2 h. The final $RhFeO_x/SiO_2$ catalyst was kept under an inert gas atmosphere prior to use. Metal loadings by ICP-OES (wt%): 2.53 Rh, 2.01 Fe. Elemental analysis after catalysis (wt%): 1.57 C, 0.48 H, 0.00 N.

Synthesis of carbonyl-derived Rh/(Fe,Mn)O_x. The Rh/(Fe,Mn)O_x was synthesized by a similar procedure as described for $RhFeO_x/SiO_2$. High surface area Mn_3O_4 (2.48 g) was impregnated with a solution of $NEt_4[RhFe_2(CO)_{10}]$ (0.234 g, 0.374 mmol) in THF (3.63 mL). The pre-catalyst was reduced by thermal treatment in flowing 10 % H_2/Ar (total flow 500 mL/min) at 260 °C (T ramp 10 K/min) for 2 h. The final Rh/(Fe,Mn)O_x catalyst was kept under an inert gas atmosphere prior to use. Metal loadings by ICP-OES (wt%): 1.14 Rh, 1.04 Fe. Elemental analysis (wt%): before catalysis: 0.16 C, 0.18 H, 0.00 N; after catalysis: 1.53 C, 0.12 H, 0.00 N.

Synthesis of carbonyl-derived Rh/SiO_2 reference materials. A solution of $Rh_4(CO)_{12}$ (70.6 mg, 94.4 µmol) in DCM (3.69 mL) was impregnated on SiO_2 (1.36 g). The pre-catalyst was activated by thermal treatment in flowing 10 % H_2/Ar (total flow 500 mL/min) at 260 °C (T ramp 10 K/min) for 2 h. The final Rh/SiO_2 catalyst was kept under an inert gas atmosphere prior to use. Metal loadings by ICP-OES (wt%): 2.11 Rh.

Synthesis of FeO_x/SiO_2 reference materials. An aqueous solution of iron(III) nitrate $Fe(NO_3)_3$ was impregnated on silica (pretreated at 550 °C in air for 6 h). A subsequent calcination in synthetic air at 300 °C was conducted providing the FeO_x/SiO_2 pre-catalyst. The pre-catalyst was reduced in 5 % H_2/N_2 at 265 °C (1 h) *in situ* prior the catalyst testing. Metal loadings by ICP-OES (wt%): 2.7 Fe.

Elemental analyses. Determination of mass fractions of carbon, hydrogen, nitrogen and sulfur were carried out on a Thermo Finnigan FlashEA 1112 Organic Elemental Analyzer. Air- or moisture sensitive samples were prepared in silver capsules inside a glove box.

Powder X-ray diffraction (XRD). XRD measurements were performed in Bragg-Brentano geometry on a D8 Advance II theta/theta diffractometer (Bruker AXS), using Ni-filtered Cu $K\alpha_{1,2}$ radiation and a position sensitive energy dispersive LynxEye silicon strip detector. The sample powder was filled into the recess of a cup-shaped sample holder, the surface of the powder bed being flush with the sample holder edge (front loading).

High-resolution transmission electron microscopy (HRTEM), scanning transmission electron microscopy (STEM) in combination with electron energy loss spectroscopy (EELS) and energy-dispersive X-ray spectroscopy (EDX). The samples were investigated on a double aberration-corrected JEOL JEM-ARM200CF transmission electron microscope. The microscope is equipped with a large-angle silicon drift EDX detector with the solid angle of 0.7 steradians from a detection area of 100 mm^2 and Gatan GIF Quantum 965, that allow EDX and EELS measurements, respectively. For HRTEM imaging, a Gatan OneView 4K x 4K CMOS camera was used.

Overview STEM, STEM-EDX, and particle size distributions. Overview STEM was conducted on a FEI Talos F200X microscope. The microscope was operated at an

acceleration voltage of 200 kV. STEM-EDX elemental maps were recorded by a Super-X system including four silicon drift detectors. Background-corrected and fitted intensities were used for image visualization. All samples were prepared on holey carbon-coated copper grids (Plano GmbH, 400 mesh). Particle size distributions were determined by measuring of at least 250 particles with three different domains by using ImageJ software[33].

X-ray photoelectron spectroscopy (XPS). XPS was measured on K-Alpha™ + X-ray Photoelectron Spectrometer (XPS) System (Thermo Scientific), with Hemispheric 180° dual-focus analyzer with 128-channel detector. X-ray monochromator is Micro focused Al-Kα radiation. For the measurement, the as-prepared samples were directly loaded onto the sample holder for measurement. The data was collected with an X-ray spot size of 200 μm, 20 scans for survey, and 50 scans for regions.

Moessbauer Spectroscopy. Zero-field Moessbauer spectra were recorded on a SEECO MS6 spectrometer that comprises the following instruments: a JANIS CCS-850 cryostat, including a CTI-CRYOGENICS closed cycle 10 K refrigerator and a CTI-CRYOGENICS 8200 helium compressor. The cold head and sample mount are equipped with calibrated DT-670-Cu-1.4L silicon diode temperature probes and heaters. The temperature was controlled by a LAKESHORE 335 temperature controller. Spectra were recorded using an LND-45431 Kr gas proportional counter with beryllium window connected to the SEECO W204 γ-ray spectrometer that includes a high voltage supply, a 10 bit and 5 μs ADC and two single channel analyzers. Motor control and recording of spectra was taken care of by the W304 resonant γ-ray spectrometer. For the reported spectra, a RIVERTEC MCO7.114 source (^{57}Co in Rh matrix) with an activity of about 1 GBq was used. All spectra were recorded as solids in a plastic sample-holder at 13 K and data were accumulated for about 72 hours. Isomeric shifts are referenced to α-iron at room temperature.

In situ **CO chemisorption diffuse reflectance infrared Fourier transform spectroscopy (CO-DRIFTS).** CO-DRIFTS measurements were conducted using Agilent Cary 680 and Thermo Fisher Nicolet iS50 FTIR spectrometers with MCT detectors. About 50 mg of sample was packed into a Harrick Praying Mantis low temperature reaction chamber ($RhFeO_x/SiO_2$ and $RhFe/FeO_x/SiO_2$) or a Harrick Praying Mantis high temperature reaction chamber (Rh/SiO_2) mounted in Harrick Praying Mantis diffuse reflectance attachments. $RhFeO_x/SiO_2$ and Rh/SiO_2 were reduced *in situ* at 260 °C in 10 % H_2/Ar for 2 h. $RhFe/FeO_x/SiO_2$ spent sample was mounted inside a glove box and transferred to the spectrometer under Ar atmosphere. For CO chemisorption experiments, the reaction chambers were purged with Ar (20 mL/min) at room temperature for 30 min to acquire baseline spectra. 20 mL/min of 10 % CO/Ar was then introduced for 15 min for complete CO chemisorption. The samples were again purged

with pure Ar (20 mL/min), and final DRIFTS spectra were acquired at a spectral resolution of 2 cm^{-1} and an accumulation of 128 scans.

Catalytic testing for synthesis gas conversion. The catalytic testing of the syngas-to-ethanol reaction was performed in a four-fold parallel testing unit. 0.5 g (~1 mL) of catalyst with a particle size of 100-200 µm were loaded into each stainless-steel reactor with an effective inner diameter of 6.25 mm. The reaction temperature was monitored by temperature sensors with three thermocouples along the catalyst bed.

Four mass flow controllers were used to adjust the flow rates of the inlet gases N_2 (99.999%), CO (99.997%), H_2 (99.999%), and Ar (99.999%, all Air Liquide). The CO feed line was equipped with a carbonyl trap to remove all metal carbonyls that might be formed by high pressure of CO in contact with stainless steel. The carbonyl trap consisted of a U-shaped ½" stainless steel tube filled with Al_2O_3 and heated to 170 °C by a heating sleeve.

Compounds in the effluent gas that condense below 180 °C were removed by a coalescence filter in the downstream oven. All remaining compounds in the effluent gas were analyzed with an online gas chromatograph (Agilent 7890B) equipped with two thermal conductivity detectors (TCD) and one flame ionization detector (FID) using He as the carrier gas. TCDs detect the inlet gases H_2, Ar, N_2, and CO as well as methane, CO_2, and H_2O. The FID is used to detect a large variety of paraffins, olefins, and oxygenates (alcohols, acetaldehyde, acetic acid) with a combination of a Porabond Q and an RTX-Wax column. The carbon balance was 96–102% for all measurements.

The catalysts were reduced *in situ* at 54 bar, 265 °C with 5 % H_2 in N_2 for 1 h with a volume flow of 58.3 mL min^{-1}. Subsequently, the temperature was decreased to 243 °C and synthesis gas feedstock mixture containing CO:H_2:N_2:Ar (20:60:10:10%, v:v) was admitted. The volume flow was kept constant to achieve a GHSV of 3500 h^{-1}. The temperature was increased to 260 °C in three steps and subsequently decreased in the same manner. Each step was held constant for at least 15 h to allow the catalysts to equilibrate.

The obtained concentrations of all compounds were corrected for volume changes due to the reaction and the subsequent N_2 dilution. Therefore, the mole fraction of Ar was used as inert internal standard according to Equation (1).

$$x_{i,corrected} = x_{i,GC} \cdot \frac{x_{Ar,bypass}}{x_{Ar,reactor}} \quad (1)$$

$x_{i,corrected}$ is the corrected mole fraction of compound i. $x_{i,reactor}$, and $x_{i,bypass}$ are the mole fractions of compound i originally obtained by the gas chromatograph sampling the respective reactor or the bypass line.

Carbon monoxide conversion X_{CO} was calculated based on the sum of carbon numbers in all products (Equation 2).

$$X_{CO} = \frac{\sum n_j C_j}{n_{CO,0}} \quad (2)$$

$n_{CO,0}$ is the mole fraction of CO in the inlet gas, and C_i is the carbon number of the product *i*. The selectivity *S* for each product *i* was determined based on the number of C atoms by Equation 3.

$$S_i = \frac{n_i C_i}{\sum n_{i,j} C_{i,j}} \quad (3)$$

5.3 Results and Discussion

In the following, we describe the synthesis and characterization of a well-defined, freshly reduced $RhFeO_x/SiO_2$ model catalyst. The sample was strictly handled under a protective atmosphere to avoid any changes to its structure or chemical state during characterization. The reduced $RhFeO_x/SiO_2$ material was then tested for the direct conversion of synthesis gas to ethanol. The long-term stability of the $RhFeO_x/SiO_2$ catalyst is discussed, including the critical formation phase. A thorough characterization of the spent catalyst finally leads to clarification of a structure-function relationship, which is further proved through the synthesis of a more stable $Rh/(Fe,Mn)O_x$ catalyst achieved by decreasing Fe mobility.

5.3.1 Synthesis and Characterization of $RhFeO_x/SiO_2$ Model Catalyst

A single-source precursor (SSP) approach was chosen for the synthesis of a uniform $RhFeO_x/SiO_2$ model catalyst (Scheme 5.1). This approach provides a well-defined metal-metal ratio and close proximity of both metals on an atomic level by using a SSP with pre-defined metal-metal bonds.[21] In this study, a solution of the literature-known $NEt_4[RhFe_2(CO)_{10}]$ carbonyl cluster in tetrahydrofuran was impregnated *via* the incipient wetness method on Davisil (grade 635), a commercially available silica with a BET surface area of 480 m^2/g.[34] The silica-supported $NEt_4[RhFe_2(CO)_{10}]$ cluster was handled under a protective atmosphere and finally transferred into an active catalyst by thermal treatment in 10 % H_2/Ar at 260 °C. The final catalyst has a molar Rh:Fe ratio of 1:2 with nominal mass loadings of 2.8 and 3.0 wt%, respectively. Other Rh:Fe ratios can easily be attained by choosing a different SSP, e.g. $[Rh_4Fe_2(CO)_{16}]^{2-}$ or $[Rh_4Fe(CO)_{15}]^-$,[34] or by follow-up treatments in the form of surface-mediated synthesis.[35,36] The as-prepared catalyst was characterized by a combination of integral characterization methods such as XRD, Moessbauer, and CO-DRIFTS as well as local methods like HRTEM, STEM combined with EDX and EELS.

Sample overview on high-angle annular dark-field (HAADF) STEM images show relatively small nanoparticles homogenously distributed over the silica support (Figure 5.1b). Particle sizes of a large set of particles from three different sample areas were measured and used to determine particle size distribution (see *Experimental Details*). The mean particle size is about 1.7 nm with a narrow distribution reflected in a small standard deviation of 0.3 nm (Figure 5.1d).

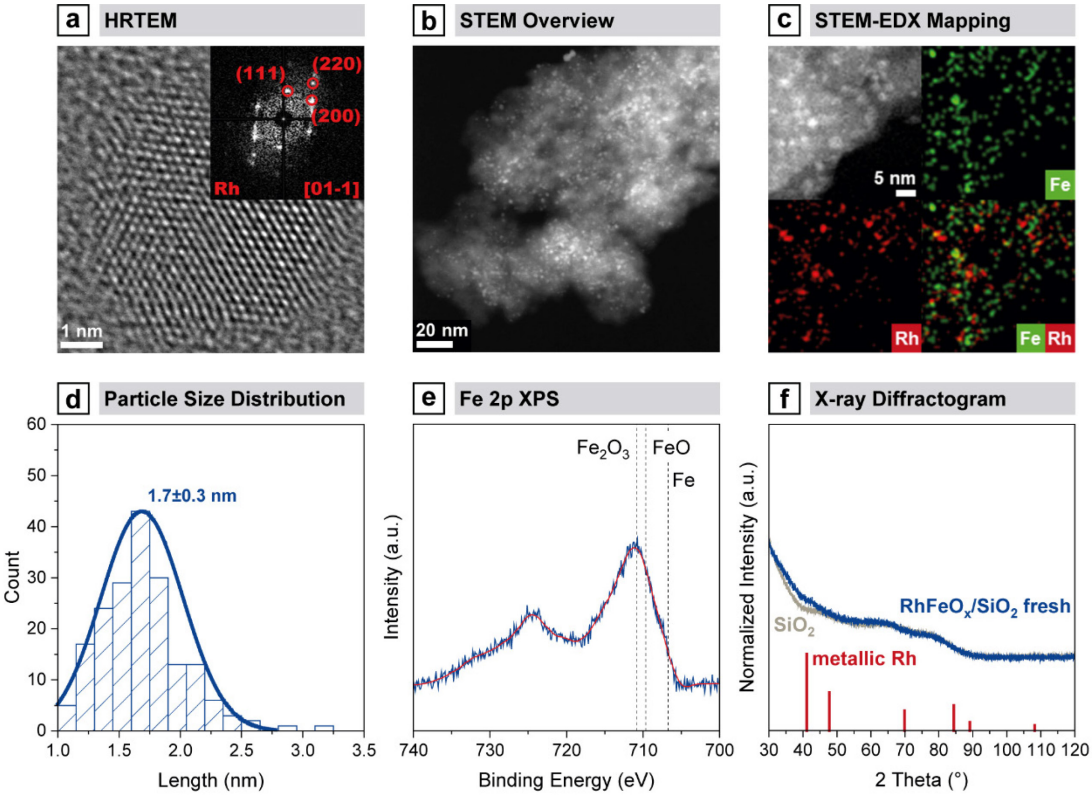

Figure 5.1. Structural and chemical characterization of fresh $RhFeO_x/SiO_2$ catalyst after H_2 activation at 260 °C: (a) HRTEM micrograph of relevant Rh nanoparticle viewed along [01-1] zone-axis and corresponding Fast Fourier transformation (FFT) as an inset. The evaluated *d*-spacings are matched to fcc structure of metallic Rh; (b) HAADF-STEM overview image with corresponding (c) superposition of STEM-EDX maps of Rh L and Fe K. Individual maps of all components and respective EDX spectrum are given in the Supporting Information; (d) particle size distribution of fresh catalyst; (e) Fe 2p XPS spectra after H_2 activation; (f) X-ray diffractogram (blue) compared to SiO_2 support (grey). Rh (red, C5-685) reference was taken from ICDD database.

XRD was performed for phase identification of the as-synthesized $RhFeO_x/SiO_2$ catalyst. No sharp reflections could be identified due to the XRD detection limit of supported crystallites below 3 nm (Figure 5.1f).[37] By comparing the diffractograms of $RhFeO_x/SiO_2$ and Davisil, a small deviation in the region of $2\theta = 41°$ is visible which might be attributable to the Rh(111) phase at $2\theta = 40.8°$.

For the reason of the insufficient phase identification based on XRD investigations, lattice fringe analyses were performed on high-resolution transmission electron microscopy (HRTEM) images of size-representative crystalline particles (Figure 5.1a). For these investigations, the sample was handled under an inert atmosphere and transferred to the microscope by using a vacuum transfer holder. This procedure prevents oxidation of the sample and ensures that the sample investigated is in the same oxidation state as was before catalytic testing.

The indicated lattice fringes with *d*-spacings of 2.2 and 1.9 Å are consistent with face centered cubic (fcc) {111} and {200} planes of metallic Rh (space group of Fm-3m). Metallic Fe or crystalline FeO_x particles were not observed during HRTEM imaging. This

leads to the conclusion that Fe is mostly present as an amorphous oxide phase. This is also supported by XRD data where crystalline FeO_x or metallic Fe phases were not found.

The Fe oxidation state was determined by XPS without contact to an oxidative atmosphere. The $RhFeO_x/SiO_2$ sample shows the typical spin-orbit splitting in the Fe 2p spectrum with a peak maximum for the Fe $2p_{3/2}$ binding energy of 711.1 eV (Figure 5.1e). This binding energy shift is typical for oxidized Fe (709.3–711.6 eV). Mossbauer spectroscopy under an inert atmosphere was conducted for an extended investigation of the Fe oxidation state. A combination of two doublets is visible, which is consistent with Fe^{2+} and Fe^{3+} doublets in reported FeO_x/SiO_2 and $RhFeO_x/SiO_2$ samples (Figure S5.1a).[38]

HAADF-STEM imaging combined with EDX was used to investigate the distribution of Rh and FeO_x as well as the chemical composition of the catalyst. Metallic Rh particles are in close proximity to an amorphous FeO_x phase as shown in the representative superimposed EDX mapping of Rh and Fe (Figure 5.1c; for single-element maps of all components see Figure S5.2). Areas in which their colors mix indicate the Rh-FeO_x interface as a result of their overlapping EDX signals. This finding is further supported by other investigated areas (Figure S5.3a-d). Although the majority of particles remain small, some larger particles are found in HRTEM analysis. These particles occur as an alloyed structure after the H_2 treatment at 260 °C for 2 h (Figure S5.4). It is apparent that these crystalline nanoparticles reflect a minority as no corresponding reflections could be observed in XRD (Figure 5.1f). Evidence of a few larger alloyed RhFe nanoparticles suggests that the alloy formation is induced by migration of Fe on a support.

5.3.2 Reactivity of $RhFeO_x/SiO_2$ Catalyst

The as-prepared $RhFeO_x/SiO_2$ material was tested as a catalyst for the direct conversion of StE in a fixed-bed parallel test setup at common reaction conditions for syngas chemistry (GHSV = 3500 h^{-1}, p = 54.0 bar, and T = 243–260 °C). The catalyst was compared with monometallic Rh/SiO_2 and FeO_x/SiO_2 materials at 250 and 260 °C (Table 5.1, entries 1–5). Modification of Rh/SiO_2 with Fe leads to increased CO conversion and enhanced selectivity towards alcohols, mainly methanol (MeOH) and ethanol (EtOH). The product distribution reported in Table 5.1 reveals that the increased alcohol selectivity is accompanied by the suppression of methane and C_{2+} hydrocarbon (C_{2+} HC) selectivities. Likewise, $RhFeO_x/SiO_2$ is less selective towards C_{2+} oxygenates, mainly acetaldehyde (AcH) and acetic acid (AcOH), as compared to the monometallic Rh/SiO_2 reference. It is consequently assumed that Fe facilitates the fast hydrogenation of acetaldehyde towards ethanol and prevents a further reaction to acetic acid. This assumption is consistent with a previously reported study about RhFe catalysts.[23]

Table 5.1. CO Conversion and Product Selectivity from Syngas Conversion on Reference and Rh-based Catalysts[a]

#	Sample	Precursor	T (°C)	H_2/CO	TOS (h)	r_{CO} (μmol/s/g_{Rh})	X_{CO} (%)	Product Selectivities (%)							
								CH_4	MeOH	EtOH	AcH	AcOH	C_{2+} Oxy	C_{2+} HCs	CO_2
1	Rh/SiO_2	$Rh_4(CO)_{12}$	250	3	72	22.8	2.7	49.9	2.7	6.9	8.2	14.0	4.4	11.9	2.0
2			260	3	101	27.3	3.2	52.7	3.3	7.6	6.8	12.4	4.1	11.3	1.7
3	FeO_x/SiO_2[d]	$Fe(NO_3)_3$	320	2	209	6.82	3.0	49.2	0.0	0.0	0.0	1.6	0.0	39.5	9.3
4	$RhFeO_x/SiO_2$	$[RhFe_2(CO)_{11}]^-$	243	3	7	72.8	14.2	31.2	30.4	31.6	1.9	0.0	0.4	1.7	2.7
5			250	3	37	88.8	17.4	29.8	43.7	19.7	0.4	0.0	0.7	2.1	3.7
6			260	3	71	119.4	23.4	30.8	48.2	15.0	0.2	0.0	0.6	1.8	3.4
7			250	3	104	80.6	15.8	24.9	60.8	10.8	0.0	0.3	0.4	1.1	1.7
8			243	3	122	63.3	12.4	22.3	65.6	9.5	0.0	0.8	0.4	0.9	0.4
9	Rh/MnO_x	$Rh(NO_3)_3$	243	3	44	11.1	3.3	28.5	5.7	18.1	5.1	4.2	6.8	15.5	16.2
10			243	2	20	16.7	2.2	28.0	5.4	14.3	5.9	4.2	6.4	16.9	18.9
11			250	3	105	17.5	5.1	25.2	5.1	20.2	4.2	4.0	7.0	16.1	18.3
12	$Rh/(Fe,Mn)O_x$	$[RhFe_2(CO)_{11}]^-$	243	3	6	30.7	6.8	39.8	7.02	16.0	3.8	0.1	2.2	4.1	26.9
13			250	3	39	43.9	9.7	28.7	11.6	20.9	2.8	2.1	0.4	2.4	31.2
14			260	3	72	72.9	16.2	24.7	13.0	21.3	1.2	0.7	2.0	2.0	35.2
15			250	3	106	31.9	7.1	21.6	16.5	22.2	1.3	0.0	0.3	2.8	35.4
16			243	3	123	19.4	4.3	20.4	18.9	22.1	1.3	0.0	1.2	1.6	34.5

[a]Reaction conditions: 54.0 bar, $p(H_2)$ = 32.4 bar, $p(CO)$ = 10.8 bar, GHSV = 3500 h^{-1}. Product formation rates, selectivities at H_2/CO ratio of 2 and selectivities on CO_2-free basis are provided in the Support Information. [b]C_{2+} oxy includes alcohols, aldehydes, acetates, and acids. [c]C_{2+} HCs includes alkanes and alkenes. [d]Monometallic FeO_x/SiO_2 material was measured at different reaction conditions due to its low activity.

The overall oxygenate selectivity of 62.0 % is significantly higher than for other reported Fe-promoted Rh catalysts. According to a recent review, the $RhFeO_x/SiO_2$ catalyst is among the most selective Rh-based catalysts.[12] The molecular single-source precursor approach is thus an effective synthesis route towards more uniform model catalysts.

The FeO_x/SiO_2 reference shows negligible oxygenate selectivity. The main products are methane and higher hydrocarbons as expected for a typical Fischer-Tropsch catalyst with a Flory-Schulz distribution.[39] Furthermore, FeO_x/SiO_2 demonstrates water-gas shift activity resulting in a CO_2 selectivity of 9.3 %. As known from previous reports, higher Fe oxides are reduced to lower Fe oxides or metallic Fe during catalytic conversion of CO/H_2O to CO_2/H_2.[40] As a consequence, selectivity towards CO_2 can be considered as an indication for the amount of "free" FeO_x on the catalyst support. The $RhFeO_x/SiO_2$ catalyst is likewise water-gas shift active with a selectivity towards CO_2 of 2.7 %. For this reason, Fe might be in an oxidized state and accessible for CO conversion. This finding is in accordance with the characterization of the as-prepared $RhFeO_x/SiO_2$ catalyst where it was shown that Fe is not alloyed with Rh.

5.3.3 Formation Phase and Long-Term Catalytic Studies of $RhFeO_x/SiO_2$ Catalyst

The $RhFeO_x/SiO_2$ catalyst shows only a slight deactivation from 72.8 to 63.3 µmol/s/g_{Rh} during 140 h on stream (Table 5.1, entries 4 and 8; for detailed TOS behavior see Figure S5.5). The loss of activity is probably attributable to a change in particle size. Statistical particle size analysis of a large set of particles in different domains reveals a broader size distribution with a standard deviation of 0.6 nm (Figure 5.3d). The mean particle size is significantly larger with a value of 2.4 nm. In addition to these nanoparticles, agglomerates of particles with sizes of up to 20 nm are also found (Figure 5.3b).

In the case of methane, methanol, and ethanol, a significant change in selectivity could be observed (Figure 5.2). The MeOH:EtOH selectivity ratio changes from 1:1 at 7 h to 7:1 at 122 h on stream. This change in selectivity is induced by a structural transformation of the $RhFeO_x/SiO_2$ catalysts during the catalytic conversion of syngas.

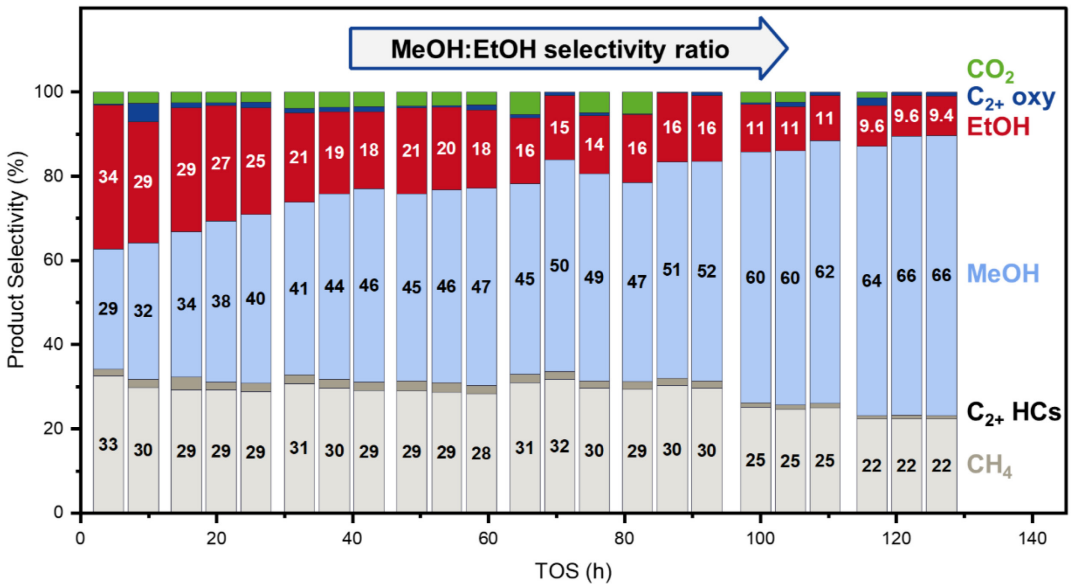

Figure 5.2. Product selectivities of the $RhFeO_x/SiO_2$ catalyst over 125 h on stream. Selectivities of methane (CH_4, light grey), C_{2+} hydrocarbons (C_{2+} HCs, dark grey), methanol (MeOH, light blue), ethanol (EtOH, red), C_{2+} oxygenates (C_{2+} oxy, dark blue), and carbon dioxide (CO_2, green) are shown. Measuring conditions: 243–260 °C, 54.0 bar, p(H_2) = 32.4 bar, p(CO) = 10.8–16.2 bar, GHSV 3500 h^{-1}. S(C_{2+} HCs) includes alkanes and alkenes. S(C_{2+} oxy) includes C_{3+} alcohols, aldehydes, acids, and acetates.

Powder XRD measurement of the spent catalyst revealed the formation of RhFe alloy crystallites with a molar composition of 1:1. The three most intense reflections are clearly visible in the corresponding diffractogram and fit to a literature-reported Rh_1Fe_1 alloy phase (ICDD C25-1408; Figure 5.3f). Likewise, the detected (110) reflection at 42.70° appears exactly at the position of the reported Rh_1Fe_1 phase at 42.72°. To confirm the elemental composition of RhFe nanoparticles, STEM-EDX point analyses have been performed on several particles from different domains (Figure S5.6 and Table S5.4). An

overall Rh:Fe ratio of approx. 0.97 was determined, which is in accordance with the result obtained from XRD investigation. The crystallite size could be evaluated as 3.7 nm from the respective X-ray reflections by Scherrer equation.

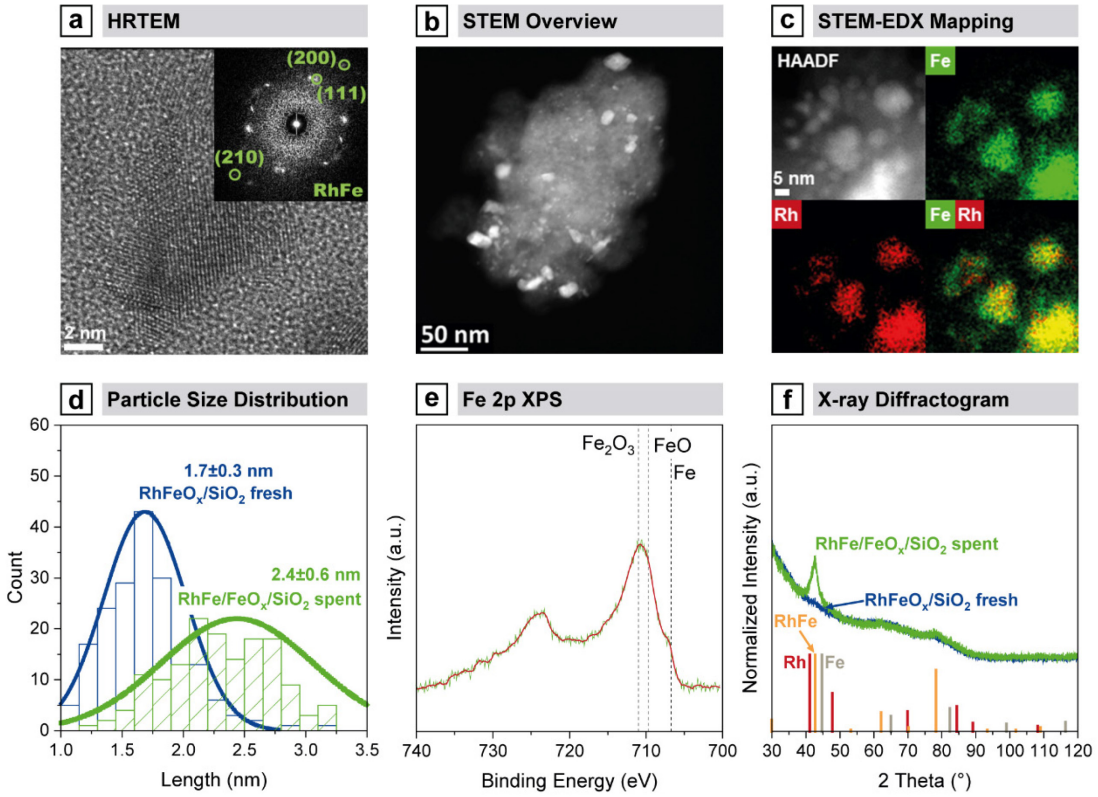

Figure 5.3. Structural and chemical characterization of spent $RhFe/FeO_x/SiO_2$ catalyst after catalytic testing: (a) HRTEM image of a representative crystalline nanoparticle and corresponding FFT as inset. The evaluated *d*-spacings are consistent with fcc planes of RhFe alloy; (b) HAADF-STEM overview image; (c) ADF-STEM image and corresponding STEM-EDX maps of Rh L, Fe K and superposition of Rh L and Fe K. Individual maps of all components and respective EDX spectrum are given in the Supporting Information; (d) particle size distribution; (e) Fe 2p XPS data; (f) X-ray diffractogram (green) in comparison with fresh $RhFeO_x/SiO_2$ (blue). References for Rh (red, C5-685), Fe (grey, C6-696), and Rh_1Fe_1 (orange, C25-1408) were taken from ICDD database.

Representative lattice fringe analysis on HRTEM images of smaller particles yields *d*-spacings of 2.1, 1.5, and 1.2 Å, which are consistent with {111}, {200}, and {211} lattice planes of fcc Rh_1Fe_1 alloy with the space group of Pm3m and a RhFe ratio of 1:1 (Figure 5.3a). The RhFe alloy formation is also reflected in XPS and Moessbauer spectra. Fe is in a more reduced state after catalytic testing, as indicated by a binding energy shift in the Fe 2p spectrum of -0.64 eV (Figure 5.3e). This shift suggests a modification of the electronic structure, which is probably caused by the alloying of Fe and Rh. Although Fe carbide phases could lead to similar shifts in Fe 2p spectra, no indications for their formation have been found during STEM-EELS and HRTEM analyses. Furthermore, typical hyperfine splitting for a Fe carbide is absent in the respective Moessbauer spectrum (Figure S5.1b). Moreover, a similar binding energy shift was observed in MnO_x-promoted $RhFe/SiO_2$ catalysts by Huang and co-workers.[20] Additionally, the partial reduction of Fe is indicated by a decrease in Fe^{3+} and Fe^{2+} doublets in Moessbauer

spectroscopy (Figure S5.1b). The reduced character of Fe is further confirmed by EELS. In comparison to Fe oxides, L3 and L2 edges of FeO_x are shifted to lower energies. Thus, Fe oxidation state is between 0 and 2+ (Figure S5.7). Lastly, STEM-EELS spot analysis and STEM-EDX mappings visualize the RhFe alloy formation through the local enrichment of Rh and Fe in the same areas (Figure 5.3c; for single-element maps of all components see Figure S5.8).

As a result of the continually increasing selectivity towards methanol over time on stream, it is apparent that the $RhFeO_x/SiO_2$ catalyst lost C–C coupling ability, resulting in decreased ethanol formation. According to Schweicher and co-workers, the CO insertion step is crucial for chain lengthening in CO hydrogenation rather than a coupling of CH_x surface fragments.[41] Thus, a loss of molecular CO adsorption sites would affect CO insertion ability and formation of higher oxygenates. CO-DRIFTS was used to identify CO adsorption modes on the $RhFeO_x/SiO_2$ catalyst. For this purpose, the surface sites were probed by CO adsorption at room temperature. The DRIFTS spectrum of the fresh $RhFeO_x/SiO_2$ catalyst shows typical vibrational bands of linear (2065 cm^{-1}) and bridged CO (1910 cm^{-1}) adsorbed on metallic Rh sites as indicated by direct comparison with a Rh/SiO_2 reference sample (Figure S5.9a,b). A redshift due to RhFe surface alloy formation, as reported for RhFe on TiO_2 and CeO_2,[42] has not been observed. Besides these typical vibrational bands on metallic sites, two distinct bands at 2092 and 2035 cm^{-1} were observed (Figure S5.9a), which are commonly assigned to *gem*-dicarbonyl $Rh^+(CO)_2$ surface species.[43] The typical CO band positions of CO adsorbed on metallic Rh sites and the evidence of *gem*-dicarbonyl species presupposes that Rh is unalloyed and accessible for CO adsorption in the fresh $RhFeO_x/SiO_2$ catalyst. Whereas the CO-DRIFTS spectrum of the spent $RhFe/FeO_x/SiO_2$ catalyst does not show an indication for a *gem*-dicarbonyl species and only a band at 2084 cm^{-1} which could not be assigned to a CO adsorption mode on Rh. The disappearance of the distinct *gem*-dicarbonyl bands might be attributable to the RhFe nanoalloy formation and the decreased amount of FeO_x in close proximity to Rh. This is in accordance with Rh 3d XP spectra of the fresh $RhFeO_x/SiO_2$ and spent $RhFe/FeO_x/SiO_2$ catalysts (Figure S5.10). Direct comparison of these XP spectra with a calcined and reduced Rh/SiO_2 reference sample suggests that a certain amount of oxidized Rh is present on the fresh $RhFeO_x/SiO_2$ sample. The oxidation state of this oxidized Rh species is probably between Rh^{3+} and Rh^0 due to an increase intensity in the range of 308.7 and 307.7 eV. This feature disappeared on the spent $RhFe/FeO_x/SiO_2$ sample after catalysis, which further supposes a decrease in Rh^+ surface sites (Figure S5.10). Previous studies also demonstrated the stabilizing effect of FeO_x on *gem*-dicarbonyl $Rh^+(CO)_2$ sites on $RhFe/TiO_2$ and $RhFe/CeO_2$ catalysts.[22,44] This leads to the assumption that $Rh^+(CO)_2$ surface sites are relevant for CO insertion and that their site fraction is thereby directly connected to the C–C coupling ability over CO insertion on Rh-based catalysts.

In summary, the structural transformation of unalloyed $RhFeO_x$ to alloyed $RhFe/FeO_x$ nanostructures during the catalytic conversion of synthesis gas leads to a continuous loss of C-C coupling ability. This nanoalloy formation is probably conditioned by high mobility of Fe on the silica support and further affected by the reducibility of Fe at the Rh-FeO_x interface. The reduction of FeO_x occurs most likely in the vicinity of Rh through a hydrogen spillover from metallic Rh surface sites.[45] This, in turn, leads probably to a decrease in Rh-FeO_x interfacial sites, resulting in less Rh^+ surface sites and thus less CO insertion capabilities.

5.3.4 From Structure-Function Relationships to a More Stable Rh/(Fe,Mn)O_x Catalyst

Preventing RhFe nanoalloy formation under StE reaction conditions is vital for stable ethanol selectivities on $RhFeO_x$ catalysts. Rh-based catalysts on silica supports suffer from high mobility of Fe, leading to increased reducibility at the Rh-FeO_x interface. Anchoring FeO_x to the support surface through strong support interactions might be one promising strategy to prevent RhFe nanoalloy formation. An extended electron microscopy study demonstrated the formation of (Fe,Mn)O_x mixed oxide phases in the multi-promoted $RhMnFe/SiO_2$ catalysts, which was further proved by integral characterization methods.[19,20,46] Therefore, the formation of (Fe,Mn)O_x mixed oxides might drastically reduce the Fe mobility. For this reason, a novel high surface area Mn_2O_3 material was used as a support for the synthesis of a Rh/(Fe,Mn)O_x catalyst (Scheme 5.1).

The Mn_2O_3 support was synthesized through a modified, literature-known nanocasting procedure.[47] For this purpose, the ordered mesoporous silica KIT-6 was used as a template.[48] It was impregnated with a Mn acetate solution in ethanol and subsequently decomposed to a Mn_2O_3/KIT-6 composite *via* drying at 150 °C and calcination at 550 °C. The Mn_2O_3 material was characterized by BET, TEM, and ICP-OES.[30]

Similar to the synthesis of the $RhFeO_x/SiO_2$ catalyst, the final Rh/(Fe,Mn)O_x catalyst was synthesized by using $NEt_4[RhFe_2(CO)_{10}]$ as a precursor in a SSP approach. During the last step in the SSP approach, the thermal treatment in 10 % H_2/Ar at 260 °C, the porous Mn_2O_3 support was reduced to Mn_3O_4 as proved by XRD before and after thermal treatment (Figure S5.11). Respective BET analyses confirmed that the reduction was not accompanied by a change in surface area. The surface area of the freshly reduced Rh/(Fe,Mn)O_x catalyst is about 106 m^2/g. Using this novel high surface area Mn_3O_4 material as a support ensures the close proximity of Rh and the metal oxide promoter. This close proximity is known to be the key requirement for enhanced performance of Rh-based catalysts in CO hydrogenation.[18–21]

The reduced Rh/(Fe,Mn)O_x catalyst was characterized by XRD, STEM-EDX, EDX line profile scans, and ICP-OES. Overview STEM images revealed that the particles are

homogenously distributed over the Mn_3O_4 support (Figure 5.4a). Statistical particle size analysis on a large set of particles shows a mean particle size of 1.4 nm with a narrow size distribution (Figure 5.4c). In comparison, the mean particle size is significantly smaller than that observed for the $RhFeO_x/SiO_2$ catalysts. In contrast to the $RhFeO_x/SiO_2$ catalyst, the FeO_x phase is well distributed over the Mn_3O_4 support and is most likely forming a mixed oxide surface structure as indicated by the STEM-EDX mapping (Figure 5.4b; for single-element maps of all components see Figure S5.12) and supported by XRD analysis (Figure S5.11). As no indications for Fe agglomeration or particle formation are present in all investigated domains, it is assumed that Mn_3O_4 as support can drastically reduce the Fe mobility.

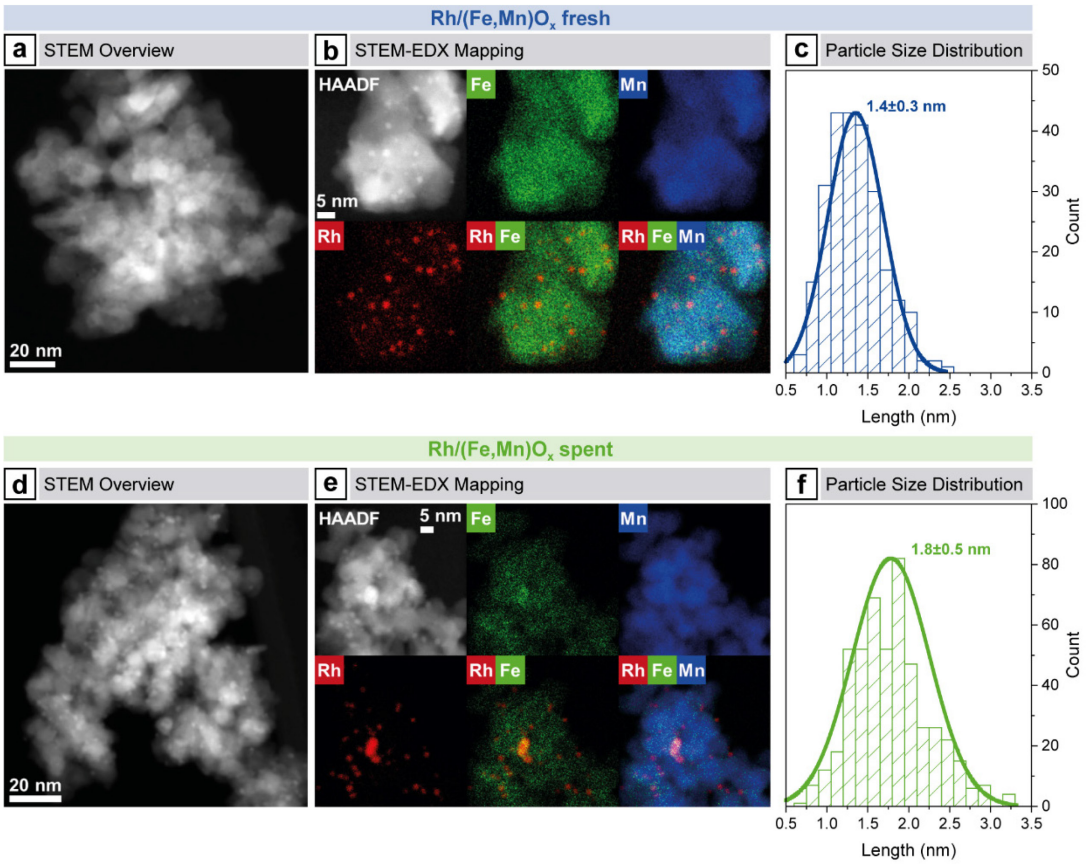

Figure 5.4. Morphology and chemical composition analyses of the fresh $Rh/(Fe,Mn)O_x$ catalyst after H_2 activation: (a) HAADF-STEM overview image, (b) HAADF image and corresponding EDX mapping of Rh L, Fe K, and Mn K as well as (c) particle size distribution. For the spent $Rh/(Fe,Mn)O_x$ catalyst after 125 h on stream: (d) HAADF-STEM overview image, (e) HAADF-STEM image and corresponding EDX mapping of Rh L, Fe K, and Mn K as well as (f) particle size distribution. Individual maps of all components and respective EDX spectra are given in the Supporting Information.

The reduced $Rh/(Fe,Mn)O_x$ catalyst was tested for CO hydrogenation at the same reaction conditions as described above (see Reactivity of $RhFeO_x/SiO_2$ catalyst) and compared to a Rh/MnO_x reference material. The activity in terms of the overall CO consumption rate was more than doubled with a factor of 2.75 (Table 5.1, entries 9 and 12). With a slightly increased ethanol selectivity of 22.1 % (33.7 % on CO_2-free basis; see Table S5.3 for CO_2-free product selectivities), the ethanol formation rate was

substantially increased from 0.8 to 2.4 µmol/s/g_{Rh} at reference conditions (243 °C) and was determined with a value of 7.8 µmol/s/g_{Rh} at the best performance mark (260 °C; Table S5.1). Moreover, methane and C_{2+} hydrocarbons selectivities could be substantially decreased over the Rh/(Fe,Mn)O_x catalyst. However, CO_2 selectivities of up to 34.5 % have been measured, which are most likely caused by the water gas shift (WGS) reaction.[14,23] The WGS reaction is a common side-reaction in syngas conversion.[14] Thus, a competitive formation of CO_2 could be probably suppressed through an optimization of the reaction conditions, e.g., co-feeding of CO_2.[13,49] Considering CO_2 as a side-product, the overall alcohol selectivity could be significantly increased from 30.9 to 59.8 % on a CO_2-free basis (Table S5.3, entries 11 and 15).

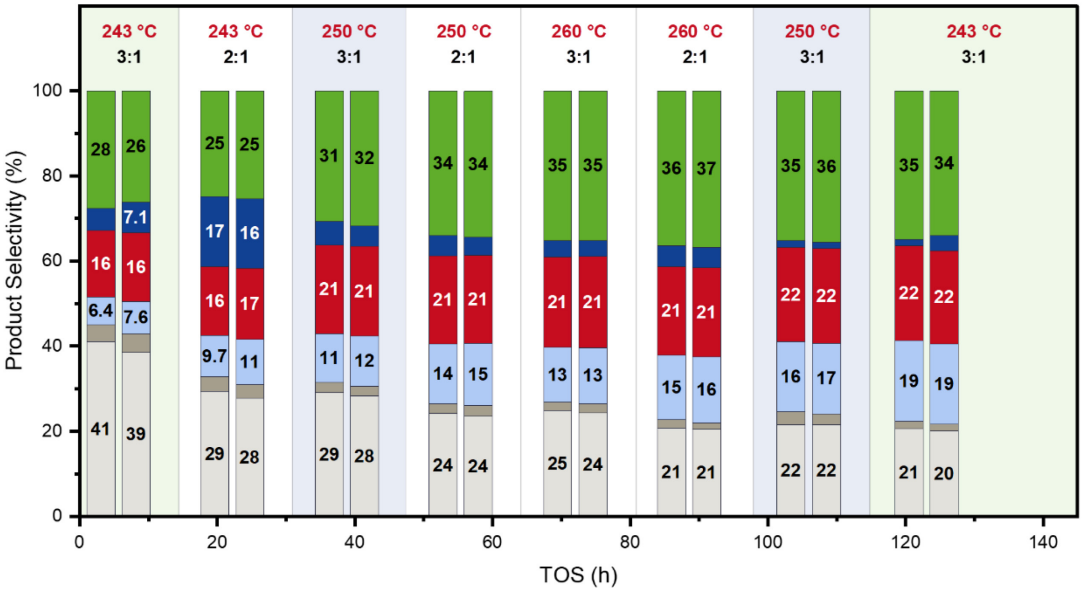

Figure 5.5. Product selectivities of the Rh/(Fe,Mn)O_x catalyst over 125 h on stream. Selectivities of methane (CH_4, light grey), C_{2+} hydrocarbons (C_{2+} HCs, dark grey), methanol (MeOH, light blue), ethanol (EtOH, red), C_{2+} oxygenates (C_{2+} oxy, dark blue), and carbon dioxide (CO_2, green) are shown. Measuring conditions: 243–260 °C, 54.0 bar, p(H_2) = 32.4 bar, p(CO) = 10.8 bar for H_2:CO = 3:1 and 16.2 bar for H_2:CO = 2:1, GHSV 3500 h^{-1}. S(C_{2+} HCs) includes alkanes and alkenes. S(C_{2+} oxy) includes C_{3+} alcohols, aldehydes, acids, and acetates. For each condition two measurements are shown. Areas with same color indicate reference conditions.

In this case as well, a loss in activity was observed during the long-term catalytic test. The CO consumption rate changes from 30.7 µmol/s/g_{Rh} at 6 h to 19.4 µmol/s/g_{Rh} at 123 h on stream, which corresponds to a percentage change of -37 % (Table 5.1, entries 12 and 16; for detailed TOS behavior see Figure S5.13). This deactivation might not be induced by particle sintering alone as the mean particle size of 1.8±0.5 nm is only slightly larger than that of the fresh Rh/(Fe,Mn)O_x catalyst with a value of 1.4±0.3 nm (Figure 5.4c,f). For this reason. the active metal surface areas (SA_{metal}) of the fresh and spent Rh/(Fe,Mn)O_x catalysts have been calculated from the particle size distributions obtained by STEM. For this purpose, a cuboctahedral metal cluster model has been used (more details are provided in the Supporting Information as Figure S5.14). This model demonstrates that the increase in particle diameter of the Rh/(Mn,Fe)O_x catalyst of

0.4 nm leads to a decrease in SA_{metal} from 4.04 to 3.12 m^2/g_{cat}. This change in SA_{metal} of -23 % further suggests that beside particle sintering another mechanism contributes to the catalyst deactivation. Two possible pathways have been considered: blocking of active Rh sites *via* partial coverage by MnO or through coke formation.

Yang and co-workers investigated Rh/SiO_2 catalysts modified by atomic layer deposition through selective deposition of MnO as a support layer or an overlayer. A lower activity in CO hydrogenation has been observed for the MnO overlayer modified Rh/SiO_2 catalyst, and it has been subsequently assumed that the MnO overlayer may adversely block active Rh sites.[18] Such a MnO overlayer has also been observed by STEM-EDX mapping of a $RhMnFe/SiO_2$ catalyst.[20] STEM-EDX area-selective analyses on the fresh and spent $Rh/(Mn,Fe)O_x$ catalysts show that the Mn:Rh ratio has been significantly increased after catalysis (Figure S5.15 and Table S5.4). This result might indicate that active Rh surface sites are partially covered by MnO similar to catalysts in a reactive metal–support interaction state.[50] However, a direct atomistic confirmation, as reported for the $Cu/ZnO/Al_2O_3$ methanol synthesis catalyst, is required for a clear proof.[51]

Another possible explanation for the deactivation might be coke formation as proofed by elemental analysis before and after catalysis. The carbon content increased from 0.16 on the fresh to 1.53 wt% on the spent $Rh/(Fe,Mn)O_x$ sample. As $MnCO_3$ has been formed during catalysis and contributes to the increase in carbon content, phase composition analysis has been performed through Rietveld refinement of the corresponding X-ray diffractogram (Figure S5.16). The relative amount of carbon, which could not be attributed to $MnCO_3$ formation, is about 0.49 wt%. This amount seems to be relatively low compared to coke formation on reforming and dehydrogenation catalyst, which usually ranges from 6–9 wt%.[52–54] Notwithstanding, the increased amount of carbon on the $Rh/(Fe,Mn)O_x$ suggests that coke formation might also contribute to its deactivation.

After a relatively short formation phase of 35 h on stream, the ethanol selectivity was stable and did not change during the remaining 90 h on stream (Figure 5.5). We reason that this stability in ethanol selectivity is a consequence of stable, metallic Rh nanostructures which are not alloyed with Fe. This assumption is in accordance with a recent *in situ* XRD study of $MnRh/Fe_2O_3$ catalysts, correlating increased ethanol selectivities with MnO, FeO_x, and mixed $(Fe,Mn)O_x$ phases in vicinity to Rh.[44] As previously mentioned, Fe might be less mobile on the MnO_x support due to the strong support interaction resulting from the formation of a mixed $(Fe,Mn)O_x$ surface oxide. This might decrease the Fe mobility as well as preventing further reduction of FeO_x at the Rh-FeO_x interface. We also proved the formation of such a mixed $(Fe,Mn)O_x$ surface oxide in the spent catalysts after the formation phase and long-term catalytic studies. STEM-EDX mapping and line scanning profile analyses were performed (Figure 5.6b,c; for corresponding STEM image and single-elements maps see Figure 5.4e) for this

purpose. While the EDX map already indicates a homogenous distribution of Fe over the MnO_x support (Figure 5.4e), the representative elemental line profile analysis provides further confirmation for the well-defined $(Fe,Mn)O_x$ surface oxide structure (Figure 5.6b). Similar to the fresh $Rh/(Fe,Mn)O_x$ catalyst (Figure 5.4a–c), Fe agglomeration or particle formation were not observed (Figure 5.4d,e). Consequently, not even high pressures of synthesis gas could cause increased Fe mobility. The formation of a $(Fe,Mn)O_x$ mixed oxide further affected the expected MnO reflections in the corresponding X-ray diffractogram of the spent $Rh/(Fe,Mn)O_x$ sample (Figure 5.6a). The observed MnO reflections are slightly shifted to higher angles as expected for $(Mn,Fe)O_x$ mixed oxide phases indicating the incorporation of FeO at the surface. Reflections from RhFe crystallites have not been observed, which is in accordance with STEM-EDX results.

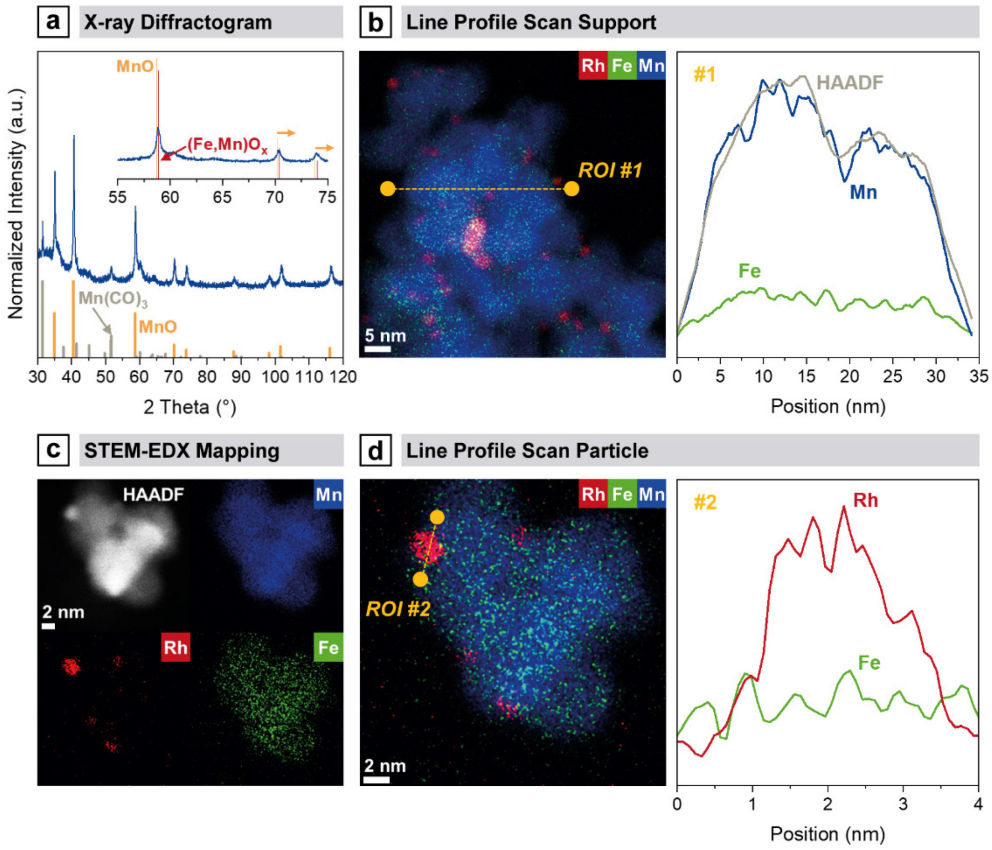

Figure 5.6. Phase identification and extended electron microscopy analysis of spent $Rh/(Fe,Mn)O_x$ catalyst: **(a)** X-ray diffractogram (blue) with a detailed view of the mixed oxide induced reflection shifts as inset. References for MnO (orange, C7-230), $MnCO_3$ (grey, C44-1472), and $(Fe,Mn)O_x$ (red, C77-2362) were taken from ICDD database. Chemical formula of $(Fe,Mn)O_x$ mixed oxide reference is $(FeO)_{0.099}(MnO)_{0.901}$. Additional diffractogram with reference patterns of RhFe and Rh is provided in the Supporting Information; **(b)** superposition of STEM-EDX maps of Rh L, Fe K, and Mn K with line scan path highlighted in yellow (ROI #1) and corresponding line scan profiles of Fe K (green), Mn K (blue) and HAADF (grey) intensities; **(c)** high-resolution STEM image and corresponding EDX mapping of Rh L, Fe K, and Mn K; **(d)** superposition of STEM-EDX maps of Rh L, Fe K, and Mn K with line scan path over a representative Rh particle (red) highlighted in yellow (ROI #2) and corresponding line scan profiles of Rh L (red) and Fe K (green). Individual maps of all components and respective EDX spectrum are given in the Supporting Information.

Additional STEM-EDX elemental line scans at high magnifications confirmed the unalloyed state of the observed Rh nanoparticles in the spent Rh/(Fe,Mn)O_x catalyst (Figure 5.6d; corresponding STEM image and single-element maps see Figure S5.17). The representative line profiles of Rh and Fe clearly demonstrate that there is no local enrichment of Fe in areas of increased Rh intensity (Figure 5.6d). These local enrichments are essential to form RhFe alloyed nanostructures as present in RhFe/FeO_x/SiO_2 after catalysis (for line-profile scans see Figure S5.18).

In brief, the use of high surface area MnO_x as support for RhFe catalysts decreases Fe mobility through the formation of mixed (Fe,Mn)O_x surface oxides. As a reason of the decreased Fe mobility and reducibility, the formation of RhFe nanoalloyed structures is unfavored on MnO_x as support and thereby Rh remains in a stable metallic state.

5.4 Conclusions

The formation phase of a $RhFeO_x/SiO_2$ catalyst was identified to be critical in CO hydrogenation to ethanol. Herein, we reported a generic method for investigating this critical phase at high partial pressure of synthesis gas. During a long-term catalytic test, a significant change in oxygenate selectivity was observed. Combining integral and local characterization methods (XPS, XRD, HRTEM, HAADF, STEM-EELS, and STEM-EDX), we could ascribe this dynamic behavior to a structural transformation of an unalloyed $RhFeO_x$ to an alloyed $RhFe/FeO_x$ nanostructure. This transformation was probably induced by high mobility of Fe and led to the continuous loss of C–C coupling and thus also to a decrease in ethanol formation abilities. Finally, these selectivity dependencies on the nanostructure of RhFe catalysts provide an explanation for the great variations in reported results of catalytic reactivity and different proposed structure models of the active phase, which range from unalloyed over core-shell to alloyed RhFe nanostructures.

The structure-function relationship we identified finally provides the opportunity for new catalyst design strategies: decreasing Fe mobility and reducibility is vital to improve Fe-promoted Rh catalysts and should lead to more stable catalysts in terms of ethanol selectivity. As one example, we reported the usage of a novel high surface area Mn_2O_3 material as a support. It was shown that the formation of a $(Fe,Mn)O_x$ mixed surface oxide drastically reduces the Fe mobility. Anchoring FeO_x on the Mn_2O_3 surface through strong support interactions prevents the formation of RhFe nanoalloy structures and led to stable ethanol selectivities during a long-term catalytic study.

In summary, the reported generic method of investigating the critical formation phase provides meaningful insights into the structural behavior of catalysts under reaction conditions and addresses explanations for controversially discussed catalytic results. We foresee that this method will not remain limited to Rh-based catalysts in CO hydrogenation and will be applicable to many other catalyst systems, such as $CuCo/SiO_2$ or $PtCo/SiO_2$, and other hydrogenation reactions.

5.5 References

(1) Chen, S.; Abdel-Mageed, A. M.; Li, D.; Bansmann, J.; Cisneros, S.; Biskupek, J.; Huang, W.; Behm, R. J. Morphology-Engineered Highly Active and Stable Ru/TiO_2 Catalysts for Selective CO Methanation. *Angew. Chem. Int. Ed.* **2019**, *58* (31), 10732–10736.

(2) Rezvani, A.; Abdel-Mageed, A. M.; Ishida, T.; Murayama, T.; Parlinska-Wojtan, M.; Behm, R. J. CO_2 Reduction to Methanol on Au/CeO_2 Catalysts: Mechanistic Insights from Activation/Deactivation and SSITKA Measurements. *ACS Catal.* **2020**, *10* (6), 3580–3594.

(3) Abdel-Mageed, A. M.; Klyushin, A.; Knop-Gericke, A.; Schlögl, R.; Behm, R. J. Influence of CO on the Activation, O-Vacancy Formation, and Performance of Au/ZnO Catalysts in CO_2 Hydrogenation to Methanol. *J. Phys. Chem. Lett.* **2019**, *10* (13), 3645–3653.

(4) Bergmann, A.; Roldan Cuenya, B. Operando Insights into Nanoparticle Transformations during Catalysis. *ACS Catal.* **2019**, *9* (11), 10020–10043.

(5) Yang, N.; Medford, A. J.; Liu, X.; Studt, F.; Bligaard, T.; Bent, S. F.; Nørskov, J. K. Intrinsic Selectivity and Structure Sensitivity of Rhodium Catalysts for C_{2+} Oxygenate Production. *J. Am. Chem. Soc.* **2016**, *138* (11), 3705–3714.

(6) Hartman, T.; Geitenbeek, R. G.; Whiting, G. T.; Weckhuysen, B. M. Operando Monitoring of Temperature and Active Species at the Single Catalyst Particle Level. *Nat. Catal.* **2019**, *2* (11), 986–996.

(7) Fischer, N.; Claeys, M. In Situ Characterization of Fischer–Tropsch Catalysts: A Review. *J. Phys. D: Appl. Phys.* **2020**, *53* (29), 293001.

(8) Tinnemans, S. J.; Kox, M. H. F.; Sletering, M. W.; Nijhuis, T. A. (Xander); Visser, T.; Weckhuysen, B. M. Dealing with a Local Heating Effect When Measuring Catalytic Solids in a Reactor with Raman Spectroscopy. *Phys. Chem. Chem. Phys.* **2006**, *8* (20), 2413.

(9) Meunier, F. C. The Design and Testing of Kinetically-Appropriate Operando Spectroscopic Cells for Investigating Heterogeneous Catalytic Reactions. *Chem. Soc. Rev.* **2010**, *39* (12), 4602.

(10) Bañares, M. A.; Guerrero-Pérez, M. O.; Fierro, J. L. G.; Cortez, G. G. Raman Spectroscopy during Catalytic Operations with On-Line Activity Measurement (Operando Spectroscopy): A Method for Understanding the Active Centres of Cations Supported on Porous Materials. *J. Mater. Chem.* **2002**, *12* (11), 3337–3342.

(11) Goodman, E. D.; Johnston-Peck, A. C.; Dietze, E. M.; Wrasman, C. J.; Hoffman, A. S.; Abild-Pedersen, F.; Bare, S. R.; Plessow, P. N.; Cargnello, M. Catalyst Deactivation via Decomposition into Single Atoms and the Role of Metal Loading. *Nat. Catal.* **2019**, *2* (9), 748–755.

(12) Luk, H. T.; Mondelli, C.; Ferré, D. C.; Stewart, J. A.; Pérez-Ramírez, J. Status and Prospects in Higher Alcohols Synthesis from Syngas. *Chem. Soc. Rev.* **2017**, *46* (5), 1358–1426.

(13) Subramani, V.; Gangwal, S. K. A Review of Recent Literature to Search for an Efficient Catalytic Process for the Conversion of Syngas to Ethanol. *Energy & Fuels* **2008**, *22* (2), 814–839.

(14) Spivey, J. J.; Egbebi, A. Heterogeneous Catalytic Synthesis of Ethanol from Biomass-Derived Syngas. *Chem. Soc. Rev.* **2007**, *36* (9), 1514.

(15) Gu, T.; Wang, B.; Chen, S.; Yang, B. Automated Generation and Analysis of the Complex Catalytic Reaction Network of Ethanol Synthesis from Syngas on Rh(111). *ACS Catal.* **2020**, *10* (11), 6346–6355.

(16) Ao, M.; Pham, G. H.; Sunarso, J.; Tade, M. O.; Liu, S. Active Centers of Catalysts for Higher Alcohol Synthesis from Syngas: A Review. *ACS Catal.* **2018**, *8* (8), 7025–7050.

(17) Schumann, J.; Medford, A. J.; Yoo, J. S.; Zhao, Z.-J.; Bothra, P.; Cao, A.; Studt, F.; Abild-Pedersen, F.; Nørskov, J. K. Selectivity of Synthesis Gas Conversion to C_{2+} Oxygenates on fcc(111) Transition-Metal Surfaces. *ACS Catal.* **2018**, *8* (4), 3447–3453.

(18) Yang, N.; Yoo, J. S.; Schumann, J.; Bothra, P.; Singh, J. A.; Valle, E.; Abild-Pedersen, F.; Nørskov, J. K.; Bent, S. F. Rh-MnO Interface Sites Formed by Atomic Layer Deposition Promote Syngas Conversion to Higher Oxygenates. *ACS Catal.* **2017**, *7* (9), 5746–5757.

(19) Dimitrakopoulou, M.; Huang, X.; Kröhnert, J.; Teschner, D.; Praetz, S.; Schlesiger, C.; Malzer, W.; Janke, C.; Schwab, E.; Rosowski, F.; Kaiser, H.; Schunk, S.; Schlögl, R.; Trunschke, A. Insights into Structure and Dynamics of $(Mn,Fe)O_x$-Promoted Rh Nanoparticles. *Faraday Discuss.* **2018**, *208*, 207–225.

(20) Huang, X.; Teschner, D.; Dimitrakopoulou, M.; Fedorov, A.; Frank, B.; Kraehnert, R.; Rosowski, F.; Kaiser, H.; Schunk, S.; Kuretschka, C.; Schlögl, R.; Willinger, M.-G.; Trunschke, A. Atomic-Scale Observation of the Metal–Promoter Interaction in Rh-Based Syngas-Upgrading Catalysts. *Angew. Chem. Int. Ed.* **2019**, *58* (26), 8709–8713.

(21) Preikschas, P.; Bauer, J.; Huang, X.; Yao, S.; Naumann d'Alnoncourt, R.; Kraehnert, R.; Trunschke, A.; Rosowski, F.; Driess, M. From a Molecular Single-Source Precursor to a Selective High-Performance $RhMnO_x$ Catalyst for the Conversion of Syngas to Ethanol. *ChemCatChem* **2019**, *11* (2), 885–892.

(22) Haider, M.; Gogate, M.; Davis, R. Fe-Promotion of Supported Rh Catalysts for Direct Conversion of Syngas to Ethanol. *J. Catal.* **2009**, *261* (1), 9–16.

(23) Liu, Y.; Göeltl, F.; Ro, I.; Ball, M. R.; Sener, C.; Aragão, I. B.; Zanchet, D.; Huber, G. W.; Mavrikakis, M.; Dumesic, J. A. Synthesis Gas Conversion over Rh-Based Catalysts Promoted by Fe and Mn. *ACS Catal.* **2017**, *7* (7), 4550–4563.

(24) Wang, J.; Zhang, Q.; Wang, Y. Rh-Catalyzed Syngas Conversion to Ethanol: Studies on the Promoting Effect of FeO_x. *Catal. Today* **2011**, *171* (1), 257–265.

(25) Burch, R.; Petch, M. I. Investigation of the Reactions of Acetaldehyde on Promoted Rhodium Catalysts. *Appl. Catal. A.* **1992**, *88* (1), 61–76.

(26) Burch, R.; Hayes, M. J. The Preparation and Characterisation of Fe-Promoted Al_2O_3-Supported Rh Catalysts for the Selective Production of Ethanol from Syngas. *J. Catal.* **1997**, *165* (2), 249–261.

(27) Gogate, M. R.; Davis, R. J. X-Ray Absorption Spectroscopy of an Fe-Promoted Rh/TiO_2 Catalyst for Synthesis of Ethanol from Synthesis Gas. *ChemCatChem* **2009**, *1* (2), 295–303.

(28) Mo, X.; Gao, J.; Umnajkaseam, N.; Goodwin Jr., J. G. La, V, and Fe Promotion of Rh/SiO_2 for CO Hydrogenation: Effect on Adsorption and Reaction. *J. Catal.* **2009**, *267* (2), 167–176.

(29) Carrillo, P.; Shi, R.; Teeluck, K.; Senanayake, S. D.; White, M. G. In Situ Formation of FeRh Nanoalloys for Oxygenate Synthesis. *ACS Catal.* **2018**, *8* (8), 7279–7286.

(30) Palomino, R. M.; Magee, J. W.; Llorca, J.; Senanayake, S. D.; White, M. G. The Effect of Fe-Rh Alloying on CO Hydrogenation to C_{2+} Oxygenates. *J. Catal.* **2015**, *329*, 87–94.

(31) Klapproth, M. Synthesis of High Surface Area Metal Oxides and Supported Metal Oxide Catalysts for the Oxidative Coupling of Methane. Doctoral Thesis, Technische Universität Berlin, December 2017. https://doi.org/10.14279/depositonce-6881.

(32) Guzman-Jimenez, I. Y.; van Hal, J. W.; Whitmire, K. H. Metal Cluster Catalysis: A Kinetic and Mechanistic Study of the Carbonylation of Methanol to Give Methyl Formate as Catalyzed by $[Et_4N]_2[Fe_3(CO)_9E]$ (E = S, Se, Te). *Organometallics* **2003**, *22* (9), 1914–1922.

(33) Schneider, C. A.; Rasband, W. S.; Eliceiri, K. W. NIH Image to ImageJ: 25 Years of Image Analysis. *Nat. Methods* **2012**, *9* (7), 671–675.

(34) Ceriotti, A.; Longoni, G.; Pergola, R. Della; Heaton, B. T.; Smith, D. O. Bimetallic Iron–Rhodium Anionic Carbonyl Clusters: $[Fe_2Rh(CO)_x]^-$ (X= 10 or 11), $[FeRh_4(CO)_{15}]^{2-}$, $[Fe_2Rh_4(CO)_{16}]^{2-}$, and $[FeRh_5(CO)_{16}]^-$. *J. Chem. Soc., Dalt. Trans.* **1983**, *3* (7), 1433–1440.

(35) Xu, Z.; Kawi, S.; Rheingold, A. L.; Gates, B. C. Surface-Mediated Synthesis of $[PtRh_5(CO)_{15}]^-$ on MgO. *Inorg. Chem.* **1994**, *33* (19), 4415–4417.

(36) Cariati, E.; Dragonetti, C.; Roberto, D.; Ugo, R.; Lucenti, E. Surface-Mediated Organometallic Synthesis: High-Yield Syntheses of $[Rh_4(CO)_{12}]$, $[Rh_6(CO)_{16}]$, $[Rh_5(CO)_{15}]^-$ and $[Rh_{12}(CO)_{30}]^{2-}$ by Controlled Reduction of Silica-Supported $RhCl_3$ or $[Rh(CO)_2Cl]_2$ in the Presence of CH_3CO_2Na, Na_2CO_3 or K_2CO_3. *Inorganica Chim. Acta* **2003**, *349*, 189–194.

(37) O'Connell, K.; Regalbuto, J. R. High Sensitivity Silicon Slit Detectors for 1 nm Powder XRD Size Detection Limit. *Catal. Letters* **2015**, *145* (3), 777–783.

(38) Niemantsverdriet, J. W.; Van der Kraan, A. M.; Van Loef, J. J.; Delgass, W. N. In Situ Moessbauer Spectroscopy of Bimetallic Iron-Rhodium (FeRh)/Silica Catalysts at 295 K. *J. Phys. Chem.* **1983**, *87* (8), 1292–1294.

(39) Zhang, C.-H.; Wan, H.-J.; Yang, Y.; Xiang, H.-W.; Li, Y.-W. Study on the Iron–Silica Interaction of a Co-Precipitated Fe/SiO_2 Fischer–Tropsch Synthesis Catalyst. *Catal. Commun.* **2006**, *7* (9), 733–738.

(40) Zhu, M.; Wachs, I. E. Iron-Based Catalysts for the High-Temperature Water–Gas Shift (HT-WGS) Reaction: A Review. *ACS Catal.* **2016**, *6* (2), 722–732.

(41) Schweicher, J.; Bundhoo, A.; Kruse, N. Hydrocarbon Chain Lengthening in Catalytic CO Hydrogenation: Evidence for a CO-Insertion Mechanism. *J. Am. Chem. Soc.* **2012**, *134* (39), 16135–16138.

(42) Magee, J. W.; Palomino, R. M.; White, M. G. Infrared Spectroscopy Investigation of Fe-Promoted Rh Catalysts Supported on Titania and Ceria for CO Hydrogenation. Catal.

Lett. 2016, 146 (9), 1771–1779.

(43) Yang, C.; Garl, C. W. Infrared Studies of Carbon Monoxide Chemisorbed on Rhodium. *J. Phys. Chem.* **1957**, *61* (11), 1504–1512.

(44) Liu, W.; Wang, S.; Sun, T.; Wang, S. The Promoting Effect of Fe Doping on Rh/CeO_2 for the Ethanol Synthesis. *Catal. Letters* **2015**, *145* (9), 1741–1749.

(45) Lebedeva, O. E.; Chiou, W.-A.; Sachtler, W. M. H. Metal Migration from Zeolites onto Iron Oxide: An Alternative to Hydrogen Spillover. *J. Catal.* **1999**, *188* (2), 365–374.

(46) Carrillo, P.; Shi, R.; Senanayake, S. D.; White, M. G. In Situ Structural Study of Manganese and Iron Oxide Promoted Rhodium Catalysts for Oxygenate Synthesis. *Appl. Catal. A.* **2020**, *608*, 117845.

(47) Smått, J.-H.; Weidenthaler, C.; Rosenholm, J. B.; Lindén, M. Hierarchically Porous Metal Oxide Monoliths Prepared by the Nanocasting Route. *Chem. Mater.* **2006**, *18* (6), 1443–1450.

(48) Choi, M.; Heo, W.; Kleitz, F.; Ryoo, R. Facile Synthesis of High Quality Mesoporous SBA-15 with Enhanced Control of the Porous Network Connectivity and Wall Thickness. *Chem. Commun.* **2003**, *3* (12), 1340–1341.

(49) Zhou, W.; Zhou, C.; Yin, H.; Shi, J.; Zhang, G.; Zheng, X.; Min, X.; Zhang, Z.; Cheng, K.; Kang, J.; Zhang, Q.; Wang, Y. Direct Conversion of Syngas into Aromatics over a Bifunctional Catalyst: Inhibiting Net CO_2 Release. *Chem. Commun.* **2020**, *56* (39), 5239–5242.

(50) Penner, S.; Armbrüster, M. Formation of Intermetallic Compounds by Reactive Metal-Support Interaction: A Frequently Encountered Phenomenon in Catalysis. *ChemCatChem* **2015**, *7* (3), 374–392.

(51) Behrens, M.; Studt, F.; Kasatkin, I.; Kuhl, S.; Havecker, M.; Abild-Pedersen, F.; Zander, S.; Girgsdies, F.; Kurr, P.; Kniep, B.-L.; Tovar, M.; Fischer, R. W.; Norskov, J. K.; Schlogl, R. The Active Site of Methanol Synthesis over $Cu/ZnO/Al_2O_3$ Industrial Catalysts. *Science* **2012**, *336* (6083), 893–897.

(52) Martín, N.; Viniegra, M.; Zarate, R.; Espinosa, G.; Batina, N. Coke Characterization for an Industrial $Pt–Sn/\gamma\text{-}Al_2O_3$ Reforming Catalyst. *Catal. Today* **2005**, *107–108*, 719–725.

(53) Ingale, P.; Guan, C.; Kraehnert, R.; Naumann d'Alnoncourt, R.; Thomas, A.; Rosowski, F. Design of an Active and Stable Catalyst for Dry Reforming of Methane *via* Molecular Layer Deposition. *Catal. Today* **2021**, *362*, 47–54.

(54) Sahoo, S. K.; Rao, P. V. C.; Rajeshwer, D.; Krishnamurthy, K. R.; Singh, I. D. Structural Characterization of Coke Deposits on Industrial Spent Paraffin Dehydrogenation Catalysts. *Appl. Catal. A Gen.* **2003**, *244* (2), 311–321.

5.6 Supporting Information

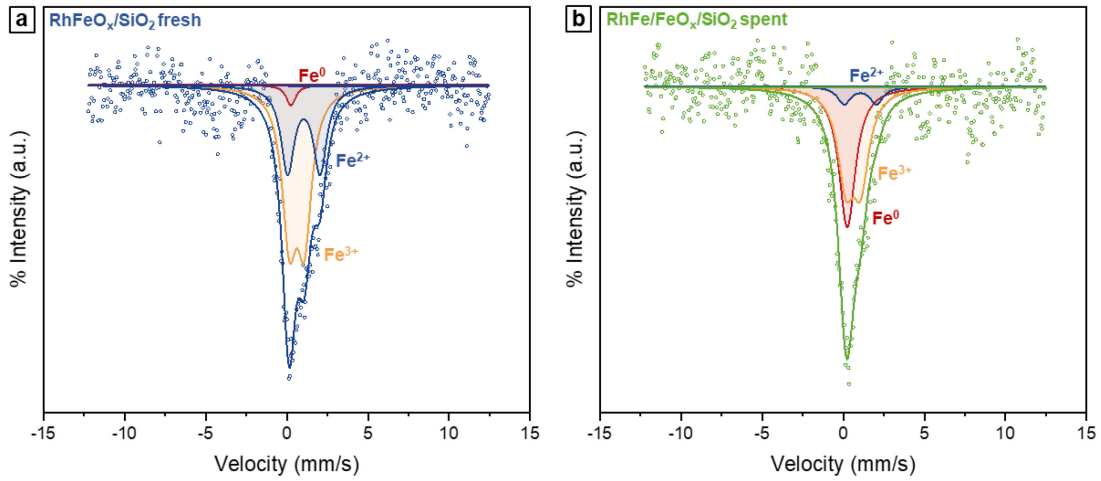

Figure S5.1. Moessbauer spectrum of (a) fresh $RhFeO_x/SiO_2$ catalyst after H_2 activation at 260 °C and (b) spent $RhFe/FeO_x/SiO_2$ catalyst after catalytic testing. Individual fits of Fe^0 (alloy), Fe^{2+}, and Fe^{3+} are color-coded in red, blue, and orange, respectively. Due to the low signal-to-niose ratio, a full quantitative analysis could be performed with certainty. Literature-reported isomer shifts (IS) and quadrupole splittings (QS) have been used as constraints.[1–4] Fit parameters of fresh $RhFeO_x/SiO_2$ and spent $RhFe/FeO_x/SiO_2$ (mm/s): Fe^0 (IS = 0.25), Fe^{2+} (IS = 1.05, QS = 2.00), and Fe^{3+} (IS = 0.62, QS = 0.88 (fresh), 0.92 (spent)). Spectra were folded and fitted to Lorentzian line shapes using MossA software[5].

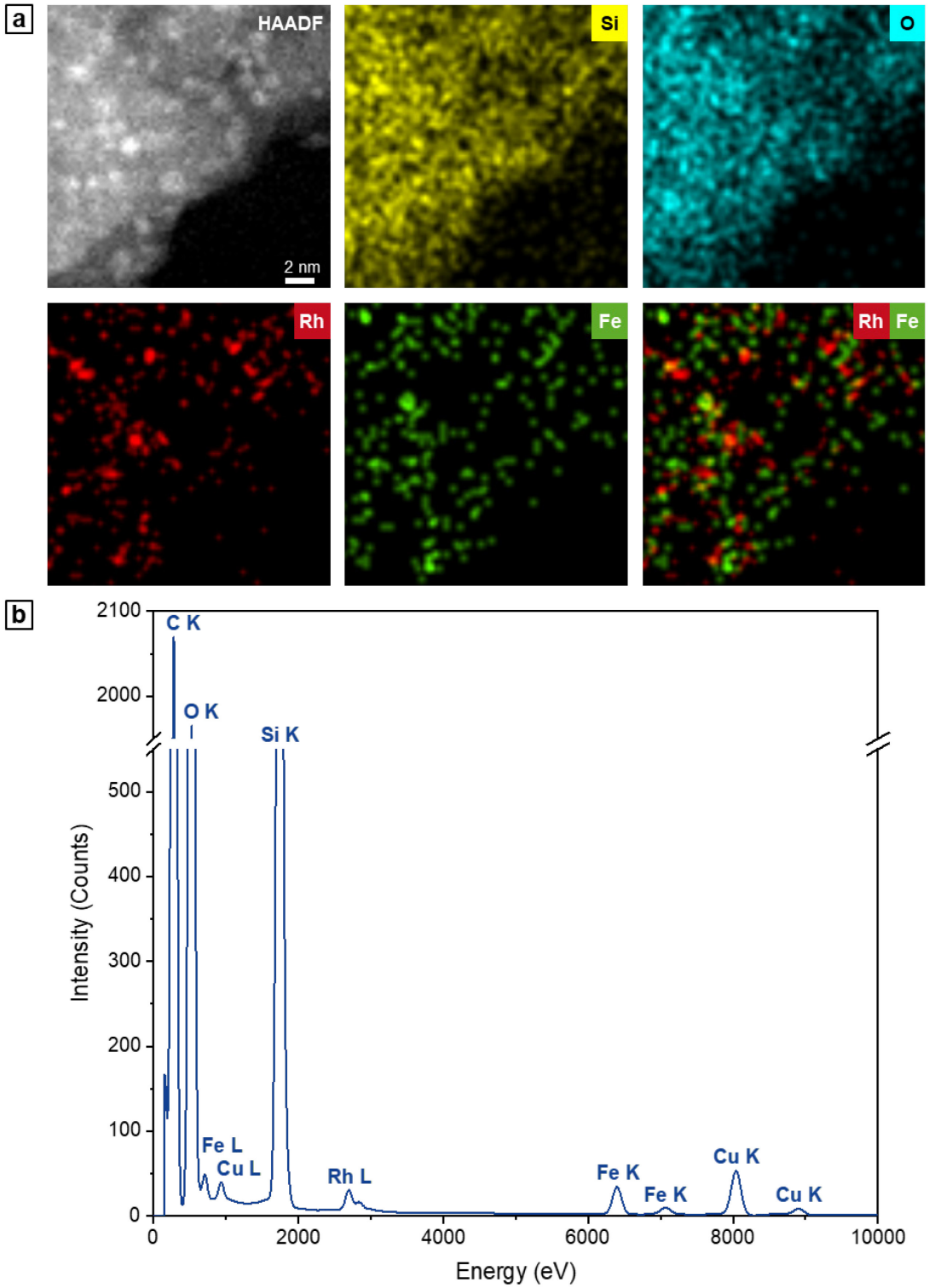

Figure S5.2. STEM-EDX analysis of fresh $RhFeO_x/SiO_2$ catalyst: (a) HAADF micrograph, single-element maps (Rh L, Si K, O K, Fe K), and (c) corresponding EDX spectrum. Cu signals from TEM grids used.

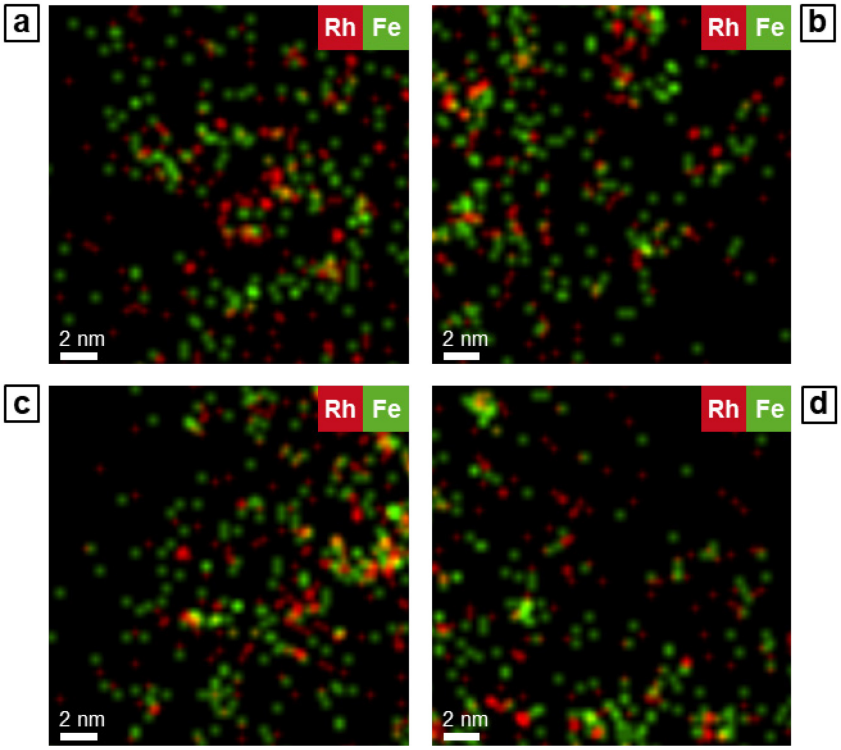

Figure S5.3. Additional superpositions of STEM-EDX maps (Rh L, Fe K) taken from four different domains of fresh $RhFeO_x/SiO_2$ catalyst.

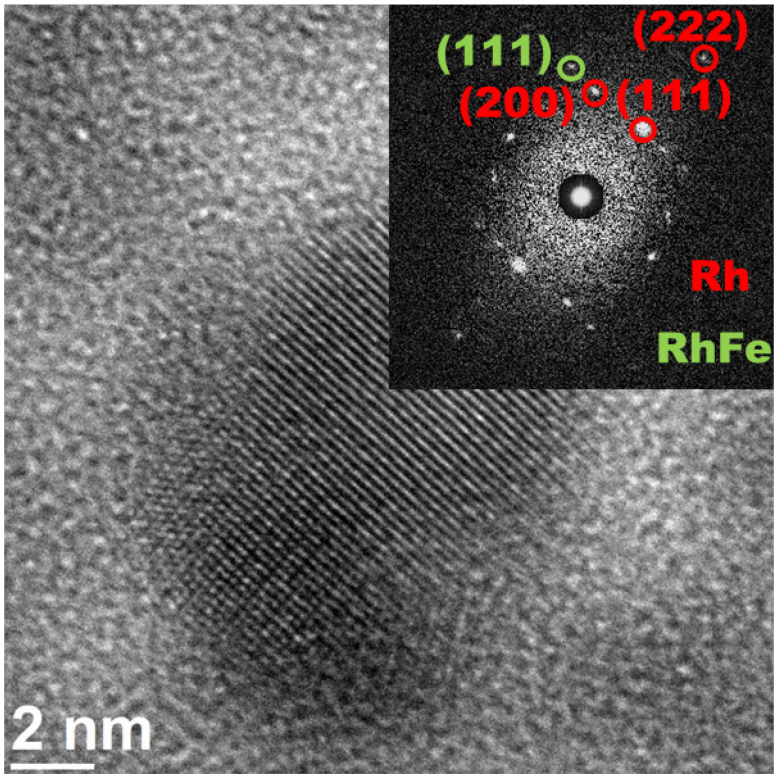

Figure S5.4. HRTEM image of minority particle of fresh $RhFeO_x/SiO_2$ catalyst after H_2 activation at 260 °C.

Table S5.1. Product Formation Rates over Reference and Rh-based Catalysts[a]

#	Sample	Precursor	T (°C)	H_2/CO	TOS (h)	r_{CO} (µmol/s/g_{Rh})	Product Formation Rates (µmol/s/g_{Rh})					
							CH_4	MeOH	EtOH	AcH	AcOH	CO_2
1	Rh/SiO_2	$Rh_4(CO)_{12}$	250	3	72	22.8	11.4	0.6	0.8	0.9	1.6	0.4
2			260	3	101	27.3	14.4	0.9	1.0	0.9	1.7	0.5
3	FeO_x/SiO_2[d]	$Fe(NO_3)_3$	320	2	209	6.82	0.2	0.0	0.0	0.0	0.0	0.0
4	$RhFeO_x/SiO_2$	$[RhFe_2(CO)_{11}]^-$	243	3	7	72.8	22.7	22.1	11.5	0.7	0.0	1.9
5			250	3	37	88.8	26.5	38.8	8.7	0.2	0.0	3.3
6			260	3	71	119.4	36.8	57.6	8.9	0.1	0.0	4.1
7			250	3	104	80.6	20.1	49.0	4.4	0.0	0.1	1.3
8			243	3	122	63.3	14.1	41.5	3.0	0.0	0.3	0.3
9	Rh/MnO_x	$Rh(NO_3)_3$	243	3	44	11.1	3.2	0.6	1.0	0.3	0.2	1.8
10			243	2	20	16.7	4.7	0.9	1.2	0.5	0.4	3.2
11			250	3	105	17.5	4.4	0.9	1.8	0.4	0.4	3.2
12	$Rh/(Fe,Mn)O_x$	$[RhFe_2(CO)_{11}]^-$	243	3	6	30.7	12.2	2.2	2.4	0.6	0.0	8.3
13			250	3	39	43.9	12.6	5.1	4.6	0.6	0.5	13.7
14			260	3	72	72.9	18.0	9.5	7.8	0.4	0.2	25.6
15			250	3	106	31.9	6.9	5.3	3.5	0.2	0.0	11.3
16			243	3	123	19.4	4.0	3.7	2.1	0.1	0.0	6.7

[a]Reaction conditions: 54.0 bar, $p(H_2)$ = 32.4 bar, $p(CO)$ = 10.8 bar, GHSV = 3500 h^{-1}. [b]C_{2+} oxy includes alcohols, aldehydes, acetates, and acids. [c]C_{2+} HCs includes alkanes and alkenes. [d]Monometallic FeO_x/SiO_2 material was measured at different reaction conditions due to its low activity.

Table S5.2. Product Selectivities of $RhFeO_x/SiO_2$ and $Rh/(Fe,Mn)O_x$ at H_2/CO Ratio of 2[a]

#	Sample	Precursor	T (°C)	H_2/CO	TOS (h)	r_{CO} (µmol/s/g_{Rh})	X_{CO} (%)	Product Selectivities (%)							
								CH_4	MeOH	EtOH	AcH	AcOH	C_{2+} Oxy	C_{2+} HCs	CO_2
1	$RhFeO_x/SiO_2$	$[RhFe_2(CO)_{11}]^-$	243	2	21	65.5	8.5	29.1	37.6	27.4	0.7	0.0	0.4	2.3	2.5
2			250	2	54	83.8	10.9	28.7	45.8	19.5	0.4	0.0	0.3	2.2	3.2
3			260	2	87	111.8	14.6	29.8	50.3	16.0	0.2	0.0	0.2	1.8	1.7
4	$Rh/(Fe,Mn)O_x$	$[RhFe_2(CO)_{11}]^-$	243	2	22	31.9	4.71	28.6	10.1	16.5	4.7	11.6	0.1	3.3	25.1
5			250	2	55	38.2	5.64	23.9	14.3	20.7	3.0	1.1	0.5	2.4	34.2
6			260	2	89	64.5	9.53	20.6	15.3	20.9	1.5	0.7	2.5	1.8	36.6

[a]Reaction conditions: 54.0 bar, $p(H_2)$ = 32.4 bar, $p(CO)$ = 10.8 bar, GHSV = 3500 h^{-1}. [b]C_{2+} oxy includes alcohols, aldehydes, acetates, and acids. [c]C_{2+} HCs includes alkanes and alkenes.

Table S5.3. Product Selectivities on CO_2-free Basis from Syngas Conversion over Reference and Rh-based Catalysts[a]

#	Sample	Precursor	T (°C)	H_2/CO	TOS (h)	X_{CO} (%)	Product Selectivities on CO_2-free basis (%)						
							CH_4	MeOH	EtOH	AcH	AcOH	C_{2+} Oxy	C_{2+} HCs
1	Rh/SiO_2	$Rh_4(CO)_{12}$	250	3	72	2.7	50.9	2.8	7.0	8.4	14.3	4.5	12.2
2			260	3	101	3.2	54.5	0.0	0.0	0.0	1.8	0.0	43.7
3	FeO_x/SiO_2[d]	$Fe(NO_3)_3$	320	2	209	3.0	54.5	0.0	0.0	0.0	1.8	0.0	43.7
4	$RhFeO_x/SiO_2$	$[RhFe_2(CO)_{11}]^-$	243	3	7	14.2	32.1	31.3	32.4	2.0	0.0	0.5	1.8
5			250	3	37	17.4	31.0	45.3	20.4	0.4	0.0	0.7	2.1
6			260	3	71	23.4	31.9	49.9	15.5	0.2	0.0	0.6	1.9
7			250	3	104	15.8	25.3	61.8	11.0	0.0	0.3	0.4	1.1
8			243	3	122	12.4	22.4	65.9	9.6	0.0	0.8	0.4	0.9
9	Rh/MnO_x	$Rh(NO_3)_3$	243	3	44	3.3	34.0	6.8	21.6	6.1	5.0	8.1	18.5
10			243	2	20	2.2	34.5	6.7	17.6	7.2	5.2	7.9	20.8
11			250	3	105	5.1	30.8	6.2	24.7	5.1	4.9	8.6	19.7
12	$Rh/(Fe,Mn)O_x$	$[RhFe_2(CO)_{11}]^-$	243	3	6	6.8	54.5	9.6	21.9	5.2	0.1	3.0	5.7
13			250	3	39	9.7	41.7	16.9	30.4	4.0	3.0	0.5	3.5
14			260	3	72	16.2	38.0	20.0	32.9	1.9	1.0	3.0	3.1
15			250	3	106	7.1	33.4	25.5	34.3	2.0	0.0	0.4	4.3
16			243	3	123	4.3	31.1	28.9	33.7	1.9	0.0	1.8	2.5

[a]Reaction conditions: 54.0 bar, $p(H_2)$ = 32.4 bar, $p(CO)$ = 10.8 bar, GHSV = 3500 h^{-1}. [b]C_{2+} oxy includes alcohols, aldehydes, acetates, and acids. [c]C_{2+} HCs includes alkanes and alkenes. [d]Monometallic FeO_x/SiO_2 material was measured at different reaction conditions due to its low activity.

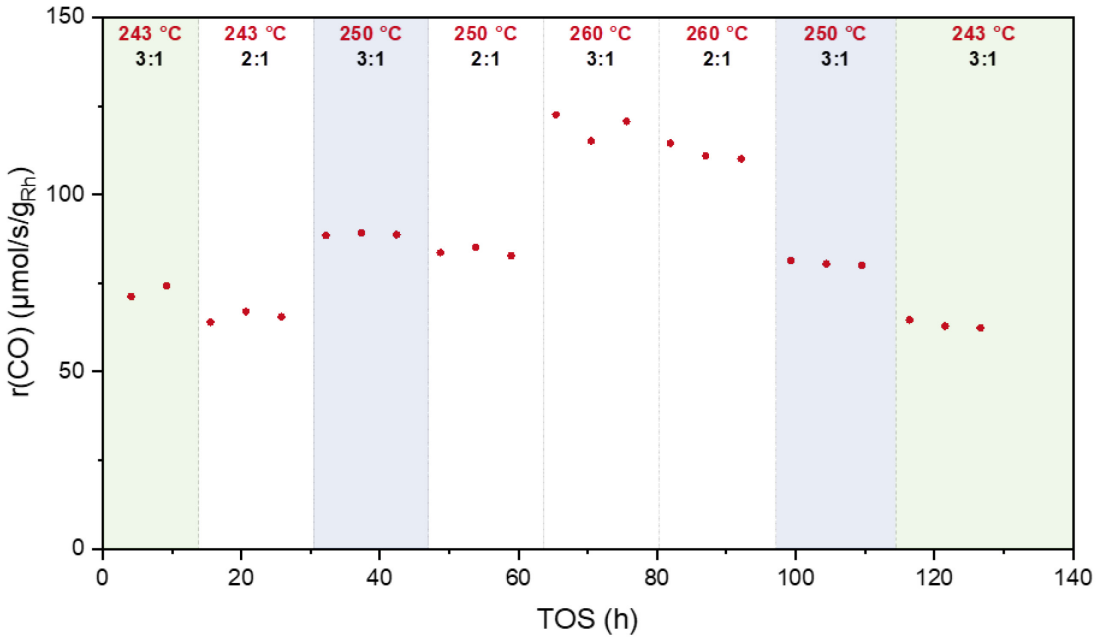

Figure S5.5. CO consumption rate of $RhFeO_x/SiO_2$ catalyst over time on stream. Areas with same color indicate reference conditions. Measuring conditions: 243–260 °C, 54.0 bar, p(H_2) = 32.4 bar, p(CO) = 10.8 bar for H_2:CO = 3:1 and 16.2 bar for H_2:CO = 2:1, GHSV 3500 h^{-1}.

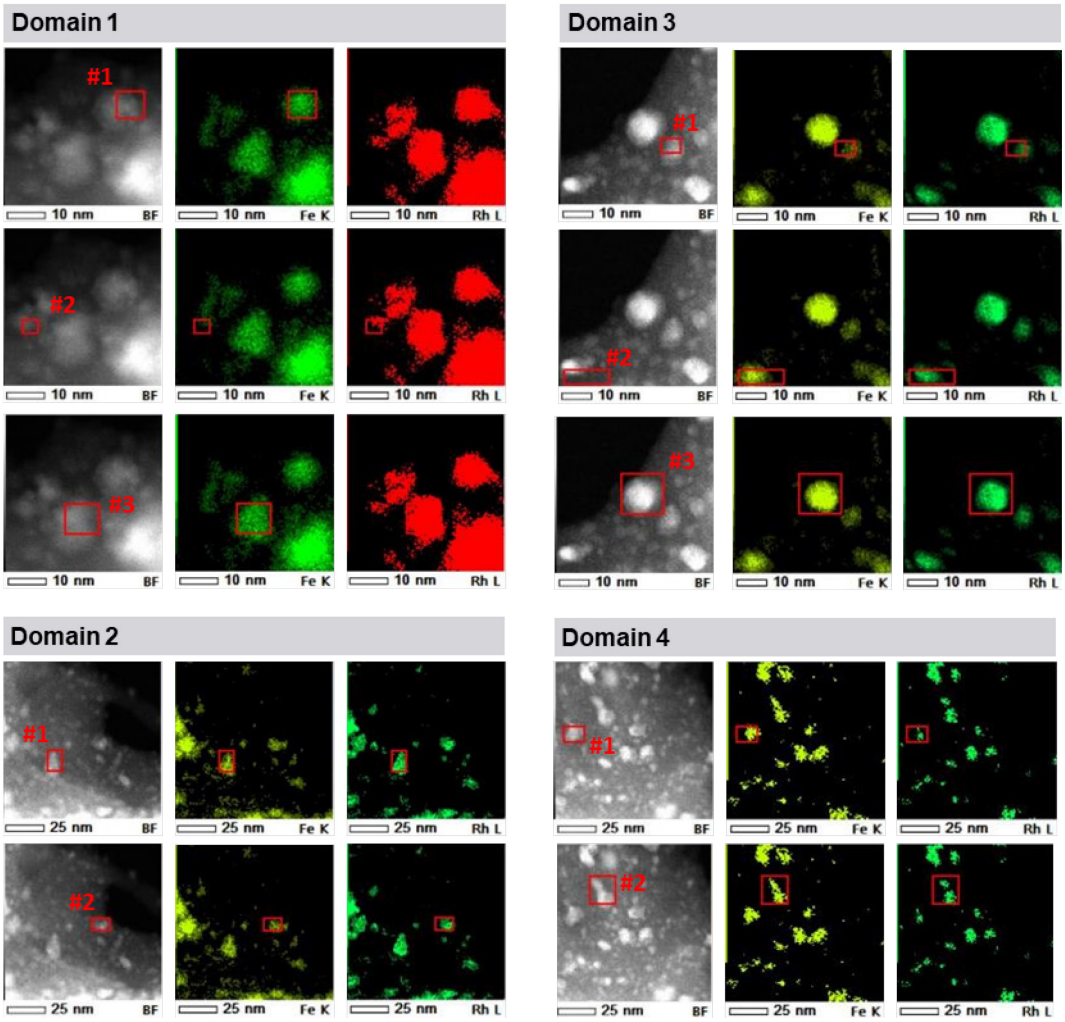

Figure S5.6. HAADF micrographs, STEM-EDX superpositions of Rh L and Mn K, and map of Rh L of (a) fresh and (b) spent Rh/(Mn,Fe)O_x catalyst corresponding to STEM-EDX area-selective analyses. Particles investigated are encircled in yellow. Individual maps of all components and respective EDX spectrum are given in Figures 5.S10 and S12.

Table S5.4. Compositions of RhFe alloy particles from STEM-EDX point analysis (Figure S5.6).

Domain	Particle	Composition (at%)		Rh:Fe ratio
		Rh K	Fe L	
1	1	11.9	11.4	1.05
	2	4.83	4.63	1.04
	3	9.56	9.28	1.03
2	1	7.40	6.83	1.08
	2	11.8	9.52	1.24
3	1	7.49	6.35	1.18
	2	11.3	12.7	0.89
	3	15.2	14.7	1.03
4	1	5.07	6.69	0.76
	2	5.05	5.62	0.90
Average Rh:Fe ratio				1.02

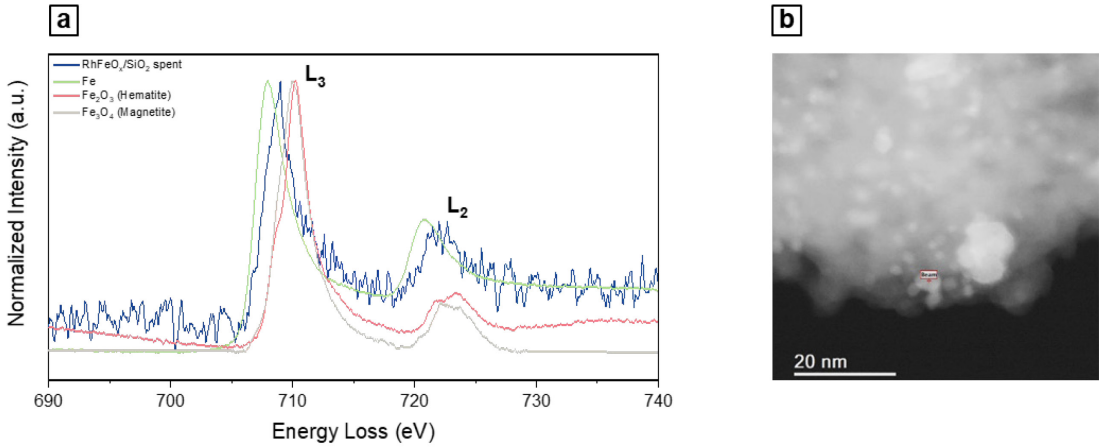

Figure S5.7. EEL spectrum of core-loss Fe $L_{2,3}$ edges of spent $RhFe/FeO_x/SiO_2$ catalyst (blue) after catalytic testing in comparison with Iron oxide reference spectra with respective STEM image of the location investigated. EELS reference spectra were taken from EELS Data Base.[6]

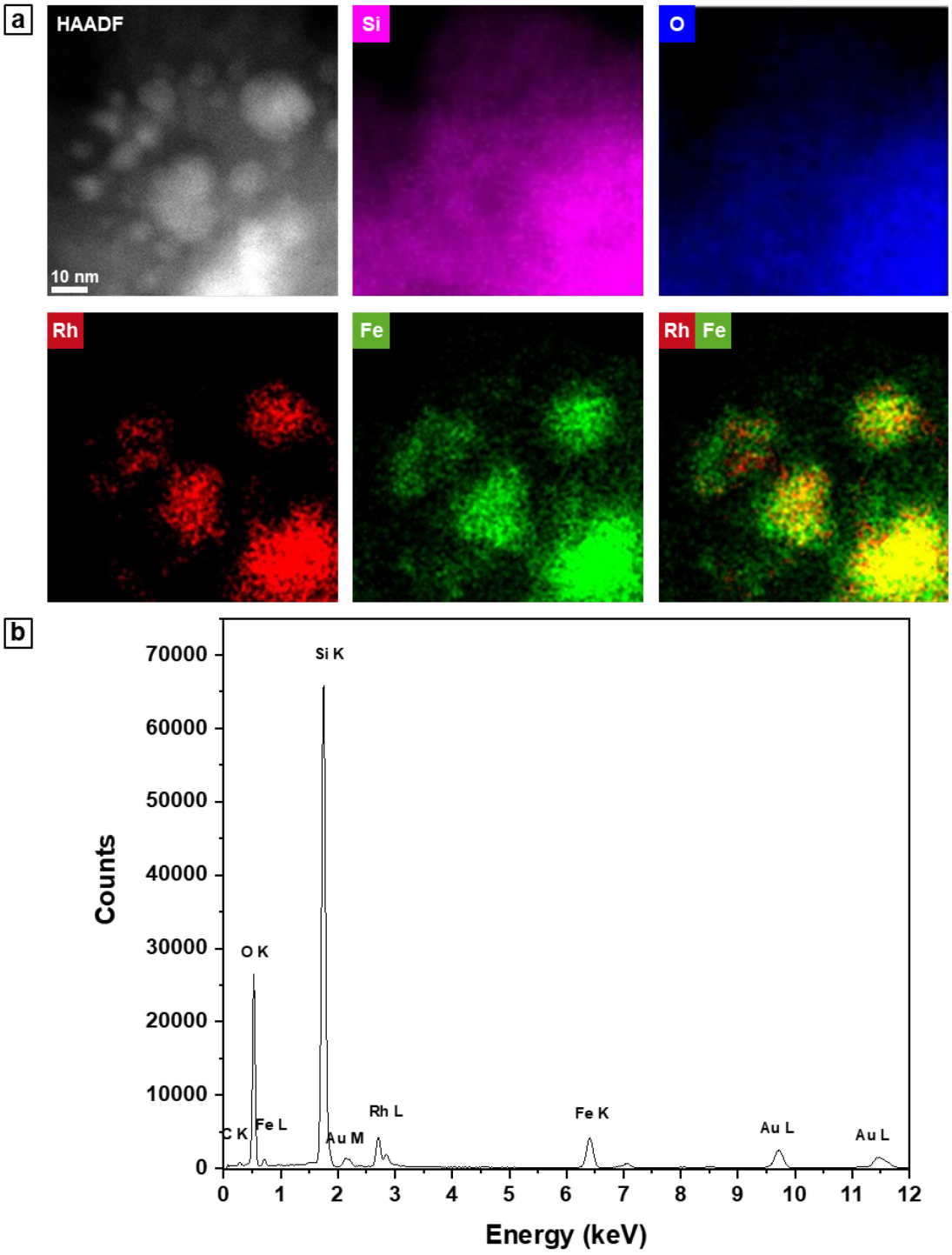

Figure S5.8. STEM-EDX analysis of spent RhFe/FeO_x/SiO_2 catalyst: (a) HAADF micrograph, single-element maps (Rh L, Si K, O K, Fe K), and (b) corresponding EDX spectrum. Au from TEM grids used.

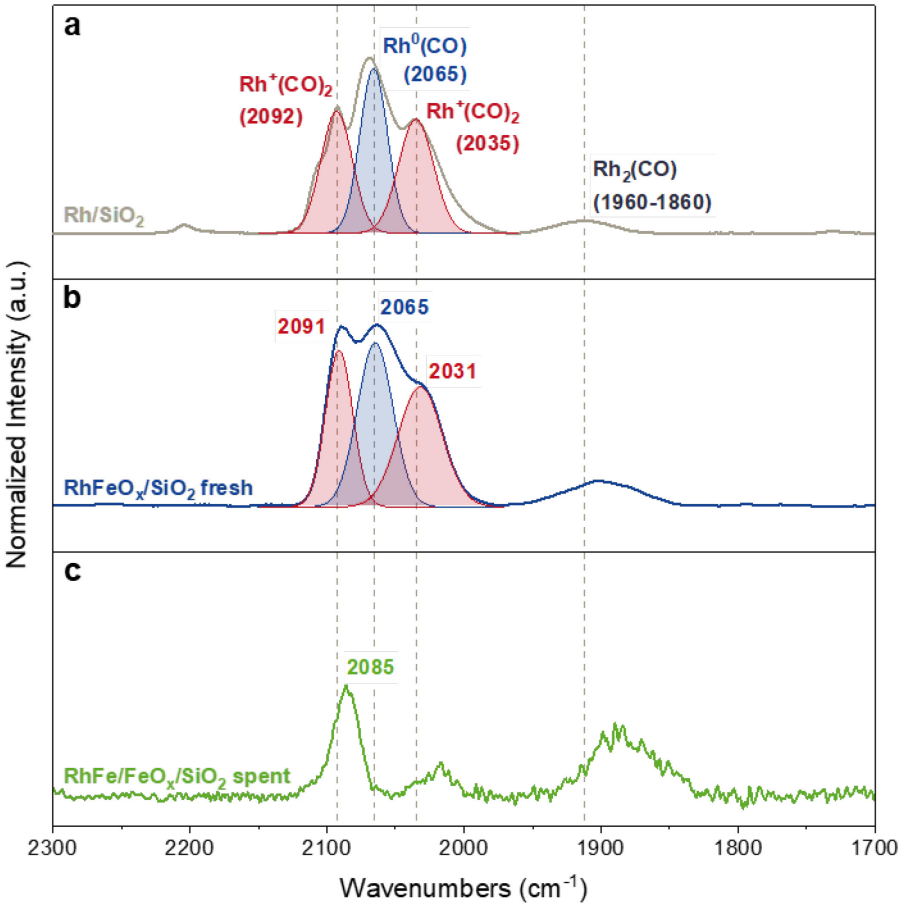

Figure S5.9. DRIFT spectra of (a) fresh Rh/SiO_2 reference catalyst (grey) after *in situ* H_2 activation at 260 °C, (b) fresh $RhFeO_x/SiO_2$ catalyst (blue), and (c) spent $RhFe/FeO_x/SiO_2$ catalyst (green) after catalytic testing. Stretching vibration band positions (as wavenumbers) of *gem*-dicarbonyls $Rh^+(CO)_2$ (red), linear adsorbed CO (blue), and bridged CO (black) on Rh/SiO_2 are highlighted as dashed lines.

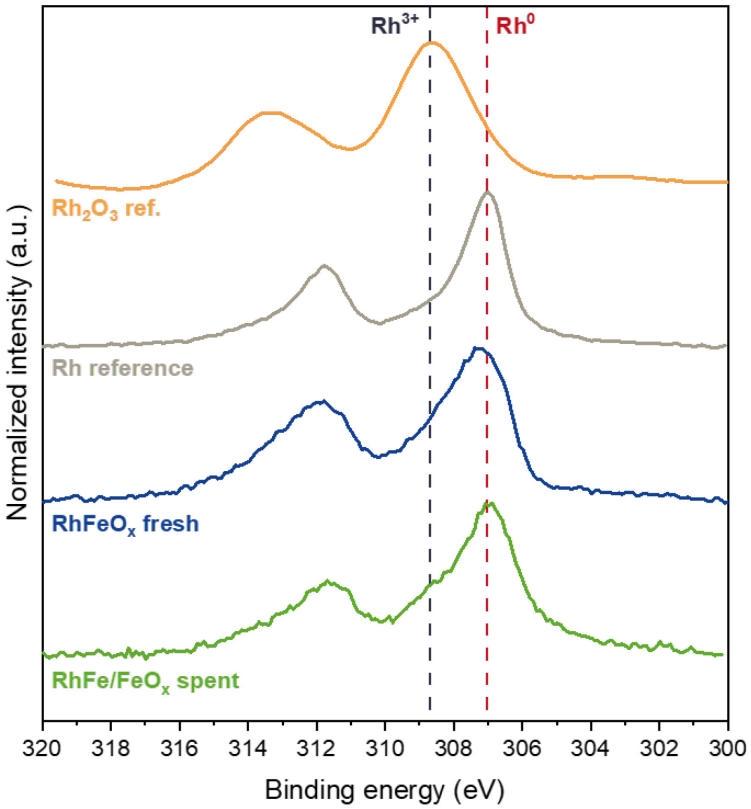

Figure S5.10. Rh 3d XP spectra of calcined Rh_2O_3/SiO_2 reference (orange), reduced Rh/SiO_2 reference (grey), fresh $RhFeO_x/SiO_2$ (blue), and spent $RhFe/FeO_x/SiO_2$ (green) samples. Dotted lines indicate binding energy shifts of oxidized Rh^{3+} (black) and metallic Rh^0 (red) from reference samples.

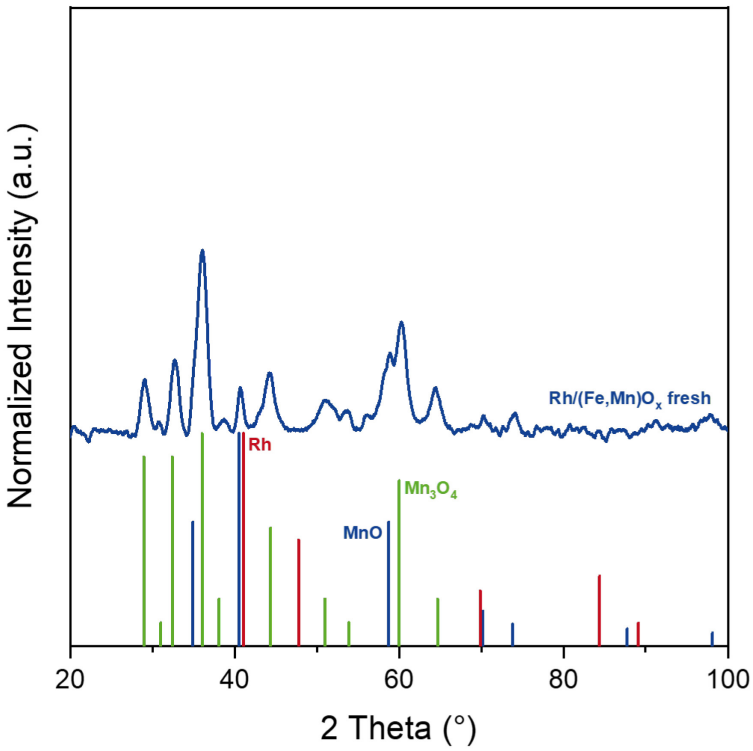

Figure S5.11. X-ray diffractogram of fresh Rh/(Fe,Mn)O_x catalyst. The three most intense reflections are consistent with Mn_3O_4 reference (blue). Furthermore, reflections of a MnO phase (green) were observable. Rh (red, C5-685), MnO (blue, C7-230), and Mn_3O_4 (C18-803) references were taken from ICDD database.

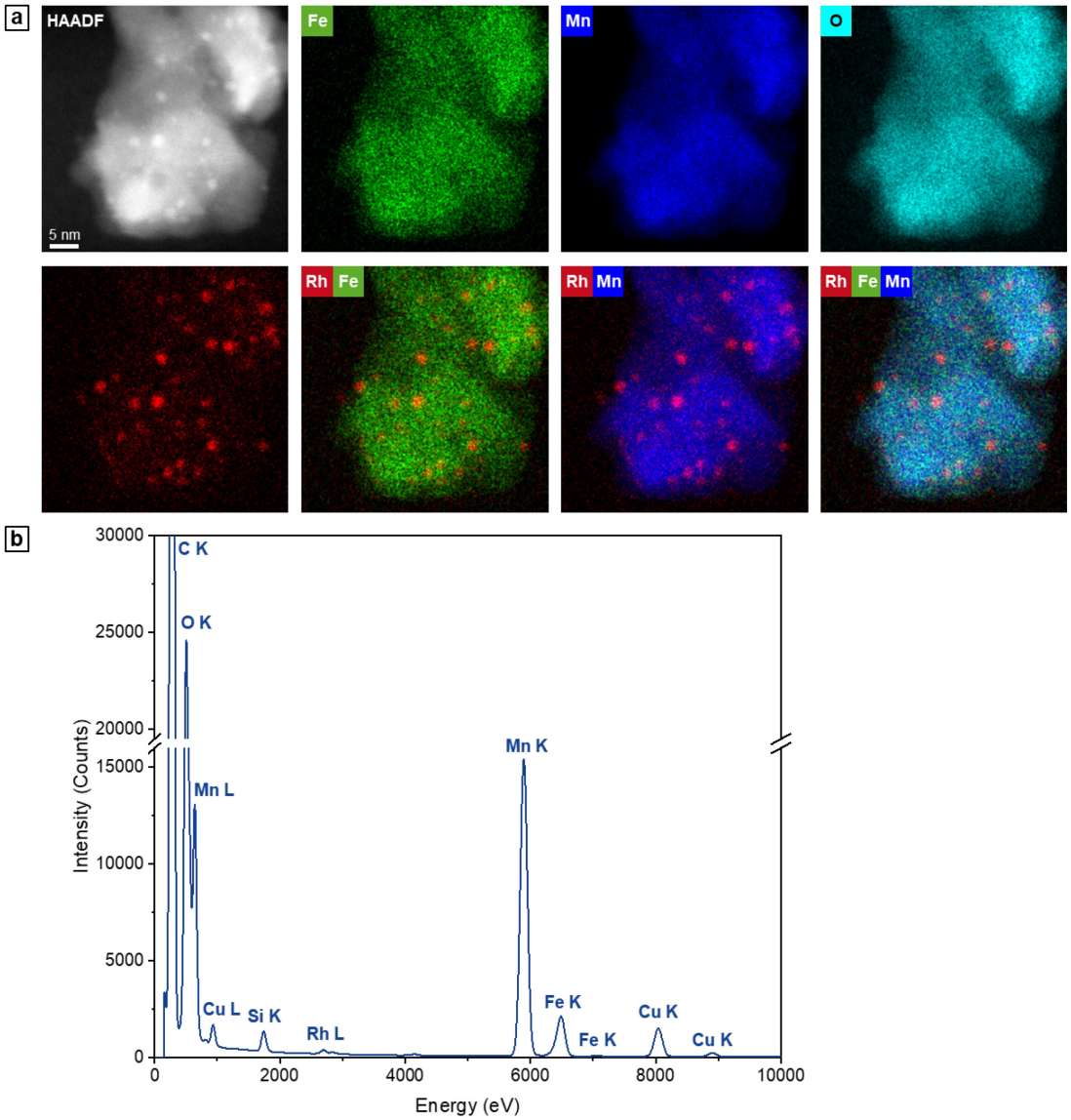

Figure S5.12. STEM-EDX analysis of fresh Rh/(Fe,Mn)O_x catalyst: (a) HAADF micrograph, single-element maps (Fe K, Mn K, O K, Rh L), and (b) corresponding EDX spectrum. Cu and Si signals from TEM grids used and silicon drift detectors, respectively.

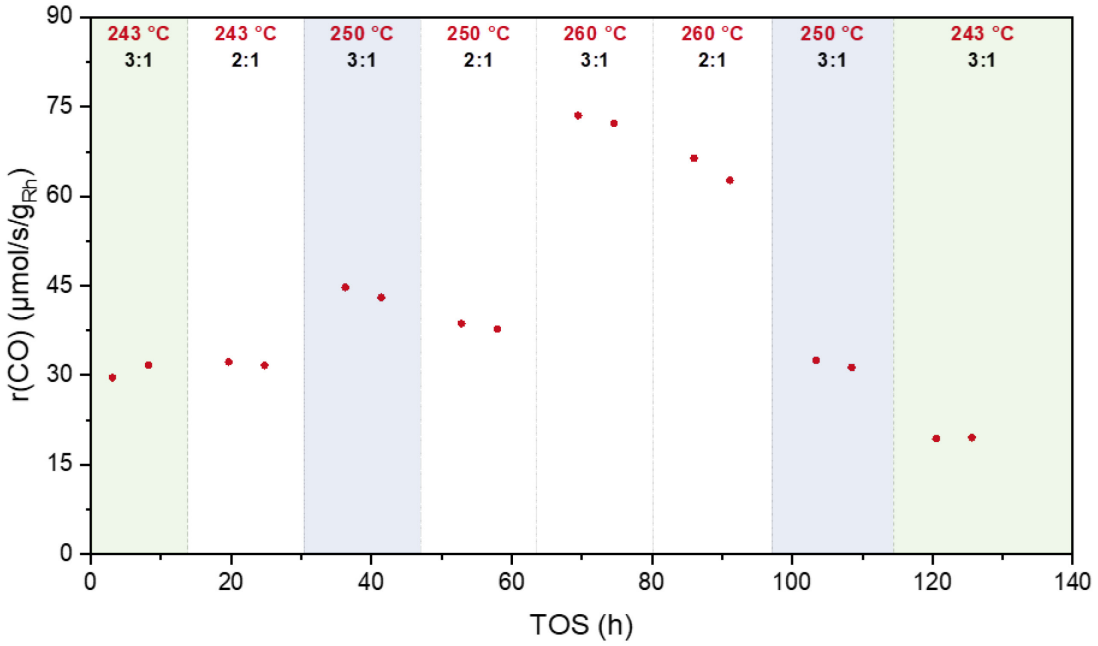

Figure S5.13. CO consumption rate of Rh/(Fe,Mn)O_x catalyst over time on stream. Areas with same color indicate reference conditions. Measuring conditions: 243–260 °C, 54.0 bar, p(H_2) = 32.4 bar, p(CO) = 10.8 bar for H_2:CO = 3:1 and 16.2 bar for H_2:CO = 2:1, GHSV 3500 h^{-1}.

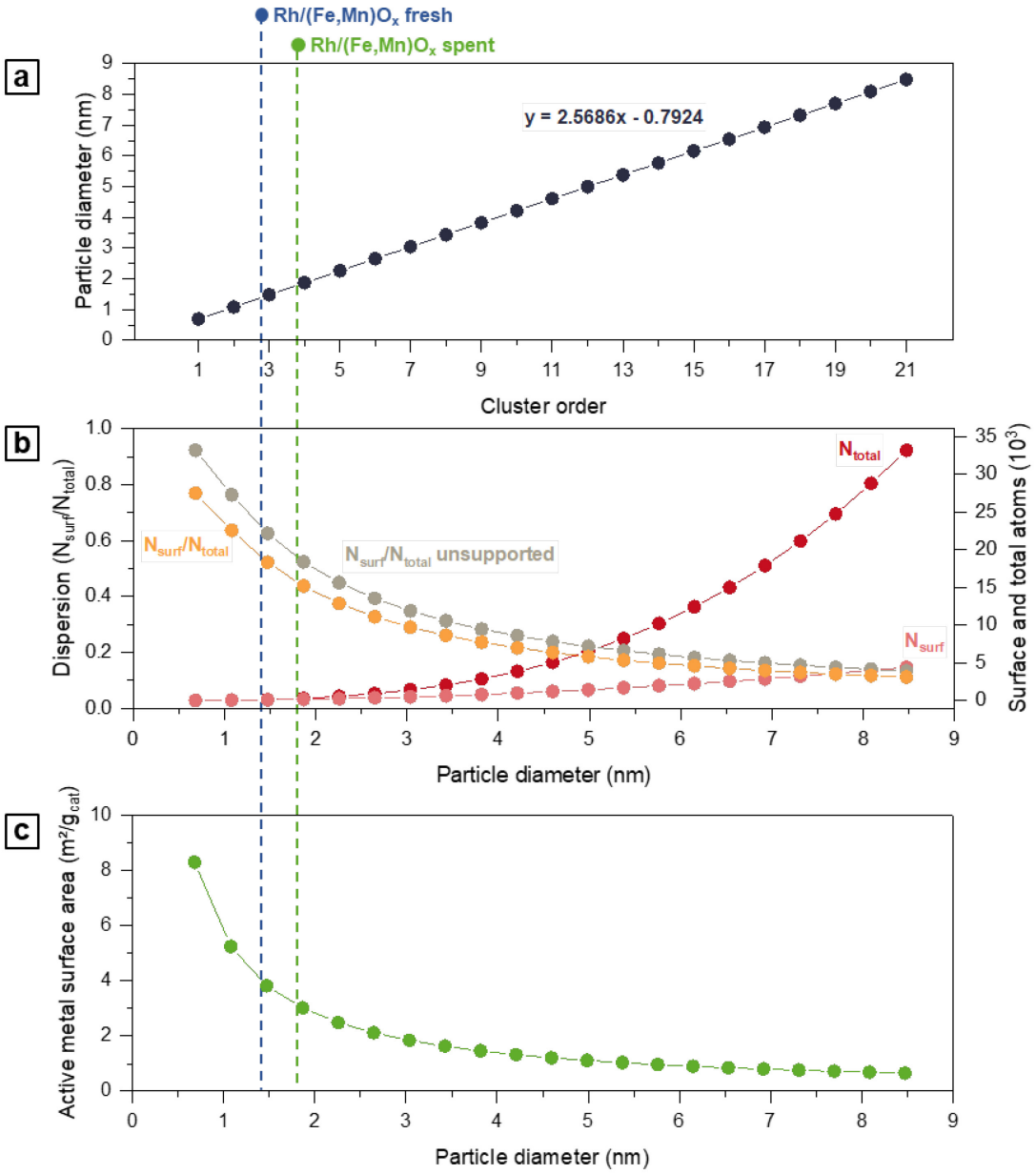

Figure S5.14. Cuboctahedral model of fcc Rh nanoparticles based on Montejano-Carrizales *et al.*'s metal cluster model.[7] This model has been adopted to calculate metal dispersions and active metal surface areas for the fresh and spent Rh/(Fe,Mn)O_x catalysts from particle size distribution obtained from STEM analysis. A similar procedure has been used for calculating metal dispersion of supported Pd particles from TEM.[8] The cluster model provides an expression of total number of atoms (N_{total}; dark red) as function of cluster order: $N_{total} = (10/3)m^3 + 5m^2 + (11/3)m + 1$.[7] m = 1 represents the smallest metal cluster with only one central atom fully saturated with 12 atoms in the surrounding layer. Successive addition of atomic monolayers leads to an incremental increase in metal order. (a) Calculated particle diameter as function of cluster order. Particle diameters have been calculated from covalent radius (1.345 Å) and effective volume (13.75 Å^3) of Rh.[9] (b) Metal dispersion (N_{surf}/N_{total}; orange) as function of particle diameter. Number of surface atoms (N_{surf}; light red) has been calculated by $N_{surf} = 5m^2 + 1$.[7] (c) Active metal surface area (SA_{metal}) as function of particle diameter. SA_{metal} values have been calculated from area and mass of corresponding Rh cuboctahedrons, and metal loading. Dispersion and active surface metal area of fresh and spent Rh/(Fe,Mn)O_x samples have been determined by converting average particle diameters from STEM into metal cluster orders. Dispersions have been corrected with a reduction factor of 0.83 under assumption of weak metal–support interactions.[10,11]

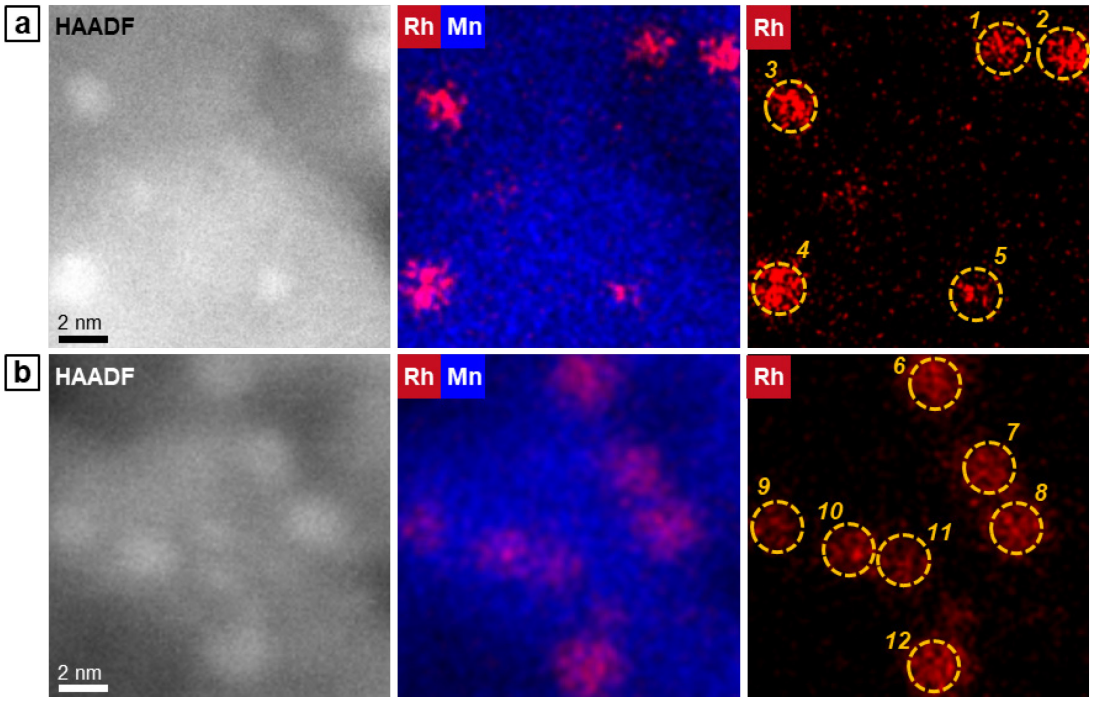

Figure S5.15. HAADF micrographs, STEM-EDX superpositions of Rh L and Mn K, and map of Rh L of (a) fresh and (b) spent Rh/(Mn,Fe)O_x catalyst corresponding to STEM-EDX area-selective analyses. Particles investigated are encircled in yellow. Individual maps of all components and respective EDX spectrum are given in Figures 5.S10 and S12.

Table S5.5. Compositions of Rh and Mn from STEM-EDX area-selective analyses of particles highlighted in Figure S5.15.

Particle	Sample	Composition (wt%)		Mn:Rh ratio
		Rh K	Mn L	
1	Rh/(Fe,Mn)O_x fresh	39.1	60.9	1.6
2		30.9	69.1	2.2
3		33.6	66.4	2.0
4		25.0	75.0	3.0
5		23.7	76.4	3.2
	Average Mn:Rh ratio			2.4
6	Rh/(Fe,Mn)O_x spent	19.4	80.6	4.2
7		20.5	79.5	3.9
8		25.0	75.0	3.0
9		10.6	89.4	8.4
10		21.3	78.7	3.7
11		13.4	86.6	6.5
12		19.4	80.6	4.2
	Average Mn:Rh ratio			4.9

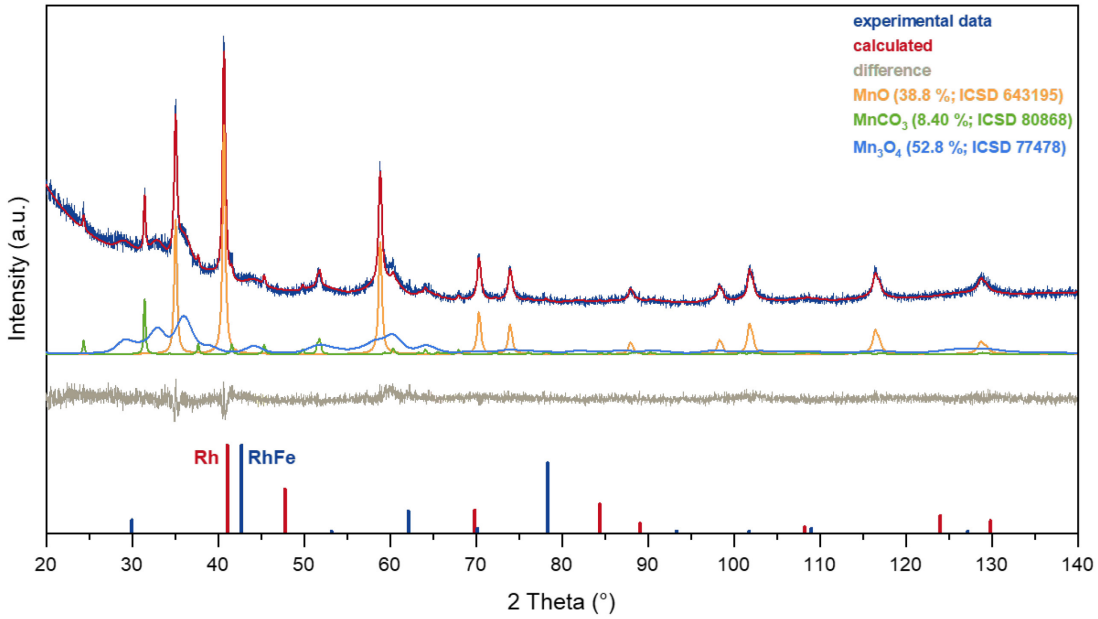

Figure S5.16. X-ray diffractogram (dark blue) and Rietveld fit of spent Rh/(Mn,Fe)O_x catalyst with calculated diffraction pattern (red) and corresponding difference curve (grey). For individual fits of MnO (orange), $MnCO_3$ (green), and Mn_3O_4 (light blue), data from ICSD were used. References for MnO (orange, C7 230), MnCO3 (grey, C44¬ 1472), and (Fe,Mn)Ox (red, C77 2362) were taken from ICDD database. References for Rh (red, C5-685), and Rh_1Fe_1 (blue, C25-1408) were taken from ICDD database.

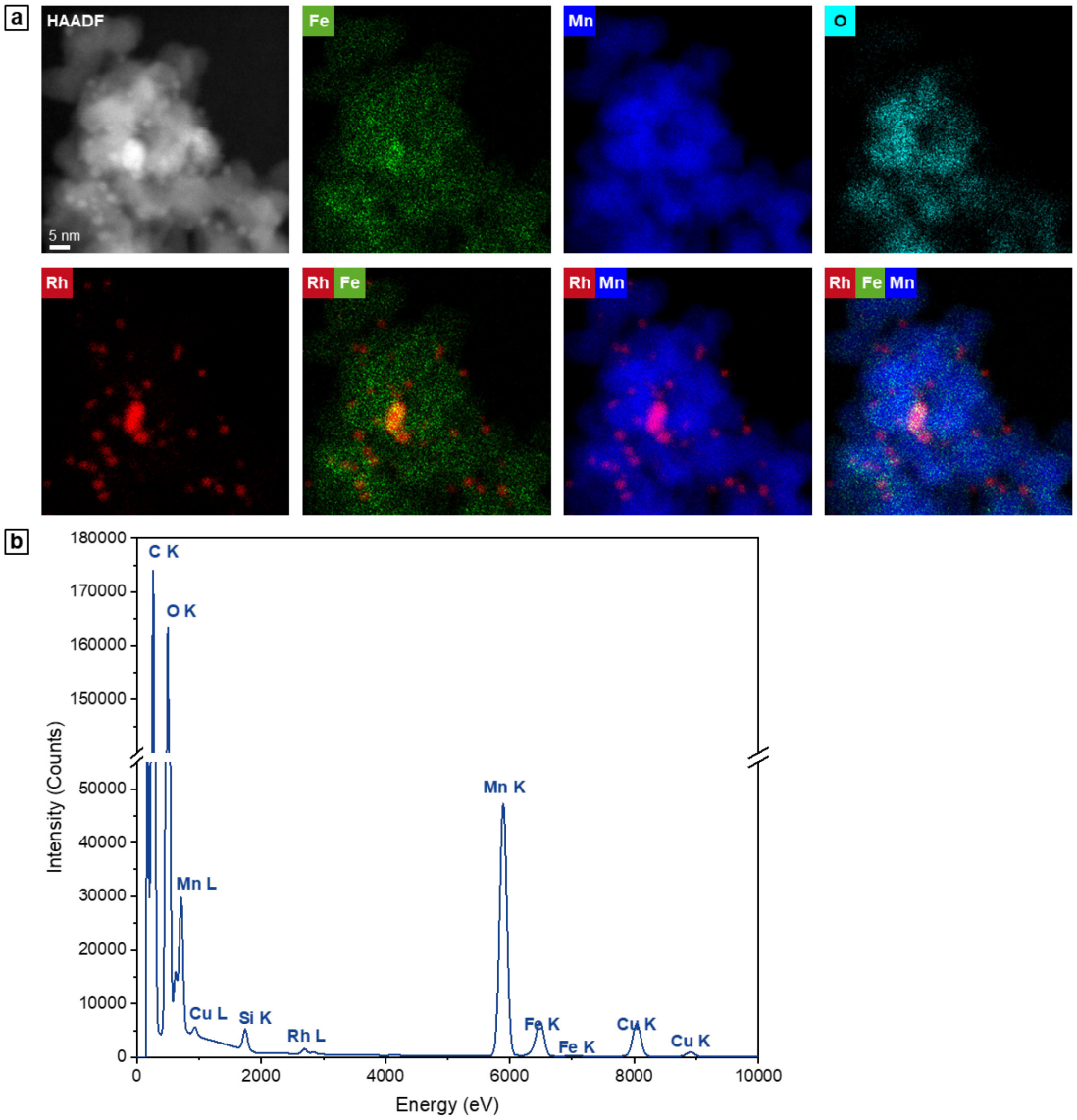

Figure S5.17. STEM-EDX analysis of spent Rh/(Fe,Mn)O_x catalyst: (a) HAADF micrograph, single-element maps (Fe K, Mn K, O K, Rh L), and (b) corresponding EDX spectrum. Cu and Si signals from TEM grids used and silicon drift detectors, respectively.

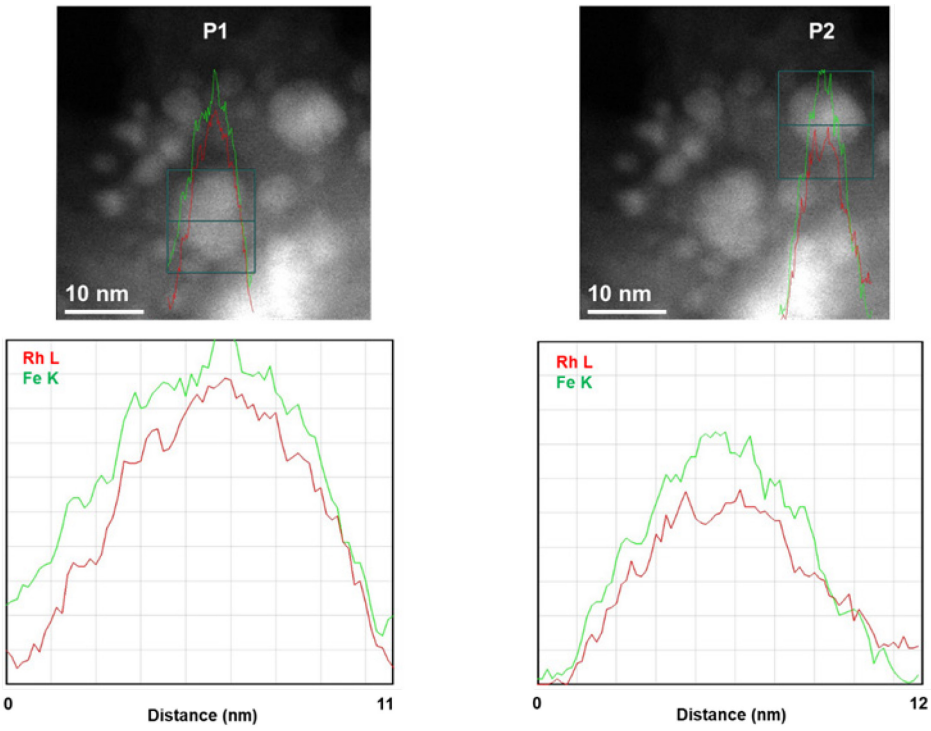

Figure S5.18. Line profile scans of representative RhFe nanoparticles on spent $RhFeO_x/SiO_2$ catalyst.

5.7 References of Supporting Information

(1) Niemantsverdriet, J. W.; Van der Kraan, A. M.; Van Loef, J. J.; Delgass, W. N. In Situ Moessbauer Spectroscopy of Bimetallic Iron-Rhodium (FeRh)/Silica Catalysts at 295 K. *J. Phys. Chem.* **1983**, *87* (8), 1292–1294.

(2) Niemantsverdriet, J. W.; Aschenbeck, D. P.; Fortunato, F. A.; Delgass, W. N. Mössbauer Investigation of Bimetallic FeRu/SiO_2 and FeRh/SiO_2 Fischer-Tropsch Catalysts. *J. Mol. Catal.* **1984**, *25* (1–3), 285–293.

(3) Schuenemann, V.; Trevino, H.; Sachtler, W. M. H.; Fogash, K.; Dumesic, J. A. Characterization of RhFe Clusters in Zeolite NaY by Moessbauer Spectroscopy, XPS, and Temperature-Programmed Reduction. *J. Phys. Chem.* **1995**, *99* (4), 1317–1321.

(4) Wielers, A. F. H.; Kock, A. J. H. M.; Hop, C. E. C. A.; Geus, J. W.; van Der Kraan, A. M. The Reduction Behavior of Silica-Supported and Alumina-Supported Iron Catalysts: A Mössbauer and Infrared Spectroscopic Study. *J. Catal.* **1989**, *117* (1), 1–18.

(5) Prescher, C.; McCammon, C.; Dubrovinsky, L. MossA: A Program for Analyzing Energy-Domain Mössbauer Spectra from Conventional and Synchrotron Sources. *J. Appl. Crystallogr.* **2012**, *45* (2), 329–331.

(6) Ewels, P.; Sikora, T.; Serin, V.; Ewels, C. P.; Lajaunie, L. A Complete Overhaul of the Electron Energy-Loss Spectroscopy and X-Ray Absorption Spectroscopy Database: eelsdb.eu. *Microsc. Microanal.* **2016**, *22* (3), 717–724.

(7) Montejano-Carrizales, J. M.; Aguilera-Granja, F.; Morán-López, J. L. Direct Enumeration of the Geometrical Characteristics of Clusters. *Nanostructured Mater.* **1997**, *8* (3), 269–287.

(8) Feng, H.; Libera, J. A.; Stair, P. C.; Miller, J. T.; Elam, J. W. Subnanometer Palladium Particles Synthesized by Atomic Layer Deposition. *ACS Catal.* **2011**, *1* (6), 665–673.

(9) Mori, T.; Hegmann, T. Determining the Composition of Gold Nanoparticles: A Compilation of Shapes, Sizes, and Calculations Using Geometric Considerations. *J. Nanoparticle Res.* **2016**, *18* (10), 295.

(10) Torrente-Murciano, L. The Importance of Particle-Support Interaction on Particle Size Determination by Gas Chemisorption. *J. Nanoparticle Res.* **2016**, *18* (4), 1–7.

(11) Agostini, G.; Pellegrini, R.; Leofanti, G.; Bertinetti, L.; Bertarione, S.; Groppo, E.; Zecchina, A.; Lamberti, C. Determination of the Particle Size, Available Surface Area, and Nature of Exposed Sites for Silica−Alumina-Supported Pd Nanoparticles: A Multitechnical Approach. *J. Phys. Chem. C* **2009**, *113* (24), 10485–10492.

6 Summary

It is widely accepted that a close proximity of promoter and Rh as active metal is needed for effective ethanol synthesis from syngas.[1–4] Although the influence of Fe and Mn on the reactivity of Rh-based catalysts is often reasoned in this immediate vicinity of Rh and its promoters, it should be considered more as a prerequisite for developing specific Rh–promoter interactions. However, a fundamental understanding of these interactions is still missing hampering a rational design of new catalysts.

This thesis aimed to elucidate specific promoter effects of Fe and Mn in traditionally prepared catalysts through precise metal-organic synthesis approaches. As most publications focus on catalysts from metal salt precursors, a literature-reported $RhMnFe/SiO_2$ catalyst from the respective metal nitrates has been identified for a comprehensive formation phase and stability study. This study has been covered by the publication entitled "Formation, dynamics, and long-term stability of Mn- and Fe-promoted Rh/SiO_2 catalysts in CO hydrogenation" and will be referred to as **Paper 1**.

As a result, a synthesis approach based on heterobimetallic metal-organic precursors has been developed and reported in **Paper 2** for a Mn-promoted Rh/SiO_2 catalyst given the title "From a molecular single-source precursor to a selective high-performance $RhMnO_x$ catalyst for the conversion of syngas to ethanol".

The same metal-organic approach has been chosen to investigate the RhFe nanoalloy formation in **Paper 3**, "Tuning the Rh–FeO_x interface in ethanol synthesis through formation phase studies at high pressures of synthesis gas". Besides a detailed characterization of an SSP-derived $RhFeO_x/SiO_2$ catalyst before and after the formation phase, a novel high surface area Mn_2O_3 support has been used to stabilize the Rh–FeO_x interface.

6.1 Molecular Single-Source Precursor Approach

The alloy formation is a pivotal element in syngas conversion over promoted Rh-based catalysts and is often reported as responsible for ethanol synthesis for Fe- and Mn-promoted Rh catalysts.[5–7] Traditional preparation methods might suffer from inhomogeneous distribution of the active metal and promoters over the support. Thus, a constant metal–promoter ratio is often not reachable on an atomic level, which might hinder nanoalloy formation. For instance, the STEM-EDX analysis of the spent $RhFe/SiO_2$ catalyst within **Paper 1** indicated nanoalloy formation. However, no exact RhFe alloy composition could be determined from compositional analysis based on EDX area-selective investigations due to different degrees of alloying for the nanoparticles investigated. Besides Rh-rich alloy nanoparticles, even pure Rh nanoparticles were found.

For this reason, a synthesis approach based on molecular single-source precursors (SSPs) has been developed and reported in **Paper 2**, which has been further applied within **Paper 3**. For this synthesis approach, a suitable SSP with predefined Rh–Me (Me = Fe or Mn) bonds and highly volatile CO ligands is impregnated on an oxide support. As a prerequisite, the Rh–Me bonds of the supported $[RhMe(CO)_n]$ cluster should remain intact after impregnation. After the cluster's integrity has been proven, the silica-supported $[RhMe(CO)_n]$ cluster is transferred into the final bimetallic catalyst through a mild thermal treatment under a reductive atmosphere. Finally, the respective nanostructure formed during the decomposition of the supported SSP is mainly controlled by specific metal–support interactions and enthalpy of alloy formation, yielding segregated or nanoalloyed structures (Figure 6.1).

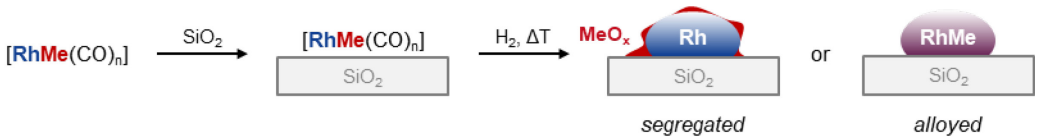

Figure 6.1. Single-source precursor (SSP) approach. A heterobimetallic precursor with predefined Rh–Me bonds is impregnated on an oxide support and transferred into an active catalyst with segregated or alloyed nanostructures.

Assuming that the enthalpy of alloy formation is significantly lower through already predefined heterobimetallic bonds, the SSP approach provides the optimal conditions for nanoalloy formation. However, the resulting nanostructure can usually not be predicted from simple thermodynamic calculations or bulk phase diagrams. In fact, nanoalloys might be formed even though the corresponding bulk alloy might not be stable and *vice versa*. In this manner, even metals immiscible in the bulk could be realized as nanosized alloy structures.[8,9]

Whereas the literature-reported $[RhFe_2(CO)_{11}]^-$ carbonyl cluster has been identified as appropriate for the synthesis of a $RhFe/SiO_2$ catalyst (**Paper 3**), no suitable [RhMn] SSP has been found in the literature. For this reason, the first molecular carbonyl RhMn cluster $[Rh_3Mn_3(CO)_{18}]^{2-}$ has been synthesized and fully characterized (**Paper 2**). However, as proven by extended HRTEM and STEM-EDX analyses, the decomposition of the silica-supported SSPs resulted in segregated nanostructures of Rh particles surrounded by FeO_x and MnO phases, respectively (**Paper 2** and **3**). The formation of segregated nanostructures is most likely induced by strong support interactions of Fe and Mn with the silica surface. This assumption has been proven in **Paper 2** by the impregnation of the metalate $Na[Mn(CO)_5]$, bearing Mn in the low oxidation state of –1, on silica. The surface reaction caused the immediate oxidation of the metalate, and the preparation of a zero-valent Mn species could not be realized.

Nevertheless, in all SSP-derived catalysts of **Paper 2** and **3**, significantly smaller Rh nanoparticles could be synthesized compared to the traditionally prepared catalysts of

Paper 1. With mean particle sizes of 1.3 and 1.7 nm, the Rh nanoparticles on the SSP-derived $RhMn/SiO_2$ and $RhFe/SiO_2$ catalysts were about 48 % and 41 % smaller compared to the traditionally prepared catalysts. Furthermore, detailed STEM-EDX investigations revealed that a more uniform spatial distribution of Mn and Fe at the Rh–promoter interface could be realized. This increase in interfacial sites led to higher initial ethanol selectivities of the SSP-derived catalysts than the $RhMn/SiO_2$ and $RhFe/SiO_2$ catalysts from **Paper 1**. Specifically, the ethanol selectivity over the $RhMn/SiO_2$ catalyst could be substantially increased by a factor of 1.54 from 15.7 to 24.1 % (compared at iso-conversion of 17 %). This ethanol selectivity in **Paper 2** is among the highest selectivities reported for single-promoted RhMn catalyst in CO hydrogenation.

To summarize, the SSP approach leads to well-defined metal–promoter ratios on an atomic level through predefined metal–metal bonds in the SSP. Although the formed nanostructures cannot be predicted, a close proximity of the active metal and promoter can be realized as an alloy or segregated nanostructures. In the case segregated structures have been formed, a better spatial distribution can be reached, creating more interfacial sites.

6.2 Promoter Effects in Rh/SiO_2 Catalysts

The roles of Mn and Fe as promoters or modifiers in traditionally prepared catalysts have been controversially discussed in past literature. However, the influence of Mn and Fe on Rh's morphological and electronic properties needed to be clarified before more sophisticated catalyst design strategies became viable. Several publications focused on multi-promoted Rh-based catalysts, as they demonstrated the most promising results in ethanol synthesis so far. Nonetheless, profound knowledge about the single-promoted $RhMn/SiO_2$ and $RhFe/SiO_2$ catalysts was necessary to combat the complexity of the multi-promoted $RhMnFe/SiO_2$ catalyst and identify prospective co-promotional effects. For this reason, the unpromoted and single-promoted catalysts have been systematically investigated besides the complex multi-promoted $RhMnFe/SiO_2$ catalyst in **Paper 1**. These four catalysts have been synthesized from metal nitrates and thoroughly characterized in different states: calcined, reduced, and after catalysis.

In addition, the formation and stability of unpromoted and promoted Rh-based catalysts have rarely been investigated in the past.[4] However, the distinct interactions of Fe and Mn with Rh develop during a relatively long time on stream of up 120 h under reaction conditions and are significantly different from those at the beginning of the catalytic tests. With about 60 h on stream,[7] the longest reported catalytic investigation does not even cover the critical formation phase observed in the long-term catalytic study of **Paper 1** or the *in situ* RhFe nanoalloy formation of **Paper 3**. These publications demonstrate thereby the relevance of investigating the formation of catalysts during this initial time period.

In the following chapters, the specific promoter effects of Mn and Fe on Rh/SiO_2 will be discussed based on the findings of the single-promoted catalysts from metal nitrates of **Paper 1** and the SSP-derived catalysts from **Paper 2** and **3**. Furthermore, a short discussion of prospective co-promotional effects in the multi-promoted Rh/SiO_2 catalyst is given.

6.2.1 Syngas Conversion at the Rh–MnO_x Interface

The actual nanostructure of Mn-promoted Rh/SiO_2 catalysts has been controversially discussed. Whereas several publications report MnO as the prevailing phase and Rh–MnO interfacial sites as vital for ethanol formation, RhMn nanoalloys have been proposed from theoretical studies to enhance activity and selectivity toward ethanol in syngas conversion.[10,11] Additionally, Mei *et al.* have suggested that RhMn nanoalloy structures formed under syngas conditions by *ex situ* XRD, XPS, and TEM investigations. They further assumed that RhMn nanoalloys might be formed under reaction conditions and will segregate once exposed to air, yielding a MnO passivation layer.[12]

STEM-EDX elemental mapping on the reduced $RhMn/SiO_2$ catalyst of **Paper 1** suggested that Rh is not alloyed with Mn. Moreover, a MnO shell was not observed in the spent $RhMn/SiO_2$ catalyst by STEM-EDX as expected from segregated RhMn nanoalloys upon air contact. To further prove a prospective nanoalloy formation, the SSP approach under a reductive atmosphere has been chosen to retain Mn's low oxidation state and use optimal nanoalloy formation conditions in **Paper 2**. Lattice fringes analysis on HRTEM images revealed crystalline Rh nanoparticles, and STEM-EDX further confirmed that Mn is in the vicinity of Rh.

Although $Na_2[Rh_3Mn_3(CO)_{18}]$ has been used as SSP with both metals in low oxidation states, XPS without air contact shows typical binding energies of oxidized Mn in the corresponding high-resolution Mn 2p spectra. Following the XPS results from **Paper 1**, Mn is most likely in a formal oxidation state of +2 due to typical satellite peaks in the respective Mn 2p spectra. Consequently, it is assumed that Rh–MnO interfacial sites are the prevailing phase, and RhMn nanoalloy structures are most likely not formed on silica supports.

Statistical particle size analysis of the reduced $RhMn/SiO_2$ catalyst revealed a significantly lower mean particle diameter of 2.4 nm compared to the unpromoted Rh/SiO_2 catalyst with 2.9 nm (**Paper 1**). The SSP approach in **Paper 2** led to even smaller Rh nanoparticles with a mean particle size of 1.3 nm. Mn addition does not change Rh's intrinsic product spectrum. Consequently, it is assumed that Mn serves more likely as a structural modifier (Figure 6.2).

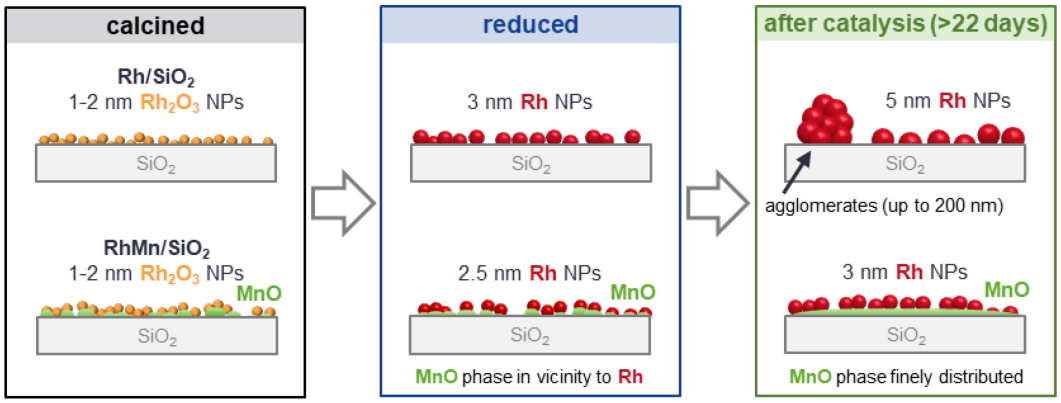

Figure 6.2. Mn serves as structural modifier on Rh-based catalysts yielding smaller nanoparticles on freshly reduced samples. After catalysis, Rh particles are less sintered on Mn-containing samples, and no agglomerates have been formed. Thus, Mn mainly retards sintering and particle agglomeration.

This assumption is further supported by current literature proposing that Mn does not influence Rh's electronic properties.[13] Hence, this higher Rh dispersion might result in more Rh–MnO_x interfacial sites present on Mn-promoted Rh/SiO_2 catalysts and on SSP-derived catalysts, in particular. Finally, the apparent increase in Rh–MnO interfacial sites led to a significantly higher selectivity toward ethanol. In addition, only a slight particle growth and no agglomeration of particles have been observed for all RhMn/SiO_2 catalysts after catalysis (**Paper 1** and **3**). Therefore, Mn mainly retards sintering and prevents particle agglomeration.

6.2.2 Syngas Conversion at the Rh–FeO_x Interface

In contrast to the Mn-promoted Rh catalysts, the addition of Fe led to a strongly altered product composition compared to the Rh/SiO_2 catalyst. The RhFe/SiO_2 catalyst produces methanol as the main product with a selectivity of 50 %, whereas unpromoted Rh/SiO_2 demonstrates almost no methanol selectivity. Therefore, the addition of Fe leads to a tremendous loss of C–C coupling ability reflected in an overall C_{2+} oxygenate selectivity below 20 %, which is the lowest among the catalysts investigated. These findings illustrate that Fe serves as an electronic modifier on Rh/SiO_2 (**Paper 1**).

Representative STEM-EDX analysis of the RhFe/SiO_2 catalyst before and after catalysis indicates the *in situ* formation of RhFe nanoalloy structures. However, an exact composition could not be determined in **Paper 1**. Compositional analysis based on STEM-EDX area-selective investigations yielded a mean Rh:Fe ratio of 3:1. Nonetheless, the composition of the observed RhFe nanoalloy structures differ significantly from 1.4–5.7, and even pure Rh particles have been found. Furthermore, an indication of metallic Fe as expected for a RhFe alloy phase was not observed in the corresponding high-resolution Fe 2p spectrum showing mainly oxidized Fe. Due to the low Fe content and ultimately low signal-to-noise ratio, a prospective contribution of metallic Fe might be hidden by the observed oxide phase. Lastly, it should be noted that with a Rh:Fe bulk

composition of 3:1 and separated metal precursors, the conditions were not ideal for RhFe alloy formation, considering Rh_1Fe_1 as the thermodynamically most stable phase.

Since **Paper 1** suggested that the reactivity of Fe-promoted Rh/SiO_2 catalysts depends on reaction time, a formation phase study has been covered by **Paper 3**. At the beginning of the catalytic test, the conversion of syngas over $RhFeO_x$ yields mainly methane, methanol, and ethanol in similar selectivities. With an oxygenate selectivity of 62.0 %, the SSP-derived $RhFeO_x/SiO_2$ catalyst ranges among the most selective Rh-based catalysts, according to the review by Luk and co-workers.[4] Throughout the formation phase (1–122 h on stream), a significant change in the MeOH:EtOH selectivity ratio from 1 to 7 has been observed. This change in selectivity was probably caused by a structural transformation from an unalloyed $RhFeO_x/SiO_2$ to an alloyed $RhFe/FeO_x/SiO_2$ nanostructure (Figure 6.3). This nanoalloy formation has been proven by integral and local characterization methods (XRD, XPS, HRTEM, STEM-EELS, STEM-EDX, and Mössbauer) before and after the formation phase study.

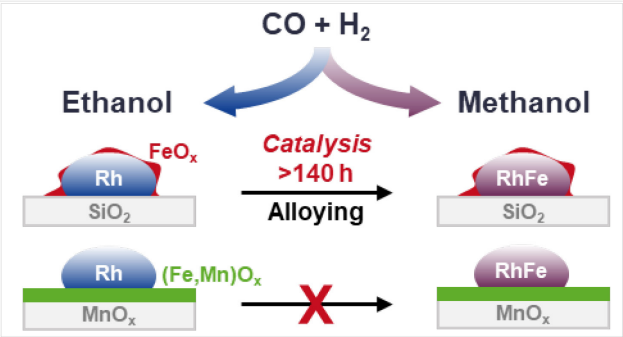

Figure 6.3. Proposed RhFe nanostructures in CO hydrogenation. Initially, metallic Rh nanoparticles are surrounded by a FeO_x (probably Fe_2O_3) phase, and the conversion of syngas yields mainly ethanol. During a formation phase of 140 h on stream, a nanoalloyed $RhFe/FeO_x/SiO_2$ catalyst has been formed resulting in electronic modification of Rh and methanol as main product. Using a novel high surface area MnO_x support caused a decreased Fe mobility and reducibility through formation of a mixed $(Mn,Fe)O_x$ surface oxide. A similar alloying of Rh and Fe has been prevented resulting in stable ethanol selectivities.

Furthermore, this structural transformation was probably induced by the high mobility of Fe and led to a continuous loss of C–C coupling and ethanol formation abilities. With this finding, an explanation for the great variations in reported catalytic results and different nanostructures has been provided. This structure–function relationship finally created the opportunity for new catalyst design strategies by decreasing Fe mobility and reducibility to prevent the RhFe nanoalloy formation and, thus, creating more $Rh–FeO_x$ interfacial sites. As one example, the same RhFe SSP supported on a novel high surface area Mn_2O_3 support has been reported in **Paper 3**. Similar to the $RhFe/SiO_2$ catalyst, decomposition of the supported RhFe cluster on Mn_2O_3 in 10 % H_2/Ar led to relatively small metallic Rh particles with a mean particle size of 1.4 nm. Extended STEM-EDX analysis and XRD indicated the formation of a $(Mn,Fe)O_x$ mixed surface oxide.

Finally, the formation phase of the reduced Rh/(Mn,Fe)O_x catalyst has been investigated under the same conditions applied for the silica-supported RhFe catalyst. In contrast to the RhFe/SiO_2 catalyst, the Rh/(Mn,Fe)O_x catalyst demonstrated a stable ethanol selectivity of 22.1 % (33.7 % on a CO_2-free basis) throughout the catalytic investigation. Likewise, no RhFe nanoalloy structures have been found after catalysis. The formation of the (Fe,Mn)O_x mixed surface oxide probably led to the anchoring of FeO_x to the Mn_2O_3 support and reduced Fe mobility.

6.2.3 Co-Promotion of Fe and Mn

As a co-promotional effect could not be excluded, the multi-promoted RhMnFe/SiO_2 catalyst has been investigated in **Paper 1**. The combination of Mn and Fe as modifiers led to combined effects on Rh's structural and electronic properties. After reduction, the Rh nanoparticles are well-dispersed over the support and not alloyed with Mn or Fe as proven by STEM-EDX. After catalysis, RhFe nanoalloys have been formed surrounded by the MnO phase. Similar to the case of the single-promoted RhMn/SiO_2 catalyst, the nanoparticles are only slightly increased, and no agglomeration occurred.

The overall product spectrum observed for the RhMnFe/SiO_2 catalyst is similar to RhFe/SiO_2 suggesting the electronic modification of Rh through Fe addition. The selectivity toward ethanol has been significantly increased, accompanied by a decrease in methanol selectivity. However, the selectivity toward C_2 oxygenates is significantly lower than that observed for single-promoted RhMn/SiO_2. This lower selectivity might be caused by a co-promotional effect of Mn and Fe. In this manner, the presence of Fe probably leads to fast hydrogenation of formed C_2 oxygenates to ethanol. Since the formation of longer hydrocarbons has also been suppressed, another explanation would be the selective conversion of syngas to ethanol at RhFe–MnO interfacial sites or a combination of both effects.

6.3 Long-Term Stability and Particle Sintering

In past literature, the long-term stability of Rh-based catalysts in CO hydrogenation has only rarely been addressed with a maximum time on stream of 60 h.[7] Likewise, only some of the reported studies about Rh-based catalysts include the characterization of spent catalysts after catalytic investigation.[4] Therefore, a lack of detailed insights into Rh's morphological and electronic properties under high-pressure syngas conditions still exists. Likewise, detailed formation phase studies have not been reported so far, yielding controversial catalytic results in the past. One reason for this discrepancy might be the still existing pressure gap between experimental *in situ*/*operando* and industrially relevant high-pressure conditions.[14,15]

As considering peak performance marks only does not necessarily lead to a suitable catalyst for industrial application, the long-term and thermal stability of Rh-based

catalysts has been investigated in **Paper 1**. Furthermore, with over 22 days on stream time, the reported long-term catalytic study of **Paper 1** is the longest reported catalytic test for Rh-based catalysts in CO hydrogenation yet. In addition, a similar formation phase study for Rh-based catalysts as reported in **Paper 3** has not been covered by the literature so far.

During all catalytic investigations, deactivation of all Rh-based catalysts has been observed. About 80–120 h on stream were required to obtain stable catalytic behavior (**Paper 1–3**). For all Mn-free catalysts, agglomerates with sizes of 20–200 nm have been observed in some areas by STEM after catalysis (**Paper 1** and **3**). High-resolution STEM imaging on the unpromoted Rh/SiO_2 catalyst in **Paper 1** could resolve their individual nanoparticles. However, in most of the investigated areas, an agglomeration to the extent has not been observed.

Besides agglomeration of particles on Mn-free catalysts, particle growth has been observed for all catalysts, following the trends in deactivation. This growth in particle size is probably caused by particle sintering (**Paper 1**). As agglomeration of particles has been observed, sintering over migration of particles followed by coalescence might be excluded. Furthermore, coalescence would probably cause larger particles or aggregates as calculatable from cuboctahedral metal cluster models. Another way for particle sintering and described as the most important sinter mechanism is the migration of atoms through Ostwald ripening.[16]

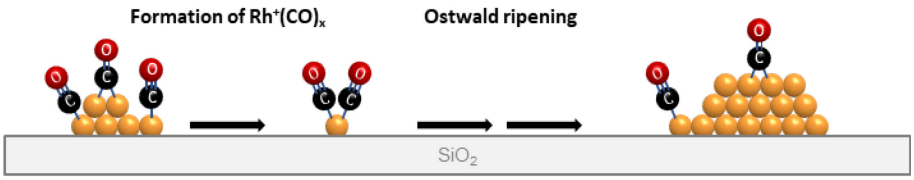

Figure 6.4. Proposed mechanism of particle growth through Ostwald ripening: CO-induced particle disintegration and formation of atomically dispersed $Rh(CO)_2$ dicarbonyls. Migration of these surface dicarbonyls over the hydroxylated SiO_2 support leads to particle growth through sintering under the expense of smaller particles and metal clusters (Ostwald ripening).

As described within **Paper 1**, some studies proposed that metallic Rh clusters and nanoparticles can disintegrate into isolated Rh^+ sites through CO chemisorption.[17] The role of these isolated Rh^+ sites in CO hydrogenation is still under debate and controversially discussed. Although, it is proposed that CO/CHO insertion into $Rh–CH_x$ bonds occurs over these sites, the stability and reactivity of $Rh^+(CO)_2$ dicarbonyl or $Rh^+CO(H)_x$ (x = 1 or 2) carbonyl hydride species under relevant reaction conditions is not clarified yet. Assuming that isolated Rh^+ sites can be formed under reaction conditions, a prospective disintegration of Rh nanoparticles or clusters should not be considered alone as a dynamic interplay between disintegration and ripening is rather likely under reaction conditions (Figure 6.4). Similar to Ostwald ripening in cobalt Fischer-Tropsch catalysts,[18] particle growth might occur through $Rh^+(CO)_x$ migration over the

hydroxylated silica surface. This sinter mechanism becomes viable when considering the high amount of water produced during the conversion of syngas over Rh-based catalysts. However, further experimental and theoretical investigations are required for a clear proof.

Besides a prospective deactivation through Ostwald ripening in **Paper 1**, coke formation might also contribute, as discussed in **Paper 3**. The formation of coke has been proven by elemental analysis before and after catalysis. The relative amount of carbon formed during the catalytic conversion of syngas over the Rh/(Fe,Mn)O_x catalyst was about 0.49 wt%. Although this amount seems to be relatively low compared to coke formation on reforming and dehydrogenation catalysts, which usually ranges from 6–9 wt%,[19–21] a respective contribution to the deactivation cannot be entirely excluded.

To conclude, the initial deactivation of Rh-based catalysts within the first 120 h on stream is most likely caused by particle sintering through CO-induced Ostwald ripening. This finding is in agreement with the usual time scales for Ostwald ripening observed in different catalyst systems.[16] A contribution by coke formation cannot be excluded and might explain the relatively slow deactivation after the initial period. Although particle agglomeration has been observed, it is assumed that it plays a minor part in deactivation.

6.4 Conclusion and Outlook

In the presented work, Mn- and Fe-promoted Rh catalysts have been investigated in the direct conversion of synthesis gas to ethanol under industrially relevant reaction conditions. A combination of metal-organic synthesis approaches, detailed catalysts characterization, formation phase studies, and long-term catalytic investigations led to the identification of specific Rh–promoter interactions.

The thorough analysis of traditionally prepared catalysts before and after long-term (>22 days) and high-temperature (up to 320 °C) investigations provided a detailed view on surface compositions, electronic properties, and morphologies of promoted Rh/SiO_2 catalysts (**Paper 1**). Since this study suggested the importance of controlling the Rh–promoter interactions in the form of nanoalloy formation or creation of interfacial sites, a synthesis approach based on metal-organic precursors has been developed (**Paper 2**). This single-source precursor (SSP) approach provides the optimal conditions for supported nanoalloy formation or a high control of interfacial site creation due to a more uniform spatial distribution of Rh and the promoter. In **Paper 2**, the Rh–MnO interface could be effectively tuned using a novel Rh_3Mn_3 carbonyl cluster as SSP, yielding the highest reported ethanol selectivity among Mn-promoted Rh catalysts. The SSP approach is thereby a compelling synthesis route toward well-defined bimetallic catalysts. This SSP approach has been further applied to investigate the formation phase of a $RhFeO_x/SiO_2$ catalyst (**Paper 3**). This publication demonstrated the relevance of formation phase studies in CO hydrogenation. However, the CO-induced restructuring and redispersion of nanoparticles should not be limited to Rh-based catalysts. Therefore, it is foreseen that formation phase studies could provide meaningful insights into the structural behavior of other catalytic systems under reaction conditions, such as $CuCo/SiO_2$ or $PtCo/SiO_2$.

The three publications delivered a holistic view of the crucial interplay of Rh-promoter interactions, reaction conditions, and reaction times. Mn serves most likely as a structural modifier retarding particle sintering and preventing agglomeration. The overall product spectrum over Mn-promoted Rh catalysts is thereby similar to unpromoted Rh with an enhanced selectivity toward C_{2+} oxygenates and suppressed methane formation. In contrast, Fe addition significantly alters Rh's intrinsic product spectrum. As the $RhFeO_x/SiO_2$ catalyst drastically changed from an ethanol to a methanol synthesis catalyst, it is suggested that the *in situ* RhFe nanoalloy formation led to the modification of Rh's electronic structure. The combination of Mn and Fe results mainly in combined promotional effects. However, the relatively low C_{2+} oxygenate (without ethanol) and enhanced ethanol selectivity indicate a co-promotional effect of Mn and Fe. Once C_{2+} oxygenates like acetaldehyde and acetic acid are formed at the Rh–MnO

interface, fast hydrogenation leads to an increased ethanol formation over the $RhMnFe/SiO_2$ catalyst.

Nevertheless, RhFe nanoalloy formation results in a significant amount of methanol as a by-product. Furthermore, Fe-containing catalysts are usually less active in terms of the overall CO consumption rate compared to the single-promoted RhMn catalyst. It is consequently proposed that the spatial separation of C_{2+} oxygenate formation over a RhMn catalyst and the hydrogenation toward ethanol over a Fe-containing catalyst could, in principle, warrant the necessary ethanol yields required for an industrial application. Following the similar concept of separating elementary steps in syngas conversion over Rh, another prospective combination would be the formation of methanol over $RhFe/SiO_2$, subsequent methanol carbonylation at Rh^+ single sites, and hydrogenation of acetic acid over a hydrogenation catalyst. Although a similar concept has already been proposed for traditional methanol synthesis catalysts,[22] the combination of RhFe and Rh^+ single sites benefits from similar reaction conditions required for optimal reactant conversion.

Although the addition of Fe demonstrated the highest potential in increasing the ethanol selectivity, the *in situ* formation of nanoalloys must be prevented before RhFe catalysts will become attractive for an effective synthesis of ethanol. Therefore, stabilizing the FeO_x phase at the Rh interface will be necessary to achieve reasonable ethanol yields. However, under the harsh conditions used in StE conversion, the reduction of FeO_x through hydrogen spillover from metallic Rh surface sites is most likely. In **Paper 3**, the *in situ* RhFe nanoalloy formation could be prevented by forming a $(Mn,Fe)O_x$ mixed surface oxide on a high surface area MnO_x support resulting in stable ethanol selectivities. Nevertheless, the use of the MnO_x material as support also led to increased CO_2 formation *via* WGSR. For this reason, additional optimization of such a catalytic system is required. One promising strategy might be the formation of reduction-stable oxide or mixed oxide phases by a tailored support surface modification, e.g., solution layer deposition of Fe and Mn oxides on SiO_2.[23]

Another crucial aspect identified through the three related publications is the stability of Rh-based catalysts over time-on-stream. All Rh-based catalysts deactivated within an initial period of 80–120 h on stream depending on catalyst composition and synthesis approach. This deactivation behavior of Rh-based catalysts has not been reported before as past catalytic studies covered less than 60 h on stream. Likewise, a lack of spent catalyst characterization hindered the identification of deactivation mechanisms. The thorough characterization of the unpromoted and promoted Rh/SiO_2 catalysts of **Paper 1** suggested particle growth through CO-induced sintering. Similar to Ostwald

ripening reported for Co-based FTS catalysts, a migration of atomically dispersed Rh surface species over the hydroxylated silica support might occur, resulting in particle growth under the expense of smaller particles or metal clusters. These isolated Rh surface species are most likely $Rh(CO)_2$ dicarbonyls or $Rh(CO)H_x$ (x = 1–2) carbonyl hydrides. Even though the formation of those Rh^+ carbonyl species has been proven experimentally under ambient pressures, direct evidence under reaction conditions is still missing. Although *operando* experimentation is challenging for a high-pressure syngas reaction, transmission FTIR spectroscopy with a cell design drastically minimizing dead volume might allow the identification of Rh^+ carbonyl species under process-relevant high-pressure conditions. Moreover, direct spectroscopic insights into the formation and stability of these isolated Rh^+ sites might ultimately provide strategies for catalyst regeneration or to avoid deactivation.

In summary, it has been shown that the Rh–metal oxide interface is vital for ethanol synthesis from syngas. Likewise, no indications for a beneficial effect of nanoalloys in the StE reaction have been found. The promotion of Rh-based catalysts with MnO demonstrated that a modification of Rh's electronic structure is not required to increase ethanol formation rates. More importantly, metal oxides seem to stabilize active Rh sites at their interface. Therefore, a close proximity of Rh and promoter is required and can be effectively tuned by the developed SSP approach. These active sites at the Rh–promoter interface might be atomically dispersed Rh probably present as Rh^+ surface carbonyl species under reaction conditions.

Nonetheless, the specific role of these isolated Rh^+ sites has not been clarified yet, although it is proposed that they are of utmost importance for the C–C coupling reaction and selective synthesis of ethanol. Furthermore, the dramatically increased Rh price necessitates the search for alternative catalysts and the replacement of Rh with other noble or non-noble metals. Although promising results have been achieved, Rh-free catalytical systems do not yet meet the requirements for industrial applications, especially for ethanol as target product. Moreover, avoiding the formation of higher alcohols and oxygenates remains challenging if Rh as active metal is replaced in its entirety. The key to reducing the Rh content might lie in the bifunctionality required for ethanol formation. Separating the Rh active sites responsible for CH_x fragment formation and C–C coupling might provide the opportunity of lowering the Rh content, which will be necessary for the cost-efficient synthesis of ethanol. In this manner, replacing the metallic Rh^0 sites with other metals active for CH_x surface fragment formation might be one possible strategy. This strategy, however, requires the stabilization of isolated Rh^+ sites on the support surface. Besides modifying the support surface, two other concepts might be applicable. On the one hand, the anchoring of Rh single sites to the nanoparticle

surface of another metal through the formation of single-atom alloys (SAAs), such as Rh/Cu.[24] On the other hand, the stabilization of Rh single sites in the form of Ga–Rh supported catalytically active liquid metal solutions (SCALMS).[25]

6.5 References

(1) Ao, M.; Pham, G. H.; Sunarso, J.; Tade, M. O.; Liu, S. Active Centers of Catalysts for Higher Alcohol Synthesis from Syngas: A Review. *ACS Catal.* **2018**, *8* (8), 7025–7050.

(2) Huang, X.; Teschner, D.; Dimitrakopoulou, M.; Fedorov, A.; Frank, B.; Kraehnert, R.; Rosowski, F.; Kaiser, H.; Schunk, S.; Kuretschka, C.; Schlögl, R.; Willinger, M.-G.; Trunschke, A. Atomic-Scale Observation of the Metal–Promoter Interaction in Rh-Based Syngas-Upgrading Catalysts. *Angew. Chem. Int. Ed.* **2019**, *58* (26), 8709–8713.

(3) Yang, N.; Yoo, J. S.; Schumann, J.; Bothra, P.; Singh, J. A.; Valle, E.; Abild-Pedersen, F.; Nørskov, J. K.; Bent, S. F. Rh-MnO Interface Sites Formed by Atomic Layer Deposition Promote Syngas Conversion to Higher Oxygenates. *ACS Catal.* **2017**, *7* (9), 5746–5757.

(4) Luk, H. T.; Mondelli, C.; Ferré, D. C.; Stewart, J. A.; Pérez-Ramírez, J. Status and Prospects in Higher Alcohols Synthesis from Syngas. *Chem. Soc. Rev.* **2017**, *46* (5), 1358–1426.

(5) Hartman, T.; Geitenbeek, R. G.; Whiting, G. T.; Weckhuysen, B. M. Operando Monitoring of Temperature and Active Species at the Single Catalyst Particle Level. *Nat. Catal.* **2019**, *2* (11), 986–996.

(6) Carrillo, P.; Shi, R.; Teeluck, K.; Senanayake, S. D.; White, M. G. In Situ Formation of FeRh Nanoalloys for Oxygenate Synthesis. *ACS Catal.* **2018**, *8* (8), 7279–7286.

(7) Mao, W.; Su, J.; Zhang, Z.; Xu, X. C.; Fu, D.; Dai, W.; Xu, J.; Zhou, X.; Han, Y. F. A Mechanistic Basis for the Effects of Mn Loading on C_{2+} Oxygenates Synthesis Directly from Syngas over Rh-MnO_x/SiO_2 Catalysts. *Chem. Eng. Sci.* **2015**, *135*, 301–311.

(8) Zafeiratos, S.; Piccinin, S.; Teschner, D. Alloys in Catalysis: Phase Separation and Surface Segregation Phenomena in Response to the Reactive Environment. *Catal. Sci. Technol.* **2012**, *2* (9), 1787.

(9) Ferrando, R.; Jellinek, J.; Johnston, R. L. Nanoalloys: From Theory to Applications of Alloy Clusters and Nanoparticles. *Chem. Rev.* **2008**, *108* (3), 845–910.

(10) Wang, J.; Liu, Z.; Zhang, R.; Wang, B. Ethanol Synthesis from Syngas on the Stepped Rh(211) Surface: Effect of Surface Structure and Composition. *J. Phys. Chem. C* **2014**, *118* (39), 22691–22701.

(11) Ma, X.; Su, H.; Deng, H.; Li, W.-X. Carbon Monoxide Adsorption and Dissociation on Mn-Decorated Rh(111) and Rh(553) Surfaces: A First-Principles Study. *Catal. Today* **2011**, *160* (1), 228–233.

(12) Mei, D.; Rousseau, R.; Kathmann, S. M.; Glezakou, V.-A.; Engelhard, M. H.; Jiang, W.; Wang, C.; Gerber, M. A.; White, J. F.; Stevens, D. J. Ethanol Synthesis from Syngas over Rh-Based/SiO_2 Catalysts: A Combined Experimental and Theoretical Modeling Study. *J. Catal.* **2010**, *271* (2), 325–342.

(13) Schwartz, V.; Campos, A.; Egbebi, A.; Spivey, J. J.; Overbury, S. H. EXAFS and FT-IR Characterization of Mn and Li Promoted Titania-Supported Rh Catalysts for CO Hydrogenation. *ACS Catal.* **2011**, *1* (10), 1298–1306.

(14) Fischer, N.; Claeys, M. In Situ Characterization of Fischer–Tropsch Catalysts: A Review. *J. Phys. D. Appl. Phys.* **2020**, *53* (29), 293001.

(15) Kim, J.; Choi, H.; Kim, D.; Park, J. Y. Operando Surface Studies on Metal-Oxide Interfaces of Bimetal and Mixed Catalysts. ACS Catal. 2021, 11 (14), 8645–8677.

(16) Hansen, T. W.; DeLaRiva, A. T.; Challa, S. R.; Datye, A. K. Sintering of Catalytic Nanoparticles: Particle Migration or Ostwald Ripening? *Acc. Chem. Res.* **2013**, *46* (8), 1720–1730.

(17) Suzuki, A.; Inada, Y.; Yamaguchi, A.; Chihara, T.; Yuasa, M.; Nomura, M.; Iwasawa, Y. Time Scale and Elementary Steps of CO-Induced Disintegration of Surface Rhodium Clusters. *Angew. Chem. Int. Ed.* **2003**, *42* (39), 4795–4799.

(18) Claeys, M.; Dry, M. E.; van Steen, E.; van Berge, P. J.; Booyens, S.; Crous, R.; van Helden, P.; Labuschagne, J.; Moodley, D. J.; Saib, A. M. Impact of Process Conditions on the Sintering Behavior of an Alumina-Supported Cobalt Fischer–Tropsch Catalyst Studied with an in Situ Magnetometer. *ACS Catal.* **2015**, *5* (2), 841–852.

(19) Martín, N.; Viniegra, M.; Zarate, R.; Espinosa, G.; Batina, N. Coke Characterization for an Industrial Pt–Sn/γ-Al_2O_3 Reforming Catalyst. *Catal. Today* **2005**, *107–108*, 719–725.

(20) Ingale, P.; Guan, C.; Kraehnert, R.; Naumann d'Alnoncourt, R.; Thomas, A.; Rosowski, F. Design of an Active and Stable Catalyst for Dry Reforming of Methane via Molecular Layer Deposition. *Catal. Today* **2021**, *362*, 47–54.

(21) Sahoo, S. K.; Rao, P. V. C.; Rajeshwer, D.; Krishnamurthy, K. R.; Singh, I. D. Structural Characterization of Coke Deposits on Industrial Spent Paraffin Dehydrogenation Catalysts. *Appl. Catal. A Gen.* **2003**, *244* (2), 311–321.

(22) Zhou, W.; Kang, J.; Cheng, K.; He, S.; Shi, J.; Zhou, C.; Zhang, Q.; Chen, J.; Peng, L.; Chen, M.; Wang, Y. Direct Conversion of Syngas into Methyl Acetate, Ethanol, and Ethylene by Relay Catalysis via the Intermediate Dimethyl Ether. *Angew. Chem. Int. Ed.* **2018**, *57* (37), 12012–12016.

(23) Cure, J.; Piettre, K.; Coppel, Y.; Beche, E.; Esvan, J.; Collière, V.; Chaudret, B.; Fau, P. Solution Layer Deposition: A Technique for the Growth of Ultra-Pure Manganese Oxides on Silica at Room Temperature. *Angew. Chem. Int. Ed.* **2016**, *55* (9), 3027–3030.

(24) Hannagan, R. T.; Giannakakis, G.; Flytzani-Stephanopoulos, M.; Sykes, E. C. H. Single-Atom Alloy Catalysis. *Chem. Rev.* **2020**, *120* (21), 12044–12088.

(25) Raman, N.; Maisel, S.; Grabau, M.; Taccardi, N.; Debuschewitz, J.; Wolf, M.; Wittkämper, H.; Bauer, T.; Wu, M.; Haumann, M.; Papp, C.; Görling, A.; Spiecker, E.; Libuda, J.; Steinrück, H. P.; Wasserscheid, P. Highly Effective Propane Dehydrogenation Using Ga-Rh Supported Catalytically Active Liquid Metal Solutions. *ACS Catal.* **2019**, *9* (10), 9499–9507.